The Impact of Maternal Autoantibodies and Immune Signaling Molecules on Postnatal Neurodevelopment

By

MATTHEW BRUCE
DISSERTATION

Submitted in partial satisfaction of the requirements for the degree of

DOCTOR OF PHILOSOPHY

in

Immunology

in the

OFFICE OF GRADUATE STUDIES

of the

UNIVERSITY OF CALIFORNIA

DAVIS

_____

Judy Van de Water, Chair

_____

Pamela J Lein

_____

Athena Soulika

Committee in Charge

2022

Acknowledgements/Dedications:

This work is dedicated to my wife and life partner of nearly a decade for the support, love, and patience that keeps me going through the hard times and provides purpose for my pursuits.

I'd also like to thank my mom, dad, and sister who provided their unwavering support throughout my journey, no matter the number of wayward excursions. I would not be here without you.

Finally, I wouldn't be writing this without my mentor and her husband who opened their home and hearts to us. You will always be the family we chose, and I am forever grateful for your generosity.

To all those that come after, I will do my best to leave the door open. You are more powerful than you realize.

Abstract

Substantial research now suggests that immune cells and related signaling molecules are involved in central nervous system (CNS) development, homeostasis, and disease. Neurodevelopmental disorder (NDD) is one such case where individual or familial autoimmunity and dysregulation of immune cell subsets and specific cytokines have been implicated. A particularly salient example being the role of maternal autoantibodies in autism spectrum disorder (ASD), termed maternal autoantibody related (MAR) ASD. The first chapter of this work will provide the necessary background to understand the above topics and information detailed in subsequent chapters.

To increase our understanding of how a peripheral immune challenge during early life may impact CNS immune signaling, Chapter 2 details a set of experiments where rats were injected peripherally with a cocktail of immune stimulants and effects on the CNS were measured. Luminex analysis of serum and brain region-specific cytokine profiles revealed significantly different immune responses in the CNS compared to the periphery. This finding was accompanied by altered brain glial fibrillary acidic protein (GFAP) and allograft inflammatory factor 1 (IBA1) immunoreactivity in a strain- and sex-dependent manner. These results lay the groundwork for future studies examining CNS immune signaling in response to different peripheral stimuli.

Beyond aberrant cytokine signaling, pro-inflammatory stimuli may lead to the production of autoantibodies (aAbs) that could interfere with target protein function. Chapter 3 describes the effects of endogenous aAb exposure using a mouse model of MAR-ASD, where aAbs present in

maternal circulation are known to target antigens enriched in the developing brain. To examine this concept, mouse dams were induced to create aAbs to MAR-ASD targets and offspring outcomes were assessed postnatally. Findings support that MAR-ASD aAb exposure results in effects on offspring behavior and brain structure that were sex-specific and suggested network-level desynchronization of regional brain volume. Expanding upon these findings, Chapter 4 details a similar design of MAR-ASD aAb exposure using a rat model. Rats were chosen due to the enhanced behavioral and neuroanatomical complexity of rats. Results broadly corroborated findings observed in MAR-ASD mice providing additional insight regarding regional effects on brain volume by sex. Furthermore, the use of magnetic resonance spectroscopy (MRS) revealed altered levels of several neurometabolites in the cortex of rats supporting a molecular basis for MAR-ASD-induced effects.

Research regarding the influence of immune signaling in the CNS is still limited, the studies included herein provide support for robust CNS cytokine response following peripheral induction and the influence of maternally-transferred autoreactive immunoglobulin G (IgG) on neurodevelopmental trajectory of offspring. Chapter 5 provides further details on the significance of these findings, how they may inform therapeutic intervention clinically, and future studies that will be important to understand potential mechanisms of maternal immune influence on neurodevelopment.

Table of Contents

Title Page i

Acknowledgements ii

Abstract iii

Table of Contents v

Chapter 1: Neuroimmune Signaling in the Developing CNS 1

Immune Landscape of Developing Brain 2

Role of the Immune System in Neurodevelopmental Disorders 5

Maternal Autoantibodies in Autism 6

References 9

Chapter 2: Acute Peripheral Immune Activation Alters Cytokine Expression and Glial Activation in the Early Postnatal Rat Brain 15

Abstract 16

Introduction 17

Methods 19

Results 25

Discussion 38

References 45

Supplemental Data 52

Chapter 3: Sexually Dimorphic Neuroanatomical Differences Relate to ASD-relevant Behavioral Outcomes in a Maternal Autoantibody Mouse Model 55

Abstract 56

Introduction 56

Methods 58

Results 60

Discussion 69

References 73

Supplemental Data 77

Chapter 4: Autism-specific Maternal Autoantibodies Alter Behavior, Brain Cysteine Metabolism, and Structural Development in Offspring 95

Abstract 96

Introduction 96

Methods 98

Results 117

Discussion 131

References 139

Supplemental Data 148

Chapter 5: Conclusions and Future Directions 153

References 155

CHAPTER 1

Neuroimmune Signaling in the Developing CNS

Immune Landscape of the Developing Brain

The prevailing dogma for the last century regarding brain immune privilege posited that immune cells were normally restricted from interacting with CNS or sampling brain antigens due to the presence of physiological barriers and the absence of brain lymphatic vasculature (*1*). Support for this concept came from early studies suggesting that brain allografts did not elicit the same pro-inflammatory immune rejection that was seen under conditions of peripheral transplantation (*2*). The result being that immune cells have been historically overlooked in the context of homeostatic brain function and studied almost solely under conditions of cell stress or infection, where barrier breach could occur. However, work in the last decade has led to an upheaval in this doctrine, as it is now understood that immune cells can sample draining CNS antigens in the deep cervical lymph nodes via a newly re-discovered network of brain lymphatic vessels (*3, 4*). Additionally, substantial research has determined that immune cells and related signaling molecules do indeed play an active role in brain processes under normal conditions. For example, interleukin 17α (IL-17α) has been evidenced to regulate anxiety-like behavior (*5, 6*), while IL-4 has been linked to memory (*7*), and interferon gamma (IFNγ) to social behavior in mice (*8*). Furthermore, rodent neuroimaging studies, using structural magnetic resonance imaging (sMRI), have identified an effect of immunodeficiency on regional brain structure, likely with developmental origins (*9, 10*).

For the reasons outlined above, investigation into immune signaling within the CNS has historically skewed toward the study of microglia; the tissue-resident macrophages of the brain parenchyma. However, the implementation of novel methods allowing greater sensitivity to detect under-represented cell populations, and the aforementioned re-discovery of meningeal

lymphatic vessels harboring a wide range of immune cell subtypes, has resulted in evidence suggesting that meningeal and perivascular immune cells are also important to maintain proper CNS function as well as defense against insult (*11*). Therefore, while microglia will be discussed, the role of other CNS-resident immune cells and their potential influence on early brain development will be highlighted.

Immune cell development occurs in a structured fashion: starting with a wave of primitive hematopoiesis, followed by more definitive phases in the placenta, yolk sac, and fetal liver. This process results in the production of initial erythromyeloid and lymphoid progenitors, as well as the first hematopoietic stem cells (HSCs) (*12*). These fetal progenitors subsequently give rise to microglia and border associated macrophages that begin to seed the developing CNS by approximately embryonic day 10 (E10) (*13*). Following this initial colonization by tissue-resident macrophages, waves of innate-like lymphoid cells seed the brain meninges during the late stages of embryogenesis into the first postnatal week. This innate leukocyte colonization is dominated by gamma-delta T cells, B1 cells, and innate lymphoid cells (ILCs) 1-3 (*14-16*); the innate counterparts to traditional T and B lymphocytes. As full maturation of primary lymphoid organs (e.g., thymus and bone marrow) doesn't occur until after the first postnatal month in rodents, or the first year in humans (*17*), the representation of mature CD4/CD8 T and B cells in the developing CNS is relatively low. Instead, the CNS immune repertoire during early postnatal life is dominated by monocytes and innate-like lymphocytes which may be crucial to shape structural and functional development of the CNS.

Due to the relative novelty of studying neuroimmune interactions, existing literature on the role of immune cells and related signaling molecules on CNS development is sparse. For example, while ILCs are known to colonize the brain meninges during late embryogenesis, no studies to date have characterized a specific role for these cells in neurodevelopment or homeostatic CNS functioning. It could be the case that ILCs do not play an important role in these processes; however, it is more likely that this subtype is simply understudied, and more information will be uncovered as technologies continue to improve. On the other hand, an increasing amount of research has been published on the topic of neuroimmune interactions regarding microglia and border-associated macrophages (BAMs) in the CNS. Specifically, microglia play a crucial role in modulating both the pool of newborn neuronal precursor cells (*18, 19*) as well as the number of neuronal synapses during development (*20, 21*). Additionally, microglial function is thought to be important for activity-dependent myelin dynamics through phagocytosis of myelin within the developing CNS (*22*). BAMs, on the other hand, reside within the perivascular spaces and brain borders where they play an important role in neurovascular development (*23*) and act as the first line of defense from infection at the blood brain barrier (BBB) (*24*). Finally, innate-like lymphocytes such as gamma-delta T cells and B1 cells also predominate the brain immune compartment during the perinatal period (*15*). While no studies have specifically looked at gamma-delta T cell function in relation to early CNS development, subsets of these cells have the capacity to secrete IFNγ or IL-17α, two cytokines that can act directly on neural cells (*8, 14, 25, 26*). Additionally a role for B1 cells has been directly determined for CNS development, whereby B1 cells present in the brain meninges secrete IgM which directs oligodendrocyte maturation (*27*).

Role of the Immune System in Neurodevelopmental Disorder

Recent estimates from the Centers for Disease Control and Prevention suggest that 1 in 6 children are diagnosed with neurodevelopmental disorder (NDD) in the United States (U.S.) (*28*). Despite this high prevalence rate, the etiology of most NDD remains largely unknown. While numerous studies have revealed a genetic component to these disorders (*29, 30*), evidence suggests that dysregulation of the immune system may also play a significant role in NDD development (*31-33*).

The most commonly diagnosed NDDs are attention deficit hyperactivity disorder (ADHD) and ASD (*34*). In each of these disorders, researchers have identified a role for the immune system in disorder development or symptomology. For example, studies have found a high co-occurrence of inflammatory and autoimmune disorders in individuals with ADHD, such as type 1 diabetes (T1D) and psoriasis, as well as asthma and eczema (*35, 36*). Multiple recent studies, using separate study populations, have also found elevated levels of IL-6 in the sera of children with ADHD (*37, 38*). Additionally, individuals with ADHD are known to present with aAbs to a variety of brain-enriched antigens including anti-Yo antibodies (*38*), which target Purkinje cells of the cerebellum, and antibodies against the dopamine transporter (*39*), which is crucial for dopamine reuptake in the brain. Whether these commonly comorbid conditions simply present alongside ADHD or may have a role in etiology of the disorder remains unclear. However, substantial evidence supports a role for immune dysregulation in ADHD.

The second most common NDD in the U.S. by diagnosis is ASD. Despite the fact that ASD is highly heterogeneous in both origin and presentation, ample evidence has linked altered immune

function and ASD diagnosis. A range of immune cell subsets have been implicated in the disorder, including NK cells, where reduced NK cell function has been repeatedly reported in individuals with ASD (*40-43*), higher monocyte/macrophage numbers and altered activation of these cells (*44-46*), as well as modified numbers of CD4 T cells (*47*) and an imbalance in the ratio of T regulatory (Treg) to Th17 cells (*48*). Various secreted immune factors have also been linked to ASD with high confidence including increased levels of IL-1B, IL-4, IL-6, IL-8, and IFNγ via studies using either neonatal blood spots or plasma (*49-52*). In addition to findings observed in individuals with ASD, a recurrent finding is the influence of maternal immune status on ASD diagnosis in offspring. This can be classified into two major categories: maternal immune activation (MIA) occurring during gestation, or pre-existing maternal autoimmunity including the incidence of aAb production. The concept behind MIA is that a pro-inflammatory event during gestation can result in production of cytokines, such as IL-6 and IL-17α, which may either cross the placental or operate locally to propagate inflammation that is harmful to the developing fetus (*53*). This theory is supported clinically through work noting that maternal fever during pregnancy is a risk factor for development of ASD in offspring (*54, 55*). Alternatively, pre-existing autoimmunity in mothers such as T1D, rheumatoid arthritis, or lupus (*56, 57*) can also significantly increase the odds ratio of having a child with ASD. Alongside cases of specific autoimmunity in mothers of children with ASD, circulating aAbs to brain-enriched antigens have been consistently noted and observed in approximately 20% of cases, a phenomenon known MAR-ASD (*58, 59*).

Maternal Autoantibodies in Autism

Given the abundance of evidence suggesting a role for the immune system in ASD etiology, and the identification of MAR-ASD, the most prevalent ASD endophenotype observed to date, the topic of maternal aAbs in autism warrants further detail.

The concept of maternal aAb transfer and impact on offspring outcomes has precedence across multiple well-documented conditions: such as Lupus (*60*), Grave's Disease (*61*), and Myasthenia Gravis (*62*). Now substantial research suggests that gestational transfer of maternal IgG reactive to proteins enriched in developing brain tissue may be a contributing factor in ASD (*63*). The first evidence for this phenomenon came from a seminal study which found that serum from mothers of children with autism displayed reactivity against brain tissue via immunohistochemistry (IHC) (*64*). Following this, multiple independent research groups reported a similar phenomenon using immunoblot techniques but found that reactivity of maternal sera was highest to fetal brain lysates compared to early postnatal or adult brain tissue (*65-67*), suggesting that the protein targets of these maternal aAbs present in mothers of ASD children were likely enriched in the developing brain. Following validation across multiple study cohorts, the next step was to identify which proteins are bound by these maternal aAbs. Using a combination of two-dimensional gel electrophoresis of fetal rhesus macaque brain followed by mass spectrometry and peptide sequencing of aAb-reactive gel spots, Braunschweig et al., identified 6 proteins as targets of maternal aAbs: lactate dehydrogenase (LDH), collapsing response mediator protein 1 (CRMP1), collapsing response mediator protein 2 (CRMP2), stress-induced phosphoprotein 1 (STIP1), cypin, or guanine deaminase (GDA), and Y-box-binding-protein (YBX1). Serum reactivity to these proteins was significantly enriched in mothers of children with ASD (*59*). This list was later expanded to include LDHA & B separately, as well

as neuron specific enolase (NSE) for a total of 8 MAR-ASD antigens (*68*). As IgG antibodies naturally have antigenic specificity based on the peptides presented during affinity maturation, the next step was to identify the specific epitopes bound by MAR-ASD aAbs. To this end, overlapping peptide microarrays were used to identify the immunodominant epitopes across the MAR-ASD proteins that were significantly enriched in maternal plasma of mothers of children with ASD (*68, 69*). This resulted in both an increase in the specificity and sensitivity of the clinical diagnostic criteria and allowed the creation of translational models with high construct validity.

Early MAR-ASD animal models relied on injection of total purified IgG from either mothers of children with ASD, or those of typically developing children. These initial passive transfer models, conducted in both mice and non-human primates, provided substantial evidence for a direct effect of MAR-ASD IgG on offspring outcomes, including altered behavior, brain size, and cortical development (*70-72*). However, identification of the clinically-relevant MAR-ASD epitopes allowed the creation of an endogenous exposure model. In this model female animals are injected with MAR-ASD peptide epitopes alongside adjuvant prior to breeding to induce a specific antibody response reflective of that observed in mothers of children with ASD. This process exhibits greater translational relevance as it mimics the generation and transfer of autoreactive MAR-ASD IgG to offspring. Mouse offspring exposed to MAR-ASD aAbs via endogenous transfer displayed deficits across multiple behavioral domains as well as sex-specific neuroanatomical differences (*73, 74*). Overall, the animal model data collected to date support a role for MAR-ASD aAbs in altered offspring outcomes with relevance to what is seen clinically.

Through the work detailed above and that which will be discussed in the following chapters, the immune system and CNS appear to exhibit complex interactions that have a role in brain development, homeostasis, and disease.

References

1. M. J. Carson, J. M. Doose, B. Melchior, C. D. Schmid, C. C. Ploix, CNS immune privilege: hiding in plain sight. *Immunological reviews* **213**, 48-65 (2006).
2. R. A. Willis, A. Keith, Experiments on the intracerebral implantation of embryo tissues in rats. *Proceedings of the Royal Society of London. Series B - Biological Sciences* **117**, 400-412 (1935).
3. A. Louveau, J. Herz, M. N. Alme, A. F. Salvador, M. Q. Dong, K. E. Viar, S. G. Herod, J. Knopp, J. C. Setliff, A. L. Lupi, S. Da Mesquita, E. L. Frost, A. Gaultier, T. H. Harris, R. Cao, S. Hu, J. R. Lukens, I. Smirnov, C. C. Overall, G. Oliver, J. Kipnis, CNS lymphatic drainage and neuroinflammation are regulated by meningeal lymphatic vasculature. *Nat Neurosci* **21**, 1380-1391 (2018).
4. A. Louveau, I. Smirnov, T. J. Keyes, J. D. Eccles, S. J. Rouhani, J. D. Peske, N. C. Derecki, D. Castle, J. W. Mandell, K. S. Lee, T. H. Harris, J. Kipnis, Structural and functional features of central nervous system lymphatic vessels. *Nature* **523**, 337-341 (2015).
5. K. Alves de Lima, J. Rustenhoven, S. Da Mesquita, M. Wall, A. F. Salvador, I. Smirnov, G. Martelossi Cebinelli, T. Mamuladze, W. Baker, Z. Papadopoulos, M. B. Lopes, W. S. Cao, X. S. Xie, J. Herz, J. Kipnis, Meningeal gammadelta T cells regulate anxiety-like behavior via IL-17a signaling in neurons. *Nat Immunol* **21**, 1421-1429 (2020).
6. M. Ribeiro, H. C. Brigas, M. Temido-Ferreira, P. A. Pousinha, T. Regen, C. Santa, J. E. Coelho, I. Marques-Morgado, C. A. Valente, S. Omenetti, B. Stockinger, A. Waisman, B. Manadas, L. V. Lopes, B. Silva-Santos, J. C. Ribot, Meningeal gammadelta T cell-derived IL-17 controls synaptic plasticity and short-term memory. *Sci Immunol* **4**, (2019).
7. N. C. Derecki, A. N. Cardani, C. H. Yang, K. M. Quinnies, A. Crihfield, K. R. Lynch, J. Kipnis, Regulation of learning and memory by meningeal immunity: a key role for IL-4. *J Exp Med* **207**, 1067-1080 (2010).
8. A. J. Filiano, Y. Xu, N. J. Tustison, R. L. Marsh, W. Baker, I. Smirnov, C. C. Overall, S. P. Gadani, S. D. Turner, Z. Weng, S. N. Peerzade, H. Chen, K. S. Lee, M. M. Scott, M. P. Beenhakker, V. Litvak, J. Kipnis, Unexpected role of interferon-gamma in regulating neuronal connectivity and social behaviour. *Nature* **535**, 425-429 (2016).
9. D. J. Fernandes, S. Spring, C. Corre, A. Tu, L. R. Qiu, C. Hammill, D. A. Vousden, T. L. Spencer Noakes, B. J. Nieman, D. M. E. Bowdish, J. A. Foster, M. R. Palmert, J. P. Lerch, Mouse models of immune dysfunction: their neuroanatomical differences reflect their anxiety-behavioural phenotype. *Mol Psychiatry*, (2022).
10. K. C. Rilett, M. Friedel, J. Ellegood, R. N. MacKenzie, J. P. Lerch, J. A. Foster, Loss of T cells influences sex differences in behavior and brain structure. *Brain Behav Immun* **46**, 249-260 (2015).

11. K. Alves de Lima, J. Rustenhoven, J. Kipnis, Meningeal Immunity and Its Function in Maintenance of the Central Nervous System in Health and Disease. *Annu Rev Immunol* **38**, 597-620 (2020).
12. X. Gao, C. Xu, N. Asada, P. S. Frenette, The hematopoietic stem cell niche: from embryo to adult. *Development* **145**, (2018).
13. J. P. Lopez-Atalaya, K. E. Askew, A. Sierra, D. Gomez-Nicola, Development and maintenance of the brain's immune toolkit: Microglia and non-parenchymal brain macrophages. *Dev Neurobiol* **78**, 561-579 (2018).
14. K. Alves de Lima, J. Rustenhoven, S. Da Mesquita, M. Wall, A. F. Salvador, I. Smirnov, G. Martelossi Cebinelli, T. Mamuladze, W. Baker, Z. Papadopoulos, M. B. Lopes, W. S. Cao, X. S. Xie, J. Herz, J. Kipnis, Meningeal γδ T cells regulate anxiety-like behavior via IL-17a signaling in neurons. *Nature Immunology*, (2020).
15. S. Tanabe, T. Yamashita, B-1a lymphocytes promote oligodendrogenesis during brain development. *Nat Neurosci* **21**, 506-516 (2018).
16. A. Zelco, V. Borjesson, J. K. de Kanter, C. Lebrero-Fernandez, V. M. Lauschke, E. Rocha-Ferreira, G. Nilsson, S. Nair, P. Svedin, M. Bemark, H. Hagberg, C. Mallard, F. C. P. Holstege, X. Wang, Single-cell atlas reveals meningeal leukocyte heterogeneity in the developing mouse brain. *Genes Dev* **35**, 1190-1207 (2021).
17. K. S. Landreth, Critical windows in development of the rodent immune system. *Hum Exp Toxicol* **21**, 493-498 (2002).
18. J. W. VanRyzin, A. E. Marquardt, K. J. Argue, H. A. Vecchiarelli, S. E. Ashton, S. E. Arambula, M. N. Hill, M. M. McCarthy, Microglial Phagocytosis of Newborn Cells Is Induced by Endocannabinoids and Sculpts Sex Differences in Juvenile Rat Social Play. *Neuron* **102**, 435-449 e436 (2019).
19. C. L. Cunningham, V. Martinez-Cerdeno, S. C. Noctor, Microglia regulate the number of neural precursor cells in the developing cerebral cortex. *J Neurosci* **33**, 4216-4233 (2013).
20. R. C. Paolicelli, G. Bolasco, F. Pagani, L. Maggi, M. Scianni, P. Panzanelli, M. Giustetto, T. A. Ferreira, E. Guiducci, L. Dumas, D. Ragozzino, C. T. Gross, Synaptic pruning by microglia is necessary for normal brain development. *Science* **333**, 1456-1458 (2011).
21. B. Stevens, N. J. Allen, L. E. Vazquez, G. R. Howell, K. S. Christopherson, N. Nouri, K. D. Micheva, A. K. Mehalow, A. D. Huberman, B. Stafford, A. Sher, A. M. Litke, J. D. Lambris, S. J. Smith, S. W. John, B. A. Barres, The classical complement cascade mediates CNS synapse elimination. *Cell* **131**, 1164-1178 (2007).
22. A. N. Hughes, B. Appel, Microglia phagocytose myelin sheaths to modify developmental myelination. *Nat Neurosci* **23**, 1055-1066 (2020).
23. S. Chen, N. Tisch, M. Kegel, R. Yerbes, R. Hermann, H. Hudalla, C. Zuliani, G. S. Gulculer, K. Zwadlo, J. von Engelhardt, C. Ruiz de Almodovar, A. Martin-Villalba, CNS Macrophages Control Neurovascular Development via CD95L. *Cell Rep* **19**, 1378-1393 (2017).
24. M. M. Polfliet, P. J. Zwijnenburg, A. M. van Furth, T. van der Poll, E. A. Dopp, C. Renardel de Lavalette, E. M. van Kesteren-Hendrikx, N. van Rooijen, C. D. Dijkstra, T. K. van den Berg, Meningeal and perivascular macrophages of the central nervous system play a protective role during bacterial meningitis. *J Immunol* **167**, 4644-4650 (2001).

25. M. D. Reed, Y. S. Yim, R. D. Wimmer, H. Kim, C. Ryu, G. M. Welch, M. Andina, H. O. King, A. Waisman, M. M. Halassa, J. R. Huh, G. B. Choi, IL-17a promotes sociability in mouse models of neurodevelopmental disorders. *Nature* **577**, 249-253 (2020).
26. L. Li, T. L. Walker, Y. Zhang, E. W. Mackay, P. F. Bartlett, Endogenous interferon gamma directly regulates neural precursors in the non-inflammatory brain. *J Neurosci* **30**, 9038-9050 (2010).
27. S. Tanabe, T. Yamashita, The role of immune cells in brain development and neurodevelopmental diseases. *International immunology*, (2018).
28. B. Zablotsky, L. I. Black, M. J. Maenner, L. A. Schieve, M. L. Danielson, R. H. Bitsko, S. J. Blumberg, M. D. Kogan, C. A. Boyle, Prevalence and Trends of Developmental Disabilities among Children in the United States: 2009-2017. *Pediatrics* **144**, e20190811 (2019).
29. B. P. Coe, H. A. F. Stessman, A. Sulovari, M. R. Geisheker, T. E. Bakken, A. M. Lake, J. D. Dougherty, E. S. Lein, F. Hormozdiari, R. A. Bernier, E. E. Eichler, Neurodevelopmental disease genes implicated by de novo mutation and copy number variation morbidity. *Nat Genet* **51**, 106-116 (2019).
30. W. F. Hu, M. H. Chahrour, C. A. Walsh, The diverse genetic landscape of neurodevelopmental disorders. *Annu Rev Genomics Hum Genet* **15**, 195-213 (2014).
31. H. O. Atladottir, M. G. Pedersen, P. Thorsen, P. B. Mortensen, B. Deleuran, W. W. Eaton, E. T. Parner, Association of family history of autoimmune diseases and autism spectrum disorders. *Pediatrics* **124**, 687-694 (2009).
32. L. A. Croen, J. K. Grether, C. K. Yoshida, R. Odouli, J. Van de Water, Maternal autoimmune diseases, asthma and allergies, and childhood autism spectrum disorders: a case-control study. *Arch Pediatr Adolesc Med* **159**, 151-157 (2005).
33. T. L. Sweeten, S. L. Bowyer, D. J. Posey, G. M. Halberstadt, C. J. McDougle, Increased prevalence of familial autoimmunity in probands with pervasive developmental disorders. *Pediatrics* **112**, e420 (2003).
34. V. Scandurra, L. Emberti Gialloreti, F. Barbanera, M. R. Scordo, A. Pierini, R. Canitano, Neurodevelopmental Disorders and Adaptive Functions: A Study of Children With Autism Spectrum Disorders (ASD) and/or Attention Deficit and Hyperactivity Disorder (ADHD). *Front Psychiatry* **10**, 673 (2019).
35. R. Y. Zhou, J. J. Wang, J. C. Sun, Y. You, J. N. Ying, X. M. Han, Attention deficit hyperactivity disorder may be a highly inflammation and immune-associated disease (Review). *Mol Med Rep* **16**, 5071-5077 (2017).
36. P. R. Nielsen, M. E. Benros, S. Dalsgaard, Associations Between Autoimmune Diseases and Attention-Deficit/Hyperactivity Disorder: A Nationwide Study. *J Am Acad Child Adolesc Psychiatry* **56**, 234-240.e231 (2017).
37. A. E. Elsadek, A. H. Al-Shokary, W. E. Abdelghani, N. M. Kamal, A. O. Ibrahim, H. H. El-Shorbagy, H. A. Suliman, N. F. Barseem, Y. H. Abdel Maksoud, S. M. Azab, D. M. Nour El Din, Serum Levels of Interleukin-6 and Tumor Necrosis Factor Alpha in Children With Attention-Deficit Hyperactivity Disorder. *J Pediatr Neurosci* **15**, 402-408 (2020).
38. R. Donfrancesco, P. Nativio, A. Di Benedetto, M. P. Villa, E. Andriola, M. G. Melegari, E. Cipriano, M. Di Trani, Anti-Yo Antibodies in Children With ADHD: First Results About Serum Cytokines. *J Atten Disord* **24**, 1497-1502 (2020).

39. W. Adriani, E. Romano, M. Pucci, E. Pascale, L. Cerniglia, S. Cimino, R. Tambelli, P. Curatolo, O. Granstrem, M. Maccarrone, G. Laviola, C. D'Addario, Potential for diagnosis versus therapy monitoring of attention deficit hyperactivity disorder: a new epigenetic biomarker interacting with both genotype and auto-immunity. *Eur Child Adolesc Psychiatry* **27**, 241-252 (2018).
40. S. Ebrahimi Meimand, Y. Rostam-Abadi, N. Rezaei, Autism spectrum disorders and natural killer cells: a review on pathogenesis and treatment. *Expert Rev Clin Immunol* **17**, 27-35 (2021).
41. A. M. Enstrom, L. Lit, C. E. Onore, J. P. Gregg, R. L. Hansen, I. N. Pessah, I. Hertz-Picciotto, J. A. Van de Water, F. R. Sharp, P. Ashwood, Altered gene expression and function of peripheral blood natural killer cells in children with autism. *Brain Behav Immun* **23**, 124-133 (2009).
42. A. Vojdani, E. Mumper, D. Granpeesheh, L. Mielke, D. Traver, K. Bock, K. Hirani, J. Neubrander, K. N. Woeller, N. O'Hara, A. Usman, C. Schneider, F. Hebroni, J. Berookhim, J. McCandless, Low natural killer cell cytotoxic activity in autism: the role of glutathione, IL-2 and IL-15. *J Neuroimmunol* **205**, 148-154 (2008).
43. R. P. Warren, A. Foster, N. C. Margaretten, Reduced natural killer cell activity in autism. *J Am Acad Child Adolesc Psychiatry* **26**, 333-335 (1987).
44. H. K. Hughes, M. E. Rowland, C. E. Onore, S. Rogers, A. V. Ciernia, P. Ashwood, Dysregulated gene expression associated with inflammatory and translation pathways in activated monocytes from children with autism spectrum disorder. *Transl Psychiatry* **12**, 39 (2022).
45. A. M. Enstrom, C. E. Onore, J. A. Van de Water, P. Ashwood, Differential monocyte responses to TLR ligands in children with autism spectrum disorders. *Brain Behav Immun* **24**, 64-71 (2010).
46. T. L. Sweeten, D. J. Posey, C. J. McDougle, High blood monocyte counts and neopterin levels in children with autistic disorder. *Am J Psychiatry* **160**, 1691-1693 (2003).
47. D. R. Rose, H. Yang, M. Careaga, K. Angkustsiri, J. Van de Water, P. Ashwood, T cell populations in children with autism spectrum disorder and co-morbid gastrointestinal symptoms. *Brain Behav Immun Health* **2**, 100042 (2020).
48. P. Ellul, M. Rosenzwajg, H. Peyre, G. Fourcade, E. Mariotti-Ferrandiz, V. Trebossen, D. Klatzmann, R. Delorme, Regulatory T lymphocytes/Th17 lymphocytes imbalance in autism spectrum disorders: evidence from a meta-analysis. *Mol Autism* **12**, 68 (2021).
49. L. S. Heuer, L. A. Croen, K. L. Jones, C. K. Yoshida, R. L. Hansen, R. Yolken, O. Zerbo, G. DeLorenze, M. Kharrazi, P. Ashwood, J. Van de Water, An Exploratory Examination of Neonatal Cytokines and Chemokines as Predictors of Autism Risk: The Early Markers for Autism Study. *Biol Psychiatry* **86**, 255-264 (2019).
50. P. Krakowiak, P. E. Goines, D. J. Tancredi, P. Ashwood, R. L. Hansen, I. Hertz-Picciotto, J. Van de Water, Neonatal Cytokine Profiles Associated With Autism Spectrum Disorder. *Biol Psychiatry* **81**, 442-451 (2017).
51. A. Masi, D. S. Quintana, N. Glozier, A. R. Lloyd, I. B. Hickie, A. J. Guastella, Cytokine aberrations in autism spectrum disorder: a systematic review and meta-analysis. *Mol Psychiatry* **20**, 440-446 (2015).
52. P. Ashwood, P. Krakowiak, I. Hertz-Picciotto, R. Hansen, I. Pessah, J. Van de Water, Elevated plasma cytokines in autism spectrum disorders provide evidence of immune

dysfunction and are associated with impaired behavioral outcome. *Brain Behav Immun* **25**, 40-45 (2011).
53. M. L. Estes, A. K. McAllister, Maternal immune activation: Implications for neuropsychiatric disorders. *Science* **353**, 772-777 (2016).
54. L. A. Croen, Y. Qian, P. Ashwood, O. Zerbo, D. Schendel, J. Pinto-Martin, M. Daniele Fallin, S. Levy, L. A. Schieve, M. Yeargin-Allsopp, K. R. Sabourin, J. L. Ames, Infection and Fever in Pregnancy and Autism Spectrum Disorders: Findings from the Study to Explore Early Development. *Autism Res* **12**, 1551-1561 (2019).
55. M. Hornig, M. A. Bresnahan, X. Che, A. F. Schultz, J. E. Ukaigwe, M. L. Eddy, D. Hirtz, N. Gunnes, K. K. Lie, P. Magnus, S. Mjaaland, T. Reichborn-Kjennerud, S. Schjolberg, A. S. Oyen, B. Levin, E. S. Susser, C. Stoltenberg, W. I. Lipkin, Prenatal fever and autism risk. *Mol Psychiatry* **23**, 759-766 (2018).
56. H. K. Hughes, E. Mills Ko, D. Rose, P. Ashwood, Immune Dysfunction and Autoimmunity as Pathological Mechanisms in Autism Spectrum Disorders. *Front Cell Neurosci* **12**, 405 (2018).
57. A. M. Comi, A. W. Zimmerman, V. H. Frye, P. A. Law, J. N. Peeden, Familial clustering of autoimmune disorders and evaluation of medical risk factors in autism. *J Child Neurol* **14**, 388-394 (1999).
58. A. Ramirez-Celis, M. Becker, M. Nuño, J. Schauer, N. Aghaeepour, J. Van de Water, Risk Assessment Analysis for Maternal Autoantibody Related Autism (MAR-ASD): A Subtype of Autism. *Molecular Psychiatry*, (2020).
59. D. Braunschweig, P. Krakowiak, P. Duncanson, R. Boyce, R. L. Hansen, P. Ashwood, I. Hertz-Picciotto, I. N. Pessah, J. Van de Water, Autism-specific maternal autoantibodies recognize critical proteins in developing brain. *Transl Psychiatry* **3**, e277 (2013).
60. F. Kalush, E. Rimon, E. Mozes, Neonatal lupus erythematosus in offspring of mothers with experimental systemic lupus erythematosus. *Am J Reprod Immunol* **28**, 264-268 (1992).
61. I. Bucci, C. Giuliani, G. Napolitano, Thyroid-Stimulating Hormone Receptor Antibodies in Pregnancy: Clinical Relevance. *Front Endocrinol (Lausanne)* **8**, 137 (2017).
62. N. E. Gilhus, Y. Hong, Maternal myasthenia gravis represents a risk for the child through autoantibody transfer, immunosuppressive therapy and genetic influence. *Eur J Neurol* **25**, 1402-1409 (2018).
63. J. McLellan, D. H. J. Kim, M. Bruce, A. Ramirez-Celis, J. Van de Water, Maternal Immune Dysregulation and Autism–Understanding the Role of Cytokines, Chemokines and Autoantibodies. *Frontiers in Psychiatry* **13**, (2022).
64. P. Dalton, R. Deacon, A. Blamire, M. Pike, I. McKinlay, J. Stein, P. Styles, A. Vincent, Maternal neuronal antibodies associated with autism and a language disorder. *Ann Neurol* **53**, 533-537 (2003).
65. H. S. Singer, C. M. Morris, C. D. Gause, P. K. Gillin, S. Crawford, A. W. Zimmerman, Antibodies against fetal brain in sera of mothers with autistic children. *J Neuroimmunol* **194**, 165-172 (2008).
66. D. Braunschweig, P. Ashwood, P. Krakowiak, I. Hertz-Picciotto, R. Hansen, L. A. Croen, I. N. Pessah, J. Van de Water, Autism: maternally derived antibodies specific for fetal brain proteins. *Neurotoxicology* **29**, 226-231 (2008).

67. A. W. Zimmerman, S. L. Connors, K. J. Matteson, L. C. Lee, H. S. Singer, J. A. Castaneda, D. A. Pearce, Maternal antibrain antibodies in autism. *Brain Behav Immun* **21**, 351-357 (2007).
68. A. Ramirez-Celis, E. Edmiston, J. Schauer, T. Vu, J. Van de Water, Peptides of neuron specific enolase as potential ASD biomarkers: From discovery to epitope mapping. *Brain Behav Immun* **84**, 200-208 (2020).
69. E. Edmiston, K. L. Jones, T. Vu, P. Ashwood, J. Van de Water, Identification of the antigenic epitopes of maternal autoantibodies in autism spectrum disorders. *Brain Behav Immun* **69**, 399-407 (2018).
70. J. Ariza, J. Hurtado, H. Rogers, R. Ikeda, M. Dill, C. Steward, D. Creary, J. Van de Water, V. Martinez-Cerdeno, Maternal autoimmune antibodies alter the dendritic arbor and spine numbers in the infragranular layers of the cortex. *PLoS One* **12**, e0183443 (2017).
71. V. Martinez-Cerdeno, J. Camacho, E. Fox, E. Miller, J. Ariza, D. Kienzle, K. Plank, S. C. Noctor, J. Van de Water, Prenatal Exposure to Autism-Specific Maternal Autoantibodies Alters Proliferation of Cortical Neural Precursor Cells, Enlarges Brain, and Increases Neuronal Size in Adult Animals. *Cereb Cortex* **26**, 374-383 (2016).
72. M. D. Bauman, A. M. Iosif, P. Ashwood, D. Braunschweig, A. Lee, C. M. Schumann, J. Van de Water, D. G. Amaral, Maternal antibodies from mothers of children with autism alter brain growth and social behavior development in the rhesus monkey. *Transl Psychiatry* **3**, e278 (2013).
73. M. R. Bruce, K. L. Jones, A. C. Vernon, J. L. Silverman, J. N. Crawley, J. Ellegood, J. P. Lerch, J. Van De Water, Sexually dimorphic neuroanatomical differences relate to ASD-relevant behavioral outcomes in a maternal autoantibody mouse model. *Molecular Psychiatry*, (2021).
74. K. L. Jones, M. C. Pride, E. Edmiston, M. Yang, J. L. Silverman, J. N. Crawley, J. Van de Water, Autism-specific maternal autoantibodies produce behavioral abnormalities in an endogenous antigen-driven mouse model of autism. *Mol Psychiatry*, (2018).

CHAPTER 2

Acute Peripheral Immune Activation Alters Cytokine Expression and Glial Activation in the Early Postnatal Rat Brain

****Published in Journal of Neuroinflammation****

M. Bruce, K. M. Streifel, C. A. Boosalis, L. Heuer, E. A. Gonzalez, S. Li, D. J. Harvey, P. J. Lein, J. Van de Water, Acute peripheral immune activation alters cytokine expression and glial activation in the early postnatal rat brain. *J Neuroinflammation* **16**, 200 (2019).

Abstract

Neuroinflammation can modulate brain development; however, the influence of an acute peripheral immune challenge on neuroinflammatory responses in the early postnatal brain is not well characterized. To address this gap in knowledge, we evaluated the peripheral and central nervous system (CNS) immune responses to a mixed immune challenge in early postnatal rats of varying strains and sex. On postnatal day 10 (P10), male and female Lewis and Brown Norway rats were injected intramuscularly with either a mix of bacterial and viral components in adjuvant, adjuvant-only, or saline. Immune responses were evaluated at 2- and 5-days post-challenge. Cytokine and chemokine levels were evaluated in serum and in multiple brain regions using a Luminex multiplex assay. Multi-factor ANOVAs were used to compare analyte levels across treatment groups within strain, sex, and day of sample collection. Numbers and activation status of astrocytes and microglia were also analyzed in the cortex and hippocampus by quantifying immunoreactivity for GFAP, IBA-1, and CD68 in fixed brain slices. Immunohistochemical data were analyzed using a mixed-model regression analysis.

Acute peripheral immune challenge differentially altered cytokine and chemokine levels in the serum versus the brain. Within the brain, the cytokine and chemokine response varied between strains, sexes, and days post-challenge. Main findings included differences in T helper (Th) type cytokine responses in various brain regions, particularly the cortex, with respect to IL-4, IL-10, and IL-17 levels. Additionally, peripheral immune challenge altered GFAP and IBA-1 immunoreactivity in the brain in a strain- and sex-dependent manner. These findings indicate that genetic background and sex influence the CNS response to an acute peripheral immune challenge during early postnatal development. Additionally, these data reinforce that the

developmental time point during which the challenge occurs has a distinct effect on the activation of CNS-resident cells.

Introduction

An acute peripheral immune response can be widely systemic, affecting a variety of tissues and organ systems, although the tissue-specific response may vary greatly [1]. For example, peripheral immune stimulation has been shown to influence neuroinflammatory responses in the central nervous system (CNS) [2, 3]. Specific effects seen in the brain following peripheral immune challenge include global changes in expression of interferon response genes [4] as well as alterations in cell-specific transcriptional programming, particularly in microglia [5, 6]. These transcriptional alterations of neuroimmune signaling in early life are hypothesized to result in developmental priming, potentially leading to enduring consequences in response to later life exposures (reviewed in [7, 8]). Therefore, it is important to gain a deeper understanding of the relationship between peripheral inflammation and early postnatal CNS response, to evaluate the risk factors in early life as well as identify strategies to limit adverse effects.

Under physiologic conditions, immune signaling within the CNS is coordinated primarily by resident cells such as microglia, astrocytes, and mast cells due to tightly regulated infiltration of peripheral leukocytes into the brain parenchyma [9, 10]. When activated, these resident immune cells secrete a range of cytokines, chemokines, and other regulatory factors that drive neuroinflammatory responses and contribute to normal neurodevelopment and functional homeostasis [11, 12]. Integration of systemic immune signals by CNS-resident cells may occur via coordinated signaling through the autonomic nervous system and the hypothalamic-pituitary-adrenal (HPA) axis [13], trafficking and effector functions of immune cells within the meninges

[14], and gut microbe-mediated mechanisms [15]. Each of these systems undergoes overlapping periods of development and refinement during the first few weeks following birth. Therefore, immune activation during these critical periods of development can have broad implications on neurodevelopment and neural function later in life.

In this study, we focused on understanding the relationship between the peripheral immune system and developing CNS by evaluating the respective immune responses to an acute peripheral, mixed immune challenge at an early postnatal time point. To do this, we challenged rats with either a mix of bacterial and viral components in adjuvant, adjuvant alone, or saline on postnatal day 10 (P10). The time point of P10 was chosen for exposure as it roughly translates to the first year of life in humans [16, 17] and represents an age of peak brain growth in rats [18]. We then evaluated the subsequent peripheral and CNS immune response 2 and 5 days later to compare early vs. late post-challenge immune responses. As a readout, we analyzed cytokine and chemokine levels in the serum as well as cortical, hippocampal, and cerebellar lysates. Additionally, we assessed the numbers and activation profiles of microglia and astrocytes within the cortex and hippocampus. Given the inherent heterogeneity in the immune response due to genetic background and sex [19, 20], an additional aim of the study was to compare the CNS and peripheral immune response following immune challenge in male and female Lewis and Brown Norway (BN) rats. These strains of rats were chosen as they exhibit immune response skewing, with Lewis rats skewing toward a T helper (Th) 1 cell (cellular, proinflammatory) response and BN rats skewing toward a Th2 (humoral, regulatory) response [21, 22]. While evidence exists suggesting sex-specific differences in CNS immune responsiveness during early postnatal development [23], the influence of genetic background on sex-specific immune responses is not as well documented. Therefore, a primary goal of this study was to identify potential differences

in the region-specific CNS immune response in neonatal rats to a peripheral mixed immune challenge in the context of sex and genetic background.

Material and Methods

Materials

The mixed acute peripheral immune challenge was comprised of hepatitis B (HepB) (Recombivax HB; Merck & Co., Whitehouse Station, New Jersey), diphtheria and tetanus toxoids and acellular pertussis (DTap) (DAPTACEL; Sanofi Pasteur, Swiftwater, Pennsylvania), Haemophilus influenza type b (Hib) (PedvaxHIB; Merck & Co., Inc., Whitehouse Station, New Jersey), pneumococcal conjugate (PCV) (Prevnar 13; Wyeth Pharmaceuticals Inc., Madison, New Jersey), and inactivated poliovirus (IPV) (IPOL; Sanofi Pasteur, Swiftwater, Pennsylvania) in adjuvant. To match the adjuvant pre-mixed with the above antigen preparations, a control adjuvant of 2% aluminum hydroxide gel (Alhydrogel) was obtained from InvivoGen (San Diego, California).

Animals

All animals were housed in facilities fully accredited by AAALAC International, and all studies were performed with regard to the alleviation of pain and suffering under protocols approved by the University of California-Davis Institutional Animal Care and Use Committee. Lewis and Brown Norway (BN) timed-pregnant female rats ($n = 6$ per strain) were obtained from Charles River Laboratories (Portage, MI). Rats were individually housed on a 12:12-h light:dark cycle at 22 ± 2 °C with food and water available ad libitum. Lewis dams delivered litters of 10–12 pups on average, whereas BN dams delivered litters of 3–5 pups on average. On P7, littermates from

each strain were sexed, randomly assigned to different experimental groups using a random number generator, and ear punched for identification purposes.

Peripheral Immune Challenge

To trigger a full-spectrum innate and adaptive immune response, we utilized a peripheral immune challenge that included both bacterial and viral immune-stimulating agents. Offspring were injected intramuscularly (i.m.) on P10 with one of the following: acute peripheral immune challenge in adjuvant, adjuvant mixed with saline, or saline alone. The dose (0.105 μL/g) was determined based on the human dosing for this antigen mixture and adjusted for the average pup weight (approximately 20 g). Adjuvant control animals were treated with a 1:1 solution of Alhydrogel and saline, while saline controls were injected with an equal volume of 0.9% sterile saline. All treatments were brought up in sterile saline to reach a final total volume of 25 μL and were administered i.m. to the *vastus lateralis* muscle using a sterile 25-gauge needle. After treatment, pups were returned to their home cage where they remained with their dam for 2- or 5-days post-injection until they were euthanized for tissue collection.

Blood and Brain Tissue Collection

On P12 or P15, animals were deeply anesthetized with 4% isoflurane in oxygen. Blood samples were then collected via cardiac puncture followed immediately by transcardial perfusion with sterile phosphate-buffered saline (PBS). Blood was centrifuged (12,000×*g*, 4 °C, 10 min) to obtain serum, which was then stored at − 80 °C. Whole brains of animals randomly chosen for cytokine measurement analyses were quickly removed following transcardial PBS perfusion and, using a dissection scope and sterile surgical equipment, microdissected in PBS on ice to isolate

the hippocampi, cortices, and cerebella. All tissues were snap-frozen in liquid nitrogen and stored at − 80 °C until further assayed. Animals randomly chosen for immunohistochemical analyses were anesthetized with 4% isoflurane in oxygen and subsequently perfused transcardially with 100-ml cold PBS at a rate of 15 ml/min using a Masterflex peristaltic pump (Cole Parmer, Vernon Hills, IL) followed by 100 ml of cold 4% paraformaldehyde (PFA) in PBS. Fixed tissues were removed, post-fixed in 4% PFA overnight, and then stored in 30% sucrose in PBS at 4 °C for 48 h. Fixed brains were snap-frozen in O.C.T. Compound (Sakura Finetek, Torrance, CA) and then sectioned into 10-μm-thick sagittal sections. Sections were stored at − 80 °C until further processed for immunohistochemical analyses.

Cytokine and Chemokine Measurement

Prior to cytokine measurement, brain tissue samples were thawed and lysed in Bio-Plex cell lysis buffer containing protease and phosphatase inhibitors (Bio-Rad Laboratories, Hercules, California) and supplemented with 500 mM protease inhibitor phenyl-methylsulfonyl fluoride (PMSF; Sigma-Aldrich, St. Louis, Missouri). Briefly, tissues were homogenized in 200 μL (hippocampus) or 500 μL (cortex and cerebellum) of cell lysis solution using a polytron homogenizer for 10 s. The homogenate was then frozen for 10 min at − 80 °C, thawed, sonicated for 3 min, and then centrifuged at 4500 g for 4 min. Protein was quantified in the supernatant using Pierce BCA assay (Thermo Scientific; Rockford, Illinois), and samples were stored at − 80 °C until further analyzed.

Concentrations of 10 cytokines and chemokines were determined using a commercially available multiplex magnetic bead-based kit (Bio-Plex Pro™ Cytokine Reagent Rat Cytokine Assay; Bio-Rad Laboratories, Hercules, California) in accordance with the kit-specific protocols provided by

Bio-Rad. The following cytokines and chemokines were measured: granulocyte macrophage colony-stimulating factor (GM-CSF), interferon gamma (IFN-γ), interleukin-1α (IL-1α), IL-1β, IL-4, IL-6, IL-10, IL-17, monocyte chemotactic protein-1 (MCP-1), and tumor necrosis factor α (TNF-α). Briefly, lyophilized rat cytokine standards were first reconstituted with either cell lysis buffer (brain samples) or the kit-provided standard diluent (serum samples), and a standard dilution series was made. Homogenized brain samples were run in duplicate at 1 mg/mL, whereas serum samples were run neat. Fifty microliters of samples, standards, and corresponding buffer blanks were incubated on a plate shaker at room temperature (RT) with antibody-coupled magnetic beads for 1 h. After a series of washes, biotinylated detection antibodies were added and incubated on a shaker at room temperature for 30 min. The reaction mixture was detected by the addition of streptavidin-phycoerythrin following a wash step and incubated on a plate shaker at room temperature for 10 min. Following a repeat of the washing step, beads were re-suspended in assay buffer for 30 s at room temperature on the plate shaker. Plates were read on a Bio-Plex 200 system (Bio-Rad Laboratories, Hercules, CA, USA) and analyzed using Bio-Plex Manager software (Bio-Rad Laboratories) with a five-parameter model used to calculate final concentrations and values (expressed in pg/mL). Reference samples were run on each plate to determine assay consistency. All wash steps were performed at room temperature using a Bio-Plex handheld magnetic washer (Bio-Rad Laboratories).

Immunohistochemistry

Sections were immunostained for glial fibrillary acidic protein (GFAP; 1:1000 dilution; Cell Signaling Technology, Danvers, Massachusetts), ionized binding adaptor protein 1 (IBA-1; 1:500 dilution; Wako Bioproducts, Richmond, Virginia), and CD68 (1:200 dilution; Serotec; Raleigh, NC). Antibody-antigen complexes were visualized using secondary antibodies labeled

with Alexa Fluor 488, 568, or 647 (Molecular Probes; Eugene, OR), and slides were mounted in media containing 4′,6-diamidino-2-phenylindole (DAPI; Invitrogen, Carlsbad, CA) to identify cell nuclei. Images of the anterior cingulate (cortex) and dentate gyrus (hippocampus) were captured automatically by the ImageXpress Micro Widefield High Content Screening System (Molecular Devices, Sunnyvale, California) using thresholds set using region-matched saline controls. Images were acquired in an unbiased manner using the DAPI channel for each region. Average fluorescence intensity of the target antigen, as well as the number of GFAP immunopositive cells or the number of total IBA-1 immunopositive cells and percentage of IBA-1 immunopositive cells also immunopositive for CD68, was quantified from five fields per region of interest from three serial sections per brain for a total of 15 microscopic fields per brain. These values were averaged within a given animal for each brain region. A total of 3–5 animals were imaged per group.

Experimental Design and Statistical Analysis

Experimental groups were randomized. Different pups were used for cytokine analyses versus immunohistochemical analyses, and animals were randomly assigned to an outcome measure (cytokine measurement or immunohistochemistry) and day of collection (2- or 5-days post-challenge) prior to euthanasia. A total of 93 Lewis and 90 BN male and female offspring were included in this study (Luminex: 51 Lewis and 48 BN; IHC: 42 Lewis and 42 BN).

To assess cytokine levels, statistical analyses were performed using SPSS software (SPSS Version 22; IMB Corp., Armonk, NY); p values < 0.05 for two-tailed tests were considered statistically significant. Data graphs were created using GraphPad Prism (Version 6; GraphPad Software Inc., La Jolla, CA); all results are presented as mean ± SEM. All data were first

assessed for the detection of outliers using the ROUT method, with Q set to 1%. As the distribution of the cytokine and chemokine concentration values were skewed, natural log transformations were used in order to approximate normality. For all values that were below the limit of detection (LOD), we assigned a value of LOD/2 prior to log transformation. A preliminary five-way ANOVA was conducted to determine the effects of sample type (cortex, cerebellum, hippocampus, or serum), cytokine/chemokine, treatment, offspring sex, and day of collection (P12 or P15). The initial five-way ANOVA results led us to run separate ANOVAs for each sample type and cytokine, as significant source × cytokine effects and interactions were noted for all variables. Therefore, individual three-way ANOVAs were conducted for each cytokine/chemokine and sample type, examining the effects of treatment, offspring sex, and day of collection on levels of cytokine/chemokines in each sample type. All post hoc pairwise comparisons of significant interactions within these three-factorial ANOVAs were Sidak-adjusted for multiple comparisons.

For IHC analyses, primary outcomes included average GFAP intensity, total GFAP count, number of IBA-1+ cells, and percentage of IBA-1+ cells co-labeled for CD68 in the hippocampus and cortex for each animal. Mixed-effects regression models, including animal-specific random effects, were used to assess the differences between three groups of animals (mixed immune, adjuvant, and saline) across the brain regions. Exploratory analysis indicated that a natural logarithmic transformation was needed for all outcomes other than colocalization to stabilize the variance and meet the underlying assumptions of the mixed-effects models. Due to zeroes for some outcomes, all values in those outcomes were shifted by 0.1 prior to taking the natural logarithm. Due to a high percentage of zeroes, colocalization was dichotomized to 0 or 1 (colocalization > 0) and a repeated measures logistic regression model was used. Day post-

immunization (2 or 5), group (mixed immune, adjuvant, or saline), sex (male or female), and brain region (cortex, hippocampus) were all variables of interest in the models. Total cell count was included in all models as a covariate. Interactions between these variables were also considered. Akaike information criterion was used for model selection and Wald tests for comparing groups were used. Results for all outcomes other than colocalization are presented as geometric mean ratios between the immune challenge or adjuvant groups and the saline group. All IHC analyses were conducted using SAS version 9.4. Due to aspects of limited group numbers and the presence of numerous conditions, statistical comparisons between specific groups (i.e., strain) were not directly performed but were reported in parallel to relate findings.

Results

Sex- and region-specific differences in CNS cytokine expression at baseline

Immune signaling is important for early development, and sex-specific differences have been evidenced in peripheral and CNS immune signaling under normal conditions [20]. Therefore, we wanted to examine whether cytokine levels exhibited sex-specific differences at baseline, under saline control conditions, during early postnatal development in Lewis and BN rat strains. To evaluate this, and all subsequent cytokine comparisons, we used a bead-based Luminex assay to assess the levels of a set of 10 analytes including a subset of Th-related cytokines, specifically IFN-γ, IL-4, IL-17, and IL-10, as well as inflammatory chemokines in peripheral blood and within different brain regions of experimental animals. Animals were exposed to peripheral immune challenge in adjuvant, adjuvant-only, or saline on P10, and samples were collected 2 and 5 days post-challenge in male and female Lewis and BN rats (Fig. 1a). Data presented for baseline sex comparisons were collapsed between both time points of collection, P12 and P15, as

no statistically significant differences were observed between the two time points for saline control conditions.

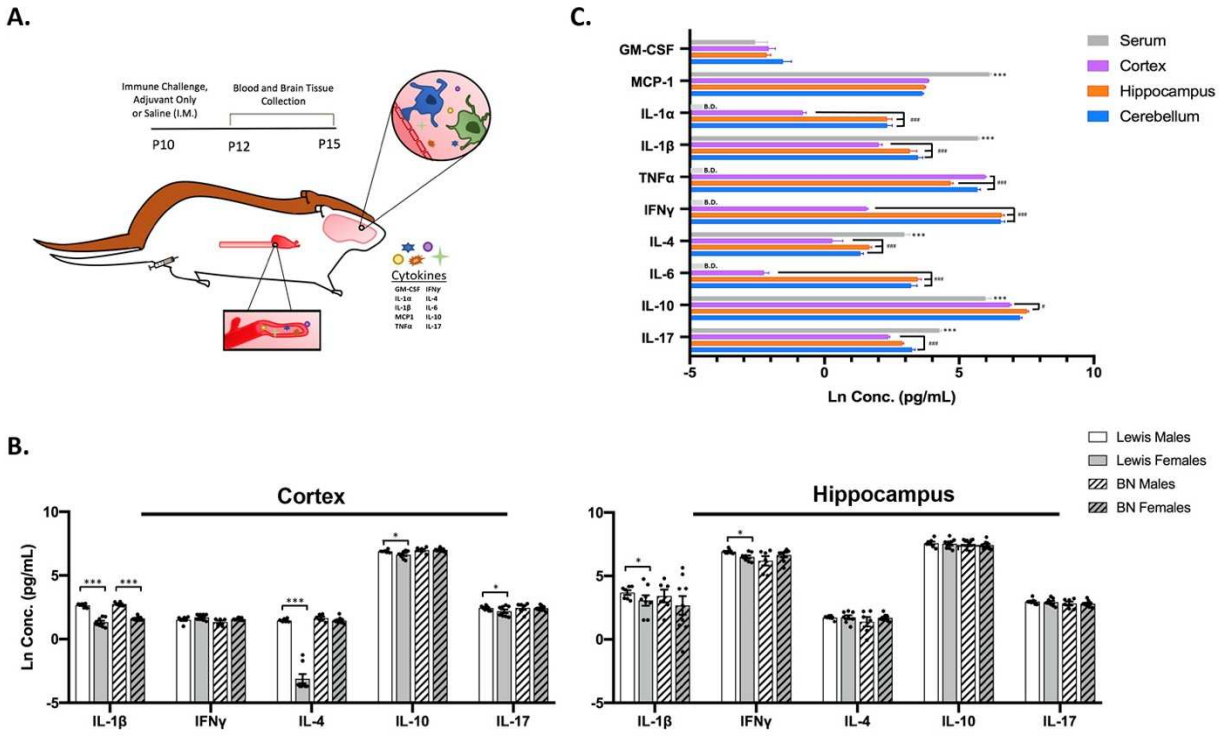

Figure 1. Sex- and region-specific differences in cytokine levels at baseline. Lewis and Brown Norway (BN) rats were injected i.m. with mixed immune challenge, adjuvant-only, or saline on P10. Samples were collected 2- or 5-days post-challenge and subjected to cytokine and chemokine profiling. **a** Illustration of experimental design with primary outcome measures. **b**, **c** Cytokine and chemokine levels under saline control conditions. **b** Cytokine levels compared within strains (BN (15; 6M, 9F), Lewis (15; 7M, 8F)) and between sexes; collapsed between time point of collection due to no differences observed. **c** Cytokine levels compared across region of collection; collapsed between sex, strain, and day of collection. $N = 30$ animals per region. Star (*) corresponds to comparisons between serum and all brain regions using the following scale: $*p < 0.05$, $**p < 0.01$, $***p < 0.001$. Hashtag (#) represents comparisons solely between brain regions only using a similar scale. B.D. defined as below detection. All data are displayed as the natural log-transformed values with mean +/− SEM. M.B. designed and created figures as well as conducted final data analysis. K.M.S. contributed to experimental design, conducted animal exposures, harvested tissues, and prepare samples for cytokine analysis. L.H. contributed to experimental design and analysis of cytokine data. S.L. and D.J.H. conducted statistical analysis of the data.

Notable sex-specific differences in baseline cytokine levels were seen in the cortex and to a lesser extent the hippocampus. In the cortex, baseline sex differences were observed in several important Th-type cytokines, such as IL-4 ($p < 0.001$), IL-10 ($p = 0.01$), and IL-17 ($p < 0.05$) as well as IL-β ($p < 0.001$), with males exhibiting an increased level of these cytokines compared to females (Fig. 1b). Interestingly, these results were only true for Lewis rats and not observed in

the BN rat strain, with the exception of higher IL-1β ($p < 0.001$) in male BN rats compared to females. When considering cytokine levels in the hippocampus, baseline sex-specific effects were more limited. Similar to the cortex, a significant difference was observed for IL-1β ($p = 0.01$) in Lewis rats. Additionally, a sex-specific increase in IFN-γ ($p < 0.05$) was also seen in the hippocampus of Lewis rats, with males displaying a higher level of IFN-γ than females (Fig. 1b).

Minimal sex-specific differences were seen in serum cytokine levels at baseline, with the only significant finding being an effect of sex on the level of MCP-1 (monocyte chemoattractant protein 1; CCL2) in Lewis rats, with males displaying a greater level of MCP-1 than females ($p = 0.004$; Additional file 1: Figure S1A). No sex-specific differences were observed in the cerebellum under saline control conditions (Additional file 1: Figure S1D). In multiple brain regions, baseline differences in GM-CSF levels were noted but data were not included in the final analysis due to several samples having values below the LOD, thus skewing group differences (Additional file 1).

Brain region-specific differences in the level of several cytokines were also noted. In serum, levels of the majority of analytes were found to be significantly different than concentrations of these same cytokines measured in brain regions of the corresponding animals (Fig. 1c). Specifically, the levels of MCP-1 ($p < 0.001$), IL-1β ($p < 0.001$), IL-4 ($p < 0.001$), and IL-17 ($p < 0.001$) were observed to be higher in serum than the cortex, hippocampus, and cerebellum, while the level of IL-10 ($p < 0.001$) appeared lower in the serum compared to selected brain regions (Fig. 1c).

Differences were also observed when comparing cytokine levels between brain regions with main findings including lower levels of many analytes in cortical lysates. The levels of IL-1α ($p < 0.001$), IL-1β ($p < 0.001$), IFN-γ ($p < 0.001$), IL-4 ($p < 0.001$), and IL-6 ($p < 0.001$) were seen to be lower in the cortex, compared to both the hippocampus and cerebellum (Fig. 1c), while IL-10 ($p < 0.05$) was significantly lower in the cortex compared to the hippocampus only, and cortical IL-17 ($p < 0.001$) was less than that measured in the cerebellum. Additionally, the hippocampal level of TNF-α was significantly lower compared to other brain regions ($p < 0.001$; Fig. 1c).

Effect of peripheral immune challenge on serum cytokines and chemokines

Next, to broadly characterize the innate and adaptive immune responses to an early postnatal peripheral immune challenge, we assessed post-challenge cytokine levels between strain, sex, region, and time point of collection as described above and outlined in Fig. 1a. Consistent with the age of the rat pups, the effect of treatment on the serum cytokine response was relatively mild (Additional file 2: Figure S2A and Additional file 3: Figure S3A). Over half of the serum samples had levels of IFN-γ, IL-1α, IL-6, and TNF-α below the LOD, and these cytokines were therefore excluded from further analysis. For serum analytes that were above the LOD and were found to be differentially regulated in response to treatment, effects were broadly similar across strains with some sex-specific skewing. For GM-CSF, significant main effects of treatment were seen in both Lewis and BN rat strains (Additional file 2: Figure S2A). Specifically, post hoc testing revealed sex-dependent increases in the level of GM-CSF in serum 5 days post-challenge in males of both strains (Lewis, $p < 0.001$; BN, $p = 0.005$; Fig. 2a), with significant increases also seen under adjuvant conditions in male Lewis rats ($p = 0.001$). In contrast, female BN rats

exhibited significant increases in GM-CSF in response to adjuvant treatment compared to saline controls at the same time point ($p < 0.001$; Fig. 2a). Of note, a significantly higher level of GM-CSF was seen under adjuvant conditions compared to immune challenge in female BN rats at 5 days post-challenge (Fig. 2a). However, this was the only instance of such a finding in the study and is likely due to several serum GM-CSF values falling below the level of detection in these animals. A main effect of treatment was observed in the level of the chemokine MCP-1 in both Lewis and BN rats (Additional file 2: Figure S2A). Higher levels of MCP-1 were detected under adjuvant-only conditions at 5 days post-challenge in female BN rats ($p = 0.02$) and at 2 days post-challenge in female Lewis rats ($p = 0.001$), or 2 days following mixed immune challenge in Lewis males ($p = 0.016$; Fig. 2b).

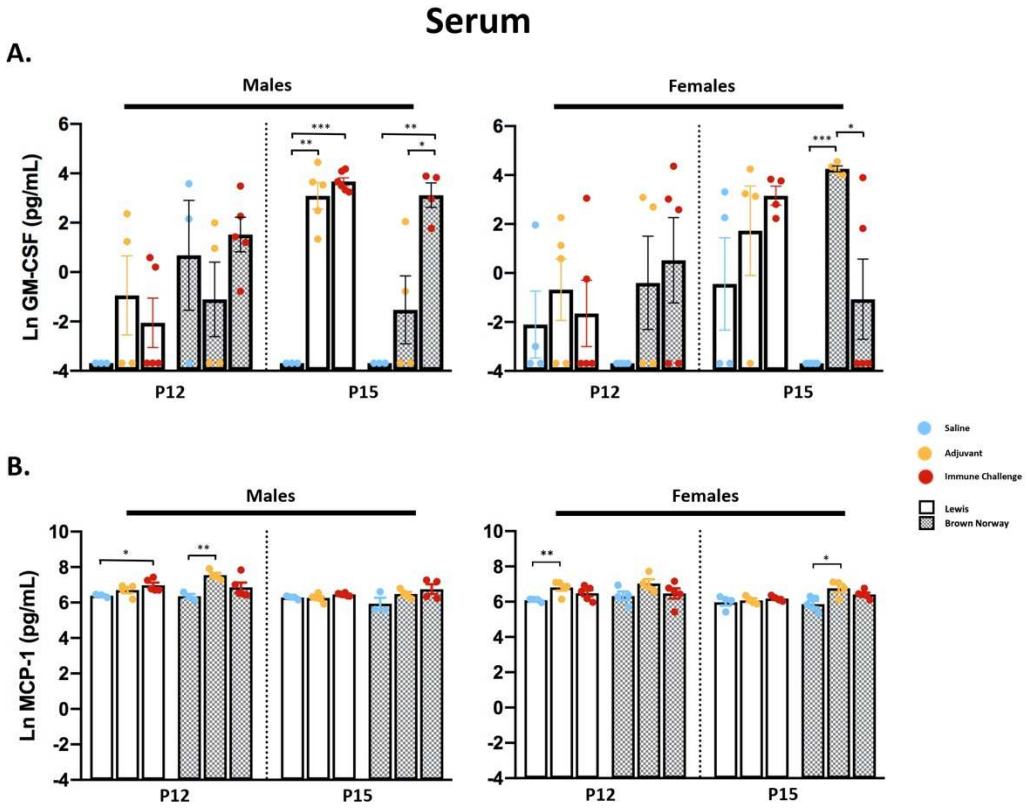

Figure 2. Peripheral immune stimulation broadly upregulates innate cytokine levels in the cortex and hippocampus. Cortical, hippocampal, and cerebellar lysates were collected from rats 2- or 5-days following exposure and subjected to cytokine and chemokine analysis. **a** Concentrations of innate cytokines in the cortex, compared between experimental conditions. Data are collapsed between sex and day due to minimal differences seen; $N = 15–20$ per condition. **b**, **c** Cytokine levels from hippocampal lysates; black solid bars above certain analytes specify time point

or sex-specific conditions. **b** Levels of several innate cytokines: GM-CSF collapsed between sex and day ($N = 13–20$ per condition), IL-1a, IL-1B shown at P12 only and MCP-1 in females collapsed between day ($N = 7–10$ per condition). **c** Hippocampal IL-6 levels across treatment and strain in female rats; $N = 4–5$ per condition. Data represent mean +/− SEM, *$p < 0.005$, **$p < 0.01$, ***$p < 0.001$. M.B. designed and created figures as well as conducted final data analysis. K.M.S. contributed to experimental design, prepare samples for cytokine analysis. L.H. contributed to experimental design and analysis of cytokine data. S.L. and D.J.H. conducted statistical analysis of the data.

Innate immune cell-related cytokine response in the CNS

To understand the CNS immune response to an acute peripheral immune challenge, we evaluated cytokine and chemokine levels in tissue lysates from the cortex, hippocampus, and cerebellum of male and female Lewis and BN rats. The most striking results and greatest inflammatory response to the mixed immune challenge were seen in the cortex. In both male and female Lewis and BN rats, a significant main effect of treatment was observed for several cytokines associated with the innate immune response in the cortex at 2 and 5 days following treatment (Additional file 2: Figure S2B). Specifically, IL-1α, IL-1β, and IL-6 were significantly upregulated following either peripheral immune challenge or adjuvant-only exposure in both strains (Fig. 3a). Similar effects of treatment were noted for GM-CSF and MCP-1, both important innate immune cell recruitment and activation molecules (Fig. 3a). Representative cortical innate immune cytokine data are collapsed across sex and time point of collection as a response to treatment appeared similar between these conditions. The only exception to this pattern was the lack of increased MCP-1 expression in the cortex in male BN rats exposed to either peripheral immune challenge or adjuvant-only (Additional file 3: Figure S3B).

In the hippocampus, a main effect of treatment was also seen for the majority of cytokines (Additional file 2: Figure S2C). A significant increase in GM-CSF compared to saline controls was observed at both 2 and 5 days post-challenge across experimental conditions, strains, and sexes (Fig. 3b, Additional file 3: Figure S3C). In both sexes, significant increases in IL-1α ($p < 0.05$) and IL-1β ($p < 0.001$) were noted in BN rats, while a significant increase in IL-

1β ($p < 0.001$), but not IL-1α, was observed in Lewis rats at 2 but not 5 days post-challenge (Fig. 3b). Elevated levels of MCP-1 were seen only in female Lewis rats at 2 days ($p = 0.01$) and 5 days ($p = 0.034$) post-challenge (Fig. 3b). Interestingly, immune challenge decreased hippocampal IL-6 relative to saline control in female rats of both strains ($p < 0.05$; Fig. 3c). Other cytokines, such as IL-1α and IL-1β, were also decreased by peripheral immune challenge or exposure to adjuvant-only at 5 days post-challenge (Additional file 3: Figure S3C). The effect of peripheral immune challenge on the cytokine response in the cerebellum was both weak and varied (Additional file 2: Figure S2D), with the exception of a significant increase in GM-CSF, similar to that seen in the hippocampus and cortex (Additional file 3: Figure S3D).

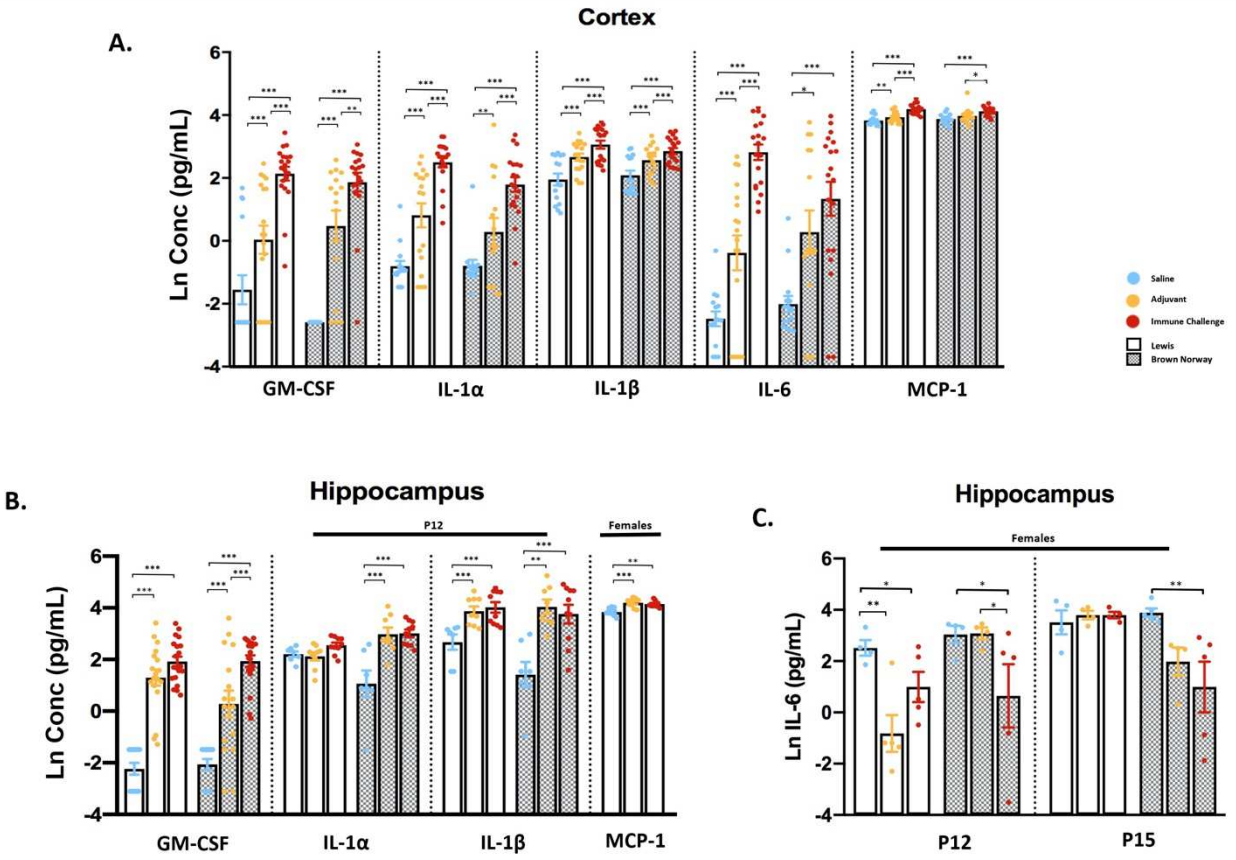

Figure 3. Peripheral immune stimulation broadly upregulates innate cytokine levels in the cortex and hippocampus. Cortical, hippocampal, and cerebellar lysates were collected from rats 2- or 5-days following exposure and subjected to cytokine and chemokine analysis. **a** Concentrations of innate cytokines in the cortex, compared between

experimental conditions. Data are collapsed between sex and day due to minimal differences seen; $N = 15–20$ per condition. **b**, **c** Cytokine levels from hippocampal lysates; black solid bars above certain analytes specify time point or sex-specific conditions. **b** Levels of several innate cytokines: GM-CSF collapsed between sex and day ($N = 13–20$ per condition), IL-1a, IL-1B shown at P12 only and MCP-1 in females collapsed between day ($N = 7–10$ per condition). **c** Hippocampal IL-6 levels across treatment and strain in female rats; $N = 4–5$ per condition. Data represent mean +/− SEM, *$p < 0.005$, **$p < 0.01$, ***$p < 0.001$. M.B. designed and created figures as well as conducted final data analysis. K.M.S. contributed to experimental design and prepared samples for cytokine analysis. L.H. contributed to experimental design and analysis of cytokine data. S.L. and D.J.H. conducted statistical analysis of the data.

Th-type cytokine responses in the CNS

Due to evidence suggesting that the immune responses in Lewis and BN rats are skewed toward a Th1- or Th2-specific response, respectively [21, 22], a primary aim of this study was to evaluate the contribution of a different genetic immune background on the response to immune challenge. In cortical lysates from both strains, a main effect of treatment was observed for all canonical Th-type cytokines measured (Additional file 2: Figure S2B). Interestingly, the level of IFN-γ (a major Th1 cytokine) in the cortex following mixed immune challenge was significantly elevated in males of both strains ($p < 0.001$), with similar effects at 2 and 5 days post-challenge (Fig. 4a). In female rats of either strain, cortical IFN-γ levels were significantly increased at 5 days ($p < 0.01$) but not at 2 days post-challenge (Fig. 4a). In contrast to the cortical response, peripheral immune challenge had little or no significant effect on IFN-γ levels in the hippocampus and cerebellum of Lewis or BN rats (Additional file 3: Figures S3C and D). Striking strain and sex differences were seen in the response to immune challenge in cortical levels of IL-4, an indicator of Th2-type responses. Specifically, peripheral immune challenge significantly increased cortical IL-4 levels in female Lewis rats at 2 days ($p = 0.003$) and 5 days ($p < 0.001$) post-challenge, while exposure to adjuvant-only treatment only resulted in elevated cortical IL-4 levels at 5 days post-exposure ($p < 0.001$; Fig. 4b). In contrast, compared to saline controls, cortical IL-4 levels were significantly decreased in female BN rats in response to mixed immune challenge ($p < 0.01$) or adjuvant ($p < 0.01$), or unchanged in male rats of either strain

(Fig. 4b; Additional file 3: Figure S3B). Coincident with these responses, post hoc analysis revealed a lack of effect of either immune challenge or adjuvant-only on IL-17 levels in the BN rat cortex at both 2- and 5-days post-challenge. However, cortical IL-17 levels were significantly elevated compared to controls in response to mixed immune challenge in male Lewis rats ($p < 0.001$) and in response to either mixed immune ($p < 0.05$) or adjuvant treatment ($p < 0.05$) in female Lewis rats (Fig. 4c). Cortical IL-10 levels were similar between strains, although significantly increased levels of IL-10 in response to experimental manipulation were seen only in male rats, with no apparent effects in females (Fig. 4d). Data for cortical IL-17 and IL-10 levels were collapsed between day of collection due to minimal differences seen for those two analytes over time (Additional file 3: Figure S3B).

In the hippocampus, male BN rats exhibited significant increases in IFN-γ ($p < 0.001$), IL-4 ($p = 0.035$), IL-10 ($p = 0.037$), and IL-17 ($p < 0.001$) in response to treatment at 2 days post-immune challenge (Fig. 4e). Interestingly, there were no significant increases in the levels of these cytokines in the hippocampus of female BN rats or either sex of Lewis rats (Additional file 3: Figure S3C). While a main effect of treatment on Th-type responses in the cerebellum was apparent under certain conditions (Additional file 2: Figure S2D), post hoc analysis revealed effects of treatment on cytokine production in the cerebellum to be largely non-significant across most conditions (Additional file 3: Figure S3D).

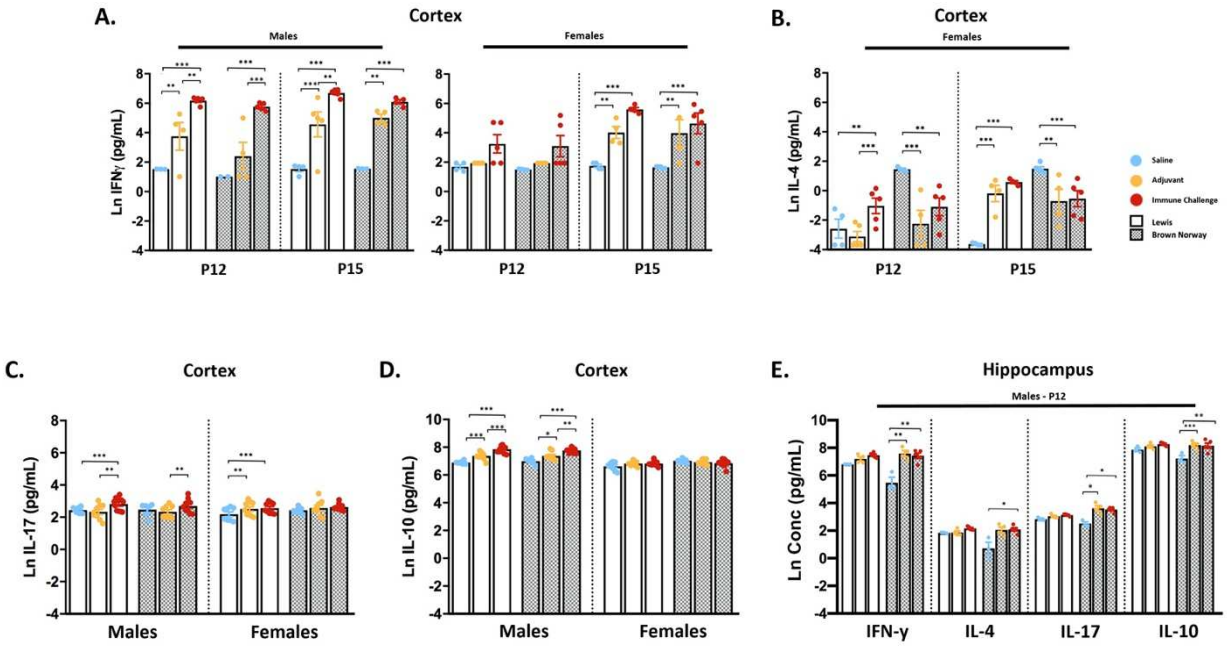

Figure 4. CNS Th-type responses to peripheral immune stimulation are sex- and strain-specific. Th-type cytokine responses were evaluated in brain lysates. Cortical IFN-γ; $N = 3–6$ per condition (**a**), IL-4; $N = 3–5$ per condition (**b**), IL-17; $N = 7–11$ per condition (**c**) and IL-10; $N = 7–10$ per condition (**d**) levels. IL-4 displayed only in female rats due to no differences seen in males; IL-10 and IL-17 levels collapsed between day. **e** Hippocampal Th-type cytokine levels in male rats at 2 days post-challenge; $N = 3–5$ per condition. Data represent mean +/− SEM, $*p < 0.005$, $**p < 0.01$, $***p < 0.001$. M.B. designed and created figures as well as conducted final data analysis. K.M.S. contributed to experimental design and prepared samples for cytokine analysis. L.H. contributed to experimental design and analysis of cytokine data. S.L. and D.J.H. conducted statistical analysis of the data.

Evaluation of CNS cellular immune response

To understand the effects of mixed immune challenge or adjuvant-only exposure on the brain-specific cellular response, the number of GFAP immunopositive cells and the average intensity of GFAP immunofluorescence were evaluated as indicators of astrogliosis, whereas the total number of IBA-1 immunopositive cells and percentage of IBA-1 immunopositive cells also immunoreactive for CD68 were quantified to assess the microglial response.

GFAP is an intermediate filament expressed mainly in astrocytes that is upregulated under conditions of hypertrophy and activation [24]. In both the cortex and hippocampus, GFAP average fluorescence intensity was significantly increased within both strains at 2- and 5-days post-challenge. In Lewis rats, across all conditions, the average intensity of GFAP

immunoreactivity was significantly higher in the hippocampus than in the cortex, whereas no significant regional differences were observed in BN rats (Fig. 5a–c). In addition to brain region-specific strain differences, sex-specific effects of both mixed immune challenge and adjuvant-only exposure on average intensity of GFAP immunofluorescence were observed. While exposure to either treatment significantly increased the average intensity of GFAP immunofluorescence in male and female BN rats across brain regions at 2 and 5 days post-challenge (Fig. 5d), exposure to either treatment in Lewis rats significantly increased the average intensity of GFAP immunofluorescence in males only (Fig. 5e). Due to best-fit statistical modeling used for IHC analysis, conditions were collapsed between groups when no differences were observed. With regard to GFAP intensity as noted here, a similar response to immune challenge was seen across the brain region within a rat strain.

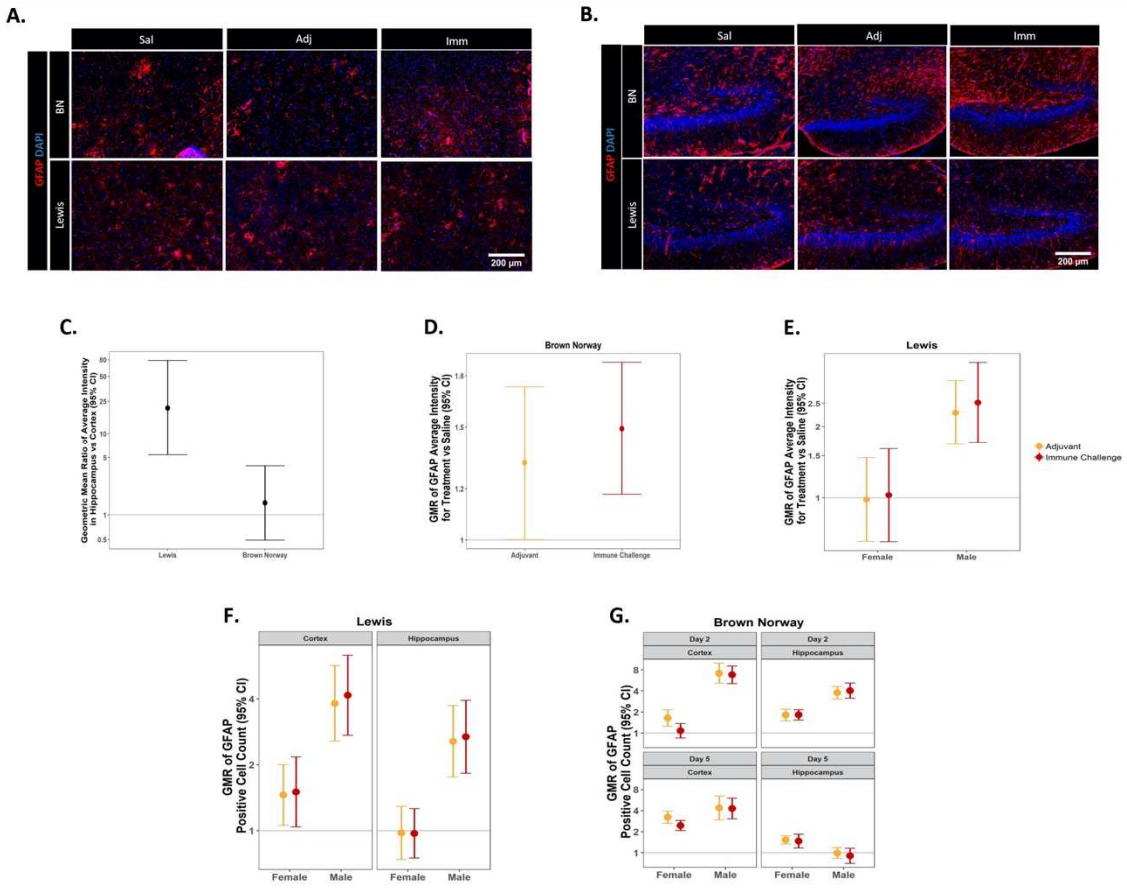

Figure 5. Sex- and strain-specific increases in the average intensity of GFAP immunoreactivity and numbers of GFAP immunopositive cells. GFAP immunoreactivity was assessed at 2- and 5-days post-exposure. Representative photomicrographs of GFAP immunoreactivity and DAPI labeling in the cortex (**a**) of female rats and the hippocampus (**b**) of male BN and female Lewis rats; Sal=saline, Adj=adjuvant-only, Imm=immune challenge. **c** Geometric mean ratio (GMR) of GFAP average intensity in response to immune challenge, adjuvant-only, or saline control conditions in the hippocampus versus the cortex within each strain; collapsed between sex and day of collection ($N = 42$ per strain; BN (19Imm, 19Adj, 4Sal); Lewis(16Imm(8M/8F), 17Adj(9M/8M), and 9Sal(5M/4F)). GMR plots of GFAP average intensity in BN (**d**) and Lewis (**e**) rats collapsed between day and region, as well as GFAP-positive cell counts in Lewis (**f**) and BN (**g**) strains of each treatment relative to saline control collapsed between the day of collection in (**f**). Error bars represent 95% CI; a CI not including the normalization line (line at 1) indicates a significant difference between brain regions (**c**) or the treatment and saline controls (**d**–**g**) at $p \leq 0.05$. M.B. helped to design and create figures. K.M.S. contributed to experimental design and harvested tissues. C.A.B. contributed to design, conduct, and analyses of IHC experiments as well as preparing final figures. E.A.G. contributed to design, conduct, and analyses of IHC experiments. S.L. and D.J.H. conducted statistical analysis of the data.

A significant increase in the number of GFAP immunopositive cells was also seen in response to mixed immune challenge or adjuvant-only exposure, but these effects varied between brain regions and strains. In the cortex, GFAP immunopositive cell counts were increased following mixed immune challenge or adjuvant-only exposure in both strains at 2 and 5 days post-challenge (Fig. 5f, g) with the exception of female BN rats that exhibited no significant change in GFAP immunopositive cell counts at 2 days post-mixed immune challenge (Fig. 5g). In contrast, more consistent sex and strain differences were seen in the hippocampus. In Lewis rats, males exhibited a significant increase in the number of GFAP immunopositive cells in the hippocampus 2 and 5 days post-challenge following mixed immune challenge or adjuvant-only exposure, whereas female Lewis rats showed no differences in response to either challenge (Fig. 5f). In the BN strain, the numbers of GFAP immunopositive cells in the hippocampus significantly increased in both sexes 2 and 5 days post-challenge, with the exception of male BN rats that exhibited no effect at 5 days post-challenge (Fig. 5g).

The cellular neuroinflammatory response was further evaluated by immunostaining for IBA-1 in the cortex and hippocampus. IBA-1 is a pan-macrophage/monocyte marker used broadly in the brain to identify microglia [25]. Interestingly, in contrast to increased brain GFAP

immunofluorescence intensity and number of GFAP immunopositive cells seen across many conditions, the number of IBA-1 immunopositive cells in the cortex and hippocampus were either unchanged or significantly decreased in these regions in response to mixed immune challenge or adjuvant-only exposure, compared to saline controls (Fig. 6a, b). In BN rats, a reduction in the number of IBA-1 immunopositive cells was observed in the cortex and hippocampus of male rats exposed to either mixed immune challenge or adjuvant-only and in the cortex and hippocampus of females treated with adjuvant-only (Fig. 6b). In contrast, there was no difference in the number of IBA-1 immunopositive cells in female BN rats exposed to mixed immune challenge or Lewis rats under either treatment condition compared to saline controls (Fig. 6b, c).

Additionally, colocalization of CD68 immunoreactivity with IBA-1 was used as a measure of microglial activation in the brain, as CD68 is a lysosomal marker used broadly to indicate phagocytic activity in macrophages [26]. Following the analysis of the response to either mixed immune challenge or adjuvant exposure, there were no significant differences between treatment conditions, strain, or sex with respect to IBA-1/CD68 colocalization (Fig. 6d).

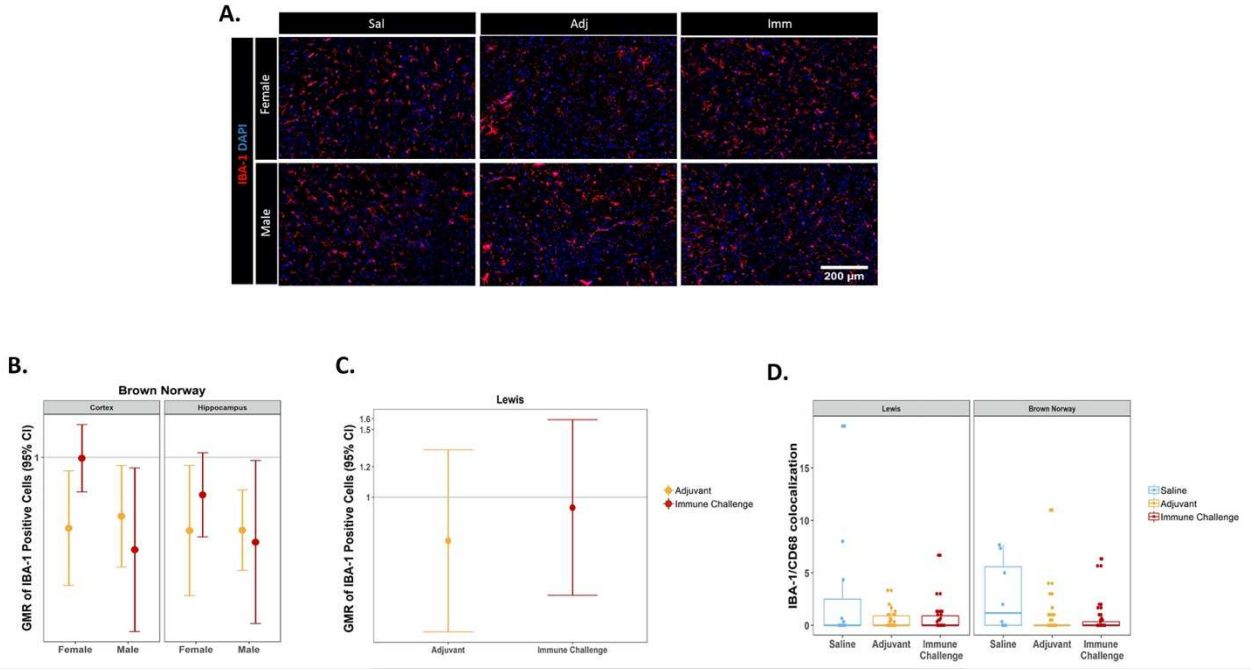

Figure 6. Minimal effects of treatment on IBA-1 immunoreactivity. The number of IBA-1 immunopositive cells was quantified in the cortex and hippocampus in response to treatment. **a** Representative photomicrographs of IBA-1 immunoreactivity and DAPI labeling in the cortex of BN rats; Sal=saline, Adj=adjuvant-only, Imm=immune challenge. Geometric mean ratio (GMR) plots displaying the number of IBA-1 immunopositive cells for treatment versus saline control in BN ($N = 40$; 18Imm(10M/8F), 18Adj(9M/9F), 4Sal(2M/2F) (**b**), and Lewis ($N = 42$; 15Imm, 15Adj, 7Sal) (**c**) rat strains. Data for IBA-1 immunopositive cell counts expressed as ratio over saline control conditions. Error bars represent 95% CI; a CI not including the normalization line (line at 1) indicates a significant difference between the treatment and saline controls at $p \leq 0.05$. **d** Quantification of IBA-1/CD68 colocalization within strains and across treatment conditions, data expressed as boxplots illustrating the distribution of data points for each animal and the interquartile range. M.B. helped to design and create figures. K.M.S. contributed to experimental design and harvested tissues. C.A.B. contributed to design, conduct, and analyses of IHC experiments as well as preparing final figures. E.A.G. contributed to design, conduct, and analyses of IHC experiments. S.L. and D.J.H. conducted statistical analysis of the data.

Discussion

The physiologic importance of the interplay between the immune and nervous systems in neurodevelopment has gained recognition in recent years, and immune molecules are increasingly implicated as important in neurogenesis, cortical development, and neurodevelopmental disorders [27,28,29,30]. Despite this, knowledge regarding the CNS response to a peripheral immune challenge during early postnatal development is limited in scope. Numerous studies have investigated perinatal immune signaling and CNS development using iterations of the maternal immune activation (MIA) paradigm (reviewed in [31]). This is

likely due to the growing body of literature on the topic, clinical relevance, and thorough characterization of the methodology [32]. Although, recent research has suggested, perhaps unsurprisingly, that MIA-induced effects on brain circuit-specific function are dissociable from those effects induced by early postnatal immune challenge, with contrasting results on glutamatergic and GABAergic signaling respectively [33]. Therefore, it is of value to develop a deeper knowledge regarding how acute peripheral immune stimulation, postnatally, may influence the production of immune effector molecules and activation of glial cells in the CNS. The latter point is particularly important as altered neural function due to perinatal immune activation may depend partly on early glial priming, contributing to long-term functional alterations in these cells [5, 6, 30].

An important aspect of our study design is the developmental window during which the acute mixed immune challenge occurred. Prior studies comparing the timeline of rat and human development suggest that preweaning ages in rats correspond to roughly the first year of life in humans [16, 17]. Therefore, to mirror the immune challenges a human infant may face in early life, we chose to expose rats on P10—a time of early postnatal development when hematopoiesis is shifted from the fetal liver and spleen to the bone marrow, and the lymphoid architecture begins to take shape [34]. Furthermore, in rodent development, P10 is a time shortly after the early critical period for sexual differentiation of the brain [35] and represents an age of peak brain growth in rats [18]. These factors are important for proper interpretation of sex- and age-specific comparisons in this study.

To characterize peripheral and central responses, we collected serum and brain samples from Lewis and BN rats at 2- and 5-days post-exposure to immune challenge, adjuvant-only, or saline. These time points were chosen to correspond to an early stage, 2 days post-exposure,

where innate immune mechanisms would be dominant, and at a later stage, 5 days post-exposure, where adaptive immune responses would potentially be active [36]. Importantly, development of the adaptive immune system in rodents is similar to humans in that perinatal lymphocyte numbers and proliferative responses in lymphoid organs are low [37]. Further evidence suggests that germinal center formation is absent at P10 in rats and, subsequently, they are thought to be incapable of mounting a proper primary immune response [38]. Therefore, it is not surprising that many cytokine levels were below the level of detection in the peripheral blood. However, it is notable that the cytokines IL-4, IL-10, and IL-17 were detectable in serum, albeit with no significant differences between experimental groups or rat strain. Relevant here, and known to be similar between species, evidence shows that early postnatal Th-type responses in rats and other mammals are skewed toward Th2 [39, 40]. Furthermore, studies in neonatal mice using exposure to various inoculation components resulted in a decreased IgG (immunoglobulin G) 2a/IgG1 ratio compared to similarly exposed adult animals [41]. These data support a bias of a Th2-type versus Th1-type response during the neonatal period. The inability to detect serum IFN-γ in our samples while observing measurable IL-4 and IL-10 levels may lend further credence to this potential skewing.

In contrast to the modest peripheral response, the cytokine and chemokine responses within the CNS were significantly more robust, with the most dramatic effects noted in the cortex. While the cytokines IL-1α and IL-6 were not detectable in the serum, they were markedly elevated in the brains of rats of both strains following the peripheral immune stimulation or adjuvant-only exposure, compared to saline control animals. Of importance, IL-1 and IL-6 are known to modulate glial responsiveness and are suggested to be crucial for glial proliferation and the release of important trophic factors to support brain plasticity [42, 43]. These current data

may support this finding, as male BN rats, which exhibited no significant differences in IL-1 or IL-6 levels in the hippocampus 5 days post-treatment, also exhibited no difference in the number of GFAP immunopositive cells in the same region at the same time point in these animals. Whereas, at other time points and between sexes, there were significant differences in relevant cytokine levels and GFAP immunopositive cell numbers. It is important to note that the relationships described here and elsewhere regarding glial activation and cytokine levels are partly speculative as direct comparisons between GFAP or IBA-1 reactivity and specific cytokines were not conducted due to the large number of groups already being compared. Another innate cytokine significantly upregulated in the brain within the majority of treatment groups was GM-CSF, long known as a regulator of macrophage differentiation and more recently believed to play a role in myeloid cell to lymphocyte communication [44, 45]. This may suggest expansion or activation of the resident macrophage population. However, no significant differences in the number of IBA-1 immunoreactive cells were noted between experimental conditions and among different brain regions in Lewis rats, whereas significant decreases in IBA-1 immunopositive cell numbers were observed in the cortex and hippocampus of BN rats, with the exception of female BN rats exposed to mixed immune challenge. MCP-1, a chemokine important for glial differentiation and motility [46], was also significantly elevated in response to treatment. However, the MCP-1 response was sex and strain-specific, with no observable relationship to changes in GFAP or IBA-1 immunostaining. Our findings that GM-CSF and MCP-1 levels did not appear to relate to the immunohistochemical results of CNS cellular immune activation are surprising due to their putative role in potentiating glial responses [47]. Possible explanations for this discrepancy could be the developmental stage of the animals at the time of exposure and sample collection, or that these molecules may act as signals to recruit

other immune cells to the CNS compartment. As limitations in this study, we did not investigate the possibility of peripheral immune cell infiltration in the brain, blood-brain barrier permeability, or the cellular source of the cytokines/chemokines. These aspects are certainly important to determine mechanistic aspects of the immune dysregulation seen but were outside the scope of the initial study aims and are definite points for future investigation.

In support of the concept that cytokine and chemokine signaling is important for glial regulation and neurodevelopment under normal conditions, levels of most cytokines and chemokines within the CNS of both Lewis and BN rats were already strikingly high under saline control conditions. This result appeared across the brain regions surveyed, with some variation at the level of single analytes. For example, IL-4, IL-10, and IL-17 were detected at surprisingly high levels throughout the brain at baseline, whereas levels of IL-6 were robust in the hippocampus and cerebellum, yet barely detectable in the cortex. These findings corroborate previously published data also observing appreciable levels of cytokines across brain regions at baseline during early postnatal development and specifically validate outcomes seen in our dataset such as lower IFN-γ in the cortex compared to the hippocampus in the second postnatal week [48]. While of interest, the biologic significance behind this brain region-specific difference in IFN-γ and other cytokines does not seem to be evident in the existing literature and will be important for further study. Additionally, our study suggests that cytokine levels at baseline appear to vary widely as a function of sex or strain. These data strongly support previous findings that immune molecule signaling in the CNS is active during normal neurodevelopment [49] and suggest consideration of sex and strain differences in the design of neuroimmunological experiments.

While innate-like cytokines and chemokines within the CNS showed broadly similar patterns across strain and sex, CNS Th-type cytokine responses varied greatly between Lewis

and BN rats. These two rat strains were chosen for comparison due to previous knowledge of the susceptibility or resistance of either strain to the development of Th-subset specific disorders [50, 51]. However, the basis of this skewing may not only involve the CD4+ T cell compartment, but also CD8+ T cells and mast cells [21, 52, 53]. Given these findings, it may be anticipated that this immune response skewing could extend to the CNS as well. Using IFN-γ as a crude marker of a Th1-type response, our results suggest that these two strains do not differ greatly in Th1-type responses within the CNS. However, when evaluating IL-4 levels as a readout of a Th2-type response, the results were dramatically different. In the cortex, where the most robust cytokine responses were noted, female Lewis rats exhibited elevated levels of IL-4 in response to mixed immune challenge or adjuvant, whereas a significant decrease in IL-4 was noted in female BN rats under the same treatment conditions. No significant treatment-related differences in the level of IL-4 were observed in male rats of either strain. These results seem in opposition of what might be expected with Lewis rats exhibiting a greater IL-4 response and BN rats showing no changes or decreases in IL-4 levels in cortical lysates. However, when considering that we also observed sex and strain differences in other Th-subtype cytokines, this outcome suggests several non-mutually exclusive possibilities. First, as supported by the current study, the CNS cytokine response is likely different than the concomitant peripheral immune response. Second, it could be that genetic immune skewing between Lewis and BN strains cannot be classified into a defined Th-subset category. Finally, sex may be a greater determinant than genetic background when considering CNS immune skewing. Inherent differences in Th1/Th2 skewing between sexes have been previously proposed, with females skewed toward a Th2 dominant response [54]. Our data are consistent with this last point, at least with regard to IL-4 levels in the CNS.

These cytokine results, coupled with IHC evidence of significant increases in GFAP reactivity in female BN rats, may suggest a model in the cortex in which decreased IL-4 levels are related to astrocytic activation. In support of this concept, recent work has shown that pretreatment with IL-4 prior to peripheral LPS exposure abolishes LPS-induced astrocytic activation in the cortex of mice, as measured by GFAP immunoreactivity and iNOS expression [55]. Additionally, under many conditions, IL-4 responses are characterized as anti-inflammatory in nature and may act as a growth or repair responses in the brain [56, 57]. Therefore, it is plausible that IL-4 levels in the brain play an important role in regulating cellular inflammatory status, at least in regard to astrocytic activation.

Surprisingly, peripheral immune challenge or adjuvant exposure alone either had no effect or significantly decreased the number of IBA-1 immunopositive cells in the cortex and hippocampus. Additionally, no significant effects were noted upon assessment of IBA-1 colocalization with CD68. This is interesting as we saw a robust increase in GFAP immunopositive cells and expression levels across most conditions. The reasoning for this could lie once again in the developmental time period of exposure, as microglia undergo distinctive rounds of maturation during the perinatal period [58, 59]. In support of this reasoning, recent work has demonstrated that peripheral LPS challenge in P14 mice resulted in a significant increase in GFAP but not IBA-1 reactivity in the hippocampus [60]. More importantly, opposite effects were observed when adult animals were subjected to the same treatment, with pronounced increases in IBA-1 reactivity but not GFAP reactivity [60]. Furthermore, a separate group found that glial activation occurred sequentially in response to a systemic immune challenge, with microglial activation occurring shortly after exposure and induction of astrocytic

activation occurring in a delayed manner [61]. These studies suggest that glial activation is tightly regulated both temporally and spatially.

The current study supports existing evidence that immune signaling molecules are highly upregulated in the brain following a peripheral immune challenge. Additionally, it emphasizes the influence of factors such as sex and genetic background on the cytokine and chemokine response, as well as astrogliosis and microgliosis within the brain. Interestingly, we observed high concentrations of various cytokines in the CNS under baseline conditions, the levels of which also varied significantly depending on strain, sex, and brain region. While this study provides a thorough characterization of the CNS immune response to a peripheral immune challenge, taking into account a broad number of factors, further study is needed to provide mechanistic support for how this cytokine/chemokine signaling and cellular activation may shape brain development.

References

1. Hu W, Pasare C. Location, location, location: tissue-specific regulation of immune responses. *J Leukoc Biol* 2013, 94:409-421.
2. Prinz M, Priller J. The role of peripheral immune cells in the CNS in steady state and disease. Nature Neuroscience 2017, 20:136.
3. Jiang NM, Cowan M, Moonah SN, Petri WA, Jr. The Impact of Systemic Inflammation on Neurodevelopment. Trends Mol Med. 2018;24(9):794-804.
4. Thomson CA, McColl A, Cavanagh J, Graham GJ. Peripheral inflammation is associated with remote global gene expression changes in the brain. J Neuroinflammation. 2014; 11:73.
5. Smith PL, Hagberg H, Naylor AS, Mallard C. Neonatal peripheral immune challenge

activates microglia and inhibits neurogenesis in the developing murine hippocampus. Dev Neurosci. 2014;36(2):119-31.

6. Mattei D, Ivanov A, Ferrai C, Jordan P, Guneykaya D, Buonfiglioli A, et al. Maternal immune activation results in complex microglial transcriptome signature in the adult offspring that is reversed by minocycline treatment. Transl Psychiatry. 2017;7(5):e1120.

7. Bilbo SD, Schwarz JM. The immune system and developmental programming of brain and behavior. Front Neuroendocrinol 2012, 33:267-286.

8. Hoeijmakers L, Lucassen PJ, Korosi A. Microglial Priming and Alzheimer's Disease: A Possible Role for (Early) Immune Challenges and Epigenetics? . Front Hum Neurosci 2016, 10:398.

9. Takeshita Y, Ransohoff RM. Inflammatory cell trafficking across the blood-brain barrier: chemokine regulation and in vitro models. Immunol Rev 2012, 248:228-239.

10. Wilson EH, Weninger W, Hunter CA. Trafficking of immune cells in the central nervous system. The Journal of Clinical Investigation. 2010;120(5):1368-79.

11. Blank T, Prinz M. Type I interferon pathway in CNS homeostasis and neurological disorders. Glia 2017, 65:1397-1406.

12. Reemst K, Noctor SC, Lucassen PJ, Hol EM. The Indispensable Roles of Microglia and Astrocytes during Brain Development. Front Hum Neurosci 2016, 10:566.

13. Chavan SS, Pavlov VA, Tracey KJ. Mechanisms and Therapeutic Relevance of Neuro-immune Communication. Immunity 2017, 46:927-942.

14. Rua R, McGavern DB. Advances in Meningeal Immunity. Trends Mol Med 2018, 24:542-559.

15. Dinan TG, Cryan JF. Gut instincts: microbiota as a key regulator of brain development,

ageing and neurodegeneration. J Physiol 2017, 595:489-503.

16. Sengupta P. The Laboratory Rat: Relating Its Age with Human's. Int J Prev Med. 2013;4:624-630.

17. Picut CA, Dixon D, Simons ML, Stump DG, Parker GA, Remick AK. Postnatal ovary development in the rat: morphologic study and correlation of morphology to neuroendocrine parameters. Toxicol Pathol. 2015;43(3):343-53

18. Semple BD, Blomgren K, Gimlin K, Ferriero DM, Noble-Haeusslein LJ. Brain development in rodents and humans: Identifying benchmarks of maturation and vulnerability to injury across species. Prog Neurobiol. 2013;106-107:1-16

19. Piasecka B, Duffy D, Urrutia A, Quach H, Patin E, Posseme C, et al. Distinctive roles of age, sex and genetics in shaping transcriptional variation of human immune responses to microbial challenges. PNAS. 2017;E488-E497

20. Sabra LK, Jaclyn MS. Sex-Specific Regulation of Peripheral and Central Immune Responses. Interactive Factory; 2018.

21. Abadie A, Prouvost-Danon A. Specific and total IgE responses to antigenic stimuli in Brown-Norway, Lewis and Sprague-Dawley rats. Immunology 1980, 39:561-569.

22. Sakamoto S, Fukushima A, Ozaki A, Ueno H, Kamakura M, Taniguchi T. Mechanism for maintenance of dominant T helper 1 immune responses in Lewis rats. Microbiol Immunol 2001, 45:373-381.

23. Nelson LH, Lenz KM. The immune system as a novel regulator of sex differences in brain and behavioral development. J Neurosci Res 2017, 95:447-461.

24. Sofroniew MV, Vinters HV: Astrocytes. biology and pathology. Acta Neuropathol 2010, 119:7-35.

25. Pierezan F, Mansell J, Ambrus A, Rodrigues Hoffmann A. Immunohistochemical expression of ionized calcium binding adapter molecule 1 in cutaneous histiocytic proliferative, neoplastic and inflammatory disorders of dogs and cats. J Comp Pathol 2014, 151:347-351.

26. Kingham PJ, Cuzner ML, Pocock JM. Apoptotic Pathways Mobilized in Microglia and Neurones as a Consequence of Chromogranin A-Induced Microglial Activation. J Neurochem 2002, 73:538-547.

27. Coulthard LG, Hawksworth OA, Li R, Balachandran A, Lee JD, Sepehrband F, Kurniawan N, Jeanes A, Simmons DG, Wolvetang E, Woodruff TM. Complement C5aR1 Signaling Promotes Polarization and Proliferation of Embryonic Neural Progenitor Cells through PKCzeta. J Neurosci 2017, 37:5395-5407.

28. Tanabe S, Yamashita T. The role of immune cells in brain development and neurodevelopmental diseases. Int Immunol 2018.

29. Garay PA, McAllister AK. Novel roles for immune molecules in neural development: implications for neurodevelopmental disorders. Front Synaptic Neurosci 2010, 2:136.

30. Bland ST, Beckley JT, Young S, Tsang V, Watkins LR, Maier SF, Bilbo SD. Enduring consequences of early-life infection on glial and neural cell genesis within cognitive regions of the brain. Brain Behav Immun 2010, 24:329-338.

31. Knuesel I, Chicha L, Britschgi M, Schobel SA, Bodmer M, Hellings JA, et al. Maternal immune activation and abnormal brain development across CNS disorders. Nat Rev Neurol. 2014;10(11):643-60.

32. Kentner AC, Bilbo SD, Brown AS, Hsiao EY, McAllister AK, Meyer U, et al. Maternal immune activation: reporting guidelines to improve the rigor, reproducibility, and

transparency of the model. Neuropsychopharmacology. 2019;44(2):245-58.

33. Li Y, Missig G, Finger BC, Landino SM, Alexander AJ, Mokler EL, et al. Maternal and Early Postnatal Immune Activation Produce Dissociable Effects on Neurotransmission in mPFC–Amygdala Circuits. The Journal of Neuroscience. 2018;38(13):3358-72.

34. Landreth KS. Critical windows in development of the rodent immune system. Hum Exp Toxicol 2002, 21:493-498.

35. McCarthy MM, Nugent BM. At the frontier of epigenetics of brain sex differences. Front Behav Neurosci. 2015;9:221.

36. Janeway CA Jr, Travers P, Walport M, et al. Immunobiology: The Immune System in Health and Disease. 5th edition. New York: Garland Science; 2001. The course of the adaptive response to infection. https://www.ncbi.nlm.nih.gov/books/NBK27125/

37. Perez-Cano FJ, Franch A, Castellote C, Castell M. The suckling rat as a model for immunonutrition studies in early life. Clin Dev Immunol 2012, 2012:537310.

38. Holsapple MP, West LJ, Landreth KS. Species comparison of anatomical and functional immune system development. Birth Defects Res B Dev Reprod Toxicol 2003, 68:321-334.

39. Adkins B, Leclerc C, Marshall-Clarke S. Neonatal adaptive immunity comes of age. Nature Reviews Immunology 2004, 4:553.

40. Bowman LM, Holt PG. Selective enhancement of systemic Th1 immunity in immunologically immature rats with an orally administered bacterial extract. Infect Immun 2001, 69:3719-3727.

41. Barrios C, Brawand P, Berney M, Brandt C, Lambert PH, Siegrist CA. Neonatal and early life immune responses to various forms of vaccine antigens qualitatively differ from

adult responses: predominance of a Th2-biased pattern which persists after adult boosting. Eur J Immunol 1996, 26:1489-1496.

42. Parish CL, Finkelstein DI, Tripanichkul W, Satoskar AR, Drago J, Horne MK. The role of interleukin-1, interleukin-6, and glia in inducing growth of neuronal terminal arbors in mice. J Neurosci 2002, 22:8034-8041.

43. Liu X, Quan N. Microglia and CNS Interleukin-1: Beyond Immunological Concepts. Front Neurol 2018, 9:8.

44. Shibata Y, Berclaz PY, Chroneos ZC, Yoshida M, Whitsett JA, Trapnell BC. GM-CSF Regulates Alveolar Macrophage Differentiation and Innate Immunity in the Lung Through PU.1. Immunity 2001, 15(4):557-67.

45. Becher B, Tugues S, Greter M. GM-CSF: From Growth Factor to Central Mediator of Tissue Inflammation. Immunity 2016, 45:963-973.

46. Yao Y, Tsirka SE. Monocyte chemoattractant protein-1 and the blood-brain barrier. Cell Mol Life Sci 2014, 71:683-697.

47. Lee KM, MacLean AG. New advances on glial activation in health and disease. World J Virol 2015, 4:42-55.

48. Garay PA, Hsiao EY, Patterson PH, McAllister AK. Maternal immune activation causes age- and region-specific changes in brain cytokines in offspring throughout development. Brain Behav Immun. 2013;31:54-68

49. Deverman BE, Patterson PH. Cytokines and CNS development. Neuron 2009, 64:61-78.

50. Dorries R, Schwender S, Imrich H, Harms H. Population dynamics of lymphocyte subsets in the central nervous system of rats with different susceptibility to coronavirus-induced demyelinating encephalitis. Immunology 1991, 74:539-545.

51. Fournie GJ, Cautain B, Xystrakis E, Damoiseaux J, Mas M, Lagrange D, Bernard I, Subra JF, Pelletier L, Druet P, Saoudi A. Cellular and genetic factors involved in the difference between Brown Norway and Lewis rats to develop respectively type-2 and type-1 immune-mediated diseases. Immunol Rev 2001, 184:145-160.

52. Cautain B, Damoiseaux J, Bernard I, Xystrakis E, Fournie E, van Breda Vriesman P, Druet P, Saoudi A. The CD8 T cell compartment plays a dominant role in the deficiency of Brown-Norway rats to mount a proper type 1 immune response. J Immunol 2002, 168:162-170.

53. Johnson D, Yasui D, Seeldrayers P. An analysis of mast cell frequency in the rodent nervous system: numbers vary between different strains and can be reconstituted in mast cell-deficient mice. J Neuropathol Exp Neurol 1991, 50:227-234.

54. Tronson NC, Collette KM. (Putative) sex differences in neuroimmune modulation of memory. J Neurosci Res 2017, 95:472-486.

55. Jang E, Kim JH, Lee S, Kim JH, Seo JW, Jin M, Lee MG, Jang IS, Lee WH, Suk K. Phenotypic polarization of activated astrocytes: the critical role of lipocalin-2 in the classical inflammatory activation of astrocytes. J Immunol 2013, 191:5204-5219.

56. Ponomarev ED, Maresz K, Tan Y, Dittel BN. CNS-derived interleukin-4 is essential for the regulation of autoimmune inflammation and induces a state of alternative activation in microglial cells. J Neurosci 2007, 27:10714-10721.

57. Gadani SP, Cronk JC, Norris GT, Kipnis J: IL-4 in the brain: a cytokine to remember. J Immunol 2012, 189:4213-4219.

58. Hanamsagar R, Alter MD, Block CS, Sullivan H, Bolton JL, Bilbo SD: Generation of a microglial developmental index in mice and in humans reveals a sex difference in

maturation and immune reactivity. Glia 2017, 65:1504-1520.

59. Lenz KM, Nelson LH: Microglia and Beyond: Innate Immune Cells As Regulators of Brain Development and Behavioral Function. Front Immunol 2018, 9:698.

60. Shen Y, Qin H, Chen J, Mou L, He Y, Yan Y, Zhou H, Lv Y, Chen Z, Wang J, Zhou YD: Postnatal activation of TLR4 in astrocytes promotes excitatory synaptogenesis in hippocampal neurons. J Cell Biol 2016, 215:719-734.

61. Norden DM, Trojanowski PJ, Villanueva E, Navarro E, Godbout JP: Sequential activation of microglia and astrocyte cytokine expression precedes increased IBA-1 or GFAP immunoreactivity following systemic immune challenge. Glia 2016, 64:300-316.

Supplemental Files

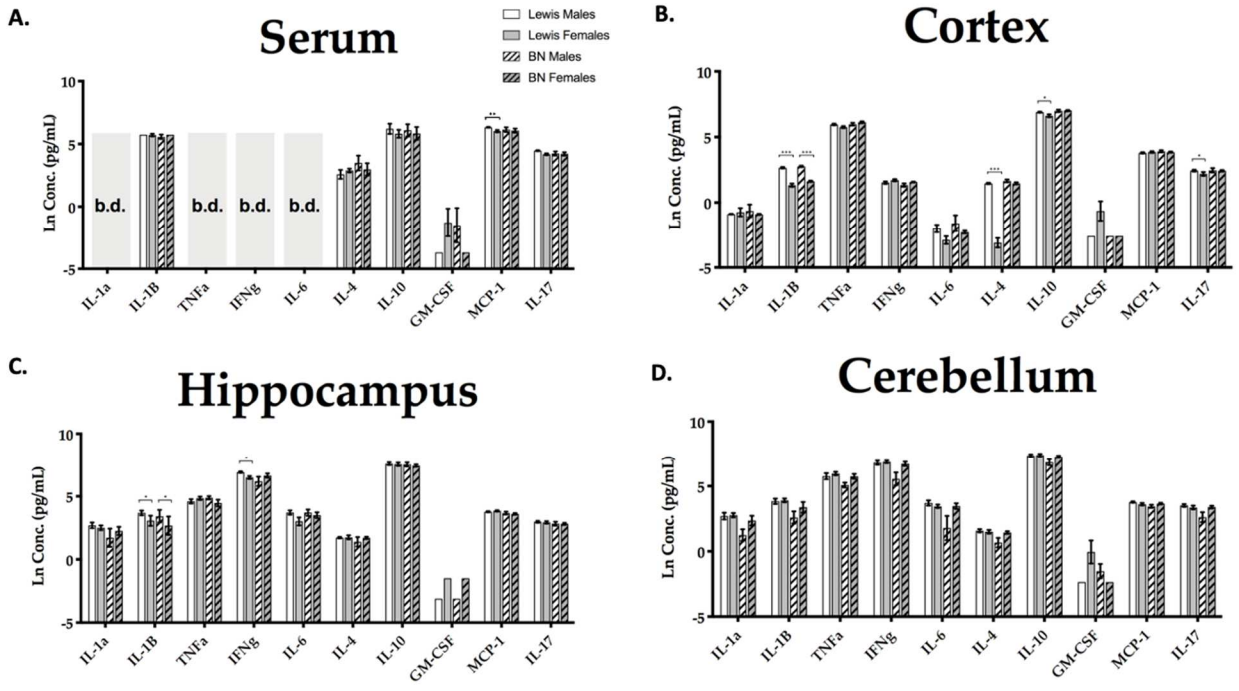

Additional file 1. Baseline cytokine results. Analysis of cytokine levels in response to saline-only conditions. Results represent cytokine concentrations in the serum **(A),** cortex **(B)**, hippocampus **(C)**, and cerebellum **(D)** of male and female Lewis (N=15; 7M, 8F) and BN (N=15; 6M, 9F) rats. Data represent mean +/- SEM, collapsed

between day of collection. Value b.d. represents analytes where >50% of samples were below the level of detection and excluded from analysis; *p<0.005, **p<0.01, ***p<0.001.

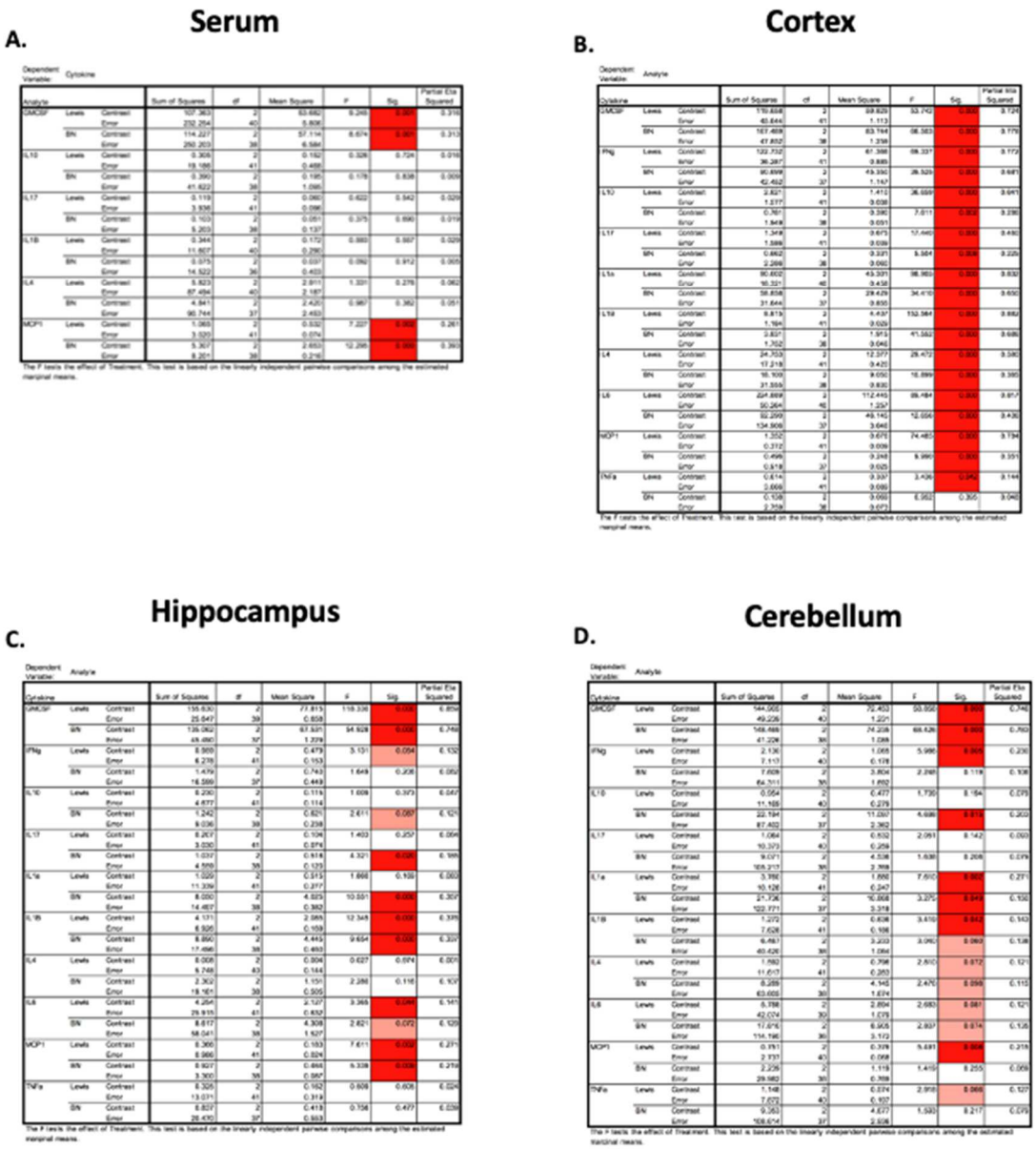

Additional file 2. Main effect of treatment on cytokine levels. Results of ANOVA analyses considering a main effect of treatment on cytokine and chemokine levels in the serum **(A),** cortex **(B)**, hippocampus **(C)**, and cerebellum **(D)** of Lewis and BN rats. Red coloring denotes a significant finding (p<0.05), while pink coloring represents a trending result (0.05<p<1).

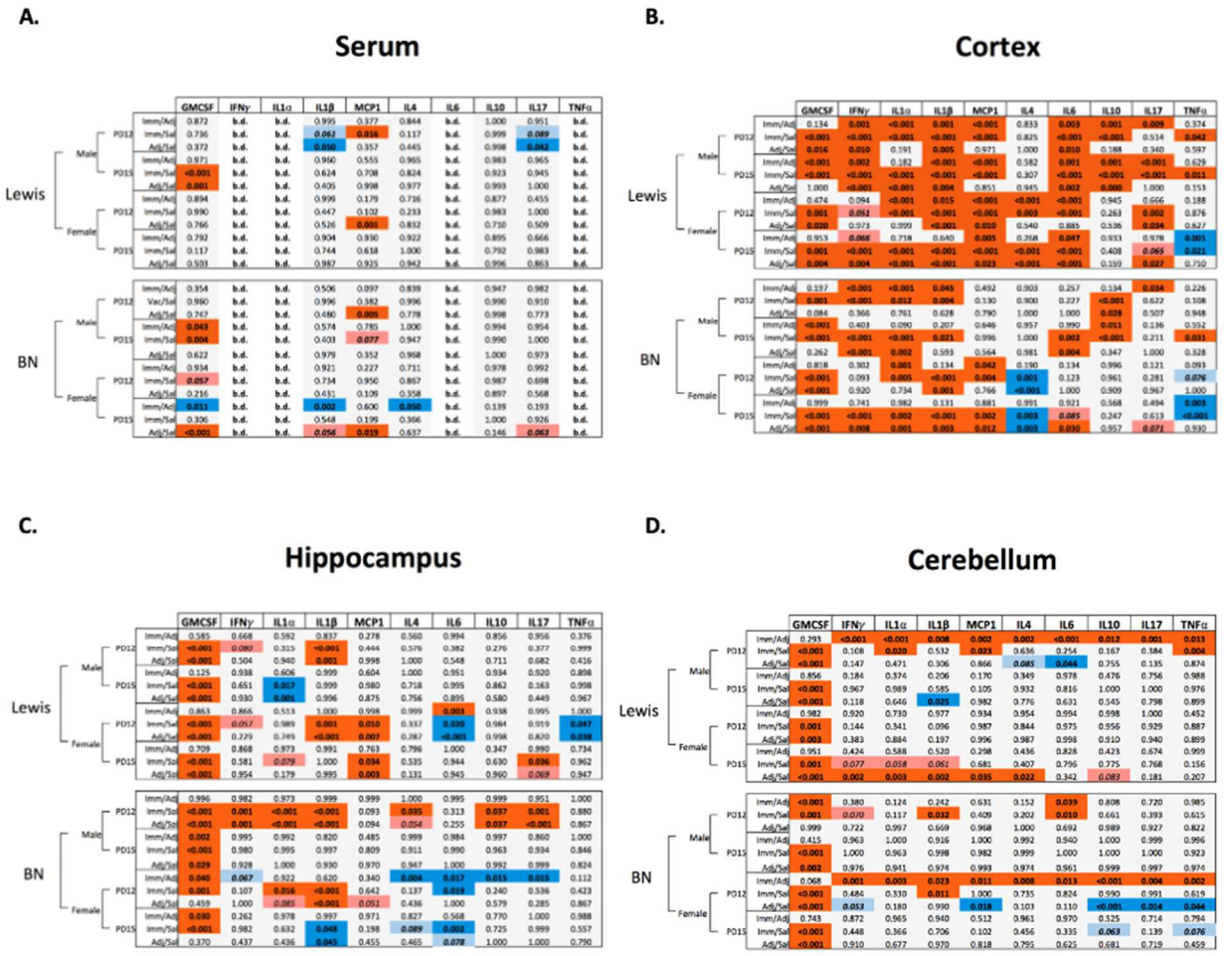

Additional file 3. Total cytokine and chemokine protein analyses of serum and brain lysates. Multi-factorial ANOVA analyses were conducted; p-values displayed here reflect Sidak-adjusted values for multiple comparisons. Tabular results of comparative cytokine and chemokine analyses between treatment conditions and within day of collection, sex, and strain; split between results in the serum **(A)**, cortex **(B)**, hippocampus **(C),** and cerebellum **(D)**. Tables display statistical analysis of immune challenge (Imm), adjuvant only (Adj) and saline (Sal) conditions with representative colors: **red**, $p<0.05$; **light red**, $0.05<p<0.1$; **dark blue**, $p<0.05$; **light blue**, $0.05<p<0.1$. Red coloring overall corresponds initial treatment conditions over the second in the row, e.g. a red cell in Imm/Sal row is interpreted as significant increase in Imm compared to Sal for that analyte, blue cells are the inverse relationship and would represent a decrease in Imm compared to Sal. A value of b.d. is indicative of cytokine/chemokine values below the level of assay detection.

CHAPTER 3

Sexually Dimorphic Neuroanatomical Differences Relate to ASD-relevant Behavioral Outcomes in a Maternal Autoantibody Mouse Model

****Published in Molecular Psychiatry****

M. R. Bruce, K. L. Jones, A. C. Vernon, J. L. Silverman, J. N. Crawley, J. Ellegood, J. P. Lerch, J. Van De Water, Sexually dimorphic neuroanatomical differences relate to ASD-relevant behavioral outcomes in a maternal autoantibody mouse model. *Molecular Psychiatry*, (2021).

Abstract

Immunoglobulin G (IgG) autoantibodies reactive to fetal brain proteins in mothers of children with ASD have been described by several groups. To understand their pathologic significance, we developed a mouse model of maternal autoantibody related ASD (MAR-ASD) utilizing the peptide epitopes from human autoantibody reactivity patterns. Male and female offspring prenatally exposed to the salient maternal autoantibodies displayed robust deficits in social interactions and increased repetitive self-grooming behaviors as juveniles and adults. In the present study, neuroanatomical differences in adult MAR-ASD and control offspring were assessed via high-resolution ex vivo magnetic resonance imaging (MRI) at 6 months of age. Of interest, MAR-ASD mice displayed significantly larger total brain volume and of the 159 regions examined, 31 were found to differ significantly in absolute volume (mm^3) at an FDR of <5%. Specifically, the absolute volumes of several white matter tracts, cortical regions, and basal nuclei structures were significantly increased in MAR-ASD animals. These phenomena were largely driven by female MAR-ASD offspring, as no significant differences were seen with either absolute or relative regional volume in male MAR-ASD mice. However, structural covariance analysis suggests network-level desynchronization in brain volume in both male and female MAR-ASD mice. Additionally, preliminary correlational analysis with behavioral data relates that volumetric increases in numerous brain regions of MAR-ASD mice were correlated with social interaction and repetitive self-grooming behaviors in a sex-specific manner. These results demonstrate significant sex-specific effects in brain size, regional relationships, and behavior for offspring prenatally exposed to MAR-ASD autoantibodies relative to controls.

Introduction

Autism spectrum disorder (ASD) is a set of heterogeneous neurodevelopmental disorders that are behaviorally classified by socio-communicative impairments accompanied by the presence of repetitive and restrictive interests and behaviors [1]. One potential non-genetic contributor to ASD is immune dysregulation, which has been described in individuals with ASD and their family members [2]. Most notably, some mothers of children with ASD have been reported to have circulating autoantibodies reactive to fetal brain proteins [3, 4] (reviewed in [5]).

Our lab has identified eight protein antigens for maternal autoantibody related (MAR) risk of ASD: lactate dehydrogenase A and B, stress-induced phosphoprotein 1, collapsin response mediator proteins 1 and 2, guanine deaminase, Y-box binding protein 1 [6], and neuron-specific enolase [7]. In addition, we mapped the antigenic epitope sequences for each of the proteins recognized by these ASD-specific maternal autoantibodies [8]. Then we created an antigen-driven mouse model for MAR risk of ASD in which autoantibodies reactive to the salient epitope sequences are generated in female dams prior to breeding. In this model, male and female offspring prenatally exposed to the maternal autoantibodies had significant alterations in developmental milestones, reduced social interactions during dyadic play, and exhibited increases in repetitive self-grooming behaviors [9]. However, there remains a critical need to identify the underlying biological mechanisms that lead to MAR-ASD.

In the current study, we examined the potential effects of brain-reactive maternal autoantibodies on neuroanatomy through cross-sectional analysis of offspring at 6 months of age. To accomplish this we conducted high-resolution ex vivo magnetic resonance imaging (MRI) on adult MAR-ASD and control offspring that had undergone behavioral testing in our previously published study [9]. In this manner, we were able to perform direct correlational analysis

between regional brain volume and behavioral outcomes to provide a comprehensive readout of potential pathology. Additionally, we used structural covariance analysis to interpret network-level dysregulation of brain volume in response to MAR-ASD autoantibody exposure.

Methods

Animals

MAR-ASD and control mice were previously created and studied in the Van de Water Lab [9]. A total of $n = 22$ MAR-ASD mice (11 male, 11 female) and $n = 23$ control mice (12 male, 11 female) aged approximately six months were perfused for MRI imaging. Please see supplemental methods for additional animal information.

Magnetic resonance imaging

A multi-channel 7.0 Tesla (7.0-T) MRI scanner (Agilent Inc., Palo Alto, CA) was used to image the brains within the skulls. A custom-built solenoid coil array was used to image 16 brains in parallel [10]. Parameters for the ex vivo MRI scans were as follows: T2-weighted, 3-D fast spin-echo sequence, with a cylindrical acquisition of k-space, and with a TR of 350 ms, and TEs of 12 ms per echo for six echoes, field-of-view of $20 \times 20 \times 25$ mm^3 and matrix size = $504 \times 504 \times 630$ giving an image with 0.040 mm isotropic voxels. Total imaging time for the acquisition was 14 h [11]. For details on registration and analysis please see Supplementary methods.

Structural covariance

To assess structural covariance by region within the dataset, the absolute volumes of all 159 atlas-segmented regions were subjected to correlational analysis using Pearson's *r* as a readout. To reduce the number of comparisons for subsequent statistical analyses correlational data were then grouped into six clusters (Posterior Cortical, Hippocampal, Anterior Cortical, Subcortical, Midbrain, and Brainstem, and Cerebellum) defined previously by others using hierarchal clustering of structural covariance in the mouse brain [12]. The identity of regions assigned to each cluster is detailed in Supplementary Table 2. Following cluster assignment, correlation values for each brain region within a cluster were then averaged, similar to that described previously [13]. Mean correlation values were then compared between treatment conditions and sex using Kruskal-Wallis non-parametric testing, with corrections for multiple comparisons using a two-stage step-up FDR method at a level of 5%. All data analysis for these methods was performed using Prism 8 with visualization conducted in R.

Behavioral correlations

To identify potential relationships between offspring behavior and absolute regional brain volume, an exploratory analysis was performed to correlate behavioral data with MRI-based neuroanatomical findings. In particular, volumes were correlated with the following behaviors previously collected by our group [9]: juvenile reciprocal social interactions (JRSI), self-grooming in an empty cage, and male-female social interaction (MFSI) behaviors. Neuroanatomical regions correlated with behavioral findings were limited to areas identified passing 5% FDR correction in the Full and female-only groups. Relationships were assessed via Pearson's correlation. Pearson's correlations were performed using SPSS software (SPSS Version 25.0; IBM Corp., Armonk, NY); p values < 0.05 for two-tailed tests were considered to be statistically significant. As these correlations were exploratory, no corrections for multiple

comparisons were made. Data visualization and clustering were conducted using the online tool ClustVis (https://biit.cs.ut.ee/clustvis/).

Results

MAR-ASD offspring display sex-specific increases in brain volume

Analysis of ex-vivo structural MRI data revealed MAR-ASD treatment-induced differences in total and regional brain volume at 6 months of age. Overall, female MAR-ASD mice exhibited significantly larger total brain volume (TBV) relative to both male and female control animals (male, $p < 0.01$; female $p < 0.05$), with a trending difference in TBV noted between sexes in MAR-ASD mice (Fig. 1a). No differences were observed in male MAR-ASD animals compared to controls. To evaluate differences by brain region, volumetric analysis of 159 separate regions was conducted. Analysis revealed that 20% (31/159) of regions examined were found to differ significantly in absolute volume (mm^3) when comparing the MAR-ASD Full Group, including both sexes, to controls at an FDR of less than 5% (Fig. 1b; Supplementary Table 1). Assessment of regional volumetric differences in MAR-ASD mice split by sex revealed that 12% (20/159) of brain regions examined displayed significant increases in absolute volume in females, at an FDR of <5%. No statistically significant differences were observed in males (Supplementary Table 1). Additionally, no differences were observed in relative regional volumes for MAR-ASD mice compared to control animals for either sex. Collectively, these data suggest that female MAR-ASD mice were primarily driving the neuroanatomical phenotype seen in the Full Group comparison.

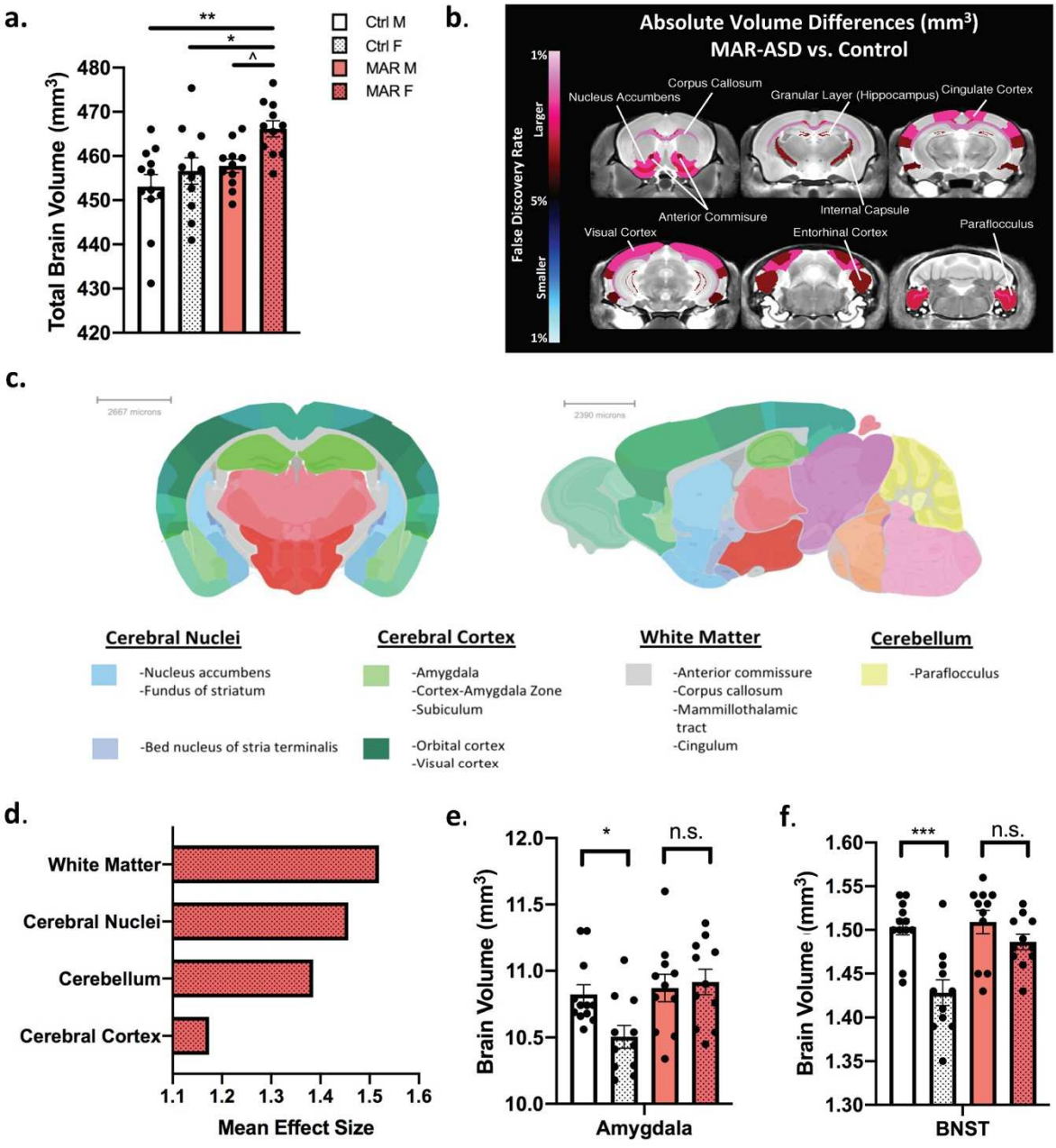

Figure 1. Female MAR-ASD offspring exhibit increases in total and regional brain volume. **a** Differences in total brain volume between treatment and sex. **b** A false discovery ratio (FDR) heatmap of significant regional differences between MAR-ASD and control animals, shown combined between sexes (Full Group). Anything highlighted in red is significantly larger in MAR-ASD compared to control animals and anything blue is significantly smaller at an FDR value of <5%. **c** Coronal and sagittal images of the mouse brain overlaid with colorimetric classification of brain areas as defined by the Allen Mouse Brain Atlas. Headings under brain sections denote areas where significant regional volumetric differences were seen in female MAR-ASD mice. **d** Average effect sizes among brain areas identified to exhibit regional changes. Data are expressed as Cohen's d values. **e**, **f** Volumetric differences in sexually dimorphic brain regions compared within treatment conditions between sexes in the amygdala (**e**) and bed nucleus of stria terminalis (BNST) (**f**). Statistical analyses were conducted using a one-way ANOVA. For data included in figures **a** and **d**–**f**: MAR (N = 11M, 11F), Ctrl (N = 12M, 11F). Error bars represent mean ± SEM. * = $p < 0.05$, ** = $p < 0.01$, *** = $p < 0.001$, ^ = $0.1 > p > 0.05$, n.s. = non-significant. M.R.B designed and created graphs as well as final analysis of data. K.L.J. contributed to study design,

created animals, and conducted tissue collection. J.E. and J.P.L. performed MRI imaging of brains. A.C.V. contributed to interpretation of analysis.

Manual annotation of the 20 regions displaying significant (5% FDR) increases in female MAR-ASD mice, using data from the Allen Mouse Brain Atlas, revealed that volumetric increases in female MAR-ASD mice were predominately seen in 4 brain areas: the cerebral nuclei, cerebral cortex, white matter, and the cerebellum. Specific regions affected are listed under each respective area (Fig. 1c) and included with more detail in the supplementary data (Supplementary Table 1). To investigate the magnitude of these volumetric changes, regional effect sizes were calculated across the MAR-ASD Full Group, and both sexes independently using Cohen's d as a metric. Effect size averaging among regions within the affected brain areas revealed white matter regions to be the most prominently affected (Fig. 1d). While analysis by region showed that the largest volumetric differences were observed in the anterior commissure, medial orbital cortex (mOFC), and nucleus accumbens (NAc) in female MAR-ASD mice (Supplementary Fig. 1a). Using data provided by the Allen Mouse Brain Connectivity Atlas (http://connectivity.brain-map.org/), an exploration of projections from the mOFC revealed that main efferent projections pass through the caudoputamen and NAc, centered around the anterior commissure pars anterior (Supplementary Fig. 1b). These findings suggest that MAR-ASD exposure results in sex-specific regional volumetric differences within the brains of offspring that may involve altered cortico-striatal connectivity.

MAR autoantibody exposure results in masculinization of sexually-dimorphic brain areas in female mice

Given that the volumetric increases in regional brain size of MAR-ASD animals were driven primarily by females, and the fact that multiple sexually dimorphic regions in the brain were

among those found to be significantly enlarged in response to MAR-ASD exposure, (specifically, the amygdala and bed nucleus of stria terminalis (BNST) (Female q values = 0.04)), we investigated the possibility that MAR-ASD treatment may result in changes in the sexual dimorphism of these regions. To examine this, we compared the volume of specific brain regions, the amygdala, BNST, and the hypothalamus between MAR-ASD and control mice. These were selected a priori based on evidence in the literature confirming sexual dimorphism and association with ASD [14, 15]. As expected, analysis of regional brain volume within these areas in control mice corroborated the sex differences reported in the literature, with female control animals displaying significantly lower amygdala ($p < 0.01$; Fig. 1e) and BNST ($p < 0.001$; Fig. 1f) volume compared to male controls. The size of the hypothalamus also appeared lower in female control animals compared to males, but differences did not reach statistical significance ($p = 0.09$; Supplementary Fig. 2a). However, when assessing sex differences in these same regions in MAR-ASD mice, brain size in females was no different than that of males across each of the sexually dimorphic regions examined (Fig. 1e, f; Supplementary Fig. 2a). Together these findings relate a loss of sexual dimorphism in amygdala and BNST volume in response to gestational MAR-ASD exposure in mice, representing "masculinization" of these regions in females.

Structural covariance analysis reveals desynchronized regional development in MAR-ASD offspring

Interestingly, while regional MRI analysis uncovered female-specific increases in brain size in MAR-ASD offspring, prior data collected on these same animals related that treatment-induced behavioral abnormalities affected male and female mice similarly [9]. A plausible explanation for this could be that MAR-ASD treatment results in network level changes in the brain volumes

that are not apparent when assessing regions individually. Previous work has found that the volume of distinct neuroanatomical systems is tightly correlated, forming structural covariance networks in the brain in both humans and rodents [12, 16]. In addition, recent data suggest that these networks may be sensitive to immune challenge during neurodevelopment [17]. Therefore, we used structural covariance analysis to examine correlations between clusters of brain regions to provide a broader picture of neuroanatomical changes in response to MAR-ASD autoantibody exposure.

Analysis of structural covariance in MAR-ASD and control animals, across the 159 segmented brain regions, revealed significant regional correlational differences in brain volumes by treatment and sex (Fig. 2a; Supplementary Fig. 3). To examine the nature of these changes, brain regions were first assigned to one of six anatomical clusters defined previously using unbiased hierarchical clustering of brain regions in mice [12] (Supplementary Table 2). Following assignment, correlation values within a cluster were then averaged and compared between groups using nonparametric testing. To focus on the most salient effects while considering the large number of regions within a given cluster, only those differences exhibiting a large effect size (Kruskal-Wallis eta squared >0.14) are described as significant here. However, all comparisons and relevant statistics are included as a table in the Supplementary material (Supplementary Table 5). Interestingly, when evaluating structural covariance between clusters across all conditions, male MAR-ASD mice displayed differences that were not apparent in female MAR-ASD offspring. Specifically, male MAR-ASD mice exhibited reduced structural covariance within the posterior cortex, and between the posterior and anterior cortices. Similarly, differences were also seen in intra-hippocampal connectivity, with MAR-ASD male mice displaying reduced correlations between hippocampal regions, compared to control animals of

either sex as well as MAR-ASD female mice (Fig. 2b). Furthermore, structural covariance analysis revealed a number of MAR-ASD treatment-induced differences that affected male and

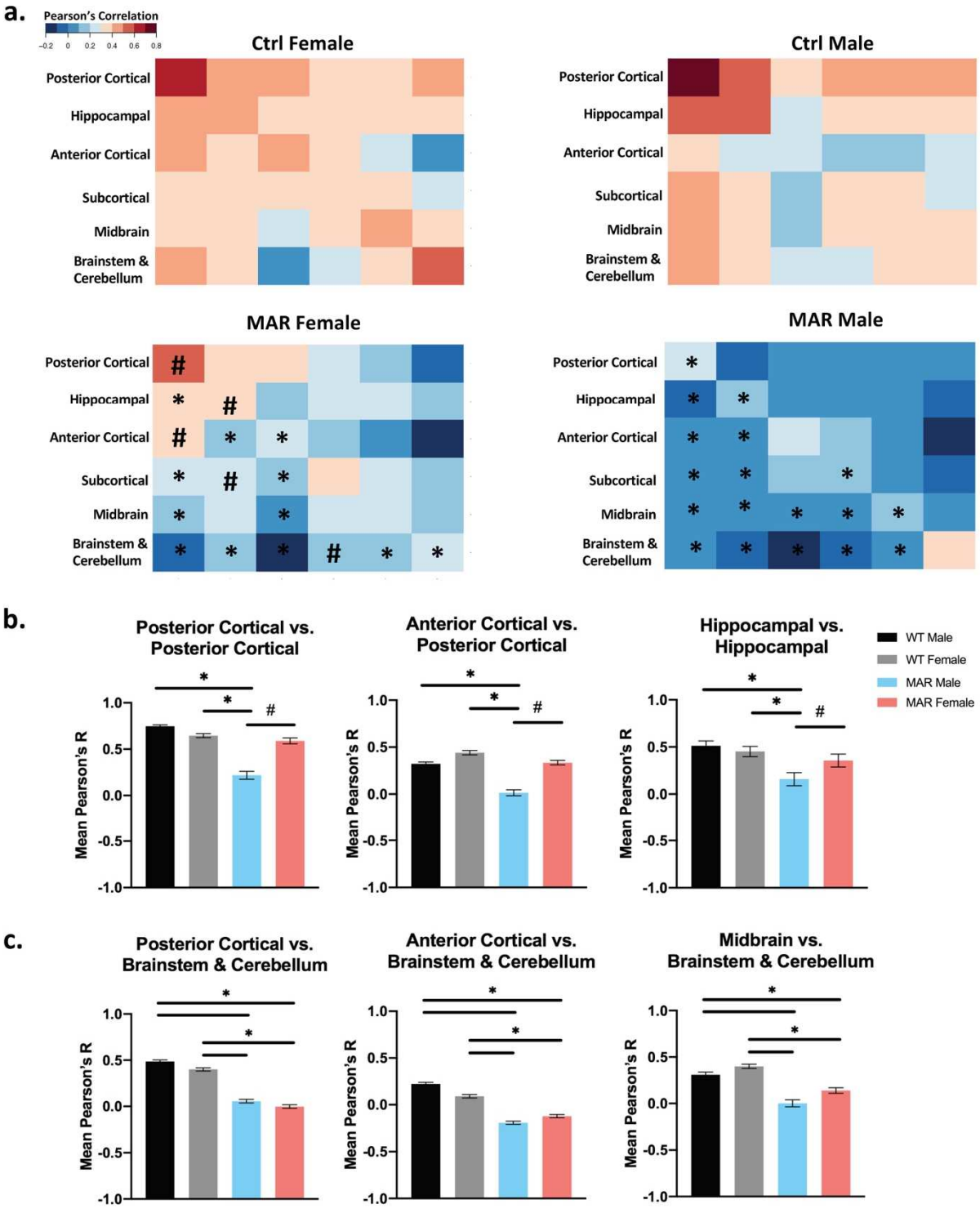

Figure 2. Analysis of regional structural covariance in the brains of MAR-ASD and control mice. **a** Heatmap-based visualization of regional correlation values organized into clusters based on anatomical location. Data represented as mean Pearson's *r* values with results split by treatment and sex. **b** Plots displaying averaged correlation values across brain region clusters determined to be different in male MAR-ASD mice only. **c** Plots displaying regional differences as a result of treatment. Data for bar plots correspond to mean Pearson's *r* values derived from correlational cluster analysis of animals within a treatment group (MAR ($N = 11$M, 11F), Ctrl ($N = 12$M, 11F)). Final *N*'s for statistical analysis reflect multiplication between regions within respective clusters (posterior cortical ($N = 19$), hippocampal ($N = 13$), anterior cortical ($N = 24$), subcortical ($N = 40$), midbrain ($N = 9$), brainstem & cerebellum ($N = 51$) (e.g., Posterior Cortex vs Posterior Cortex, $N = 19 \times 19$), a list of regions is provided as a supplemental table. *=significant treatment effects, #=significant effects within MAR-ASD animals by sex. Effects were only reported here if they passed criteria for large effect size (Kruskal Wallis eta squared >0.14). Error bars represent the mean with 95% confidence interval. M.R.B designed and created graphs as well as final analysis of data. K.L.J. contributed to study design, created animals, and conducted tissue collection. J.E. and J.P.L. performed MRI imaging of brains. A.C.V. contributed to interpretation of analysis.

female animals similarly. Specifically, the posterior cortex, anterior cortex, and midbrain exhibited treatment-specific reductions in their correlation to brainstem and cerebellar structures in both male and female MAR-ASD mice compared to controls (Fig. 2c). These data suggest a MAR-ASD-specific phenotype in covariance networks involving the hindbrain, irrespective of sex. Interestingly, nearly all MAR-ASD treatment-induced effects of inter- and intra-cluster correlations represented movement toward weaker or negative correlation values, suggesting desynchronized development of these regions. Cumulatively, these data propose that while regional volumetric effects were not found in male MAR-ASD mice, network-level desynchronization of structural brain volume extends to both sexes in response to MAR-ASD autoantibody exposure, providing a scaffolding for similar behavioral outcomes.

Brain-behavior correlations reveal inverse relationships in males and females

To investigate the relationship between neuroanatomical outcomes and behavioral findings, we conducted an exploratory correlational analysis between previous behavioral findings and those brain regions determined by structural MRI to be statistically different in the same MAR-ASD mice. Bivariate correlation analysis revealed distinct sex-specific differences in both the

magnitude and direction of brain-behavior correlations in respect to both JRSI (Supplementary Table 3), as well as self-grooming behaviors (Supplementary Table 4).

To further investigate the sex-specific correlational findings observed in MAR-ASD mice, we conducted clustering analysis to explore the relationship between JRSI behavior, where the majority of correlational findings were seen, and those brain regions displaying volumetric differences with an FDR < 5%. Heatmap-based visualization of clustering analysis reinforced the separation by sex in regional volumetric outcomes observed in MAR-ASD animals (Fig. 3a). While female MAR-ASD mice predominately displayed positive correlations between a given brain region and associated behavior, male MAR-ASD animals displayed either a negative correlation, or the absence of an effect across the majority of comparisons. The most striking of these sex-specific differences were seen in the relation of basal nuclei volume with nose-to-anogenital sniffing (NAg) behavior. When assessing male MAR-ASD animals, statistically significant negative correlations (here meaning correlations with a p value < 0.05, as no corrections for multiple comparisons were made) were seen in the BNST ($p < 0.05$, $r = -0.614$) (Fig. 3b) and basal forebrain (BF) ($p < 0.05$, $r = -0.629$) (Fig. 3c). While female MAR-ASD mice exhibited an opposing, positive relationship between NAg and regional volume in the BNST ($p < 0.01$, $r = 0.762$) and nucleus accumbens (NAc; $p < 0.05$, $r = 0.694$) (Fig. 3d). These effects appeared to be restricted to MAR-ASD animals as no statistically significant correlations were observed in control mice for either sex in regard to regional brain volume or relation to NAg (Supplementary Fig. 2b–d). In addition, visual inspection and clustering analysis of the correlational data revealed significant effects within certain brain regions with deficits spanning multiple behavioral tasks in females. Statistically significant positive correlations were observed between the volumes of the stratum granulosum of the hippocampus, caudomedial entorhinal

cortex, and paraflocculus with NAg, following, and push-crawl behaviors in the JRSI tasks (Fig. 3a, Supplementary Table 3). Cumulatively these results suggest that juvenile social behavioral deficits in MAR-ASD mice appear to correlate with adult regional brain size in a sex-dependent manner. Specifically, that better behavioral outcomes were associated with larger regional brain size in female MAR-ASD mice, with the opposite finding observed in male MAR-ASD offspring. However, it is important to keep in mind that these comparisons were preliminary. Future studies including additional animals or more stringent statistical analysis

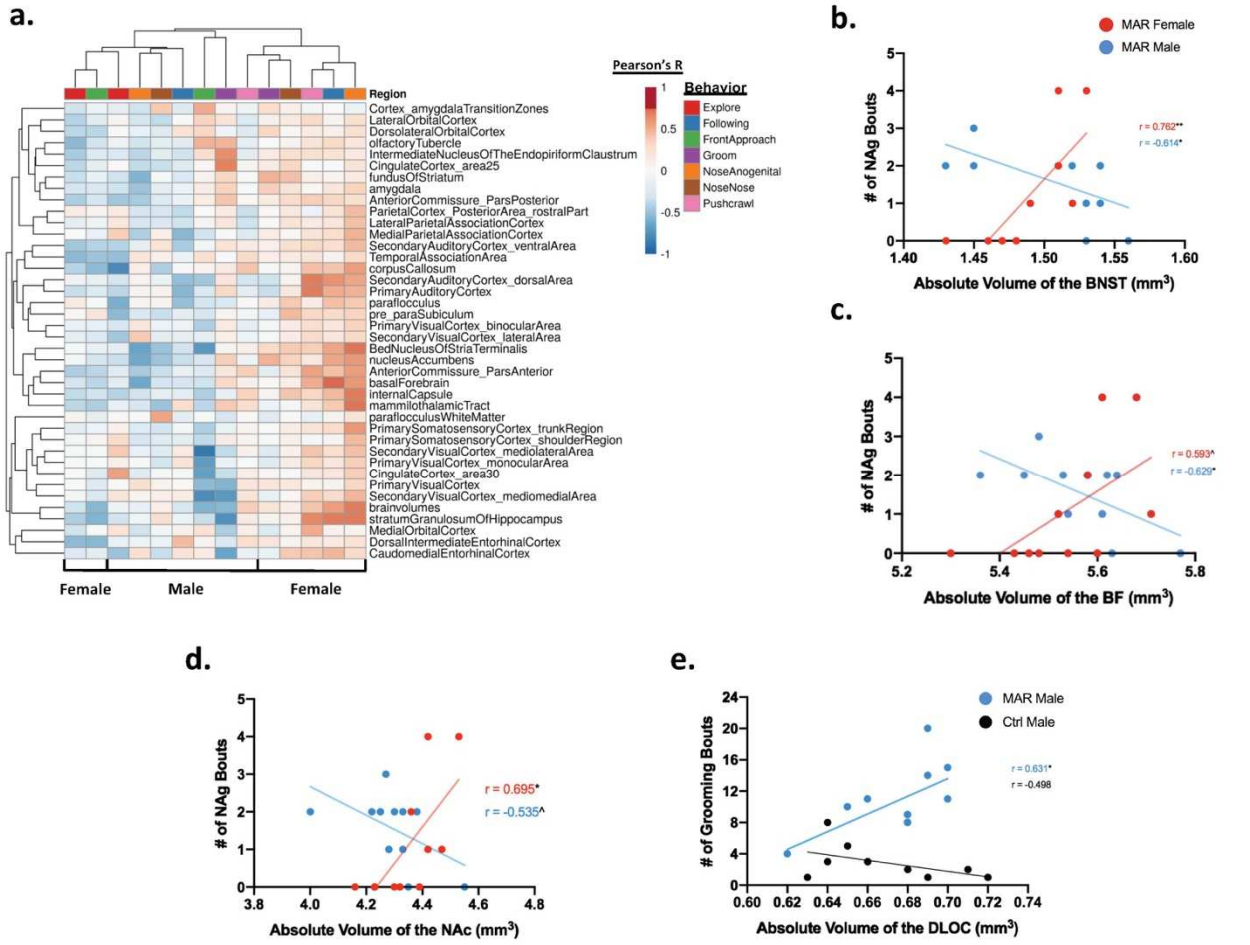

may be needed to validate findings.

Figure 3. Correlational analysis between brain regions and behavior in MAR-ASD mice. **a** Clustering analysis of correlational data shown in heatmap form. Sex and behavior are displayed on the *x*-axis with brain region annotation on the *y*-axis. Clustering was conducted using Euclidean distance and average linkage analysis via the online data visualization tool ClustVis. Heatmap color for individual cells corresponds to the Pearson's r-value, between 1 and −1, for the relationship between a given brain region and behavior in the juvenile reciprocal social interaction (JRSI)

task. Correlational analysis for all data was conducted using SPSS software. **b**–**d** Scatterplot representation of correlational analysis between the number of nose-to-anogenital (NAg) bouts and volume of the BNST (MAR (N = 11M, 11F), Ctrl (N = 11M, 11F)). **b** Basal forebrain (BF) **c** and nucleus accumbens (NAc) **d** split by sex in MAR-ASD mice. **e** Graph displaying the relationship between the number of grooming bouts and volume of the dorsolateral orbital cortex (DLOC) in male MAR-ASD and control mice (MAR (N = 11M), Ctrl (*N* = 10M)). Trendlines and Pearson's r-value displayed along with scatterplot values for each graph. * = $p < 0.05$, ** = $p < 0.01$, ^ = $0.05 < p < 0.1$. M.R.B designed and created graphs as well as final analysis of data. K.L.J. contributed to study design, created animals, and conducted tissue collection. J.L.S. and J.N.C. designed behavioral experiments and conducted all behavior. J.E. and J.P.L. performed MRI imaging of brains. A.C.V. contributed to interpretation of analysis.

Evaluation of additional behavioral tasks reported previously to be significantly different in mice in response to MAR-ASD exposure, such as MFSI and repetitive self-grooming behaviors, showed interesting but limited effects. As only males were tested during the MFSI task, correlations with brain volumes were conducted only with experimental male mice. In assessing MAR-ASD treatment-induced differences in male behavior during the MFSI task, one noteworthy finding included the relationship between dorsolateral orbital cortex (DLOC) volume and self-grooming behavior. Specifically, a statistically significant positive correlation was observed between the volume of the DLOC and the number of grooming bouts in male MAR-ASD mice as measured during the MFSI task ($p < 0.05$, $r = 0.631$) but not in male control mice (Fig. 3e). In addition, positive correlations were also seen between DLOC volume and total time spent grooming for male MAR-ASD mice in the MFSI task (Supplementary Fig. 2e) as well as in a separate empty-cage grooming task (Supplementary Fig. 2f). However, these last relationships did not pass statistical significance testing. Taken together, these data detail a male-specific relationship between the DLOC and repetitive self-grooming behavior in adulthood in response to MAR-ASD autoantibody exposure.

Discussion

Abnormal brain enlargement, measured by MRI, is well documented in the ASD literature with early studies on the topic suggesting that children with ASD exhibit premature overgrowth of brain regions during early life that is followed by a period of abnormally slow growth compared to typically developing children [18,19,20,21]. However, many of these seminal reports studied mainly male children and few if any females. Later studies revealed that female children with ASD actually display a more pronounced abnormal growth profile across a greater number of brain regions than male ASD children [20, 22]. This is relevant to our findings as we observed absolute volumetric differences in white matter tracts, cerebral nuclei, cerebellum, and cerebral cortex in adult female MAR-ASD animals that were not present in males at the same time point. Therefore, it may be possible that male and female offspring experienced an accelerated neurodevelopmental trajectory during early life, which was then normalized over time in males but persisted in female MAR-ASD animals. In support of this view, increased head size was observed in both male and female MAR-ASD mice as pre-weanlings [9]. Alternatively, female-specific brain volumetric differences could reflect masculinization of the female brain in response to MAR-ASD exposure. The concept of brain masculinization in ASD has been an active theory for nearly two decades (reviewed in [23]). However, recent work suggests that sex-specific differences in brain volume in ASD may not represent extreme male skewing, but simply dysregulation of normal sexual differentiation of the brain [24]. This theory is supported by work suggesting that although females show masculinization of certain brain regions, males do not display hypermasculinization [25]. Our data appear to mirror these findings as MAR-ASD female mice show apparent masculinization of regional volumes, but the brains of male MAR-ASD mice do not appear overtly affected.

Structural covariance represents a technique to assess relationships between brain regions based on anatomical properties. Previous work has shown that this measure is related to both structural and transcriptomic similarity among regions [26], underscoring its utility. Studies using structural covariance to determine network dysfunction in ASD have evidenced altered local connectivity [27, 28], and correlations between subcortical structures that are predictive of behavioral outcomes [29]. Assessment of network connectivity using structural covariance in this study revealed reduced local covariance within the cortex and hippocampus of male MAR-ASD mice but not in females. Suggesting that while differences in discrete regional brain volume were absent in male MAR-ASD mice in this cross-sectional study, local network desynchronization may partly account for altered behavioral outcomes. Support for this exists in the literature, as cortical underconnectivity is an active hypothesis in ASD [30, 31], with several studies observing relationships between reduced functional connectivity in the cortex and worsened behavioral outcomes in affected individuals [32,33,34]. Furthermore, our study revealed a treatment-specific phenotype in MAR-ASD mice, irrespective of sex, noting a reduction in the covariance between cortical and midbrain regions to brainstem and cerebellar structures. Disrupted cortico-cerebellar connectivity is noted in both the clinical literature and in animal models of ASD [35, 36]. In addition, a recent study using MRI and structural covariance to examine sensory networks in individuals with ASD found evidence of decreased covariation between the cerebellum and sensory cortices [27].

Together these studies provide corroboration for the translational capacity of the MAR-ASD rodent model and reinforce the findings of this study. However, limitations exist in the cross-sectional design and the fact that the neuroimaging was conducted ex vivo. Longitudinal in vivo

MRI studies will be necessary to understand the timeline and development of neuroanatomical pathology in response to MAR-ASD aAb exposure.

Structural MRI results were additionally correlated with previous behavioral findings to identify differences in neuroanatomy associated with ASD-relevant behaviors. Analysis revealed sex-specific differences in the magnitude and direction of brain-behavior correlations. Specifically, opposing relationships were observed between BF structures and social behavior in male and female MAR-ASD mice; with females displaying positive correlations while those in males were negative. Previous research has shown that inhibition of signaling in the lateral septum, a region involved in social behavior with direct inputs to the BNST, can lead to sex-dependent behavioral outcomes. Specifically, lateral septum inhibition increased juvenile social play behavior in males but decreased the same behavior in females [37]. Applying this logic to our findings, it is plausible that a volumetric increase in the BF, and a concomitant increase in local signaling, may contextualize sex differences in correlational findings between BF volume and social behavior in MAR-ASD mice. Worthy of note, lateral septal volume was larger in female MAR-ASD mice compared to control animals but did not survive FDR-correction ($q = 0.08$). While there were no statistically significant global or regional differences in brain volume seen in male MAR-ASD mice, a relationship was observed between male grooming behavior and the volume of the DLOC. This is relevant as the DLOC has been previously implicated in self-grooming behaviors using optogenetic studies in mice [38, 39]. Furthermore, the human correlate to the mouse DLOC, the dorsolateral prefrontal cortex, is thought to be involved in mediating repetitive or stereotyped behavior in clinical subjects [40, 41]. It is important to note, however, that correlational findings between regional brain volume and behavior were exploratory in nature and reflect data that were not corrected for multiple comparisons.

Speculation regarding mechanisms by which MAR-ASD autoantibodies mediate pathology may include altered developmental neuroimmune signaling. Previous work has suggested that hormones, inflammatory mediators, and the presence or absence of specific immune cells contribute to neuroanatomical sex differences in rodents. For example, neuroimaging data from T cell receptor (TCR)-deficient mice revealed that T cells were necessary for sexual dimorphism in several brain regions, including the cerebellum and BNST [42]. In addition, testosterone, endocannabinoids [43], and inflammatory molecules, such as prostaglandin E2 [44, 45], have all been implicated in brain sexual differentiation through glia-dependent signaling mechanisms. Interestingly, the window for maternal antibody transfer capable of reaching the fetal brain is defined to be between E12.5–E16.5 [46]. Neurodevelopmental events during this period include microglia colonization as well as early neurogenesis [47]. While we have not seen clear alterations to microglia in early studies of MAR-ASD embryos, we have observed autoantibody binding to radial glial cells and enhanced neurogenesis [48]. These data, alongside ongoing studies, lead us to hypothesize that MAR-ASD autoantibodies influence neuroanatomy through brain deposition and potential engagement of neuroimmune signaling pathways.

Overall, our findings suggest that MAR-ASD aAb exposure results in sex-specific changes in regional brain volume, network-level covariance among brain areas, and relationships between regional volume and ASD-relevant behaviors in a mouse model. Future studies will be necessary to establish the cellular and molecular mechanisms of MAR-ASD-induced changes in brain structure.

References

1. APA. *Diagnostic and statistical manual of mental disorders: DSM-V*, vol. 5th. American Psychiatric Association: Arlington, VA, 2013.

2. Meltzer A, Van de Water J. The Role of the Immune System in Autism Spectrum Disorder. *Neuropsychopharmacology* 2017; **42**(1)**:** 284-298.

3. Ramirez-Celis A, Becker M, Nuño M, Schauer J, Aghaeepour N, Van de Water J. Risk assessment analysis for maternal autoantibody-related autism (MAR-ASD): a subtype of autism. *Mol Psychiatry* 2021.

4. Brimberg L, Mader S, Jeganathan V, Berlin R, Coleman TR, Gregersen PK *et al.* Caspr2-reactive antibody cloned from a mother of an ASD child mediates an ASD-like phenotype in mice. *Mol Psychiatry* 2016; **21**(12)**:** 1663-1671.

5. Jones KL, Van de Water J. Maternal autoantibody related autism: mechanisms and pathways. *Mol Psychiatry* 2019; **24**(2): 252-265.

6. Braunschweig D, Krakowiak P, Duncanson P, Boyce R, Hansen RL, Ashwood P *et al.* Autism-specific maternal autoantibodies recognize critical proteins in developing brain. *Transl Psychiatry* 2013; **3:** e277.

7. Ramirez-Celis A, Edmiston E, Schauer J, Vu T, Van de Water J. Peptides of neuron specific enolase as potential ASD biomarkers: From discovery to epitope mapping. *Brain Behav Immun* 2020; **84:** 200-208.

8. Edmiston E, Jones KL, Vu T, Ashwood P, Van de Water J. Identification of the antigenic epitopes of maternal autoantibodies in autism spectrum disorders. *Brain Behav Immun* 2018; **69:** 399-407.

9. Jones KL, Pride MC, Edmiston E, Yang M, Silverman JL, Crawley JN *et al.* Autism-specific maternal autoantibodies produce behavioral abnormalities in an endogenous antigen-driven mouse model of autism. *Mol Psychiatry* 2020; **25**(11): 2994-3009

10. Bock NA, Nieman BJ, Bishop JB, Mark Henkelman R. In vivo multiple-mouse MRI at 7 Tesla. *Magn Reson Med* 2005; **54**(5)**:** 1311-1316.

11. Spencer Noakes TL, Henkelman RM, Nieman BJ. Partitioning k-space for cylindrical three-dimensional rapid acquisition with relaxation enhancement imaging in the mouse brain. *NMR Biomed* 2017; **30**(11).

12. Pagani M, Bifone A, Gozzi A. Structural covariance networks in the mouse brain. *Neuroimage* 2016; **129:** 55-63.

13. Rollins CPE, Garrison JR, Arribas M, Seyedsalehi A, Li Z, Chan RCK *et al.* Evidence in cortical folding patterns for prenatal predispositions to hallucinations in schizophrenia. *Transl Psychiatry* 2020; **10**(1)**:** 387.

14. Qiu LR, Fernandes DJ, Szulc-Lerch KU, Dazai J, Nieman BJ, Turnbull DH *et al.* Mouse MRI shows brain areas relatively larger in males emerge before those larger in females. *Nat Commun* 2018; **9**(1)**:** 2615.

15. McCarthy MM, Wright CL. Convergence of Sex Differences and the Neuroimmune System in Autism Spectrum Disorder. *Biol Psychiatry* 2017; **81**(5)**:** 402-410.

16. Mechelli A, Friston KJ, Frackowiak RS, Price CJ. Structural covariance in the human cortex. *J Neurosci* 2005; **25**(36)**:** 8303-8310.

17. Mueller FS, Scarborough J, Schalbetter SM, Richetto J, Kim E, Couch A *et al.* Behavioral, neuroanatomical, and molecular correlates of resilience and susceptibility to maternal immune activation. *Mol Psychiatry* 2021; **26**(2): 396- 410.

18. Nordahl CW, Braunschweig D, Iosif AM, Lee A, Rogers S, Ashwood P *et al.* Maternal autoantibodies are associated with abnormal brain enlargement in a subgroup of children with autism spectrum disorder. *Brain Behav Immun* 2013; **30:** 61-65.

19. Hazlett HC, Poe MD, Gerig G, Styner M, Chappell C, Smith RG *et al.* Early brain overgrowth in autism associated with an increase in cortical surface area before age 2 years. *Arch Gen Psychiatry* 2011; **68**(5)**:** 467-476.

20. Schumann CM, Bloss CS, Barnes CC, Wideman GM, Carper RA, Akshoomoff N *et al.* Longitudinal magnetic resonance imaging study of cortical development through early childhood in autism. *J Neurosci* 2010; **30**(12)**:** 4419-4427.

21. Fombonne E, Rogé B, Claverie J, Courty S, Frémolle J. Microcephaly and macrocephaly in autism. *J Autism Dev Disord* 1999; **29**(2)**:** 113-119.

22. Bloss CS, Courchesne E. MRI neuroanatomy in young girls with autism: a preliminary study. *J Am Acad Child Adolesc Psychiatry* 2007; **46**(4)**:** 515-523.

23. Ferri SL, Abel T, Brodkin ES. Sex Differences in Autism Spectrum Disorder: a Review. *Curr Psychiatry Rep* 2018; **20**(2)**:** 9.

24. Alaerts K, Swinnen SP, Wenderoth N. Sex differences in autism: a resting-state fMRI investigation of functional brain connectivity in males and females. *Soc Cogn Affect Neurosci* 2016; **11**(6)**:** 1002-1016.

25. Lai MC, Lombardo MV, Suckling J, Ruigrok AN, Chakrabarti B, Ecker C *et al.* Biological sex affects the neurobiology of autism. *Brain* 2013; **136**(Pt 9)**:** 2799-2815.

26. Yee Y, Fernandes DJ, French L, Ellegood J, Cahill LS, Vousden DA *et al.* Structural covariance of brain region volumes is associated with both structural connectivity and transcriptomic similarity. *Neuroimage* 2018; **179:** 357-372.

27. Cardon GJ, Hepburn S, Rojas DC. Structural Covariance of Sensory Networks, the Cerebellum, and Amygdala in Autism Spectrum Disorder. *Front Neurol* 2017; **8:** 615.

28. Bethlehem RAI, Romero-Garcia R, Mak E, Bullmore ET, Baron-Cohen S. Structural Covariance Networks in Children with Autism or ADHD. *Cereb Cortex* 2017; **27**(8)**:** 4267-4276.

29. Duan X, Wang R, Xiao J, Li Y, Huang X, Guo X *et al.* Subcortical structural covariance in young children with autism spectrum disorder. *Prog Neuropsychopharmacol Biol Psychiatry* 2020; **99:** 109874.

30. Anderson JS. Cortical Underconnectivity Hypothesis in Autism: Evidence from Functional Connectivity MRI. *Comprehensive Guide to Autism*2014, pp 1457-1471.

31. Kana RK, Libero LE, Moore MS. Disrupted cortical connectivity theory as an explanatory model for autism spectrum disorders. *Phys Life Rev* 2011; **8**(4)**:** 410-437.

32. Rane P, Cochran D, Hodge SM, Haselgrove C, Kennedy DN, Frazier JA. Connectivity in Autism: A Review of MRI Connectivity Studies. *Harv Rev Psychiatry* 2015; **23**(4)**:** 223-244.

33. Cheng W, Rolls ET, Gu H, Zhang J, Feng J. Autism: reduced connectivity between cortical areas involved in face expression, theory of mind, and the sense of self. *Brain* 2015; **138**(Pt 5)**:** 1382-1393.

34. Khan S, Gramfort A, Shetty NR, Kitzbichler MG, Ganesan S, Moran JM *et al.* Local and long-range functional connectivity is reduced in concert in autism spectrum disorders. *Proc Natl Acad Sci U S A* 2013; **110**(8)**:** 3107-3112.

35. Kelly E, Meng F, Fujita H, Morgado F, Kazemi Y, Rice LC *et al.* Regulation of autism-relevant behaviors by cerebellar-prefrontal cortical circuits. *Nat Neurosci* 2020; **23**(9)**:** 1102-1110.

36. Ramos TC, Balardin JB, Sato JR, Fujita A. Abnormal Cortico-Cerebellar Functional Connectivity in Autism Spectrum Disorder. *Front Syst Neurosci* 2018; **12:** 74.

37. Bredewold R, Veenema AH. Sex differences in the regulation of social and anxiety-related behaviors: insights from vasopressin and oxytocin brain systems. *Curr Opin Neurobiol* 2018; **49:** 132-140.

38. Burguiere E, Monteiro P, Feng G, Graybiel AM. Optogenetic stimulation of lateral orbitofronto-striatal pathway suppresses compulsive behaviors. *Science* 2013; **340**(6137)**:** 1243-1246.

39. Ahmari SE, Spellman T, Douglass NL, Kheirbek MA, Simpson HB, Deisseroth K *et al.* Repeated cortico-striatal stimulation generates persistent OCD-like behavior. *Science* 2013; **340**(6137)**:** 1234-1239.

40. McKinnon CJ, Eggebrecht AT, Todorov A, Wolff JJ, Elison JT, Adams CM *et al.* Restricted and Repetitive Behavior and Brain Functional Connectivity in Infants at Risk for Developing Autism Spectrum Disorder. *Biol Psychiatry Cogn Neurosci Neuroimaging* 2019; **4**(1)**:** 50-61.

41. Kadota H, Sekiguchi H, Takeuchi S, Miyazaki M, Kohno Y, Nakajima Y. The role of the dorsolateral prefrontal cortex in the inhibition of stereotyped responses. *Exp Brain Res* 2010; **203**(3)**:** 593-600.

42. Rilett KC, Friedel M, Ellegood J, MacKenzie RN, Lerch JP, Foster JA. Loss of T cells influences sex differences in behavior and brain structure. *Brain Behav Immun* 2015; **46:** 249-260.

43. VanRyzin JW, Marquardt AE, Argue KJ, Vecchiarelli HA, Ashton SE, Arambula SE *et al.* Microglial Phagocytosis of Newborn Cells Is Induced by Endocannabinoids and Sculpts Sex Differences in Juvenile Rat Social Play. *Neuron* 2019; **102**(2)**:** 435-449 e436.

44. Lenz KM, Pickett LA, Wright CL, Davis KT, Joshi A, McCarthy MM. Mast Cells in the Developing Brain Determine Adult Sexual Behavior. *J Neurosci* 2018; **38**(37)**:** 8044-8059.

45. Wright CL, McCarthy MM. Prostaglandin E2-induced masculinization of brain and behavior requires protein kinase A, AMPA/kainate, and metabotropic glutamate receptor signaling. *J Neurosci* 2009; **29**(42)**:** 13274-13282.

46. Kowal C, Athanassiou A, Chen H, Diamond B. Maternal antibodies and developing blood-brain barrier. *Immunol Res* 2015; **63**(1-3)**:** 18-25.

47. Reemst K, Noctor SC, Lucassen PJ, Hol EM. The Indispensable Roles of Microglia and Astrocytes during Brain Development. *Front Hum Neurosci* 2016; **10:** 566.

48. Martinez-Cerdeno V, Camacho J, Fox E, Miller E, Ariza J, Kienzle D *et al.* Prenatal Exposure to Autism-Specific Maternal Autoantibodies Alters Proliferation of Cortical Neural Precursor Cells, Enlarges Brain, and Increases Neuronal Size in Adult Animals. *Cereb Cortex* 2016; **26**(1)**:** 374-383.

Supplemental Methods

Animals (cont.)

Briefly, all female C57BL/6J mice randomly assigned to MAR-ASD treatment received a series of immunizations containing peptide epitope sequences of the four primary target proteins of MAR ASD (LDH-A, LDH-B, STIP1, and CRMP1) and Freund's adjuvant prior to breeding. Control females were similarly injected but replacing the peptides with saline. Following confirmation of autoantibody production to the salient epitope sequences, females were then paired with male breeders to produce the experimental offspring of interest. Experimental offspring that underwent behavioral testing as juveniles and adults, as described in Jones et al, 2018, representing 1 male and 1 female from each litter (Litter Number; Control = 11, MAR-ASD = 12), were sacrificed following completion of behavioral assays, perfused, and sent to the Mouse Imaging Centre (MICe) in Toronto, ON, Canada for ex vivo magnetic resonance imaging (MRI) scanning and analysis.

Perfusions were performed at University of California, Davis prior to being shipped overnight to the Mouse Imaging Centre (MICe). At approximately 6 months of age, mice were anesthetized with isoflurane and intracardially perfused with 30 mL of 0.1 M PBS containing 10 μL/mL heparin (Sigma) and 2 mM ProHance (Bracco Diagnostics Inc., a Gadolinium contrast agent) followed by 30 mL of 4% paraformaldehyde (PFA) containing 2 mM ProHance(14). Perfusions were performed with a minipump at a rate of approximately 60 mL/hr. After perfusion, mice were decapitated and the skin, lower jaw, ears, and the cartilaginous nose tip were removed. The brain and remaining skull structures were incubated in 4% PFA + 2 mM ProHance overnight at 4°C, then transferred to 0.1 M PBS containing 2 mM ProHance and 0.02% sodium azide for at

least one month prior to MRI scanning (15).

Registration and Analysis

To visualize and compare potential volume changes in the mouse brains, the MR images were linearly (6 parameter followed by a 12 parameter) and non-linearly registered together. All scans were then resampled with the appropriate transform and averaged to create a population atlas representing the average anatomy of the entire study sample. The result is aligned scan deformation in an unbiased fashion. This allows for the analysis needed to take each individual mouse's anatomy into this final atlas space. The log-transformed Jacobian determinants of the deformation fields were then calculated as measures of volume at each voxel. Significant volume changes are then calculated by warping a pre-existing classified MRI atlas onto the population atlas, which allows for the volume of 159 segmented structures encompassing cortical lobes, large white matter structures (i.e., corpus callosum), ventricles, cerebellum, brain stem, and olfactory bulbs to be assessed in all brains. Multiple comparisons in this study were controlled for using the False Discovery Rate (FDR). To assess whether findings varied across biological sex, three sets of analyses were completed for each region: 1) "Full" group comprised of both males and females, 2) males only, and 3) females only.

-

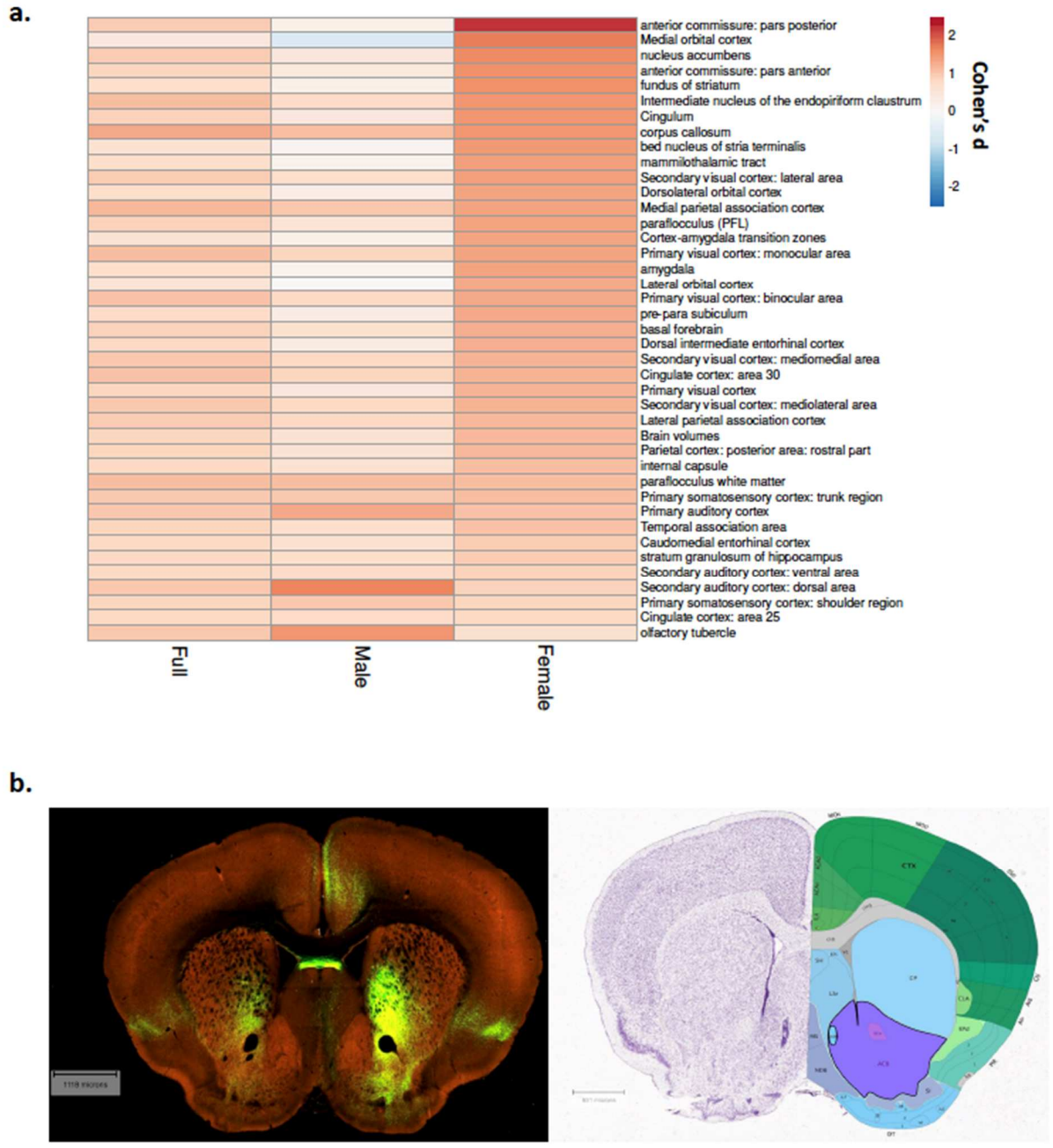

Supplementary Figure 1. Effect sizes of volumetric changes in MAR-ASD female mice implicate altered cortico-striatal connectivity. a) Heatmap plot displaying effect sizes by region for male and female MAR-ASD mice as well as combined (Full). Effect sizes represent Cohen's d values. Legend for effect sizes has a range between 2.5 & -2.5 (MAR (N = 11M, 11F), Ctrl (N =12M, 11F)). b) Images collected from the Allen Mouse Brain Connectivity and Reference Atlas's. The first image details labeling in response to fluorescent tracer injection into the mOFC of wildtype C57Bl/6 mice. The second image is for reference of labeled regions. Highlighted in purple is the nucleus

accumbens and anterior commissure pars anterior. Fluorescent staining also appears to a large extent in the caudoputamen.

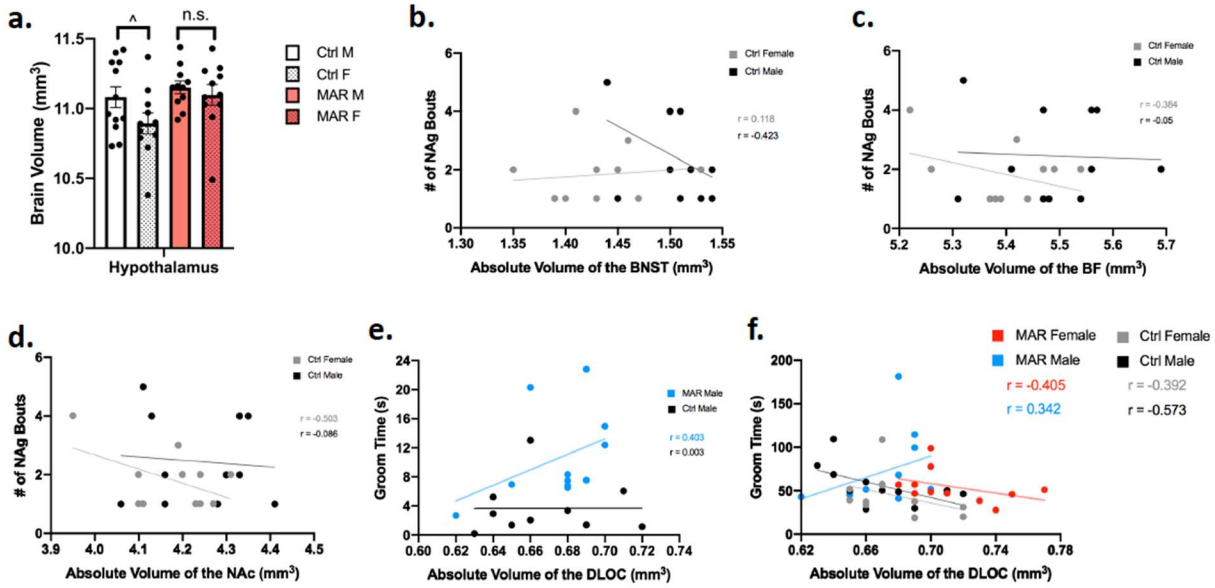

Supplementary Figure 2. Graphical representation of additional volumetric brain data and correlational findings. a) Brain volume of the hypothalamus analyzed between sexes within treatment. Statistical analysis conducted using a one-way ANOVA (MAR (N = 11M, 11F), Ctrl (N = 12M, 11F)). Error bars represent the mean +/- SEM. ^ = $0.05<p<0.1$, n.s. = non-significant. b-d) Correlation between the number of nose-to-anogential (NAg) bouts during the JRSI task and volume of the BNST (MAR (N = 11M, 11F), Ctrl (N = 11M, 11F)). (b), basal forebrain (BF) (c), and nucleus accumbens (NAc) (d) in control animals, split by sex. e) Relationship between groom time (seconds) and volume of the dorsolateral orbital cortex (DLOC) in male mice during the male female social interaction (MFSI) task (MAR (N = 11M), Ctrl (N = 10M)). f) Graph of correlations across treatment and sex for groom time (seconds), as measured during empty cage grooming behavior, and volume of the DLOC (MAR (N = 11M, 11F), Ctrl (N = 11M, 11F)). Trendlines and Pearson's r-value displayed along with scatterplot values for each graph.

Absolute Volumes	Full Group (Males + Females)							Females Only							Males Only					
	Control		MAR-ASD					Control		MAR-ASD					Control		MAR-ASD			
Regions	Mean	SD	Mean	SD	P-value	FDR		Mean	SD	Mean	SD	P-value	FDR		Mean	SD	Mean	SD	P-value	FDR
amygdala	10.671	0.308	10.894	0.323	0.023	0.075	-	**10.506**	**0.286**	**10.916**	**0.317**	**0.005**	**0.044**	*	10.822	0.251	10.871	0.342	0.701	0.929
anterior commissure: pars anterior	**1.604**	**0.042**	**1.643**	**0.048**	**0.006**	**0.039**	*	**1.587**	**0.020**	**1.645**	**0.047**	**0.001**	**0.038**	*	1.620	0.051	1.641	0.050	0.330	0.718
anterior commissure: pars posterior	**0.496**	**0.020**	**0.516**	**0.019**	**0.002**	**0.021**	*	**0.487**	**0.009**	**0.521**	**0.019**	**0.000**	**0.004**	**	0.505	0.024	0.510	0.019	0.559	0.896
basal forebrain	**5.447**	**0.109**	**5.551**	**0.112**	**0.003**	**0.026**	*	5.402	0.096	5.538	0.117	0.007	0.053	-	5.490	0.106	5.564	0.111	0.114	0.499
bed nucleus of stria terminalis	1.468	0.056	1.498	0.039	0.043	0.110		**1.428**	**0.049**	**1.487**	**0.030**	**0.003**	**0.043**	*	1.505	0.031	1.509	0.045	0.788	0.956
cerebellar peduncle: inferior	0.856	0.040	0.863	0.038	0.544	0.671		0.866	0.038	0.872	0.033	0.690	0.819		0.847	0.041	0.855	0.042	0.679	0.912
cerebellar peduncle: middle	1.356	0.083	1.364	0.065	0.714	0.805		1.398	0.076	1.402	0.044	0.861	0.917		1.318	0.071	1.326	0.060	0.769	0.948
cerebellar peduncle: superior	1.096	0.046	1.100	0.047	0.758	0.837		1.100	0.053	1.112	0.051	0.618	0.792		1.092	0.040	1.089	0.043	0.868	0.956
cerebral aqueduct	0.488	0.023	0.488	0.024	0.960	0.966		0.490	0.026	0.495	0.026	0.601	0.784		0.486	0.021	0.481	0.020	0.541	0.896
cerebral peduncle	2.414	0.062	2.448	0.058	0.061	0.137		2.410	0.057	2.455	0.061	0.087	0.191		2.418	0.069	2.442	0.057	0.375	0.745
colliculus: inferior	5.769	0.169	5.817	0.180	0.360	0.511		5.762	0.113	5.859	0.132	0.080	0.184		5.774	0.213	5.774	0.216	0.999	0.999
colliculus: superior	8.980	0.276	9.029	0.306	0.575	0.687		9.050	0.283	9.147	0.198	0.363	0.535		8.915	0.265	8.911	0.357	0.973	0.999
corpus callosum	**14.625**	**0.416**	**15.091**	**0.272**	**0.000**	**0.010**	*	**14.651**	**0.421**	**15.199**	**0.287**	**0.002**	**0.038**	*	14.602	0.430	14.984	0.219	0.015	0.301
corticospinal tract/pyramids	1.189	0.042	1.203	0.040	0.272	0.408		1.197	0.045	1.203	0.031	0.736	0.855		1.182	0.040	1.202	0.049	0.269	0.669
cuneate nucleus	0.229	0.016	0.226	0.020	0.687	0.791		0.228	0.016	0.228	0.021	0.960	0.966		0.229	0.017	0.225	0.020	0.613	0.896
dentate gyrus of hippocampus	3.371	0.105	3.455	0.126	0.019	0.066	-	3.370	0.080	3.470	0.088	0.011	0.057	-	3.371	0.127	3.440	0.159	0.260	0.666
facial nerve (cranial nerve 7)	0.244	0.011	0.245	0.010	0.828	0.889		0.246	0.014	0.248	0.012	0.737	0.855		0.242	0.008	0.242	0.008	0.862	0.956
fasciculus retroflexus	0.265	0.008	0.272	0.011	0.013	0.061	-	0.264	0.009	0.274	0.012	0.043	0.125		0.266	0.008	0.270	0.009	0.183	0.590
fimbria	3.629	0.116	3.707	0.090	0.016	0.065	-	3.651	0.116	3.722	0.059	0.084	0.187		3.610	0.119	3.693	0.115	0.103	0.499
fornix	0.714	0.018	0.728	0.019	0.013	0.061	-	0.712	0.018	0.733	0.019	0.016	0.070	-	0.715	0.019	0.723	0.018	0.326	0.718
fourth ventricle	0.826	0.048	0.834	0.049	0.580	0.688		0.840	0.050	0.840	0.035	0.998	0.998		0.813	0.044	0.828	0.061	0.504	0.862
fundus of striatum	0.190	0.008	0.195	0.008	0.021	0.071	-	**0.187**	**0.006**	**0.197**	**0.007**	**0.001**	**0.038**	*	0.192	0.009	0.194	0.009	0.613	0.896
globus pallidus	3.456	0.114	3.539	0.113	0.018	0.066	-	3.472	0.134	3.582	0.087	0.033	0.106		3.441	0.096	3.497	0.124	0.238	0.657
habenular commissure	0.029	0.002	0.030	0.004	0.255	0.386		0.030	0.002	0.031	0.003	0.214	0.362		0.028	0.002	0.029	0.005	0.612	0.896
hippocampus	20.719	0.607	21.081	0.473	0.031	0.094	-	20.578	0.574	21.068	0.391	0.030	0.103		20.848	0.632	21.094	0.562	0.336	0.723
hypothalamus	10.992	0.266	11.125	0.201	0.066	0.142		10.894	0.250	11.098	0.246	0.068	0.169		11.081	0.257	11.152	0.151	0.438	0.809
inferior olivary complex	0.182	0.006	0.182	0.010	0.833	0.889		0.183	0.006	0.180	0.006	0.267	0.420		0.181	0.006	0.185	0.012	0.347	0.727
internal capsule	**3.162**	**0.110**	**3.247**	**0.093**	**0.008**	**0.044**	*	3.196	0.116	3.305	0.067	0.015	0.068	-	3.131	0.099	3.189	0.079	0.138	0.505
interpedunclar nucleus	0.254	0.013	0.254	0.009	0.827	0.889		0.252	0.015	0.251	0.010	0.862	0.917		0.255	0.013	0.258	0.007	0.548	0.896
lateral olfactory tract	0.998	0.038	1.013	0.050	0.278	0.413		0.982	0.039	0.986	0.044	0.784	0.880		1.013	0.030	1.039	0.044	0.118	0.499
lateral septum	3.187	0.105	3.271	0.114	0.014	0.061	-	3.208	0.115	3.317	0.084	0.019	0.077	-	3.169	0.096	3.225	0.125	0.233	0.657
lateral ventricle	3.710	0.172	3.874	0.247	0.013	0.061	-	3.758	0.205	3.970	0.193	0.022	0.081	-	3.666	0.129	3.778	0.266	0.207	0.610
mammillary bodies	0.434	0.022	0.442	0.018	0.190	0.315		0.441	0.021	0.449	0.018	0.341	0.512		0.428	0.022	0.435	0.016	0.373	0.745
mammilothalamic tract	0.275	0.007	0.281	0.008	0.022	0.073	-	**0.275**	**0.006**	**0.284**	**0.007**	**0.003**	**0.043**	*	0.276	0.008	0.278	0.008	0.674	0.912
medial lemniscus/medial longitudinal fasciculus	2.276	0.060	2.312	0.059	0.046	0.114		2.258	0.064	2.290	0.040	0.175	0.310		2.291	0.055	2.334	0.069	0.112	0.499
medial septum	1.270	0.039	1.295	0.027	0.014	0.061	-	1.264	0.038	1.301	0.030	0.020	0.078	-	1.275	0.040	1.290	0.024	0.303	0.688
medulla	25.358	0.925	25.479	0.965	0.671	0.784		25.441	0.979	25.525	0.732	0.821	0.888		25.283	0.908	25.432	1.190	0.737	0.948
midbrain	14.425	0.373	14.641	0.294	0.037	0.104		14.305	0.390	14.656	0.282	0.025	0.089	-	14.536	0.334	14.626	0.319	0.517	0.875
nucleus accumbens	**4.210**	**0.111**	**4.323**	**0.121**	**0.002**	**0.021**	*	**4.176**	**0.103**	**4.349**	**0.112**	**0.001**	**0.038**	*	4.242	0.113	4.297	0.130	0.285	0.674
olfactory bulbs	25.971	0.769	25.934	0.729	0.872	0.918		25.638	0.643	25.683	0.788	0.884	0.925		26.275	0.772	26.185	0.598	0.759	0.948
olfactory tubercle	**3.356**	**0.088**	**3.445**	**0.089**	**0.002**	**0.019**	*	3.340	0.091	3.403	0.094	0.127	0.255		3.370	0.087	3.487	0.063	0.002	0.121
optic tract	1.836	0.058	1.873	0.054	0.030	0.093	-	1.836	0.059	1.874	0.059	0.146	0.267		1.835	0.060	1.872	0.051	0.126	0.501
periaqueductal grey	4.108	0.134	4.168	0.167	0.192	0.315		4.090	0.132	4.203	0.164	0.092	0.200		4.124	0.140	4.132	0.171	0.897	0.969
pons	18.011	0.672	18.029	0.537	0.920	0.942		18.180	0.726	18.250	0.535	0.801	0.880		17.855	0.606	17.809	0.460	0.838	0.956
pontine nucleus	0.741	0.076	0.742	0.066	0.968	0.968		0.794	0.062	0.785	0.037	0.689	0.819		0.693	0.054	0.699	0.061	0.800	0.956
posterior commissure	0.158	0.007	0.160	0.008	0.566	0.684		0.161	0.007	0.163	0.008	0.518	0.716		0.156	0.005	0.156	0.008	0.912	0.969
pre-para subiculum	1.977	0.070	2.025	0.053	0.013	0.061	-	**1.956**	**0.067**	**2.035**	**0.053**	**0.006**	**0.050**	*	1.997	0.069	2.016	0.053	0.469	0.838

stratum granulosum of hippocampus	**0.877**	**0.030**	**0.904**	**0.034**	**0.007**	**0.043**	*	0.880	0.028	0.905	0.024	0.032	0.106		0.874	0.034	0.903	0.043	0.087	0.488		
stria medullaris	0.718	0.019	0.725	0.028	0.368	0.518		0.725	0.015	0.738	0.024	0.136	0.260		0.712	0.020	0.711	0.026	0.927	0.970		
stria terminalis	1.040	0.045	1.064	0.027	0.038	0.104		1.052	0.048	1.071	0.021	0.239	0.392		1.029	0.042	1.057	0.032	0.089	0.488		
striatum	21.525	0.691	21.939	0.781	0.066	0.142		21.856	0.734	22.394	0.637	0.081	0.185		21.222	0.506	21.485	0.649	0.288	0.674		
subependymale zone / rhinocele	0.085	0.003	0.085	0.003	0.404	0.549		0.083	0.002	0.085	0.003	0.263	0.418		0.086	0.002	0.086	0.003	0.846	0.956		
superior olivary complex	0.750	0.036	0.754	0.031	0.704	0.799		0.760	0.043	0.765	0.032	0.760	0.875		0.741	0.028	0.743	0.026	0.872	0.956		
thalamus	18.358	0.471	18.502	0.617	0.383	0.529		18.567	0.407	18.940	0.472	0.061	0.157		18.166	0.458	18.064	0.394	0.572	0.896		
third ventricle	1.159	0.034	1.172	0.050	0.294	0.428		1.165	0.032	1.191	0.040	0.097	0.208		1.153	0.037	1.153	0.052	0.985	0.999		
ventral tegmental decussation	0.145	0.008	0.149	0.007	0.158	0.279		0.140	0.007	0.145	0.005	0.070	0.169		0.150	0.006	0.152	0.007	0.477	0.842		
lobules 1-2: lingula and central lobule (ventral)	1.603	0.098	1.659	0.095	0.057	0.132		1.595	0.106	1.647	0.101	0.254	0.407		1.609	0.094	1.671	0.093	0.129	0.501		
lobule 3: central lobule (dorsal)	1.765	0.090	1.784	0.086	0.495	0.625		1.739	0.084	1.785	0.060	0.154	0.279		1.789	0.093	1.782	0.109	0.860	0.956		
lobules 4-5: culmen (ventral and dorsal)	4.014	0.183	4.030	0.163	0.758	0.837		4.027	0.159	4.085	0.065	0.276	0.431		4.002	0.209	3.975	0.212	0.762	0.948		
lobule 6: declive	2.542	0.133	2.531	0.091	0.756	0.837		2.569	0.124	2.547	0.056	0.586	0.769		2.517	0.141	2.516	0.117	0.988	0.999		
lobule 7: tuber (or folium)	0.825	0.064	0.839	0.042	0.425	0.568		0.823	0.068	0.832	0.036	0.679	0.819		0.828	0.064	0.845	0.049	0.490	0.847		
lobule 8: pyramis	1.483	0.078	1.506	0.059	0.288	0.424		1.493	0.089	1.501	0.061	0.798	0.880		1.475	0.069	1.510	0.058	0.204	0.610		
lobule 9: uvula	2.405	0.108	2.471	0.100	0.042	0.110		2.443	0.125	2.467	0.061	0.568	0.759		2.371	0.081	2.474	0.131	0.032	0.367		
lobule 10: nodulus	1.240	0.078	1.254	0.058	0.501	0.628		1.259	0.083	1.251	0.051	0.808	0.880		1.222	0.073	1.256	0.068	0.265	0.669		
anterior lobule (lobules 4-5)	1.597	0.062	1.634	0.049	0.033	0.096	-	1.588	0.079	1.632	0.053	0.145	0.267		1.605	0.044	1.635	0.047	0.119	0.499		
simple lobule (lobule 6)	4.400	0.198	4.494	0.106	0.055	0.131		4.454	0.190	4.535	0.088	0.214	0.362		4.350	0.200	4.452	0.109	0.148	0.505		
crus 1: ansiform lobule (lobule 6)	3.760	0.198	3.849	0.110	0.073	0.148		3.817	0.172	3.884	0.120	0.303	0.466		3.708	0.212	3.813	0.091	0.144	0.505		
crus 2: ansiform lobule (lobule 7)	3.206	0.163	3.260	0.127	0.229	0.361		3.250	0.147	3.321	0.111	0.216	0.362		3.166	0.173	3.198	0.116	0.607	0.896		
paramedian lobule (lobule 7)	3.654	0.216	3.697	0.189	0.485	0.625		3.734	0.215	3.791	0.126	0.458	0.644		3.581	0.197	3.603	0.199	0.796	0.956		
copula: pyramis (lobule 8)	2.237	0.127	2.254	0.095	0.622	0.732		2.294	0.116	2.283	0.073	0.782	0.880		2.184	0.117	2.225	0.109	0.405	0.758		
flocculus (FL)	0.999	0.053	1.028	0.031	0.034	0.096	-	0.998	0.049	1.023	0.020	0.130	0.255		1.000	0.059	1.033	0.040	0.144	0.505		
paraflocculus (PFL)	**3.175**	**0.217**	**3.369**	**0.197**	**0.003**	**0.026**	*	**3.107**	**0.217**	**3.376**	**0.169**	**0.004**	**0.043**	*	3.238	0.207	3.362	0.230	0.186	0.590		
trunk of arbor vita	4.533	0.161	4.572	0.152	0.409	0.551		4.561	0.160	4.601	0.135	0.539	0.732		4.506	0.165	4.543	0.168	0.608	0.896		
lobule 1-2 white matter	0.083	0.008	0.087	0.007	0.060	0.137		0.081	0.008	0.086	0.006	0.111	0.233		0.085	0.008	0.089	0.008	0.247	0.657		
lobule 3 white matter	0.221	0.016	0.225	0.010	0.245	0.378		0.216	0.014	0.224	0.006	0.126	0.255		0.225	0.017	0.227	0.013	0.716	0.941		
trunk of lobules 1-3 white matter	0.148	0.009	0.153	0.007	0.028	0.091	-	0.145	0.009	0.151	0.004	0.050	0.137		0.150	0.008	0.155	0.008	0.196	0.599		
lobules 4-5 white matter	0.655	0.035	0.652	0.034	0.805	0.883		0.658	0.027	0.669	0.021	0.316	0.479		0.652	0.042	0.635	0.037	0.342	0.726		
lobules 6-7 white matter	0.728	0.032	0.727	0.029	0.924	0.942		0.741	0.027	0.740	0.021	0.901	0.936		0.715	0.032	0.714	0.031	0.905	0.969		
lobule 8 white matter	0.152	0.010	0.154	0.008	0.356	0.509		0.152	0.013	0.153	0.009	0.873	0.920		0.152	0.008	0.156	0.007	0.178	0.590		
trunk of lobules 6-8 white matter	0.116	0.005	0.116	0.005	0.921	0.942		0.116	0.006	0.117	0.006	0.803	0.880		0.115	0.005	0.115	0.005	0.870	0.956		
lobule 9 white matter	0.277	0.017	0.288	0.014	0.031	0.094	-	0.284	0.019	0.287	0.013	0.623	0.792		0.271	0.013	0.288	0.016	0.011	0.280		
lobule 10 white matter	0.086	0.007	0.087	0.005	0.682	0.791		0.087	0.008	0.087	0.005	0.940	0.964		0.085	0.005	0.087	0.006	0.486	0.847		
anterior lobule white matter	0.093	0.004	0.095	0.003	0.071	0.148		0.093	0.005	0.095	0.004	0.160	0.286		0.093	0.003	0.095	0.003	0.294	0.677		
simple lobule white matter	0.451	0.023	0.458	0.015	0.229	0.361		0.456	0.022	0.466	0.015	0.211	0.362		0.447	0.023	0.450	0.010	0.680	0.912		
crus 1 white matter	0.404	0.026	0.415	0.017	0.098	0.190		0.410	0.024	0.424	0.016	0.122	0.251		0.397	0.028	0.405	0.012	0.404	0.758		
trunk of simple and crus 1 white matter	0.177	0.009	0.178	0.008	0.890	0.925		0.183	0.008	0.183	0.006	0.924	0.954		0.173	0.007	0.173	0.006	0.996	0.999		
crus 2 white matter	0.255	0.015	0.259	0.014	0.376	0.525		0.259	0.015	0.268	0.011	0.139	0.261		0.252	0.015	0.251	0.011	0.805	0.956		
paramedian lobule	0.163	0.011	0.165	0.011	0.553	0.676		0.166	0.010	0.168	0.008	0.560	0.754		0.161	0.011	0.163	0.013	0.796	0.956		
trunk of crus 2 and paramedian white matter	0.350	0.022	0.351	0.016	0.885	0.925		0.360	0.018	0.360	0.011	0.956	0.966		0.341	0.022	0.342	0.015	0.950	0.987		
copula white matter	0.071	0.004	0.072	0.004	0.396	0.543		0.072	0.005	0.073	0.004	0.776	0.880		0.070	0.004	0.071	0.004	0.380	0.745		
paraflocculus white matter	**0.261**	**0.014**	**0.275**	**0.010**	**0.000**	**0.018**	*	0.261	0.018	0.277	0.011	0.016	0.070	-	0.260	0.012	0.272	0.009	0.015	0.301		
flocculus white matter	0.079	0.005	0.081	0.003	0.102	0.195		0.079	0.004	0.081	0.002	0.243	0.395		0.079	0.006	0.082	0.004	0.252	0.657		
dentate nucleus	0.367	0.015	0.371	0.017	0.480	0.625		0.370	0.014	0.373	0.013	0.659	0.806		0.365	0.016	0.368	0.020	0.611	0.896		
nucleus interpositus	0.463	0.017	0.466	0.019	0.568	0.684		0.461	0.019	0.463	0.015	0.735	0.855		0.465	0.016	0.468	0.023	0.638	0.906		
fastigial nucleus	0.506	0.017	0.513	0.023	0.253	0.386		0.503	0.018	0.515	0.020	0.137	0.260		0.510	0.017	0.512	0.026	0.837	0.956		
Cingulate cortex: area 24a	1.842	0.099	1.864	0.096	0.459	0.604		1.860	0.117	1.883	0.072	0.576	0.763		1.826	0.083	1.845	0.115	0.660	0.912		
Cingulate cortex: area 24a'	0.851	0.045	0.853	0.032	0.825	0.889		0.869	0.053	0.866	0.026	0.865	0.917		0.834	0.030	0.840	0.033	0.614	0.896		

Cingulate cortex: area 24b	1.458	0.069	1.471	0.063	0.532	0.660			1.504	0.064	1.505	0.048	0.958	0.966			1.417	0.043	1.436	0.059	0.364	0.741	
Cingulate cortex: area 24b'	0.597	0.018	0.604	0.016	0.181	0.306			0.607	0.016	0.612	0.013	0.383	0.554			0.588	0.015	0.595	0.016	0.243	0.657	
Cingulate cortex: area 25	**0.484**	**0.016**	**0.497**	**0.015**	**0.009**	**0.049**	*		0.482	0.016	0.495	0.016	0.071	0.169			0.486	0.016	0.498	0.014	0.070	0.465	
Cingulate cortex: area 29a	0.780	0.028	0.790	0.027	0.237	0.369			0.780	0.032	0.792	0.025	0.378	0.551			0.780	0.025	0.789	0.029	0.463	0.838	
Cingulate cortex: area 29b	0.340	0.016	0.351	0.016	0.029	0.091	-		0.342	0.019	0.359	0.016	0.035	0.108			0.339	0.014	0.344	0.014	0.392	0.751	
Cingulate cortex: area 29c	1.773	0.069	1.787	0.070	0.489	0.625			1.805	0.080	1.829	0.057	0.428	0.608			1.742	0.040	1.745	0.056	0.913	0.969	
Cingulate cortex: area 30	**2.870**	**0.090**	**2.967**	**0.095**	**0.001**	**0.019**	*		2.877	0.091	3.003	0.112	0.009	0.053	-		2.863	0.092	2.930	0.059	0.049	0.465	
Cingulate cortex: area 32	2.073	0.068	2.108	0.101	0.174	0.298			2.117	0.067	2.191	0.050	0.008	0.053	-		2.032	0.037	2.025	0.061	0.739	0.948	
Amygdalopiriform transition area	1.125	0.042	1.153	0.050	0.051	0.123			1.110	0.042	1.158	0.055	0.033	0.106			1.138	0.040	1.147	0.047	0.623	0.901	
Primary auditory cortex	**1.686**	**0.069**	**1.753**	**0.058**	**0.001**	**0.019**	*		1.718	0.066	1.785	0.060	0.022	0.081	-		1.655	0.060	1.720	0.035	0.005	0.185	
Secondary auditory cortex: dorsal area	**1.858**	**0.074**	**1.925**	**0.055**	**0.001**	**0.019**	*		1.897	0.079	1.959	0.055	0.045	0.125			1.823	0.050	1.891	0.029	0.001	0.106	
Secondary auditory cortex: ventral area	**1.830**	**0.069**	**1.887**	**0.068**	**0.008**	**0.044**	*		1.846	0.077	1.915	0.071	0.042	0.125			1.815	0.059	1.858	0.054	0.080	0.488	
Caudomedial entorhinal cortex	**5.028**	**0.163**	**5.142**	**0.101**	**0.007**	**0.044**	*		5.029	0.163	5.164	0.108	0.032	0.106			5.028	0.169	5.120	0.093	0.126	0.501	
Cingulum	**0.879**	**0.025**	**0.901**	**0.021**	**0.004**	**0.028**	*		**0.878**	**0.023**	**0.909**	**0.017**	**0.002**	**0.038**	*		0.881	0.028	0.893	0.022	0.280	0.674	
Claustrum	0.273	0.009	0.279	0.010	0.044	0.110			0.271	0.007	0.281	0.011	0.018	0.074	-		0.274	0.010	0.276	0.010	0.598	0.896	
Cortex-amygdala transition zones	0.814	0.036	0.836	0.035	0.041	0.110			**0.786**	**0.020**	**0.825**	**0.035**	**0.004**	**0.043**	*		0.839	0.027	0.847	0.034	0.559	0.896	
Claustrum: dorsal part	0.266	0.010	0.265	0.011	0.695	0.795			0.269	0.012	0.267	0.010	0.658	0.806			0.263	0.008	0.263	0.013	0.871	0.956	
Dorsal nucleus of the endopiriform	1.558	0.040	1.577	0.060	0.226	0.361			1.554	0.030	1.594	0.054	0.043	0.125			1.562	0.048	1.560	0.064	0.915	0.969	
Dorsal intermediate entorhinal cortex	**1.890**	**0.057**	**1.943**	**0.073**	**0.010**	**0.050**	*		1.886	0.058	1.968	0.073	0.008	0.053	-		1.895	0.058	1.918	0.066	0.391	0.751	
Dorsolateral entorhinal cortex	2.677	0.101	2.746	0.085	0.017	0.066	-		2.703	0.111	2.769	0.080	0.129	0.255			2.653	0.089	2.724	0.087	0.069	0.465	
Dorsolateral orbital cortex	0.673	0.026	0.695	0.032	0.016	0.065	-		**0.677**	**0.025**	**0.714**	**0.027**	**0.004**	**0.043**	*		0.669	0.028	0.676	0.025	0.540	0.896	
Dorsal tenia tecta	0.762	0.027	0.776	0.025	0.066	0.142			0.754	0.027	0.776	0.029	0.074	0.174			0.769	0.025	0.777	0.021	0.469	0.838	
Ectorhinal cortex	2.676	0.100	2.751	0.104	0.018	0.066	-		2.680	0.113	2.786	0.117	0.043	0.125			2.673	0.092	2.717	0.081	0.246	0.657	
Frontal cortex: area 3	0.789	0.026	0.798	0.021	0.227	0.361			0.807	0.025	0.810	0.011	0.687	0.819			0.773	0.013	0.785	0.020	0.098	0.499	
Frontal association cortex	5.397	0.203	5.512	0.331	0.168	0.290			5.549	0.139	5.783	0.236	0.010	0.056	-		5.259	0.144	5.241	0.116	0.746	0.948	
Intermediate nucleus of the endopiriform claustrum	**0.600**	**0.020**	**0.626**	**0.026**	**0.000**	**0.018**	*		**0.594**	**0.014**	**0.626**	**0.027**	**0.002**	**0.038**	*		0.606	0.023	0.626	0.027	0.069	0.465	
Insular region: not subdivided	7.184	0.221	7.188	0.227	0.947	0.959			7.184	0.248	7.236	0.219	0.613	0.792			7.183	0.205	7.141	0.235	0.649	0.912	
Lateral orbital cortex	3.050	0.105	3.118	0.140	0.071	0.148			**3.071**	**0.097**	**3.204**	**0.103**	**0.005**	**0.048**	*		3.030	0.113	3.032	0.118	0.974	0.999	
Lateral parietal association cortex	**0.237**	**0.007**	**0.245**	**0.008**	**0.002**	**0.019**	*		0.238	0.008	0.248	0.009	0.011	0.057	-		0.237	0.006	0.241	0.004	0.065	0.465	
Primary motor cortex	7.570	0.235	7.640	0.221	0.308	0.445			7.730	0.210	7.792	0.136	0.423	0.606			7.423	0.147	7.489	0.184	0.352	0.727	
Secondary motor cortex	6.354	0.202	6.447	0.203	0.133	0.244			6.484	0.159	6.580	0.126	0.135	0.260			6.235	0.163	6.314	0.178	0.280	0.674	
Medial entorhinal cortex	0.794	0.033	0.806	0.031	0.190	0.315			0.802	0.029	0.822	0.028	0.106	0.225			0.787	0.035	0.791	0.026	0.756	0.948	
Medial orbital cortex	1.604	0.038	1.635	0.081	0.103	0.195			**1.610**	**0.042**	**1.695**	**0.056**	**0.001**	**0.038**	*		1.598	0.035	1.574	0.050	0.195	0.599	
Medial parietal association cortex	**0.454**	**0.012**	**0.470**	**0.014**	**0.000**	**0.018**	*		**0.454**	**0.014**	**0.475**	**0.017**	**0.004**	**0.043**	*		0.454	0.011	0.464	0.008	0.022	0.315	
Piriform cortex	11.695	0.217	11.870	0.310	0.033	0.096	-		11.646	0.233	11.898	0.352	0.061	0.157			11.740	0.201	11.841	0.276	0.321	0.718	
Posterolateral cortical amygdaloid area	1.095	0.045	1.116	0.052	0.157	0.279			1.068	0.036	1.108	0.059	0.068	0.169			1.121	0.038	1.124	0.045	0.824	0.956	
Posteromedial cortical amygdaloid area	1.332	0.061	1.363	0.041	0.057	0.132			1.301	0.054	1.361	0.047	0.011	0.057	-		1.361	0.054	1.365	0.036	0.865	0.956	
Perirhinal cortex	2.346	0.080	2.407	0.087	0.018	0.066	-		2.359	0.091	2.434	0.092	0.071	0.169			2.333	0.069	2.380	0.076	0.138	0.505	
Parietal cortex: posterior area: rostral part	**0.120**	**0.004**	**0.124**	**0.004**	**0.004**	**0.033**	*		0.121	0.005	0.126	0.005	0.013	0.065	-		0.120	0.004	0.122	0.002	0.149	0.505	
Rostral amygdalopiriform area	0.557	0.024	0.570	0.037	0.162	0.283			0.552	0.029	0.572	0.042	0.195	0.341			0.563	0.017	0.569	0.032	0.585	0.896	
Primary somatosensory cortex	4.356	0.137	4.427	0.094	0.050	0.122			4.436	0.146	4.481	0.065	0.357	0.530			4.282	0.078	4.373	0.089	0.017	0.302	
Primary somatosensory cortex: barrel field	10.420	0.447	10.629	0.303	0.074	0.149			10.697	0.493	10.802	0.254	0.537	0.732			10.166	0.177	10.456	0.252	0.004	0.185	
Primary somatosensory cortex: dysgranular zone	0.393	0.016	0.402	0.014	0.043	0.110			0.402	0.017	0.410	0.013	0.234	0.387			0.385	0.008	0.395	0.011	0.024	0.315	
Primary somatosensory cortex: forelimb region	4.164	0.157	4.228	0.127	0.137	0.248			4.259	0.164	4.300	0.105	0.489	0.682			4.077	0.087	4.157	0.108	0.063	0.465	
Primary somatosensory cortex: hindlimb region	2.383	0.069	2.435	0.069	0.016	0.065	-		2.417	0.071	2.475	0.055	0.044	0.125			2.352	0.053	2.394	0.058	0.084	0.488	
Primary somatosensory cortex: jaw region	0.639	0.031	0.652	0.022	0.106	0.197			0.661	0.028	0.666	0.017	0.654	0.806			0.618	0.014	0.638	0.017	0.006	0.185	
Primary somatosensory cortex: shoulder region	**0.227**	**0.007**	**0.233**	**0.008**	**0.006**	**0.038**	*		0.229	0.008	0.236	0.010	0.059	0.155			0.225	0.005	0.231	0.005	0.024	0.315	
Primary somatosensory cortex: trunk region	**0.569**	**0.016**	**0.587**	**0.020**	**0.002**	**0.019**	*		0.571	0.018	0.595	0.024	0.017	0.074	-		0.567	0.014	0.579	0.011	0.027	0.328	
Primary somatosensory cortex: upper lip region	5.879	0.210	5.922	0.156	0.443	0.587			6.011	0.223	5.991	0.141	0.802	0.880			5.759	0.100	5.854	0.144	0.078	0.488	
Secondary somatosensory cortex	7.120	0.242	7.133	0.271	0.868	0.918			7.183	0.268	7.235	0.224	0.631	0.792			7.062	0.210	7.031	0.284	0.767	0.948	
Temporal association area	**3.026**	**0.114**	**3.128**	**0.117**	**0.005**	**0.036**	*		3.045	0.120	3.175	0.127	0.023	0.083	-		3.009	0.111	3.082	0.089	0.100	0.499	
Primary visual cortex	**2.249**	**0.090**	**2.335**	**0.107**	**0.006**	**0.038**	*		2.251	0.075	2.379	0.127	0.009	0.053	-		2.248	0.104	2.290	0.059	0.251	0.657	
Primary visual cortex: binocular area	**2.309**	**0.087**	**2.398**	**0.082**	**0.001**	**0.019**	*		**2.320**	**0.090**	**2.436**	**0.087**	**0.006**	**0.050**	*		2.299	0.086	2.360	0.059	0.061	0.465	
Primary visual cortex: monocular area	**1.935**	**0.072**	**2.014**	**0.070**	**0.001**	**0.018**	*		**1.940**	**0.080**	**2.046**	**0.076**	**0.005**	**0.044**	*		1.931	0.067	1.983	0.048	0.048	0.465	
Secondary visual cortex: lateral area	**3.153**	**0.113**	**3.264**	**0.111**	**0.002**	**0.019**	*		**3.177**	**0.103**	**3.329**	**0.111**	**0.003**	**0.043**	*		3.130	0.122	3.199	0.066	0.112	0.499	
Secondary visual cortex: mediolateral area	**0.980**	**0.037**	**1.021**	**0.042**	**0.001**	**0.019**	*		0.982	0.042	1.036	0.046	0.009	0.053	-		0.979	0.033	1.007	0.033	0.060	0.465	
Secondary visual cortex: mediomedial area	**1.654**	**0.069**	**1.732**	**0.080**	**0.001**	**0.019**	*		1.657	0.074	1.757	0.086	0.009	0.053	-		1.652	0.067	1.707	0.067	0.064	0.465	
Claustrum: ventral part	0.538	0.016	0.534	0.023	0.493	0.625			0.540	0.019	0.536	0.018	0.633	0.792			0.537	0.013	0.533	0.027	0.630	0.903	
Ventral nucleus of the endopiriform claustrum	0.588	0.014	0.598	0.024	0.093	0.182			0.588	0.014	0.609	0.023	0.018	0.074	-		0.588	0.015	0.588	0.021	0.927	0.970	
Ventral intermediate entorhinal cortex	1.194	0.047	1.219	0.050	0.084	0.166			1.194	0.043	1.236	0.052	0.052	0.141			1.194	0.052	1.203	0.044	0.658	0.912	
Ventral orbital cortex	1.407	0.044	1.432	0.058	0.106	0.197			1.408	0.049	1.466	0.047	0.009	0.053	-		1.406	0.042	1.398	0.048	0.682	0.912	
Ventral tenia tecta	0.130	0.007	0.134	0.008	0.072	0.148			0.128	0.008	0.131	0.008	0.305	0.466			0.131	0.005	0.136	0.009	0.107	0.499	
Brain volumes	**454.778**	**9.688**	**461.957**	**6.961**	**0.007**				**456.634**	**9.920**	**466.160**	**6.082**	**0.013**				453.077	9.574	457.754	5.090	0.164		

Supplemental Table 1. Absolute volumes of MAR-ASD and control animals. Absolute volume mm3 of the 159 different regions examined in the brain. The mean and standard deviation of the volumes are listed, as well as the p-value and corresponding FDR value. "- " FDR <10%, " * " FDR < 5%, " ** " FDR <1%.

Posterior Cortical	Hippocampal	Anterior Cortical	Subcortical	Midbrain	Brainstem & Cerebellum
Cingulate cortex: area 29a	Cingulate cortex: area 24a	Primary somatosensory cortex	Claustrum	olfactory bulbs	cerebellar peduncle: inferior
Cingulate cortex: area 29b	Cingulate cortex: area 24a'	Primary somatosensory cortex: barrel field	Piriform cortex	periaqueductal grey	cerebellar peduncle: middle
Cingulate cortex: area 29c	Ectorhinal cortex	Primary somatosensory cortex: dysgranular zone	Dorsal nucleus of the endopiriform	colliculus: inferior	cerebellar peduncle: superior
Cingulate cortex: area 30	Perirhinal cortex	Primary somatosensory cortex: forelimb region	Claustrum: ventral part	colliculus: superior	pontine nucleus
Medial parietal association cortex	pre-para subiculum	Primary somatosensory cortex: hindlimb region	Claustrum: dorsal part	Amygdalopiriform transition area	superior olivary complex
Primary visual cortex: binocular area	Caudomedial entorhinal cortex	Primary somatosensory cortex: jaw region	Insular region: not subdivided	Posterolateral cortical amygdaloid area	pons
Primary visual cortex: monocular area	stratum granulosum of hippocampus	Primary somatosensory cortex: shoulder region	Dorsal tenia tecta	Posteromedial cortical amygdaloid area	cuneate nucleus
Secondary visual cortex: lateral area	Medial entorhinal cortex	Primary somatosensory cortex: upper lip region	amygdala	Rostral amygdalopiriform area	inferior olivary complex
Secondary visual cortex: mediolateral area	Ventral intermediate entorhinal cortex	Frontal cortex: area 3	Ventral nucleus of the endopiriform claustrum	lateral olfactory tract	medulla
Secondary visual cortex: mediomedial area	Cortex-amygdala transition zones	Secondary motor cortex	Intermediate nucleus of the endopiriform claustrum		lobules 1-2: lingula and central lobule (ventral)
Temporal association area	lateral septum	Cingulate cortex: area 24b	nucleus accumbens		lobule 3: central lobule (dorsal)
Primary visual cortex	dentate gyrus of hippocampus	Cingulate cortex: area 24b'	bed nucleus of stria terminalis		lobules 4-5: culmen (ventral and dorsal)
Lateral parietal association cortex	hippocampus	Primary motor cortex	medial septum		lobule 6: declive
Primary auditory cortex		Secondary somatosensory cortex	basal forebrain		lobule 7: tuber (or folium)
Secondary auditory cortex: dorsal area		Dorsolateral orbital cortex	thalamus		lobule 8: pyramis
Secondary auditory cortex: ventral area		Lateral orbital cortex	globus pallidus		lobule 9: uvula
Primary somatosensory cortex: trunk region		Frontal association cortex	hypothalamus		lobule 10: nodulus
Dorsal intermediate entorhinal cortex		Cingulate cortex: area 32	midbrain		anterior lobule (lobules 4-5)
Dorsolateral entorhinal cortex		Cingulate cortex: area 25	mammillary bodies		simple lobule (lobule 6)
		Medial orbital cortex	olfactory tubercle		crus 1: ansiform lobule (lobule 6)
		Ventral orbital cortex	interpedunclar nucleus		crus 2: ansiform lobule (lobule 7)
		anterior commissure: pars anterior	Ventral tenia tecta		paramedian lobule (lobule 7)
		anterior commissure: pars posterior	subependymale zone / rhinocele		copula: pyramis (lobule 8)
		corpus callosum	cerebral aqueduct		flocculus (FL)
			cerebral peduncle		paraflocculus (PFL)
			Cingulum		trunk of arbor vita
			fasciculus retroflexus		lobule 1-2 white matter
			fimbria		lobule 3 white matter
*Colors correspond to clusters defined in Pagani et al; NeuroImage, 2016			fornix		trunk of lobules 1-3 white matter
			fundus of striatum		lobules 4-5 white matter
			internal capsule		lobules 6-7 white matter
			stria medullaris		lobule 8 white matter
			stria terminalis		trunk of lobules 6-8 white matter
			striatum		lobule 9 white matter
			mammilothalamic tract		lobule 10 white matter
			ventral tegmental decussation		anterior lobule white matter
			lateral ventricle		simple lobule white matter
			optic tract		crus 1 white matter
			posterior commissure		trunk of simple and crus 1 white matter
			third ventricle		crus 2 white matter
					paramedian lobule
					trunk of crus 2 and paramedian white matter
					copula white matter
					paraflocculus white matter
					flocculus white matter
					dentate nucleus
					nucleus interpositus
					fastigial nucleus
					corticospinal tract/pyramids
					facial nerve (cranial nerve 7)
					fourth ventricle
					medial lemniscus/medial longitudinal fasciculus

Supplemental Table 2. Regions classification by cluster. For structural covariance analysis, regions were binned by broad anatomical classification as described in Pagani et al, 2016. Columns represent individual clusters with brain regions listed below. Color coding performed for visualization purposes.

		Front Approach		Nose-to-Nose Sniffing		Nose-to-Anogenital Sniffing		Push-Crawl		Self-Grooming		Exploration of Arena		Following	
Regions		Males	Females	Males	Females	Males	Females	Males	Females	Males	Females	Males	Females	Males	Females
Amygdala	Pearson Correlation	0.216	-0.180	-0.096	0.297	-0.410	0.433	0.075	0.108	0.419	0.449	-0.257	-0.207	-0.009	0.264
	Sig. (2-tailed)	0.524	0.596	0.778	0.376	0.210	0.183	0.825	0.753	0.200	0.166	0.446	0.541	0.978	0.432
Anterior Commissure: Pars Anterior	Pearson Correlation	-0.170	-0.330	-0.288	0.280	-0.373	**.646***	0.440	**.626***	0.260	-0.098	-0.113	-0.357	-0.065	0.499
	Sig. (2-tailed)	0.617	0.321	0.391	0.405	0.258	**0.032**	0.175	**0.040**	0.441	0.773	0.740	0.281	0.850	0.118
Anterior Commissure: Pars Posterior	Pearson Correlation	0.191	-0.180	-0.155	0.380	-0.375	0.330	0.103	0.456	0.485	0.224	-0.387	-0.350	0.000	0.403
	Sig. (2-tailed)	0.574	0.597	0.649	0.249	0.256	0.322	0.764	0.159	0.130	0.508	0.240	0.291	1.000	0.219
Basal Forebrain	Pearson Correlation	-0.319	-0.381	-0.286	0.106	**-.629***	0.593	0.103	0.507	0.317	0.036	-0.161	-0.294	-0.260	**.747****
	Sig. (2-tailed)	*0.339*	0.248	0.394	0.756	**0.038**	0.054	0.764	0.112	0.342	0.917	0.636	0.380	0.440	**0.008**
Bed Nucleus Of Stria Terminalis	Pearson Correlation	**-.667***	-0.097	-0.449	0.429	**-.614***	**.762****	0.148	0.405	0.085	0.362	-0.104	0.016	-0.261	0.575
	Sig. (2-tailed)	**0.025**	0.777	0.166	0.188	**0.044**	**0.006**	0.665	0.217	0.803	0.274	0.761	0.964	0.439	0.064
Corpus Callosum	Pearson Correlation	0.216	-0.370	-0.276	0.209	0.254	**.730***	0.560	0.579	0.293	0.120	**-.639***	-0.264	0.121	0.569
	Sig. (2-tailed)	0.524	*0.262*	0.411	0.537	0.452	**0.011**	0.073	0.062	0.382	0.725	**0.034**	0.433	*0.722*	0.068
Fundus Of Striatum	Pearson Correlation	0.011	-0.177	-0.088	0.357	**-.644***	0.093	-0.091	0.045	0.263	0.433	-0.380	-0.419	-0.306	0.000
	Sig. (2-tailed)	0.974	0.602	0.797	0.282	**0.032**	0.785	0.791	0.895	0.435	0.183	0.249	0.199	0.359	1.000
Internal Capsule	Pearson Correlation	-0.243	-0.134	0.028	0.585	-0.137	**.873****	0.536	0.511	0.056	0.221	-0.241	-0.198	0.000	**.623***
	Sig. (2-tailed)	0.471	*0.695*	0.936	0.058	0.689	**0.000**	0.089	0.108	0.871	0.515	0.475	0.560	1.000	**0.041**
Mammilothalamic Tract	Pearson Correlation	-0.396	-0.445	-0.508	-0.065	-0.280	**.695***	0.247	0.203	0.378	-0.102	-0.151	-0.408	0.261	0.369
	Sig. (2-tailed)	0.228	0.170	0.111	0.850	0.405	**0.018**	0.464	0.550	0.251	0.765	0.657	0.213	0.438	0.264
Nucleus Accumbens	Pearson Correlation	-0.175	-0.184	-0.396	0.450	-0.535	**.694***	0.036	0.271	0.478	0.597	-0.254	0.044	-0.258	**.631***
	Sig. (2-tailed)	0.607	0.589	0.228	0.165	0.090	**0.018**	0.917	0.421	0.137	0.053	0.451	0.898	0.444	**0.037**
Olfactory Tubercle	Pearson Correlation	0.510	-0.301	-0.162	0.059	-0.323	0.192	-0.129	0.231	0.472	0.031	-0.051	-0.519	-0.170	0.321
	Sig. (2-tailed)	0.109	0.368	0.635	0.863	0.333	0.572	0.706	0.494	0.142	0.929	0.881	0.102	0.616	0.336
Pre-para Subiculum	Pearson Correlation	-0.211	0.256	-0.291	0.508	-0.189	0.411	0.016	0.387	0.124	-0.062	-0.471	0.091	-0.095	0.364
	Sig. (2-tailed)	0.533	0.447	*0.386*	0.111	0.578	0.209	0.962	0.240	0.716	0.857	0.144	0.791	0.781	0.271
Stratum Granulosum of Hippocampus	Pearson Correlation	-0.292	-0.502	0.306	0.155	-0.015	**.745****	0.212	**.709***	**-.685***	0.109	-0.241	-0.369	-0.025	**.742****
	Sig. (2-tailed)	0.383	0.115	0.359	0.650	0.964	***0.008***	0.532	**0.015**	**0.020**	0.751	0.476	0.264	0.941	**0.009**
Paraflocculus	Pearson Correlation	-0.066	0.199	0.270	**.621***	0.274	**.622***	0.231	0.354	-0.018	0.351	-0.363	0.371	-0.288	**.653***
	Sig. (2-tailed)	0.847	0.558	0.423	**0.041**	0.415	**0.041**	0.495	0.286	0.959	0.289	*0.273*	0.261	0.391	**0.029**
paraflocculus White Matter	Pearson Correlation	0.092	-0.033	**.642***	0.124	0.130	0.331	0.120	-0.007	-0.163	-0.076	0.140	0.172	-0.045	0.168
	Sig. (2-tailed)	0.787	0.924	**0.033**	0.717	0.704	0.320	0.725	0.984	0.632	0.824	0.680	0.614	0.896	0.622
Cingulate Cortex: area 25	Pearson Correlation	-0.082	-0.259	-0.460	0.211	-0.484	0.099	-0.066	-0.115	0.563	0.044	-0.111	-0.512	-0.319	-0.100
	Sig. (2-tailed)	0.810	0.442	0.155	0.534	0.132	0.772	0.847	0.735	0.072	0.898	0.745	0.107	0.339	0.770
Cingulate Cortex: area 30	Pearson Correlation	**-.609***	-0.139	0.034	0.069	-0.128	0.433	0.176	0.250	-0.294	0.091	**.617***	0.069	0.036	0.244
	Sig. (2-tailed)	**0.047**	0.683	0.921	0.840	0.708	0.183	0.605	0.458	0.381	0.791	**0.043**	0.841	0.917	0.470
Primary Auditory Cortex	Pearson Correlation	-0.187	-0.150	0.136	0.239	0.126	0.564	-0.070	**.755****	0.378	-0.285	-0.328	-0.279	-0.472	0.574
	Sig. (2-tailed)	0.583	0.659	0.689	0.479	0.713	0.071	0.837	**0.007**	0.252	0.396	0.325	0.407	0.143	0.065
Secondary Auditory Cortex: dorsal Area	Pearson Correlation	-0.486	-0.109	-0.096	0.063	0.055	0.520	-0.294	**.677***	0.183	-0.336	-0.279	-0.074	-0.512	**.602***
	Sig. (2-tailed)	0.130	0.749	0.778	0.855	0.871	0.101	0.380	**0.022**	0.591	0.312	0.405	0.828	0.107	**0.050**
Secondary Auditory Cortex: ventra lArea	Pearson Correlation	0.076	-0.277	0.372	0.382	-0.027	0.587	0.253	0.440	0.364	0.225	-0.275	-0.337	-0.326	0.400
	Sig. (2-tailed)	0.825	0.410	0.260	0.246	0.937	0.058	0.454	0.175	0.271	*0.506*	0.414	0.310	0.329	0.223
Caudomedial Entorhinal Cortex	Pearson Correlation	0.428	0.105	-0.085	**.665***	0.529	0.554	0.144	**.679***	-0.381	0.164	-0.221	0.038	0.481	**.734***
	Sig. (2-tailed)	0.189	0.758	0.804	**0.026**	0.094	0.077	0.673	**0.022**	0.247	0.629	0.513	0.911	0.134	**0.010**
Cortex-amygdala Transition Zones	Pearson Correlation	0.440	-0.151	0.314	0.024	-0.399	-0.158	-0.132	-0.120	-0.027	0.204	-0.223	-0.403	-0.268	-0.049
	Sig. (2-tailed)	0.176	0.657	0.347	0.943	0.225	0.643	0.699	0.725	0.938	0.547	0.509	0.219	0.426	0.887
Dorsal Intermediate Entorhinal Cortex	Pearson Correlation	0.325	-0.293	0.178	0.311	0.181	0.496	0.536	0.460	0.010	0.460	0.137	-0.264	**.721***	0.422
	Sig. (2-tailed)	0.329	0.383	0.601	0.352	0.594	0.120	0.089	0.154	0.977	0.154	0.688	0.433	**0.012**	0.196
Dorsolateral Orbital Cortex	Pearson Correlation	0.354	-0.357	-0.174	0.053	-0.102	0.276	-0.188	0.168	-0.029	0.368	0.043	-0.357	0.269	0.118
	Sig. (2-tailed)	0.285	0.281	0.609	0.878	0.765	0.411	0.580	0.621	0.931	0.266	0.901	0.281	0.424	0.731

Intermediate Nucleus of the Endopiriform Claustrum	Pearson Correlation	0.293	-0.204	-0.148	0.280	-0.373	0.181	-0.146	0.269	**.658***	0.178	-0.227	-0.421	-0.280	0.262
	Sig. (2-tailed)	0.382	0.548	0.664	0.405	0.258	0.595	0.669	0.425	**0.028**	0.600	0.503	0.197	0.404	0.436
Lateral Orbital Cortex	Pearson Correlation	0.389	-0.146	-0.318	0.199	-0.240	0.303	-0.185	0.335	0.259	0.143	0.086	-0.357	0.056	0.114
	Sig. (2-tailed)	0.237	0.669	0.341	0.557	0.478	0.365	0.586	0.314	0.442	0.674	0.802	0.280	0.870	0.738
Lateral Parietal Association Cortex	Pearson Correlation	0.115	0.000	-0.177	0.294	-0.194	0.507	-0.247	0.230	0.257	0.083	0.246	-0.072	-0.261	0.254
	Sig. (2-tailed)	0.736	*1.000*	0.602	0.380	0.568	0.112	0.464	0.497	0.446	0.808	0.466	0.833	0.438	0.452
Medial Orbital Cortex	Pearson Correlation	0.309	0.056	0.033	0.152	-0.226	0.149	0.195	0.592	*-0.356*	-0.138	0.309	-0.246	0.166	0.178
	Sig. (2-tailed)	0.355	0.871	0.924	0.654	0.504	0.663	*0.565*	0.055	*0.282*	0.686	0.354	0.466	0.626	0.600
Medial Parietal Association Cortex	Pearson Correlation	-0.300	-0.123	0.118	0.035	-0.421	0.485	-0.200	0.219	-0.033	0.135	0.367	0.006	-0.542	0.280
	Sig. (2-tailed)	0.370	0.718	0.729	0.918	0.197	0.130	0.556	0.517	0.922	0.693	0.267	0.986	0.085	0.404
Parietal Cortex: Posterior Area: rostral Part	Pearson Correlation	0.115	0.152	-0.177	0.265	-0.194	0.548	-0.247	0.007	0.257	0.135	0.246	0.234	-0.261	0.335
	Sig. (2-tailed)	0.736	0.656	*0.602*	0.431	0.568	0.081	0.464	0.984	*0.446*	0.693	0.466	0.488	0.438	0.314
Primary Somatosensory Cortex: shoulder Region	Pearson Correlation	**-.603***	-0.169	-0.441	-0.133	-0.508	0.229	-0.162	-0.262	-0.094	-0.255	0.068	-0.288	-0.391	-0.187
	Sig. (2-tailed)	**0.049**	0.619	*0.175*	0.697	0.111	0.498	0.634	0.437	0.784	0.449	0.843	0.390	0.235	0.582
Primary Somatosensory Cortex: trunk Region	Pearson Correlation	-0.509	-0.176	-0.372	0.042	-0.321	0.511	-0.034	0.136	-0.198	-0.073	0.000	-0.245	-0.124	0.209
	Sig. (2-tailed)	0.110	0.605	0.260	0.902	0.336	0.108	0.921	0.689	0.559	0.831	1.000	0.468	0.717	0.537
Temporal Association Area	Pearson Correlation	0.473	-0.269	0.307	0.378	0.419	0.516	0.515	0.405	0.228	0.332	-0.295	-0.304	0.131	0.280
	Sig. (2-tailed)	*0.142*	0.424	0.359	0.252	0.200	0.104	0.105	0.217	*0.499*	0.319	0.379	0.363	0.700	0.405
Primary Visual Cortex	Pearson Correlation	-0.432	-0.116	0.162	0.271	0.340	0.436	0.287	0.166	-0.475	0.291	0.109	0.067	0.136	0.149
	Sig. (2-tailed)	0.184	0.734	0.635	0.420	0.306	0.180	0.391	0.625	0.140	0.386	0.750	0.845	0.691	0.663
Primary Visual Cortex: binocular Area	Pearson Correlation	-0.421	-0.130	-0.081	0.129	0.180	0.357	-0.142	0.267	0.148	-0.044	-0.274	-0.109	-0.069	0.187
	Sig. (2-tailed)	0.197	0.703	0.812	0.706	0.596	0.281	0.678	0.427	0.665	0.899	0.414	0.749	0.841	0.581
Primary Visual Cortex: monocular Area	Pearson Correlation	**-.655***	0.040	-0.259	0.167	0.031	0.404	0.032	0.369	-0.064	-0.156	0.157	0.008	0.266	0.233
	Sig. (2-tailed)	**0.029**	0.906	*0.442*	0.624	0.928	0.218	0.925	0.264	*0.851*	0.647	0.644	0.981	0.430	0.490
Secondary Visual Cortex: lateral Area	Pearson Correlation	-0.010	-0.097	-0.044	0.263	0.511	0.447	0.053	0.417	0.236	0.109	-0.342	-0.026	-0.013	0.317
	Sig. (2-tailed)	0.976	0.777	0.898	0.435	0.108	0.168	0.878	0.202	*0.484*	0.749	0.304	0.940	0.969	0.342
Secondary Visual Cortex: mediolateral Area	Pearson Correlation	**-.796****	0.044	-0.135	0.170	-0.046	0.497	0.168	0.482	-0.286	-0.136	0.459	0.047	0.231	0.355
	Sig. (2-tailed)	**0.003**	0.898	0.692	0.616	0.893	0.120	0.622	0.134	0.394	0.690	0.156	0.892	0.495	0.283
Secondary Visual Cortex: mediomedial Area	Pearson Correlation	**-.657***	-0.145	0.231	0.141	0.169	0.589	0.312	0.480	-0.593	0.001	0.330	0.063	0.237	0.407
	Sig. (2-tailed)	**0.028**	0.670	0.495	0.679	0.619	0.056	0.350	0.135	0.055	*0.998*	0.321	0.855	0.483	0.215
Brain volumes	Pearson Correlation	-0.462	-0.442	0.209	0.210	-0.024	**.790****	0.465	0.510	-0.453	0.301	0.020	-0.231	-0.176	**.674***
	Sig. (2-tailed)	0.153	0.174	0.536	0.535	0.944	**0.004**	0.149	0.109	0.162	0.368	0.953	0.495	0.604	**0.023**

Supplemental Table 3. Correlations between absolute volumes and JRSI behavior. Correlations between previously reported behavioral phenotypes and the 40 MRI-based absolute volumes found to be significantly different between treatment groups were conducted between Full Group (both males and females), males only, and females only; irrespective of treatment group. "* " $p<0.05$, " ** " $p<0.01$.

		Ultrasonic vocalizations											
Regions		Min1		Min2		Min3		Min4		Min5		Sum	
		Ctrl	MAR-ASD	Ctrl	MAR-ASD	Ctrl	MAR-ASD	Ctrl	MAR-ASD	Ctrl	MAR-ASD	Ctrl	MAR-ASD
amygdala	Pearson Correlation	0.338	0.124	-0.102	-0.215	0.146	-0.569	0.431	-0.458	0.626	-0.093	0.352	-0.273
Anterior Commissure: Pars Anterior	Pearson Correlation	-0.612	0.459	-0.533	0.076	-0.630	-0.116	-0.301	-0.184	-0.243	-0.112	-0.592	0.082
Anterior Commissure: Pars Posterior	Pearson Correlation	0.005	0.105	0.149	-0.132	0.259	-0.435	**.765****	-0.436	0.551	-0.080	0.442	-0.218
Basal Forebrain	Pearson Correlation	0.175	0.512	-0.023	-0.005	-0.094	-0.167	0.258	-0.009	0.331	0.224	0.139	0.171
Bed Nucleus Of Stria Terminalis	Pearson Correlation	0.275	**.655***	0.077	-0.008	-0.209	-0.045	0.086	0.104	0.174	0.204	0.061	0.267
Corpus Callosum	Pearson Correlation	0.094	0.041	0.040	-0.153	-0.239	-0.178	0.294	-0.451	0.172	-0.471	0.054	-0.269
Fundus Of Striatum	Pearson Correlation	0.145	0.326	0.317	-0.043	0.346	-0.309	**.721***	-0.238	0.526	0.150	0.521	0.000
Internal Capsule	Pearson Correlation	-0.228	**.663***	-0.389	-0.017	-0.607	0.105	-0.361	0.040	-0.159	-0.092	-0.469	0.226
Mammilothalamic Tract	Pearson Correlation	-0.101	0.215	-0.604	-0.175	-0.552	-0.310	-0.140	-0.179	0.309	0.069	-0.304	-0.078
Nucleus Accumbens	Pearson Correlation	0.236	0.222	0.093	-0.098	0.047	-0.294	0.444	-0.208	0.404	0.103	0.288	-0.049
Olfactory Tubercle	Pearson Correlation	0.071	-0.358	-0.131	0.020	0.042	-0.472	-0.272	-0.506	0.120	-0.093	-0.032	-0.351
Pre-para Subiculum	Pearson Correlation	0.139	0.280	0.107	-0.561	-0.285	-0.559	0.164	-0.377	0.036	-0.339	-0.003	-0.351
Stratum Granulosum Of Hippocampus	Pearson Correlation	0.351	**.629***	-0.159	0.147	-0.387	0.380	-0.262	0.238	0.103	0.006	-0.138	0.390
Paraflocculus	Pearson Correlation	-0.587	-0.047	-0.408	-0.261	-0.261	0.271	-0.182	0.128	-0.293	0.201	-0.415	0.036
Paraflocculus White Matter	Pearson Correlation	-0.278	-0.112	0.130	-0.190	-0.011	0.127	0.344	0.167	-0.047	0.442	0.038	0.061
Cingulate Cortex: area 25	Pearson Correlation	-0.009	0.294	0.332	0.075	-0.281	-0.181	-0.118	-0.135	-0.236	-0.212	-0.113	0.006
Cingulate Cortex: area 30	Pearson Correlation	0.062	0.306	0.095	0.043	-0.310	0.237	0.092	0.549	-0.090	0.580	-0.078	0.407
Primary Auditory Cortex	Pearson Correlation	0.322	-0.080	0.308	-0.363	0.125	0.257	0.283	0.193	0.051	0.158	0.253	-0.001
Secondary Auditory Cortex: dorsal Area	Pearson Correlation	0.449	0.060	0.368	-0.371	0.083	0.260	0.162	0.334	0.040	0.115	0.247	0.068
Secondary Auditory Cortex: ventral Area	Pearson Correlation	0.216	0.125	-0.027	-0.288	0.016	0.073	0.430	-0.005	0.304	0.131	0.217	-0.004
Caudomedial Entorhinal Cortex	Pearson Correlation	0.302	-0.287	0.133	0.305	-0.235	0.050	-0.217	-0.080	-0.127	-0.158	-0.076	-0.043
Cingulum	Pearson Correlation	0.160	-0.094	0.304	0.026	0.062	**-.646***	0.573	**-.612***	0.314	-0.310	0.333	-0.369
Cortex-amygdala Transition Zones	Pearson Correlation	0.425	-0.010	0.211	0.154	**.679***	-0.156	0.525	-0.227	0.542	0.230	0.628	0.000
Dorsal Intermediate Entorhinal Cortex	Pearson Correlation	0.117	-0.091	-0.090	0.054	-0.280	-0.257	0.035	-0.267	0.095	0.046	-0.064	-0.124
Dorsolateral Orbital Cortex	Pearson Correlation	-0.080	-0.448	0.330	-0.213	0.018	**-.718***	0.275	**-.688***	-0.063	-0.335	0.112	-0.594
Intermediate Nucleus Of The Endopiriform Claustrum	Pearson Correlation	0.100	-0.025	0.087	0.054	0.233	-0.214	0.573	-0.151	0.517	0.086	0.384	-0.058
Lateral Orbital Cortex	Pearson Correlation	0.060	-0.432	0.370	0.030	0.255	-0.549	0.567	-0.466	0.281	-0.053	0.387	-0.373
Medial Orbital Cortex	Pearson Correlation	-0.119	-0.079	0.344	0.451	0.157	-0.110	0.402	-0.210	0.095	0.151	0.227	0.063
Medial Parietal Association Cortex	Pearson Correlation	0.216	0.457	0.184	0.317	-0.213	0.416	0.107	**.628***	-0.021	0.468	0.028	0.573
Parietal Cortex: Posterior Area: rostral Part	Pearson Correlation	0.216	0.189	0.184	0.420	-0.213	0.187	0.107	0.329	-0.021	-0.020	0.028	0.300
Primary Somatosensory Cortex: shoulder Region	Pearson Correlation	0.458	0.537	0.119	0.231	-0.111	0.203	-0.047	0.291	0.228	0.093	0.125	0.375
Primary Somatosensory Cortex: trunk Region	Pearson Correlation	0.440	**.706***	0.042	0.279	-0.241	0.197	-0.125	0.430	0.104	0.099	0.008	0.477
Temporal Association Area	Pearson Correlation	0.266	-0.203	-0.044	-0.177	-0.040	-0.047	0.251	-0.235	0.222	-0.109	0.141	-0.205
Primary Visual Cortex	Pearson Correlation	0.217	0.165	-0.081	-0.423	-0.341	0.034	-0.033	0.129	0.096	-0.048	-0.079	-0.042
Primary Visual Cortex: binocular Area	Pearson Correlation	0.407	0.025	0.282	**-.704***	0.020	-0.198	0.250	0.018	0.176	-0.114	0.252	-0.261
Primary Visual Cortex: monocular Area	Pearson Correlation	0.351	0.120	0.264	-0.496	-0.056	-0.248	0.272	0.108	0.143	0.135	0.206	-0.110
Secondary Visual Cortex: lateral Area	Pearson Correlation	0.391	-0.332	0.222	**-.717***	0.042	-0.263	0.302	-0.224	0.209	-0.345	0.263	-0.498
Secondary Visual Cortex: mediolateral Area	Pearson Correlation	0.236	0.365	0.184	-0.199	-0.197	0.065	0.021	0.430	-0.084	0.365	0.001	0.247
Secondary Visual Cortex: mediomedial Area	Pearson Correlation	0.127	0.396	0.058	-0.142	-0.314	0.296	-0.064	0.494	-0.068	0.387	-0.105	0.344
Brain volumes	Pearson Correlation	0.155	**.641***	-0.027	0.182	-0.376	0.537	-0.084	0.520	-0.058	0.378	-0.142	0.577

		Front Approach		Nose-to-nose sniff				Nose-to-anogenital sniff				Body sniff			
Regions		Bouts		Bouts		Time		Bouts		Time		Bouts		Time	
		Ctrl	MAR-ASD	Ctrl	MAR-ASD	Ctrl	MAR-ASD	Ctrl	MAR-ASD	Ctrl	MAR-ASD	Ctrl	MAR-ASD	Ctrl	MAR-ASD
amygdala	Pearson Correlation	-0.067	-0.279	0.039	-0.297	-0.001	0.054	-0.452	-0.538	-0.364	-0.403	-0.290	-0.398	-0.522	-0.442
Anterior Commissure: Pars Anterior	Pearson Correlation	0.073	0.025	-0.016	0.289	0.297	0.350	0.214	0.175	0.210	0.105	0.159	0.226	-0.047	0.042
Anterior Commissure: Pars Posterior	Pearson Correlation	-0.317	-0.297	-0.030	-0.255	0.063	0.008	-0.329	-0.478	-0.288	-0.335	-0.200	-0.368	-0.074	-0.410
Basal Forebrain	Pearson Correlation	-0.360	-0.392	-0.236	-0.002	-0.177	0.385	-0.562	0.038	-0.593	0.044	-0.466	0.140	**-.666***	0.143
Bed Nucleus Of Stria Terminalis	Pearson Correlation	-0.611	-0.386	-0.296	0.353	-0.357	**.654***	-0.625	0.326	**-.797****	0.200	-0.551	0.495	**-.691***	0.481
Corpus Callosum	Pearson Correlation	**-.751***	-0.258	-0.616	-0.258	-0.414	-0.166	**-.698***	-0.107	**-.728***	-0.146	**-.639***	-0.070	**-.692***	-0.348
Fundus Of Striatum	Pearson Correlation	-0.401	-0.474	-0.013	-0.177	-0.084	0.173	-0.411	-0.386	-0.406	-0.306	-0.213	-0.209	-0.040	-0.203
Internal Capsule	Pearson Correlation	-0.199	0.228	-0.107	0.356	0.074	0.363	-0.109	0.228	-0.297	0.196	-0.280	0.292	-0.508	0.129
Mammilothalamic Tract	Pearson Correlation	-0.320	-0.418	0.016	-0.012	0.211	0.280	-0.145	-0.032	-0.241	0.068	-0.190	0.039	-0.360	0.101
Nucleus Accumbens	Pearson Correlation	-0.413	-0.535	-0.338	-0.177	-0.397	0.247	**-.733***	-0.115	-0.564	-0.119	-0.432	0.052	-0.568	0.029
Olfactory Tubercle	Pearson Correlation	0.389	-0.316	**.653***	-0.482	0.543	-0.269	0.364	-0.474	0.021	-0.413	0.059	-0.442	-0.016	-0.518
Pre-para Subiculum	Pearson Correlation	**-.726***	-0.407	**-.678***	-0.017	**-.656***	0.425	**-.805****	-0.341	**-.727***	-0.448	-0.487	0.029	**-.675***	-0.058
Stratum Granulosum Of Hippocampus	Pearson Correlation	-0.519	0.264	-0.375	**.623***	-0.492	0.305	-0.599	0.229	-0.598	0.159	-0.312	0.281	-0.626	0.212
Paraflocculus	Pearson Correlation	0.557	-0.513	0.251	-0.527	0.598	-0.179	0.564	0.038	0.516	0.039	0.096	0.357	0.071	0.279
Paraflocculus White Matter	Pearson Correlation	-0.252	-0.192	-0.287	-0.513	-0.034	-0.251	-0.197	-0.201	-0.215	0.015	-0.418	0.038	-0.214	0.106
Cingulate Cortex: area 25	Pearson Correlation	-0.606	0.128	-0.111	0.304	-0.375	0.392	-0.398	0.123	**-.719***	-0.051	-0.210	0.100	-0.264	-0.001
Cingulate Cortex: area 30	Pearson Correlation	**-.671***	-0.158	**-.712***	0.034	-0.597	0.278	**-.721***	0.542	**-.689***	0.569	-0.608	0.526	**-.723***	**.671***
Primary Auditory Cortex	Pearson Correlation	-0.328	-0.291	-0.539	-0.311	-0.619	0.066	**-.762***	0.065	-0.616	-0.010	**-.701***	0.467	**-.766****	0.456
Secondary Auditory Cortex: dorsal Area	Pearson Correlation	-0.485	-0.308	-0.555	-0.013	**-.729***	0.336	**-.834****	0.245	**-.770****	0.035	**-.692***	**.612***	**-.781****	**.668***
Secondary Auditory Cortex: ventral Area	Pearson Correlation	-0.305	-0.108	-0.604	-0.354	-0.392	0.000	**-.725***	-0.142	-0.482	-0.080	**-.702***	0.209	**-.845****	0.103
Caudomedial Entorhinal Cortex	Pearson Correlation	-0.530	-0.271	-0.543	-0.491	**-.693***	**-.726***	**-.662***	-0.077	-0.619	0.053	-0.417	**-.607***	-0.586	-0.597
Cingulum	Pearson Correlation	**-.818****	-0.325	-0.511	-0.049	-0.435	0.009	**-.692***	-0.431	**-.705***	-0.390	-0.530	-0.533	-0.378	-0.558
Cortex-amygdala Transition Zones	Pearson Correlation	0.146	-0.377	0.156	-0.449	0.343	-0.299	0.063	-0.514	-0.063	-0.343	-0.454	-0.455	-0.135	-0.459
Dorsal Intermediate Entorhinal Cortex	Pearson Correlation	-0.317	0.044	-0.336	-0.359	-0.438	-0.417	**-.652***	-0.316	-0.514	0.056	-0.371	-0.548	**-.670***	-0.531
Dorsolateral Orbital Cortex	Pearson Correlation	-0.239	-0.182	-0.114	-0.106	-0.412	-0.106	-0.445	**-.658***	-0.331	-0.599	-0.045	-0.518	-0.094	-0.541
Intermediate Nucleus Of The Endopiriform Claustrum	Pearson Correlation	-0.210	-0.288	0.034	-0.486	0.118	-0.161	-0.337	-0.272	-0.385	-0.181	-0.443	-0.348	-0.331	-0.331
Lateral Orbital Cortex	Pearson Correlation	-0.271	-0.474	-0.048	-0.513	-0.267	-0.303	-0.473	-0.433	-0.373	-0.348	-0.105	-0.518	-0.079	-0.504
Medial Orbital Cortex	Pearson Correlation	-0.133	-0.149	0.071	-0.120	-0.195	-0.304	-0.290	-0.074	-0.201	0.039	0.153	-0.306	0.126	-0.366
Medial Parietal Association Cortex	Pearson Correlation	**-.762***	0.134	**-.667***	0.163	-0.562	0.287	**-.707***	0.533	**-.810****	0.415	**-.725***	0.405	**-.747***	0.482
Parietal Cortex: Posterior Area: rostral Part	Pearson Correlation	**-.762***	0.418	**-.667***	0.142	-0.562	0.022	**-.707***	0.384	**-.810****	0.252	**-.725***	-0.082	**-.747***	-0.063
Primary Somatosensory Cortex: shoulder Region	Pearson Correlation	**-.808****	0.000	-0.430	**.683***	-0.368	**.644***	-0.540	0.554	**-.793****	0.272	-0.603	0.552	-0.539	0.550
Primary Somatosensory Cortex: trunk Region	Pearson Correlation	**-.739***	0.000	-0.567	0.432	-0.561	0.439	**-.704***	0.542	**-.814****	0.385	**-.692***	0.233	**-.770****	0.293
Temporal Association Area	Pearson Correlation	-0.309	-0.166	-0.602	**-.713***	-0.440	-0.518	**-.720***	-0.252	-0.511	-0.089	**-.741***	-0.211	**-.882****	-0.383
Primary Visual Cortex	Pearson Correlation	**-.703***	-0.012	**-.639***	0.183	-0.526	0.308	**-.711***	0.201	**-.691***	0.102	**-.632***	0.523	**-.739***	0.468
Primary Visual Cortex: binocular Area	Pearson Correlation	**-.678***	-0.261	**-.640***	-0.059	**-.701***	0.369	**-.881****	-0.129	**-.809****	-0.211	**-.706***	0.315	**-.742***	0.381
Primary Visual Cortex: monocular Area	Pearson Correlation	**-.799****	-0.342	**-.765****	0.044	**-.739***	0.427	**-.899****	0.074	**-.826****	0.089	**-.704***	0.323	**-.736***	0.484
Secondary Visual Cortex: lateral Area	Pearson Correlation	-0.607	-0.303	**-.673***	-0.427	**-.648***	-0.024	**-.868****	-0.229	**-.754***	-0.319	**-.783****	0.169	**-.811****	0.083
Secondary Visual Cortex: mediolateral Area	Pearson Correlation	**-.689***	-0.120	**-.701***	0.257	-0.613	0.493	**-.708***	0.454	**-.762***	0.454	**-.746***	0.538	**-.768****	**.704***
Secondary Visual Cortex: mediomedial Area	Pearson Correlation	-0.628	-0.027	-0.548	0.226	-0.470	0.313	-0.614	0.431	**-.708***	0.471	-0.614	0.540	**-.705***	**.649***
Brain volumes	Pearson Correlation	-0.596	-0.112	**-.635***	0.135	-0.600	0.209	-.718*	**.606***	**-.664***	0.549	-0.553	0.601	**-.763***	0.535

		Self-grooming			Exploration of arena					Following			
Regions		Bouts		Time		Bouts		Time		Bouts		Time	
		Ctrl	MAR-ASD	Ctrl	MAR-ASD	Ctrl	MAR-ASD	Ctrl	MAR-ASD	Ctrl	MAR-ASD	Ctrl	MAR-ASD
amygdala	Pearson Correlation	0.067	0.075	-0.230	0.243	-0.083	-0.199	0.389	0.412	-0.565	-0.207	-0.560	-0.051
Anterior Commissure: Pars Anterior	Pearson Correlation	0.272	-0.288	0.294	-0.133	0.285	0.071	-0.264	-0.048	-0.247	0.106	-0.099	0.067
Anterior Commissure: Pars Posterior	Pearson Correlation	-0.106	-0.012	-0.367	0.218	-0.207	-0.194	0.282	0.336	-0.410	-0.076	**-.644***	0.086
Basal Forebrain	Pearson Correlation	-0.127	-0.266	-0.006	-0.193	-0.184	-0.117	0.583	-0.043	**-.881****	0.158	**-.757***	0.108
Bed Nucleus Of Stria Terminalis	Pearson Correlation	-0.196	-0.387	0.311	-0.422	-0.255	-0.019	**.743***	-0.199	**-.880****	0.121	**-.825****	-0.011
Corpus Callosum	Pearson Correlation	-0.173	-0.460	0.114	-0.087	-0.316	-0.483	**.729***	0.324	**-.879****	0.104	**-.821****	0.231
Fundus Of Striatum	Pearson Correlation	-0.218	-0.098	-0.297	-0.115	-0.399	-0.188	0.384	0.358	-0.449	-0.058	**-.670***	0.015
Internal Capsule	Pearson Correlation	0.065	-0.584	0.482	-0.230	0.128	-0.140	0.212	-0.153	**-.636***	0.123	-0.431	-0.059
Mammilothalamic Tract	Pearson Correlation	0.505	-0.144	0.453	0.176	0.136	-0.149	0.136	-0.178	-0.559	0.036	-0.482	0.138
Nucleus Accumbens	Pearson Correlation	-0.198	-0.103	-0.149	-0.060	-0.609	-0.107	0.604	0.099	**-.831****	0.117	**-.733***	0.168
Olfactory Tubercle	Pearson Correlation	0.050	0.433	0.144	0.287	0.441	0.085	-0.144	0.466	-0.083	-0.074	-0.023	0.187
Pre-para Subiculum	Pearson Correlation	-0.211	-0.214	0.198	-0.147	-0.484	-0.433	**.754***	0.474	**-.896****	-0.396	**-.766****	-0.391
Stratum Granulosum Of Hippocampus	Pearson Correlation	0.179	-0.548	0.482	-0.560	-0.220	-0.109	0.574	-0.003	**-.713***	-0.122	-0.478	-0.310
Paraflocculus	Pearson Correlation	0.016	-0.368	-0.081	-0.230	0.434	-0.322	-0.519	-0.065	0.273	0.249	0.302	0.163
Paraflocculus White Matter	Pearson Correlation	-0.426	0.074	-0.202	0.188	-0.377	-0.022	0.223	-0.149	-0.408	-0.006	-0.402	-0.034
Cingulate Cortex: area 25	Pearson Correlation	-0.443	-0.076	0.551	-0.107	-0.323	0.132	0.587	0.061	**-.774****	0.164	**-.795****	0.070
Cingulate Cortex: area 30	Pearson Correlation	-0.318	-0.097	0.183	-0.126	-0.492	0.139	**.718***	**-.685***	**-.864****	0.196	**-.685***	0.027
Primary Auditory Cortex	Pearson Correlation	-0.606	-0.214	-0.198	-0.089	**-.804****	-0.087	**.715***	-0.203	**-.728***	0.313	-0.524	0.098
Secondary Auditory Cortex: dorsal Area	Pearson Correlation	-0.560	-0.266	-0.016	-0.328	**-.780****	-0.117	**.835****	-0.220	**-.816****	0.225	-0.594	-0.061
Secondary Auditory Cortex: ventral Area	Pearson Correlation	-0.239	-0.226	-0.333	0.059	-0.489	-0.093	0.604	-0.053	**-.738***	0.187	-0.537	0.042
Caudomedial Entorhinal Cortex	Pearson Correlation	-0.209	-0.192	0.329	-0.101	-0.576	**-.628***	**.634***	0.300	**-.717***	0.091	-0.411	0.394
Cingulum	Pearson Correlation	-0.271	0.241	-0.062	0.193	-0.509	-0.108	**.699***	0.516	**-.713***	-0.270	**-.825****	0.062
Cortex-amygdala Transition Zones	Pearson Correlation	-0.129	0.125	-0.631	-0.036	0.212	-0.110	0.103	0.486	0.196	-0.086	0.065	0.090
Dorsal Intermediate Entorhinal Cortex	Pearson Correlation	-0.166	0.083	0.171	0.561	-0.558	-0.161	0.536	-0.037	**-.852****	-0.106	-0.629	0.172
Dorsolateral Orbital Cortex	Pearson Correlation	-0.498	**.631***	0.003	0.403	**-.751***	0.123	0.335	**.631***	-0.512	**-.667***	-0.548	-0.310
Intermediate Nucleus Of The Endopiriform Claustrum	Pearson Correlation	-0.226	0.039	-0.306	0.134	-0.307	-0.169	0.361	0.190	-0.597	0.277	**-.650***	0.353
Lateral Orbital Cortex	Pearson Correlation	-0.399	0.497	-0.238	0.290	-0.613	-0.016	0.378	0.437	-0.530	-0.169	**-.641***	0.178
Medial Orbital Cortex	Pearson Correlation	-0.369	0.249	-0.141	-0.004	-0.503	0.180	0.185	0.196	-0.408	-0.107	-0.512	0.168
Medial Parietal Association Cortex	Pearson Correlation	-0.338	-0.182	0.215	-0.424	-0.388	0.184	**.812****	-0.412	**-.828****	0.428	**-.712***	0.110
Parietal Cortex: Posterior Area: rostral Part	Pearson Correlation	-0.338	-0.064	0.215	-0.192	-0.388	0.048	**.812****	-0.136	**-.828****	0.414	**-.712***	0.253
Primary Somatosensory Cortex: shoulder Region	Pearson Correlation	0.036	-0.260	0.344	-0.583	-0.108	0.216	**.719***	-0.221	**-.697***	0.161	-0.563	-0.060
Primary Somatosensory Cortex: trunk Region	Pearson Correlation	-0.078	-0.540	0.374	**-.608***	-0.375	-0.273	**.791****	-0.205	**-.821****	0.254	-0.582	0.054
Temporal Association Area	Pearson Correlation	-0.246	-0.204	-0.209	0.222	-0.565	-0.388	0.619	0.146	**-.764***	0.159	-0.475	0.267
Primary Visual Cortex	Pearson Correlation	-0.042	-0.209	0.290	-0.155	-0.468	-0.084	**.691***	-0.176	**-.876****	-0.276	-0.615	-0.429
Primary Visual Cortex: binocular Area	Pearson Correlation	-0.384	-0.134	0.009	0.029	**-.753***	-0.282	**.854****	-0.018	**-.897****	-0.208	**-.696***	-0.363
Primary Visual Cortex: monocular Area	Pearson Correlation	-0.323	-0.027	0.042	0.118	**-.659***	-0.136	**.875****	-0.309	**-.883****	-0.223	**-.720***	-0.275
Secondary Visual Cortex: lateral Area	Pearson Correlation	-0.384	-0.061	-0.098	0.141	**-.741***	-0.371	**.825****	0.188	**-.867****	-0.166	**-.648***	-0.192
Secondary Visual Cortex: mediolateral Area	Pearson Correlation	-0.376	-0.152	0.189	-0.061	-0.504	0.037	**.783****	**-.632***	**-.814****	-0.022	-0.598	-0.192
Secondary Visual Cortex: mediomedial Area	Pearson Correlation	-0.262	-0.319	0.298	-0.188	-0.394	-0.050	**.688***	-0.574	**-.877****	-0.033	**-.651***	-0.229
Brain volumes	Pearson Correlation	-0.175	**-.691***	0.297	**-.608***	-0.495	-0.183	**.684***	-0.434	**-.880****	0.358	-0.607	0.106

Supplemental Table 3. Correlations between absolute volumes and MFSI behavior. Correlations between previously reported behavioral phenotypes and the 40 MRI-based absoluted volumes found to be significantly different between treatment groups; conducted only in males. "* " $p<0.05$, " ** " $p<0.01$.

Effect Sizes for Kruskal-Wallis Test

		PC vs PC				
Comparison	H (mean rank diff)	k (# of groups)	N (total values)		Effect Size	Bin
WT Female vs. WT Male	-162.3	4	1444		-0.11618056	Medium
WT Female vs. MAR Male	405.4	4	1444		0.278055556	Large
WT Female vs. MAR Female	39.75	4	1444		0.024131944	Small
WT Male vs. MAR Male	567.7	4	1444		0.390763889	Large
WT Male vs. MAR Female	202.1	4	1444		0.136875	Medium
MAR Male vs. MAR Female	-365.6	4	1444		-0.25736111	Large
		PC vs HIP				
WT Female vs. WT Male	-194.6	4	988		-0.20284553	Large
WT Female vs. MAR Male	260.3	4	988		0.25945122	Large
WT Female vs. MAR Female	0	4	988		-0.0050813	
WT Male vs. MAR Male	454.9	4	988		0.457215447	Large
WT Male vs. MAR Female	194.6	4	988		0.192682927	Large
MAR Male vs. MAR Female	-260.3	4	988		-0.26961382	Large
		PC vs AC				
WT Female vs. WT Male	225.4	4	1824		0.121098901	Medium
WT Female vs. MAR Male	661.4	4	1824		0.360659341	Large
WT Female vs. MAR Female	189.2	4	1824		0.101208791	Medium
WT Male vs. MAR Male	436	4	1824		0.236813187	Large
WT Male vs. MAR Female	-36.24	4	1824		-0.02265934	Small
MAR Male vs. MAR Female	-472.2	4	1824		-0.2621978	Large
		PC vs SC				
WT Female vs. WT Male	-153.6	4	3000		-0.05293725	Small
WT Female vs. MAR Male	859.2	4	3000		0.285113485	Large
WT Female vs. MAR Female	429.5	4	3000		0.141688919	Large
WT Male vs. MAR Male	1013	4	3000		0.336448598	Large
WT Male vs. MAR Female	583.1	4	3000		0.192957276	Large
MAR Male vs. MAR Female	-429.7	4	3000		-0.14509346	Large
		PC vs MB				
WT Female vs. WT Male	-53.98	4	675		-0.08789866	Medium
WT Female vs. MAR Male	174.7	4	675		0.25290611	Large
WT Female vs. MAR Female	142.5	4	675		0.204918033	Large
WT Male vs. MAR Male	228.7	4	675		0.33338301	Large
WT Male vs. MAR Female	196.5	4	675		0.285394933	Large
MAR Male vs. MAR Female	-32.18	4	675		-0.05540984	Small

		PC vs BCSB				
WT Female vs. WT Male	-288.2	4	3876		-0.07572314	Medium
WT Female vs. MAR Male	1086	4	3876		0.279183884	Large
WT Female vs. MAR Female	1256	4	3876		0.323088843	Large
WT Male vs. MAR Male	1374	4	3876		0.35356405	Large
WT Male vs. MAR Female	1544	4	3876		0.397469008	Large
MAR Male vs. MAR Female	169.8	4	3876		0.042561983	Small
		HIP vs HIP				
WT Female vs. WT Male	-28.5	4	676		-0.04985119	Small
WT Female vs. MAR Male	130.4	4	676		0.186607143	Large
WT Female vs. MAR Female	39.62	4	676		0.051517857	Small
WT Male vs. MAR Male	158.9	4	676		0.229017857	Large
WT Male vs. MAR Female	68.12	4	676		0.093928571	Medium
MAR Male vs. MAR Female	-90.79	4	676		-0.14254464	Large
		HIP vs AC				
WT Female vs. WT Male	106.1	4	1248		0.081270096	Medium
WT Female vs. MAR Male	305.5	4	1248		0.241559486	Large
WT Female vs. MAR Female	237	4	1248		0.186495177	Large
WT Male vs. MAR Male	199.4	4	1248		0.156270096	Large
WT Male vs. MAR Female	130.9	4	1248		0.101205788	Medium
MAR Male vs. MAR Female	-68.48	4	1248		-0.05906752	Small
		HIP vs SC				
WT Female vs. WT Male	-68.88	4	2080		-0.03558767	Small
WT Female vs. MAR Male	440.8	4	2080		0.209922929	Large
WT Female vs. MAR Female	119.6	4	2080		0.055202312	Small
WT Male vs. MAR Male	509.7	4	2080		0.243111753	Large
WT Male vs. MAR Female	188.4	4	2080		0.088342967	Medium
MAR Male vs. MAR Female	-321.3	4	2080		-0.15717726	Large
		HIP vs MB				
WT Female vs. WT Male	-6.145	4	468		-0.0240194	Small
WT Female vs. MAR Male	96.73	4	468		0.197693966	Large
WT Female vs. MAR Female	46.87	4	468		0.090237069	Medium
WT Male vs. MAR Male	102.9	4	468		0.210991379	Large
WT Male vs. MAR Female	53.02	4	468		0.103491379	Medium
MAR Male vs. MAR Female	-49.85	4	468		-0.11821121	Medium
		HIP vs BCSB				
WT Female vs. WT Male	-59.18	4	2652		-0.02423716	Small
WT Female vs. MAR Male	685.3	4	2652		0.256910876	Large
WT Female vs. MAR Female	413.8	4	2652		0.154380665	Large
WT Male vs. MAR Male	744.5	4	2652		0.279267372	Large
WT Male vs. MAR Female	473	4	2652		0.17673716	Large
MAR Male vs. MAR Female	-271.5	4	2652		-0.10441843	Medium

		AC vs AC				
WT Female vs. WT Male	452.3	4	2304		0.194478261	Large
WT Female vs. MAR Male	255.9	4	2304		0.109086957	Medium
WT Female vs. MAR Female	337.3	4	2304		0.144478261	Large
WT Male vs. MAR Male	-196.5	4	2304		-0.0876087	Medium
WT Male vs. MAR Female	-115	4	2304		-0.05217391	Small
MAR Male vs. MAR Female	81.48	4	2304		0.033252174	Small
		AC vs SC				
WT Female vs. WT Male	446	4	3840		0.114963504	Medium
WT Female vs. MAR Male	467.8	4	3840		0.120646507	Medium
WT Female vs. MAR Female	564.8	4	3840		0.145933264	Large
WT Male vs. MAR Male	21.85	4	3840		0.004392596	
WT Male vs. MAR Female	118.8	4	3840		0.029666319	Small
MAR Male vs. MAR Female	96.95	4	3840		0.023970282	Small
		AC vs MB				
WT Female vs. WT Male	68.31	4	864		0.073616279	Medium
WT Female vs. MAR Male	153.6	4	864		0.172790698	Large
WT Female vs. MAR Female	154	4	864		0.173255814	Large
WT Male vs. MAR Male	85.29	4	864		0.093360465	Medium
WT Male vs. MAR Female	85.71	4	864		0.093848837	Medium
MAR Male vs. MAR Female	0.4259	4	864		-0.00531872	
		AC vs BSCB				
WT Female vs. WT Male	-546.3	4	4896		-0.11269419	Medium
WT Female vs. MAR Male	1154	4	4896		0.234873262	Large
WT Female vs. MAR Female	873.4	4	4896		0.177514309	Large
WT Male vs. MAR Male	1700	4	4896		0.346484056	Large
WT Male vs. MAR Female	1420	4	4896		0.289247751	Large
MAR Male vs. MAR Female	-280.4	4	4896		-0.05834015	Small
		SC vs SC				
WT Female vs. WT Male	-428.1	4	6400		-0.0677142	Medium
WT Female vs. MAR Male	485.4	4	6400		0.075109443	Medium
WT Female vs. MAR Female	-21.6	4	6400		-0.00415885	
WT Male vs. MAR Male	913.5	4	6400		0.142041901	Large
WT Male vs. MAR Female	406.5	4	6400		0.062773609	Medium
MAR Male vs. MAR Female	-507	4	6400		-0.08005003	Medium
		SC vs MB				
WT Female vs. WT Male	-37.44	4	1440		-0.02955432	Small
WT Female vs. MAR Male	238.8	4	1440		0.16281337	Large
WT Female vs. MAR Female	114.5	4	1440		0.076253482	Medium
WT Male vs. MAR Male	276.3	4	1440		0.188927577	Large
WT Male vs. MAR Female	151.9	4	1440		0.10229805	Medium
MAR Male vs. MAR Female	-124.4	4	1440		-0.09011142	Medium

		SC vs BSCB				
WT Female vs. WT Male	184.4	4	8160		0.021996077	Small
WT Female vs. MAR Male	2063	4	8160		0.252329573	Large
WT Female vs. MAR Female	686.2	4	8160		0.083521334	Medium
WT Male vs. MAR Male	1878	4	8160		0.229646886	Large
WT Male vs. MAR Female	501.8	4	8160		0.060912212	Medium
MAR Male vs. MAR Female	-1376	4	8160		-0.1693232	Large
		MB vs MB				
WT Female vs. WT Male	16.54	4	324		0.0360625	Small
WT Female vs. MAR Male	58.47	4	324		0.16709375	Large
WT Female vs. MAR Female	43.51	4	324		0.12034375	Medium
WT Male vs. MAR Male	41.93	4	324		0.11540625	Medium
WT Male vs. MAR Female	26.96	4	324		0.068625	Medium
MAR Male vs. MAR Female	-14.96	4	324		-0.062375	Medium
		MB vs BSCB				
WT Female vs. WT Male	137.4	4	1836		0.072270742	Medium
WT Female vs. MAR Male	552.8	4	1836		0.299017467	Large
WT Female vs. MAR Female	399.6	4	1836		0.215393013	Large
WT Male vs. MAR Male	415.4	4	1836		0.224017467	Large
WT Male vs. MAR Female	262.3	4	1836		0.140447598	Large
MAR Male vs. MAR Female	-153.2	4	1836		-0.08635371	Medium
		BSCB vs BSCB				
WT Female vs. WT Male	1057	4	10404		0.101153846	Medium
WT Female vs. MAR Male	1371	4	10404		0.131346154	Medium
WT Female vs. MAR Female	2305	4	10404		0.221153846	Large
WT Male vs. MAR Male	313.8	4	10404		0.029692308	Small
WT Male vs. MAR Female	1248	4	10404		0.119519231	Medium
MAR Male vs. MAR Female	933.9	4	10404		0.089317308	Medium

Supplemental Table 5. Kruskal -Wallis effect sizes for structural covariance analysis. Effect sizes for comparisons between each set of regions following Kruskal-Wallis non-parametric testing. Effect size bins: Small = 0.01-0.06, Medium = 0.06-0.14, Large >0.14.

CHAPTER 4

Altered behavior, brain structure, and neurometabolites in a rat model of autism-specific maternal autoantibody exposure

****Work in Preparation****

M.R. Bruce, A.C.M. Couch, S. Grant, K. Ku, C. Chang, A. Bachman, M. Matson, J. McLellan, R.F. Berman, R. J. Maddock, D. Rowland, E. Kim, M. D. Ponzini, D. Harvey, S. L. Taylor, A. C. Vernon, M. D. Bauman, J. Van de Water, Altered behavior, brain structure, and neurometabolites in a rat model of autism-specific maternal autoantibody exposure. *In Preparation*, (2022).

Abstract

Maternal immune dysregulation is a prenatal risk factor for Autism Spectrum Disorder (ASD). Importantly, a clinically-relevant connection exists between inflammation and metabolic stress that can result in aberrant cytokine signaling and autoimmunity. In this study we examined the potential for maternal autoantibodies (aAbs) to disrupt metabolic signaling and induce neuroanatomical changes in the brains of exposed offspring. To accomplish this goal we developed a model of maternal aAb exposure in rats based on the clinical phenomenon of maternal autoantibody related ASD (MAR-ASD). Following confirmation of aAb production in rat dams and antigen-specific IgG transfer to offspring, we assessed offspring outcomes longitudinally using a battery of behavioral assays. MAR-ASD rat offspring displayed deficits in social play behavior and vocalizations, as well as increases in repetitive self-grooming behavior. To understand the biological basis of this behavior, we conducted longitudinal *in vivo* structural magnetic resonance imaging (sMRI) in a separate cohort of offspring at postnatal day 30 (P30) and P70 (P70). Analysis of sMRI data revealed sex-specific differences in total and regional brain volume, with treatment-specific differences converging on midbrain and cerebellar structures in MAR-ASD offspring. We also conducted *in vivo* ^{1}H magnetic resonance spectroscopy (^{1}H-MRS) to examine brain metabolite levels in the medial prefrontal cortex. Results showed that MAR-ASD offspring displayed decreased levels of choline-containing compounds and glutathione, accompanied by increased taurine compared to controls. Overall, we found that rats exposed to MAR-ASD aAbs present with alterations in behavior, brain structure, and neurometabolites; reminiscent of findings observed in clinical ASD

Introduction

Autism spectrum disorder (ASD) is clinically defined by a collection of symptoms including alterations in social, communicative, and stereotyped behaviors (*15*). Despite these well-defined behaviorally diagnostic criteria, the molecular basis of these behaviors remains unclear. However, evidence exists for the dysregulation of important brain signaling molecules and pathways in ASD etiology; including imbalances in key neurotransmitters, gamma aminobutyric acid (GABA) and glutamate (*16-18*), or alterations in cellular metabolism including mitochondrial function (*19, 20*) and one-carbon signaling (*21*) . Understanding which physiological systems and related signaling molecules are impacted, as well as the roles of developmental timing and biological sex on individual outcomes will aid in early diagnosis and therapeutic strategies in ASD.

Genetic influence is also an important factor in ASD, and studies investigating genetic risk have identified a multitude of candidate gene networks associated with diagnosis (*22*). These include gene networks important for synaptic function (*23*), cellular metabolism (*24*), and immune signaling (*25, 26*). The development of ASD, however, likely results from a combination of genetic and environmental factors, with early-life exposure to environmental insults playing a pivotal role (*27, 28*). In support of this view, numerous studies provide evidence that changes in maternal immune signaling during pregnancy associate with ASD diagnosis in offspring (*29-32*). Prominent among these findings is that ~20% of mothers of children subsequently diagnosed with ASD possess circulating aAbs directed against proteins known to be important for early development. This phenomenon has been termed maternal autoantibody-related (MAR) ASD (*33, 34*). We have previously shown that exposure to clinically relevant patterns of these aAbs results in changes to behavior, brain structure (as measured by sMRI), and neural progenitor cell

proliferation in mice (*35-37*). What remains to be understood are the effects of MAR-ASD aAb exposure on offspring across the lifespan, the impact of aAbs on cell signaling and target proteins, and the influence of sex as a biological variable.

Based on previous clinical findings suggesting larger total cerebral volume (*38*) in individuals from mothers with MAR-ASD aAbs, and recent data confirming that the presence of MAR-ASD aAb is positively correlated to behavioral outcomes (*33*), we hypothesized that offspring exposed to MAR-ASD aAbs would have an altered trajectory of brain growth and display changes in ASD-relevant behavioral outcomes. To test this, we created an endogenous model of MAR-ASD exposure in rats. The rat was chosen as a model system as laboratory rats have greater brain complexity and size, which begets enhanced cognitive ability, behavior, and suitability for neuroimaging studies compared to mice (*39*). This builds upon our previous work (*36*), and provides an opportunity for greater translational relevance for the MAR-ASD model. Following model creation, offspring underwent longitudinal *in vivo* structural magnetic resonance imaging (sMRI) at postnatal day 30 (P30) and P70; with ages representing a pre-pubertal and post-pubertal time points, respectively. Additionally, a battery of behavioral tests was conducted across development to examine effects of aAb exposure on measures of communication, motor and reflex development, exploration, anxiety, sensorimotor gating, and social interactions. While collecting structural data during sMRI acquisition, we were also able to acquire data on metabolite levels within a specific recording voxel placed in the frontal cortex of the rat offspring.

Methods

Animals

Male and female Sprague Dawley rats were obtained from Charles River Laboratories (Portage, MI). All rats were pair-housed in a temperature- and humidity controlled vivarium (22±2°C) on a 12:12 hr light:dark cycle with food and water available *ad libitum*. All procedures were conducted in accordance with protocols approved by the University of California, Davis Institutional Animal Care and Use Committee. Animals were kept in standard housing consisting of polypropylene cages (30.5 cm x 35.6 cm x 20.3 cm) with high-top wire lids, cob bedding, and nesting. Red enrichment boxes were provided within cages for dams to enhance quality of life and breeding success (Fisher Scientific; Cat# 14-726-564). Breeding was conducted 2 weeks following the final treatment (described below) to produce two separate cohorts for the behavioral and neuroimaging studies. Each cohort consisted of 5-6 dams per treatment group for behavior and 3-4 dams per treatment group for neuroimaging. After birth, animals were tattooed for identification purposes and litters culled to 8 (4 male/4 female). To identify rats, pups were labeled by paw tattoo on postnatal day (PND) 2-3 using non-toxic animal tattoo ink (Ketchum Manufacturing Inc., Brockville, ON, Canada) and later tail-marked with permanent marker at weaning (P21) to allow investigators to run and score behaviors blind to treatment condition. All testing was conducted during the light phase of the 12 hour light/dark cycle.

After two weeks of acclimation, naïve rat dams were randomly assigned to treatment groups (**Behavior**: MAR-ASD; N=5, Control; N=6, **Neuroimaging**: MAR-ASD; *N*= 3, Control; *N*= 4). All animals then received subcutaneous immunizations, administered once weekly for a total of four weeks. The injection schedule and components are outlined in detail in Jones et al, 2018 and only described briefly here. MAR-ASD rat dams received injections of 21 custom synthetic

peptides corresponding to the immunodominant epitopes of LDH-A, LDH-B, STIP1, and CRMP1 (LifeTein LLC; Hillsborough, NJ). Peptide solutions, dissolved in sterile saline, were mixed with Freund's complete adjuvant (CFA) for the first injection, or Freund's incomplete adjuvant (IFA) for the three subsequent injections. Control dams were injected with adjuvant and saline only using the same injection schedule.

Autoantibody Confirmation

To verify aAb production to MAR-specific epitopes, blood was collected from rat dams 4 weeks following the initial injection and centrifuged at 10,000 x g for 10 min. All blood draws and injections were conducted between the hours of 9am-12pm. Serum supernatant was then collected and stored a -80°C until use. Dam and offspring blood samples were tested using and in-house enzyme-linked immunosorbent assay (ELISA). Results are expressed as fold change over baseline for aAb levels. Briefly, Nunco Maxisorp plates (Thermo Scientific, Waltham, MA) were incubated with synthetic proteins (Expression Systems, Davis, CA) corresponding to the 4-core MAR ASD proteins (LDH-A, LDH-B, STIP1, CRMP1), at a concentration of 2ug/mL. Plates were incubated overnight at 4dC, washed with PBST the next day, blocked with 1% Protein Free Blocking Buffer (Thermo Scientific, Cat# 37572), then incubated with rat dam serum samples at a concentration of 1:250 for 30 minutes at room temperature. Plates were then washed with PBST and incubated with a highly cross-adsorbed goat anti-rat secondary antibody (InVitrogen, Cat# 62-9520) for another hour. Following additional washes in 1X PBS to remove detergent, plates were incubated with TMB substrate (3,3′, 5,5′-tetramethylbenzidine; BD OptEIA, San Jose, CA) and neutralized using 2N H_2SO4 to result in colorimetric substrate deposition. Data were read on a microplate reader at an optical density of 450 nm.

Protein Analysis

Multiplexed Cytokine Analysis. Serum collected from MAR-ASD rat dams for aAb confirmation was also used for cytokine analysis. Concentrations of cytokines and chemokines were determined using a commercially available multiplex bead-based kit according to manufacturer instructions (Bio-Plex Rat Cytokine 12-plex Assay; Bio-Rad Laboratories, Hercules, CA). Results were compared between MAR-ASD and control dams using two-way ANOVA analysis with Sidak's testing for multiple comparisons. *Western Blot.* Brain tissue samples were collected from MAR-ASD and control offspring at P2 and cell lysates were created. Approximately 50mg of tissue was microdissected from the frontal pole and cerebellum of each animal and homogenized using a hand-held sonicator in 1X RIPA buffer (ThermoFisher) with cOmplete protease inhibitors (Roche) added. Samples underwent a freeze/thaw cycle, were spun to pellet cell debris, and supernatant was collected for protein analysis. Westerns were run in a mini-blot system (ThermoFisher) using 12-well lane gels loading 15ug of total protein into each well. Blots were then probed using secondaries against CRMP1 (Abcam; ab199722), STIP1 (Abcam; ab126724), or LDH (Abcam; ab52488). GAPDH and β-actin were used as loading controls for semi-quantitative measurement. Data were analyzed using Student's t-test.

Immunohistochemistry. Offspring underwent transcardial perfusion at P2 with sterile saline and 4% paraformaldehyde to remove circulating factors and to fix the tissue. Brains were then collected and post-fixed overnight prior to embedding, freezing, and sectioning using a Leica cryostat. Coronal brain sections were placed on glass slides and immunostained for rat IgG (Jackson Immunoresearch; 112-547-003), DAPI (ThermoFisher; D1306), and NeuN (Abcam; ab177487). Representative images were taken using tiling with a 20x objective on a Leica TCS SP8 confocal microscope.

Longitudinal Behavioral Testing

A summary of the behaviors tested, relative scoring measures, and at which postnatal day (PND) they are tested is detailed in tables included below. On PND 26 and 96, subject animals performed an elevated plus maze to assess anxiety-like behaviors. On PND 29 and 100, subject rats had exploratory locomotion assessed through the open field maze, in order to control for potentially confounding effects of sedation or hyperactivity on the sociability assays. Automated social approach using a three-chambered apparatus was used to assess sociability in subject animals at PND 27-28 and 97-98. This task was measured by methodology similar to protocols described previously for mice (*40*) and rats (*41, 42*). On PND 34 and 102, rats were tested in pre-pulse inhibition (PPI), a task used to assess sensorimotor gating in rats. Reciprocal social dyad interactions were evaluated at three developmental timepoints: juvenile (PND 36-37), young adult (PND 55-56), and adult (PND 103-104) Stimulus partners were matched in age, strain, and sex and housed in the same vivarium, but were unfamiliar to test rats. The amount of time spent in nonsocial activity, self-grooming, social interaction, social proximity and social play were quantified using Noldus Observer. Before each trial, all testing chambers were thoroughly cleaned and disinfected with 10% Nolvasan solution (Fort Dodge Animal Health, Fort Dodge, IA).

Developmental milestones: On PNDs 4, 8, and 12, subject animals were removed from the dam for developmental milestones. An array of milestones were collected, including body temperature, body weight, cliff avoidance, fur development, head width, incisor eruption, negative geotaxis, pinnae detachment, righting reflex, and tail length. Fur development, incisor eruption, and pinnae detachment are given a score between 0-3 depending on the pup's development. Cliff avoidance was tested by placing the pup at the edge of a precipice with their paws just over the edge. A score

between 0-3 was given based on the degree of the response. To measure negative geotaxis, rat pups were placed facing downward on a wire mesh slanted at a 45-degree angle. Pups were given a score between 0-3, depending on their ability to turn face up and climb up the ramp. Righting reflex was tested by placing the pup on its back and recording the latency to reach an upright position with all four paws flat on the surface. This was done twice and the average of the two latencies was taken as the overall righting reflex value.

Isolation-induced pup 40-kHz ultrasonic vocalizations: On PNDs 4, 8, and 12, subject pups were removed individually from the nest at random and gently placed into an isolation container (8 cm x 6 cm x 5 cm; open top) made of plastic. The isolation container was filled with a thin layer of clean corncob bedding before the first test session and between each new test subject. The isolation container was placed in a sound attenuating chamber (18 cm x 18 cm x 18 cm) made of 4 cm thick noise-dampening Styrofoam padded walls. An ultrasonic microphone (Avisoft Bioacoustics, Berlin, Germany) was attached to the chamber roof and hung 7 cm above the chamber floor. Calls were collected for 3 min at a sampling rate of 250,000Hz via the microphone connected to an Avisoft UltraSoundGate 116 USB audio device, which was connected to a computer with Avisoft Recorder software. Immediately following the 3-min recording session, body temperature was taken with a digital thermometer placed on the abdominal surface (TH-5 Thermalert Monitoring Thermometer, Physitemp Instruments, Inc., Clifton, NJ). Ultrasonic vocalization spectrograms were displayed using the Avisoft SASLab Pro software. Pup calls in the ultrasonic range with peak frequencies higher than 20 kHz were identified manually by a trained investigator blind to treatment group.

Elevated plus maze (EPM): On PNDs 26 and 96, subject animals performed an elevated plus maze task. The maze is a black, polypropylene plus-shaped platform consisting of two opposite enclosed arms (10cm x 50cm) and two opposite open arms (10cm x 50cm). The arms meet at a center square platform (10cm x 10cm), and the enclosed arms are surrounded by 10cm high walls. The entire maze is elevated 100cm off the ground. At the start of each trial, the subject rat was placed on the open center platform facing an open arm. The rat was allowed to explore the apparatus for 5 minutes and was video-recorded using video-tracking software (Ethovision v.4.0, Noldus Information Technology, Netherlands). The tracking software used the midpoint of the body of the rat to distinguish when the test subject entered or exited an arm boundary. Trials were scored on the amount of time spent in the open arm and the number of entries into the open arm.

Open field maze: On PNDs 29 and 100, subject rats were tested for spontaneous locomotor activity. Locomotion was measured using a fully automated contrast-sensitive video-tracking program (Integra Accuscan, Columbus, OH, USA). The setup allowed the simultaneous tracking of four animals, using four separate square observation arenas (41.3cm w x 29.2cm h x 41.3cm l). At the beginning of the trial, the subject animal was placed in the center of the arena. Spontaneous activity was measured over a 60-minute period. Distance moved (cm) was calculated every 1 minute. The sampling rate was set to five samples per second. Parameters used to measure the subjects' locomotion were distance travelled, time spent in center of arena, horizontal activity, and vertical activity.

Three-chambered social approach. On PNDs 27-28 and 97-98, subject rats performed a social approach and novelty task. Stimulus animals were matched in age, strain, and sex, and were housed

in the same vivarium, but were unfamiliar to test rats. Subject and stimulus rats were placed in a dimly lit room (30 lux) and allowed to acclimate to the test room for 5 minutes. The subject rat was then placed in a square, three-chambered box made of clear plastic (101.6cm l x 101.6cm w x 33.7cm h) (Stoelting Co., Wood Dale, IL). The subject rat habituated to the empty three-chambered box for 10 minutes, with free access to all three chambers. Two plastic cylindrical cages (13.3cm diameter x 21.0cm h) were then placed in the left and right chambers. In the first trial, social approach, the first stimulus rat was placed under one of the cages in a side chamber, while the other cage was left empty and placed in the opposite side chamber, serving as a novel object. The subject rat was allowed to explore the entire arena for ten minutes. Stimulus rat and novel object placement alternated between the left and right side chambers for each individual subject. In the second trial, social novelty, the subject rat was placed back in the center chamber. The chamber with an empty cage was then replaced with a cage containing a novel stimulus animal, while the previous, familiar stimulus animal remained on the other side of the arena. The subject animal was once again allowed to explore the entire arena for ten minutes. Automated video tracking with EthoVision 10.0 XT (Noldus, Wageningen, The Netherlands) software was used to detect head-directed movement and sniffing behavior during all test phases, as well as to quantify time spent in each chamber, cumulative duration of nose within zone around cup, and the number of transitions between chambers. Typical sociability in the approach phase was defined as spending more time in the chamber containing the stimulus rat than the chamber containing the novel object, and more time spent near the cup with the stimulus rat than the novel object. Novelty preference in the novelty phase is defined as spending more time in the chamber containing the novel rat, and more time spent around the cup with the novel stimulus rat than the original stimulus rat.

Although MAR-ASD rats deviated from species-typical social interactions when allowed to interact freely with another animal, differences were not detected in the semi-automated three-chambered social approach assay that evaluates sociability as indexed by demonstration of a species-typical preference to orient to novel conspecifics rather than objects. This test is commonly used to evaluate mouse social behavior, though it may not be sensitive to more subtle impairments in social behavior detected in rats, nonhuman primates, and other species that engage in reciprocal social behaviors, such as juvenile play (*43*). The species-typical "sociability" demonstrated by MAR-ASD rat offspring suggests that prenatal exposure to MAR-ASD aAbs does not result in a global reduction in social interest, but may disrupt neural systems that support more complex, reciprocal social interactions.

Pre-pulse inhibition: On PNDs 34 and 102, rats were tested in pre-pulse inhibition (PPI), a task used to assess sensorimotor gating in rats. The subject rats were placed in a clear cylinder, which was then attached to a piezoelectric transducer platform. The platform was placed in a sound-attenuating chamber outfitted with speakers, which were controlled by specialized software (SR-Labs, San Diego Instruments, San Diego, CA). Subject rats were acclimated to the chamber for 5 minutes with a 65 dB background white noise. They were then presented with a pseudorandom set of 5 different trial types: 120dB startle, 120dB startle with a 74dB pre-pulse, 120dB startle with a 82dB pre-pulse, 120dB startle with a 90dB pre-pulse, and a no stimulus trial, or 65dB white noise. The trials occurred over a 10-minute period. Pre-pulses were introduced 120ms prior to the startle stimuli. Intertrial intervals were randomized between 10 ms and 20 ms. The following equation was used to calculate PPI percentage: PPI = [100 – (pre-pulse/max startle)] x 100].

Social Dyads. Social dyad trials were conducted at three developmental timepoints: juvenile (PND 36-37), young adult (PND 55-56), and adult (PND 103-104). Stimulus partners were matched in age, strain, and sex and housed in the same vivarium, but were unfamiliar to test rats. The social dyad apparatus consisted of three identical Plexiglas chambers (41.9cm w x 29.2 cm h x 41.9 cm l), two side chambers used for acclimation and a center arena to record dyad interactions between the subject and stimulus rat. Both subject and stimulus rats were placed into respective transfer cages and isolated in a quiet, dimly lit (12 lux) room adjacent to the test room for ten minutes, separated by a visual barrier. The subject rat and stimulus rat were then moved to a dimly lit (12 lux) test room and allowed to acclimate for 5 minutes on opposing side chambers. Both rats were placed in the center arena and video recorded using a Sony HDRCX240/B video camera with 2.7-Inch LCD, fixed to a tripod. The rats were allowed to interact undisturbed for 10 minutes. Videos were scored using Observer XT12 software (Observer Version XT12, Noldus Information Technology, the Netherlands). Focal observations were used to quantify the amount of time the subject rat spent in nonsocial activity (not interacting with the stimulus animal) and the amount of time spent in social interactions, further divided into three broad categories: (i): social play – a composite of well-characterized play behaviors including pouncing/playful nape attack, pinning, wrestling, boxing, tail pulling, and chasing (running pace); (ii): social exploration – a composite of social investigation such as sniffing and following (walking pace) or non-play contact such as grooming, licking, crawling over or under; and (iii) social proximity – scored when the rats were within 2cm of each other, but not actively engaged in investigation, contact, or play behaviors. The amount of time spent self-grooming was also quantified.

Milestone	Score	Score Definition
Fur Development	0	No fur
	0.5	Beginning of fur
	1	Slight fur
	2	More fur
	3	Fur fully present
Incisor Eruption	0	Not visible
	0.5	Beginning to emerge
	1	Slightly emerged
	2	Almost fully emerged
	3	Fully emerged
Pinnae Detachment	0	Ears flat against skin
	0.5	Top tip of ears detached
	1	Slightly attached
	2	Slightly detached
	3	Ear canal fully open and detached
Cliff Avoidance	0	No response
	1	Turns head
	2	Partial avoidance of precipice
	3	Active avoidance of precipice
Negative Geotaxis	0	No effort
	1	Hesitant to turn
	2	Some but little hesitation
	3	No hesitation

Behavioral Test	Postnatal Day (PND)	Description
Developmental Milestones	4,8,12	Screen for developmental delays (motor, reflex etc.)
Isolation USVs	4,8,12	USVs in response to temporary separation
Elevated Plus Maze (EPM)	26 96	Anxiety related behaviors
Open Field	29 100	Exploratory locomotion
Pre-pulse Inhibition (PPI)	34 102	Sensory gating
3-Chamber Social Approach	28 98	Automated assessment of interest in a novel animal
Social Dyads	36 55 103	Analysis of 10min reciprocal social behavior with a novel partner

Statistical Analysis of Behavioral Outcomes

Numeric variables were summarized as means ± SD and categorical variables as counts and percentages. Statistical analyses were conducted using R version 4.0.5 (*44, 45*).

Developmental Milestones. Developmental milestones evaluated were body temperature and weight, tail length, head width, pinnae detachment, eye opening, incisor eruption, fur development, righting reflex, cliff avoidance, and negative geotaxis. These milestones were evaluated at 3 times points: post-natal day 4, 8 and 12. Because there was no variation in incisor eruption scores at post-natal day 4 and fur development scores at post-natal day 8, these time

points were excluded from their respective analysis. Eye opening scores were the same for all groups, sexes, and ages and thus not analyzed. Linear mixed effects models (LMMs) were used to model each milestone as a function of treatment group (MAR or Cntl), sex, post-natal days (4, 8, or 12 days), and all two and three-way interactions. Post-natal days was modeled as a categorical factor. A random subject effect was included for each pup to account for within-subject correlation. The need for a random dam effect to account for correlation among pups from the same dam was assessed using a likelihood ratio test (*45*). If inclusion of a dam random effect was not found to significantly improve model fit, it was dropped and the model refit with only a random intercept for each pup. Residual plots were used to assess model assumptions. A dam random effect was included in all models except for cliff avoidance. Righting reflex was log transformed to meet model assumptions. Non-significant ($p > 0.05$) interactions were dropped and final models were fit consisting of all main effects but only statistically significant interactions. *Ultrasonic Vocalizations.* The number of ultrasonic vocalizations (USVs) were evaluated using a LMM modeling USV as a function of sex, treatment group (MAR or Cntl), post-natal days (4, 8, or 12 days), and all two and three-way interactions. Post-natal days was modeled as a categorical factor. A random subject effect was included for each pup and the need for a random dam effect assessed. A dam effect was deemed necessary based on the results of this test. Residual plots were used to assess model assumptions. A final model containing all main effects but only statistically significant interactions was fit. *Social Dyads.* Social behavior, nonsocial behavior, proximity, and investigation were measured as time spent engaged in each activity. These behaviors were evaluated using a LMM. Each behavior was modeled as a function of sex, treatment group (MAR or Cntl), age (juvenile, young adult, and adult), and all two and three-way interactions. A random subject effect was included and the need for a random

dam effect was assessed. Residual plots were used to assess model assumptions. The final model contained all main effects but only statistically significant interactions. Self-grooming and play also were reported as time spent in these activities. However, some mice did not exhibit these behaviors resulting in highly skewed distributions with a large number of 0 entries. Because the proportion of rats exhibiting these behaviors was of interest as well as the time spent in these behaviors among those who playing or self-grooming, we conducted two analyses. First, we used a mixed effect logistic regression to model the percentage of rats that played or self-groomed as a function of sex, group, and age. Second, using only rats who exhibited each behavior, we fit a LMM to relate time spent engaged in the behavior versus group, sex and age. Interactions were not included in these models due to small sample sizes for combinations of factors with the logistic model and small numbers of rats that exhibited the behavior at some ages. To control the Type I error across both models, we used a Bonferroni adjustment and evaluated significance at a 0.025 level. As with the other outcomes, we included a random pup effect and evaluated the need for a random dam effect. A random dam effect was not needed for any of the models. *Social Approach and Novelty.* Social approach and novelty experiments consist of quantifying interactions between a target rat and a novel rat or object. Outcomes are reported as time spent in a chamber or looking at the novel rat/object as well as the number of entries into the chamber with the novel rat/object. Linear mixed effect models were used to evaluate duration metrics (time spent in chamber, time spent looking) and a Poisson mixed effect model was used for counts of the number of entries. Each outcome was modeled as a function of chamber (rat vs. object), group (MAR vs. Ctrl), sex and all two and three-way interactions. For the Poisson models, the log transformed total number of chamber entries was included as an offset. A random subject effect was included and the need for a random dam effect was assessed;

inclusion of a random dam was not indicated for any outcome. Final models containing all main effects but only statistically significant interactions were fit. Residuals were examined to assess model assumptions. Juveniles and adults were modeled separately. *Pre-pulse Inhibition.* Linear mixed effects models were fit to assess the relationship between PPI and the three different pre-pulse intensities (74dB, 82dB, and 90dB), group (MAR vs. Ctrl), sex and all two and three-way interactions. A random subject effect for each rat was included and the need for a random dam effect was also evaluated; a random dam effect was not indicated. Final models containing all main effects but only statistically significant interactions were fit. Model assumptions were assessed through residual plots. Juveniles and adults were analyzed separately. *Elevated Plus Maze.* Outcomes of the elevated plus maze task are time spent in the open arms and the number of entries to the open arms. We first fit a LMM to relate time spent in the open arm to group, sex and their interaction. The need for a random litter effect to account for within-litter correlation was tested and was not found to be needed for either juveniles or adults. Therefore, multiple linear regression models were used. Residual plots were used to assess model assumptions. For final models, we retained all main effects and statistically significant interactions. Juveniles and adults were evaluated separately. The number of entries into the open arm of the maze was similarly modeled using a generalized linear mixed effects model assuming a Poisson error distribution and a log link. The log transformed total number of entries was included as an offset, thereby modeling the rate of entries. As done for the analysis of time spent in the open arm, we tested the need for a random litter effect. Because a random litter effect was not found to be necessary, a Poisson general linear model was used. Juveniles and adults were modeled separately. *Open Field.* In the open field experiment, a rat is placed in an arena alone and allowed to explore for 60 minutes. For each 5 minute increment, the distance the rat travels

horizontally, vertically, and total distance are recorded. The time spent in the center of the arena is recorded. Linear mixed effect models were used to model the trajectories of distance traveled over time. We modeled distance or center time as a function of time since the trial started, group, sex and all two and three-way interactions. A random intercept was included for each rat. We tested the need for a litter random effect; model fit was not significantly improved with the addition of a litter effect for any outcome. The midpoint of each 5 minute increment was as used for the time variable and was modeled as a numeric value. All outcomes were square root transformed to meet model assumptions and an autoregressive correlation structure assumed for correlation over time. Final models consisting of all main effects and any statistically significant interactions were fit. Juveniles and adults were evaluated separately.

Magnetic Resonance Imaging and Spectroscopy

For sMRI and ^{1}H-MRS experiments, a total of 2 male and 2 female offspring from each dam (MAR-ASD (N= 6M/6F); Control (N=8M/8F)) were selected at random. Dams in this cohort were bred specifically for neuroimaging analysis and did not overlap with those used for behavior. The sMRI and ^{1}H-MRS data were acquired from these animals *in vivo* and longitudinally at P30 and P70.

MR acquisition

MR images were acquired on a small animal horizontal bore 7 T system (Bruker; Karlsruhe, Germany) running ParaVision 5.1 software. Animals were anesthetized using 1.5% isoflurane vaporized in oxygen, administered continuously at 1 liter/minute for the duration of the scanning. PhysMonitor software was used to track body temperature and respiration rate. A remote heating device was used to maintain the body temperature of animals at a set point of 37°C. A 72 mm

volume coil was used for excitation and a 4-channel phased array surface coil for signal detection (Bruker). Anatomical T2-weighted scans were acquired using a RARE sequence (Rapid Acquisition with Relaxation Enhancement) (*46*) in axial orientation: RARE factor 8, TR = 6100 ms, TEeffective = 60 ms, matrix size 280 × 200, FOV 35 × 25 mm2 (in-plane resolution 125μm) with 44 continguous 0.5mm-thick slices. For MR spectroscopy, a single voxel of 3.8 x 2.2 x 2.0 mm3 was centered in the frontal cortex. To optimize field homogeneity, after 1st order shims were optimized, shims were readjusted including 2nd order shims. A field map was measured and shims were optimized for the localized spectroscopy using the MAPShim algorithm provided by Bruker in PV5.1. In vivo 1H-MR spectroscopy (MRS) data were acquired with a Point-Resolved Spectroscopy (PRESS) (*47*) with a total acquisition time of 8.5 min per scan (TR/TE = 2500/14 ms, 200 averages, 2048 acquisition data points, spectral width 4006.41 Hz) with VAPOR (variable power and optimized relaxation delays) water suppression (bandwidth 200 Hz) (*48*). A reference scan without water suppression was acquired for frequency and eddy current correction during each acquisition cycle. A total of 3 PRESS scans were acquired one after another.

MR image processing

MR images were visually inspected in native space for artifacts, with no images excluded on this basis. Raw MR images were converted from the manufacturer's proprietary format to the NIFTI format and processed using a combination of FSL 5.0.10 (*49*), ANTs 2.1.0 (*50*) and Quantitative Imaging Tools 2.0.2 (QUIT, (*51*)). First, N4 bias field correction was applied (*52*). Separate P30 and P70 template images were constructed from all bias-corrected P30 and P70 images using the *antsMultivariateTemplateConstruction2.sh* script with three iterations (*53*). Each image was then

non-linearly registered to its age-matched study template via sequential rigid-body, affine, and SyN registrations using the *antsRegistration* function. The P30 template was similarly registered to the P70 template, enabling normalization of all images across subjects and time points to the P70 template space. Jacobian determinant maps of the composite deformation fields from the P70 template to each subject were calculated using the *CreateJacobianDeterminantImage* function (ANTs). The P70 template was skull-stripped using the RATS algorithm implemented in QUIT using the *qimask* function (*54*). To enable atlas based segmentation (ABS) analysis of regional brain volumes, the skull-stripped P70 template was then registered to the publicly available Tohoku rat brain MRI atlas (*55*). Because the Tohoku atlas includes only cortical parcellations, the Waxholm Space (WHS) rat brain atlas (*56*), which has only subcortical parcellations, was registered to the Tohoku atlas, and the two atlases were modified and merged to obtain a full-brain parcellation consisting of 115 regions of interest (ROI). The Jacobian determinants in each atlas ROI were summed to calculate ROI volumes for each subject (*57*). The Jacobian determinant maps were log-transformed to allow voxel-wise estimation of apparent volume changes via deformation-based morphometry (DBM) (*58*).

MR image statistics: Volumetric analysis

The registration quality for each individual subject's MR images was checked visually and no animals were excluded on this basis. We then automatically extracted volumes for the 115 ROIs comprising the hybrid MRI atlas (see MR image processing). Total brain volume was calculated from the summation of each individual atlas ROI volumes (*57*). Group-level differences in total brain volume (mm^3) were assessed using parametric 2-way analysis of variance (ANOVA) for each sex separately, with "Time" (P30-P70) as within-subject factor and "Treatment"

(MAR/CON) as between-subject factor. These analyses were performed using Prism software (v8.4.2; GraphPad, La Jolla, CA, USA) with $\alpha = 0.05$. Identical statistics were performed to compare regional volume differences for the absolute (mm^3) and relative (% total brain volume) volumes of all 115 brain regions of interest (ROI) in the hybrid MRI atlas, with $\alpha = 0.05$ using R-project (*44*). The resulting p(ANOVA) values for each model term (main effects and interactions) were then corrected for multiple comparisons to account for Type I errors across the 115 individual ROIs using the false-discovery rate (FDR) in Prism software (v8.4.2; GraphPad, La Jolla, CA, USA). A threshold of 5% FDR ($q<0.05$) was considered statistically significant. To calculate the magnitude and direction of volume change for each region between groups, we calculated effect sizes, using Cohen's F, derived from the partial eta^2 effect sizes from the ANOVA models for main effects of treatment, time or treatment*time interaction. The regional brain volume analysis was run for both sexes combined and for male and female rats separately.

For DBM, the voxel-wise analysis of group-level differences in absolute volumes was carried out on the log-transformed Jacobian determinant maps using the Multivariate and Repeated Measures (MRM) MATLAB toolbox (*59*). Parametric 2-way ANOVA as with the ABS analysis, 5000 permutations and FDR correction As with the ABS analysis, parametric 2-way ANOVA was run for both sexes combined and separately, using Wilks' λ as the test statistic, voxel-level thresholding, permutation testing (5000 permutations), and FDR correction (5%, $q<0.05$).

^{1}H-MRS Analysis

PRESS data were acquired over 3 separate subscans of 200 averages each, analyzed using LCMODEL, and averaged together after phase and frequency correction for estimation of

metabolite concentrations. An analysis window between 0.2 to 4.0ppm was chosen with phase and frequency alignment using LCMODEL. Data were fitted in LCMODEL using a simulated basis set with 26 metabolites, including macromolecule and lipid resonances. Metabolites with Cramér-Rao lower bounds <15% were included in final analysis

Statistical Analyses

Eight metabolites were identified as primary outcomes of interest (Gln, Glu, GPC+PCh, GSH, Ins, MM09+Lip09, NAA, tau), while an additional five (Asp, GABA, Glu+Gln, MM14+Lip13a+L, NAA+NAAG) were identified as secondary outcomes. Factors of interest included treatment group (Control, Treatment), sex, and age (30, 70 days). Main effects and interactions among these variables were considered. All animals had observations at both 30 and 70 days. Repeated measures regression, assuming a compound symmetric covariance matrix, was used to assess differences by treatment, sex or age. Model building for each metabolite was similar, using Akaike Information Criterion to identify the best model. Due to the small number of animals, robust standard errors were used. Secondary analyses included a data quality metric (full width-half max (FWHM)) as a covariate. Results were generally consistent in these secondary analyses, unless otherwise stated.

Results

MAR-ASD aAb production is stable and does not induce persistent inflammation

We have previously demonstrated the ability to induce aAb production in mouse dams to MAR-ASD-specific antigens (*36*). Here, we replicate and expand upon these findings in a rat model to understand the impact of MAR-ASD aAb exposure on offspring development. To generate the model, rat dams were injected subcutaneously with an emulsion of MAR-ASD-specific peptide

epitopes from a core, clinically-associated protein pattern (lactate dehydrogenase A (LDHA) & B (LDHB), collapsin response mediator protein 1 (CRMP1) & stress-induced phosphoprotein 1 (STIP1); (*33, 34*)) dissolved in sterile saline and mixed at a 1:1 ratio with Freund's Adjuvant. Control animals were injected with adjuvant and saline alone at the same ratio. Injections were performed once weekly over a span of 4 weeks. After confirming the presence/absence of MAR-ASD aAbs, dams were bred to untreated sires and offspring outcomes were assessed using behavioral testing, *in vivo* longitudinal neuroimaging, and *post-mortem* analysis **(Fig. 1A).**

To verify aAb responses in rat dams, we developed an in-house enzyme linked immunosorbent assay (ELISA) to detect antibody (Ab) reactivity to LDHA, LDHB, CRMP1 & STIP1 in rat sera. Analysis of dam sera five weeks after the initial injection demonstrated robust Ab responses to MAR-ASD autoantigens in female rats **(Fig. 1B).** Moreover, these responses remained remarkably persistent across the lifespan of the animal, without the need for subsequent boosting **(Fig. 1C).** Characterization of the aAb response in rat dams revealed that antigen-specific Ab isotype and subclass followed a species-typical distribution, albeit with some variation by antigen (fig. S1A; (*60*))**.** Following confirmation of this specific aAb response present only in dams exposed to MAR-ASD autoantigens, we sought to clarify the impact of aAbs in this model by ruling out a role for active inflammation in observed outcomes, as is seen in other immune-related ASD models such as maternal immune activation (MIA) (*61-63*). Therefore, we conducted a thorough analysis of serum cytokine and chemokine levels using a multiplexed Luminex assay on rat dam samples taken one week prior to breeding. Analysis of results confirmed that the levels of circulating cytokines in MAR-ASD dams did not differ from control animals **(Fig. 1D)**. Cumulatively, these results suggest that MAR-ASD aAb responses were

robust, long-lasting, and any effects on MAR-ASD offspring are not the result of a pro-inflammatory environment at the time of breeding.

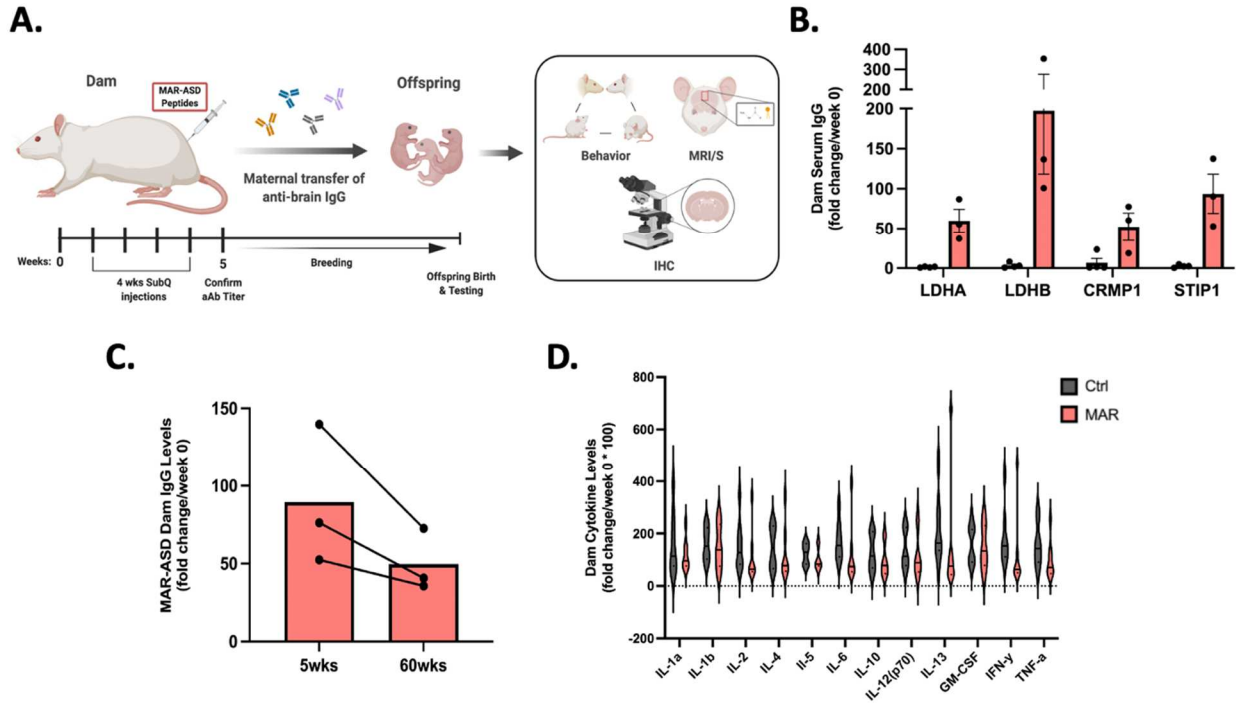

Fig. 1. **MAR-ASD autoantibody production in rat dams. (A)** Autoantibody production is induced in rat dams through injection with autism-specific autoantigens. Antibody can then transfer to offspring and influence developmental outcomes. **(B)** Levels of serum IgG Ab reactive to MAR-ASD proteins (LDHA/B, STIP1, CRMP1) in rat dams compared between aAb and control animals. Values expressed as fold-change over baseline (week 0) following 4 weeks of injections. **(C)** Longitudinal characterization of MAR-ASD IgG persistence in serum from treated dams at 5 weeks and 60 weeks following initial immunization. **(D)** Serum cytokine levels in MAR-ASD and control dams taken one week prior to breeding. Data expressed as fold change over baseline (week 0). N=3 per condition for each experiment, data is expressed as mean +/- SEM. M.R.B. created animals, conducted ELISA and Luminex analysis, as well as conducted analysis of data and figure creation.

Transfer of aAbs to offspring and effects on target protein expression

To understand if MAR-ASD aAbs may impact offspring by entering the fetal compartment and interacting with target proteins there, we first examined the sera of neonatal offspring (P2) for aAb reactivity by ELISA. We observed that antigen-specific MAR-ASD aAbs were present in offspring circulation at appreciable quantities. Immunoglobulin (IgG) reactive to LDHA, LDHB, and CRMP1 was present at ~30-50% of the observed maternal concentration, while Abs to STIP1 were present at a slightly lower level (**Fig. 2A** and fig. S1B). Given that aAbs were able to

gain access to offspring circulation, we next wanted to examine whether deposition of Ab could be observed in discrete tissues. Since ASD is a neurodevelopmental disorder and several MAR-ASD aAb targets, namely STIP1 and CRMP-family proteins, are upregulated during processes such as neural progenitor cell induction (*15, 64, 65*), we examined Ab deposition in the brains of exposed offspring. Immunohistochemical (IHC) analysis of brain tissue from P2 offspring revealed IgG deposition in the forebrain and cerebellum of MAR-ASD aAb exposed rat pups **(Figs 2B & C)**. Furthermore, IgG reactivity displayed a regional distribution and was enriched in NeuN+ positive cells in the forebrain indicating a preference for IgG binding to post-mitotic neurons **(Fig. 2B)**.

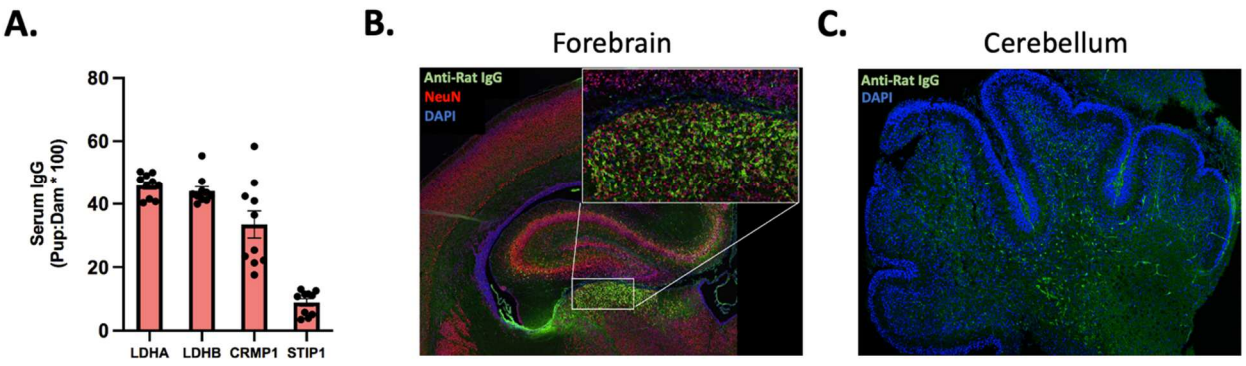

Fig. 2. Transfer of MAR-ASD aAb to offspring. (A) Levels of serum IgG reactive to MAR ASD protein targets in exposed offspring at P2. Data represents offspring ELISA reactivity expressed as a percentage of dam levels. N=10 pups, data expressed as mean +/- SEM. **(B & C)** Representative IHC images of IgG reactivity in the brain of P2 MAR-ASD offspring in both the Forebrain **(B)** and Cerebellum **(C)**. Magnification 20x objective. M.R.B. created animals, conducted ELISA analysis, processed tissue and completed IHC analysis (staining and imaging), as well as figure creation.

To understand if IgG present in the brain may exert effects on target protein expression, we conducted western blot (WB) analysis of regional brain lysates from P2 offspring to examine whether the level of STIP1, CRMP1, or LDH protein is altered in response to MAR-ASD aAb exposure. First, we generated lysates from two brain areas implicated in clinical ASD: the frontal

region and the cerebellum. Then we used standard semi-quantitative WB techniques to evaluate the presence of each protein in offspring brain lysates from MAR-ASD exposed and control animals. In both the frontal region of the brain, as well as in the cerebellum, it appeared that the levels of MAR-ASD aAb target proteins (STIP1, CRMP1, and LDH) were not significantly altered in response to MAR-ASD aAb exposure, as no statistical differences were observed between treatment groups using our methods (fig. S1C-F). Together, these results suggest that MAR-ASD aAbs produced in treated dams can cross into offspring circulation and potentially access the brain.

MAR-ASD aAb exposure results in behavioral deficits in offspring

Changes in species-typical social behavior have emerged as a feature of previous MAR-ASD mouse and non-human primate models (*36, 66*). Therefore, we assessed longitudinal social development in exposed offspring including the three-chambered social approach and novelty task, as well as unconstrained social dyad testing. Additional behavioral assays conducted include evaluation of developmental milestones, isolation-induced pup ultrasonic vocalizations (USVs), elevated-plus maze (EPM), open field, and pre-pulse inhibition (PPI). For brevity, only significant behavioral differences in MAR-ASD offspring are presented in detail.

We found that offspring from MAR-ASD rat dams exhibited behavioral alterations across multiple domains including differences in communicative, social, and stereotyped behaviors. Specifically, we found that MAR-ASD rat offspring produced significantly fewer bouts of maternal-isolation induced USVs at postnatal day 12 (P12) compared to control offspring ($p=0.006$; **Fig. 3A**). Analysis of developmental milestones in these animals revealed that MAR-

ASD rat offspring also had a significantly lower average body temperature (p=0.017; fig. S2A) and increased negative geotaxis (p=0.014; fig. S2B) at P12, suggesting a broad impact of MAR-ASD exposure on offspring development at that timepoint. No sex differences in response to treatment were observed in either USV outcomes or developmental milestones (fig. S2C).

To examine potential differences in the social behavior of MAR-ASD rat offspring compared to controls, we conducted social dyad testing at multiple timepoints. Behavioral outcomes were analyzed using a linear mixed effects model. Results revealed that MAR-ASD rat offspring spent significantly less time engaging in all social interaction behaviors compared to controls (p=0.023, **Fig. 3B**). More specifically, MAR-ASD rats were less likely to engage in social play behavior than control animals (p=0.035) and spent less time playing when they did engage in such behavior (p=0.03, **Fig. 3C**). During the social dyad testing period, we also observed that MAR-ASD rat offspring engaged in self-grooming more frequently than their control counterparts (p=0.028); however, the overall duration of self-grooming did not differ statistically between MAR-ASD and control rats (p=0.641, **Fig. 3D**). No significant differences were seen between sexes for either social play behavior (fig. S2E) or self-grooming (fig. S2F) using our statistical model. Additionally, no significant differences were observed in other post-weaning behaviors conducted on MAR-ASD rat offspring including EPM, social approach and novelty, or PPI. Overall, these data support the concept that that rat offspring exposed to MAR-ASD aAbs display behavioral differences across multiple ASD-relevant domains.

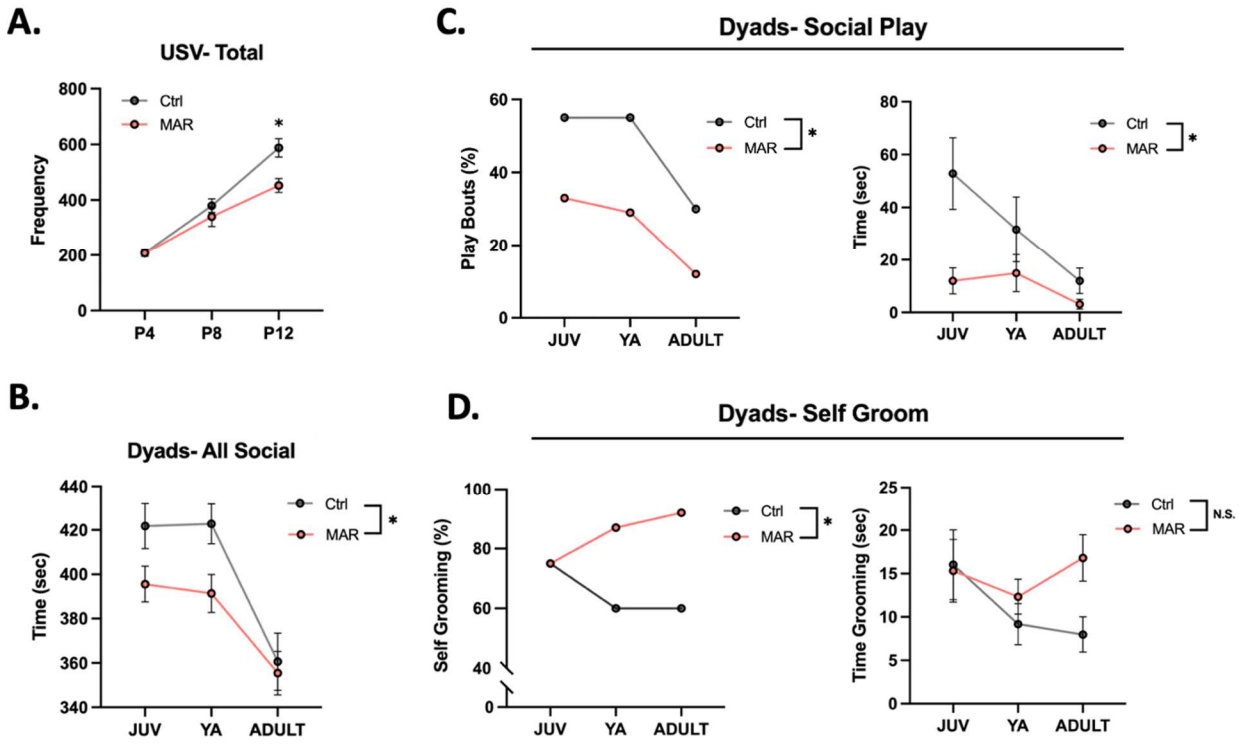

Fig. 3. MAR-ASD aAb exposure alters offspring behavior. (A) Total ultrasonic vocalizations (USVs) recorded at each timepoint, graphed longitudinally by treatment (MAR; N=48, Ctrl; N=40). **(B)** Time spent engaged in social behavior during the social dyads task, measured in seconds and compared between MAR-ASD (MAR) and control (Ctrl) animals. Data are expressed as mean +/- SEM, *p<0.05. **(C)** Proportion of social play bouts by treatment (MAR; JUV (0.33, 95% CI's=0.16, 0.55), YA (0.33, 95% CI's=016, 0.55), ADULT (0.12, 95% CI's=0.03, 0.32), Ctrl; JUV (0.55, 95% CI's=0.31, 0.77), YA (0.55, 95% CI's=0.31, 0.77), ADULT (0.3, 95% CI's=0.12, 0.54) as well as total time spent engaged in social play behavior. Data expressed as mean +/- SEM, *p<0.05. **(D)** The incidence of spontaneous self-grooming behavior by treatment (MAR; JUV (0.75, 95% CI's=0.53, 0.90), YA (0.83, 95% CI's=0.63, 0.95), ADULT (0.92, 95% CI's=0.73, 0.99), Ctrl; JUV (0.75, 95% CI's=0.51, 0.91), YA (0.75, 95% CI's=0.51, 0.91), ADULT (0.6, 95% CI's=0.36, 0.80) as well as total time spent grooming. Data expressed as mean +/- SEM, *p<0.05. MAR; N=24; Ctrl; N=20 for figures B-D. M.R.B. created animals and assisted with final figure creation. S.G., K.K, C.C, A.B., & M.M, conducted behavioral data collection and analysis. M.M. also contributed to figure creation. S.L.T. and D.P. conducted data analysis.

Sex-specific neuroanatomical alterations in MAR-ASD offspring

Data from clinical studies of individuals with ASD suggest differences in both total brain volume (TBV; e.g. macro- or microcephaly; (*67-69*)) and at the regional level across a range of areas from the cerebellum to the frontal lobe, as measured by sMRI (*70, 71*). Therefore, we characterized total and regional brain volumes in MAR-ASD exposed and control rat offspring using longitudinal *in vivo s*MRI acquired at P30 and P70, to understand whether MAR-ASD aAb

exposure results in neuroanatomical differences to better understand the pathobiology of this model.

Despite similar behavioral outcomes among males and females in response to treatment, sex-specific differences in global brain volumes were observed in MAR-ASD offspring. Specifically, while male MAR-ASD rats exhibited a decrease in total brain volume (TBV) compared to sex- and age-matched controls, female MAR-ASD rats instead displayed a volumetric increase in TBV (**Fig. 4A**). These effects in response to treatment appeared persistent in male offspring, as they were observed at both P30 & P70. In contrast, female MAR-ASD offspring displayed significant differences in TBV only at P70. To understand which regional effects may underlie the differences seen in TBV, we conducted both atlas-based segmentation (ABS) and voxel-wise deformation-based morphometry (DBM) analyses of regional brain volumes. Using absolute volumetric measurement (mm^3), ABS data revealed that female MAR-ASD rats displayed significant increases across nearly all brain regions examined (95%, 108/115 regions at 5% FDR) suggesting a global effect of increased brain volume in response to treatment. The effects of treatment in male MAR-ASD animals were comparatively more modest, with only a handful regions passing strict FDR correction ($q<0.05$) (20%, 22/115 regions) (**Fig. 4B**) Furthermore, the direction of regional effects in MAR-ASD rats corroborated those differences seen in TBV. Given the directionality of treatment-induced effects by sex, with females displaying an increase and males a decrease in absolute total and regional volumes, analyzing both sexes together abolished any statistically significant effects (**Fig. 4B;** "Both"). To correct for the fact that absolute volumetric findings are influenced by differences in TBV, as well as to understand any treatment-specific effects lost due to MAR-ASD effects by sex, we also evaluated the dataset

using relative brain volume (% of TBV) as a metric. Comparing relative regional volumes, we found that the number of significantly different regions passing FDR correction was dramatically reduced in both sexes, particularly in females. Only two regions remained significantly different (5% FDR) in relative regional analysis of MAR-ASD female offspring compared to control females, the periaqueductal gray (PAG) and the substantia nigra (**Fig. 4B**). Analysis of MAR-ASD male rats, on the other hand, revealed effects that were restricted to the sensory cortex and the cerebellum, with volumetric increases seen in areas of the sensory cortex alongside decreases in cerebellar volume (**Fig. 4B)**. Additionally, a treatment-specific regional phenotype emerged when evaluating relative volumetric results, in contrast to analysis using absolute volume. Irrespective of sex, MAR-ASD rat offspring exhibited volumetric differences in midbrain and cerebellar regions compared to controls. This included the PAG, inferior colliculus, and pretectum, as well as the inferior cerebellar peduncle and cerebellar grey matter (**Figs. 4C & D**). To complement the ABS analysis, we also carried out a voxel-wise DBM analysis, the results of which broadly supported the data derived using ABS analysis. Specifically, absolute volumetric analysis using a voxel-wise DBM approach showed that clusters of voxels with significantly increased volumes were apparent across the brains of MAR-ASD female offspring (fig. S3). The same analysis of male MAR-ASD offspring did not reveal any voxel clusters that were significantly different by treatment using 5% FDR correction. Relative voxel-wise effects by treatment were mostly absent, with exception to data analyzed when both sexes were combined where clusters of voxels with significantly increased volume were seen in the midbrain and dorsal thalamus, while voxel clusters with significantly decreased volumes were observed in the cerebellum and ventral cortical association areas (fig. S3). Discrepancies between ABS and voxel-wise DBM analysis likely reflect the larger number of comparisons inherent in voxel-wise

analysis compared to atlas-based data where changes are averaged across an entire region of interest (ROI).

Interestingly, despite male MAR-ASD rat offspring displaying a decrease in TBV, mirrored directionally by absolute regional volumes, assessment of relative regional outcomes within male brains revealed a volumetric increase in several regions within the somatosensory cortex (SSC) including the dysgranular zone (S1DZ), a region of interest in other immune-mediated models of ASD (**Figs. 4B, 4D** & fig. S4A); (*72*). Furthermore, comparing our current findings to sMRI data collected in the MAR-ASD mouse model in adulthood, there appeared to be subtle effects on SSC volume in male MAR-ASD mice (*35*). While there were no treatment effects by region in male MAR-ASD mice that passed the stringent FDR cutoff (FDR<5%), six out of nine regions within the primary SSC were significantly different prior to multiple comparison correction ($p<0.05$, $q>0.05$), and these overlapped to a surprising extent with those regions significantly enlarged in male MAR-ASD rats (fig. S4B). Overall, these findings suggest that MAR-ASD exposure results in changes to offspring brain volume that are cross-species, sex-specific, and persistent over time.

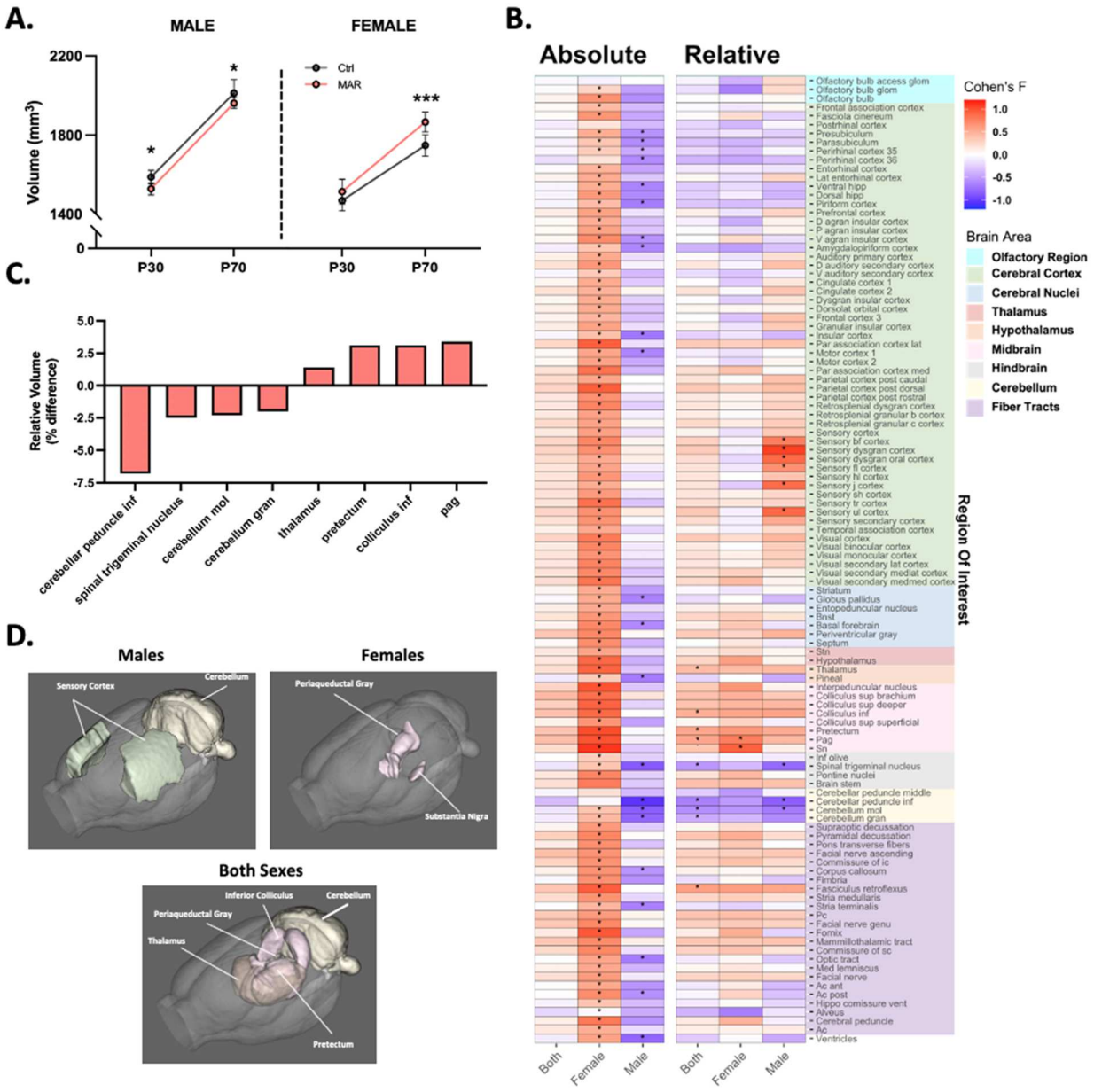

Fig. 4. Altered regional brain volume in MAR-ASD offspring. (A) Total brain volume (mm^3) in MAR-ASD and Ctrl offspring in both sexes at P30 & P70. Data represented as mean +/- SD, * = $p<0.05$, *** = $p<0.001$. MAR ASD; N=6/sex, Ctrl; N=8/sex. **(B)** Heatmap plot of absolute and relative regional volumetric differences in MAR-ASD offspring collapsed between time points. Heatmap scale corresponds to Cohen's F values for the comparisons between MAR-ASD and Ctrl animals for each region. Columns represent data either from both sexes combined ("Both"), or each sex independently. Starred (*) fields represent those comparisons that differed significantly between treatment groups and had a false discovery ratio (FDR) below 5%. Colored blocks on the right y-axis correspond to regional grouping by larger brain areas. **(C)** Graph of brain regions displaying differences by treatment using relative volumetric analysis. Data expressed as percent change with values collapsed between time point and sex. **(D)** Visual representation of brain regions displaying relative volumetric differences in MAR-ASD offspring compared to control animals in males, females, or both sexes combined. Spinal trigeminal nucleus not pictured due to orientation of rendering. Also, subregions within brain area are not broken down (i.e., sensory dysgranular cortex in males) to reduce complexity. M.R.B. created animals, conducted MRI imaging, and assisted

figure creation. A.C.M. conducted data analysis and figure creation; specifically heatmap. E.K. and A.C.V. conducted MRI image registration and analysis as well as figures.

Altered neurometabolites and relationship with structural findings

While collecting sMRI data, we were also able to interrogate the level of various soluble metabolites present in a predefined recording region using proton (^{1}H) magnetic resonance spectroscopy (MRS). This method returns a ^{1}H nuclear magnetic resonance (NMR) spectrogram from which metabolite concentrations can be quantified (*73*). For this study, the recording voxel was placed in the medial prefrontal cortex (mPFC) **(Fig. 5A)**, due to the involvement of this area in ASD (*74, 75*) and previous evidence of neocortical abnormalities in response to MAR-ASD aAb exposure (*37*). Spectral analysis was performed using LCModel software with a basis set of 26 unique metabolites. Following quality control, we were able to confidently analyze 13 of these metabolites and found treatment-specific differences in offspring exposed to MAR-ASD aAbs (fig. S5A). Specifically, we observed an increase in the level of taurine ($p<0.01$) in the mPFC **(Fig. 5B)**, accompanied by a decrease in total choline ($p<0.01$) and glutathione (GSH) ($p<0.05$) in MAR-ASD offspring compared to controls **(Fig. 5B)**. However, it is important to note that when including full width at half maximum (FWHM) as a covariate the differences in GSH levels were no longer significant. The best-fit model used for analysis determined that group differences did not vary by age or sex. A sex stratified representation of the same dataset however revealed that neurometabolite differences in MAR-ASD rat offspring may be driven predominantly by females **(Fig. 5C)**.

To adjust for unknown scaling factors in ^{1}H-MRS acquisition, metabolite data in this study were normalized against total creatine levels (creatine + phosphocreatine (Cr+PCr)). Ratio normalization of signal intensity using creatine is widely used in ^{1}H-MRS due to the strong

signal of creatine in the spectral output and low variability across brain areas and experiments (*73*). To ensure that there were no alterations in creatine levels due to treatment, which might affect results, we also conducted a water-scaled analysis to evaluate raw creatine levels between treatment groups. No significant differences were seen in creatine (Cr), phosphocreatine (PCr), or Cr+PCr between MAR-ASD and control offspring at either time point examined (fig. S5B). Additionally, the results of water-scaled analysis on other metabolites did not differ from creatine-normalized results.

Given that sMRI and ^{1}H-MRS data were collected in tandem, we were able to evaluate the relationship between metabolites and brain volume in exposed offspring. The region within our brain atlas that aligned the closest with the ^{1}H-MRS recording voxel was the cingulate cortex. Therefore, we conducted correlational analysis between the cingulate cortex and those metabolites found to differ significantly by treatment. Interestingly, we observed that taurine displayed a strong negative correlation ($r=-0.75$, $p<0.01$) with cingulate cortex volume in MAR-ASD offspring at P30, a finding that was absent in control animals **(Fig. 5D)**. This finding suggests that higher levels of taurine corresponded to lower cingulate cortex volume. Similarly, a relationship was observed between choline and cingulate volume in MAR-ASD animals that was not present in controls. Specifically that choline displayed a positive correlation to cingulate cortex volume in MAR-ASD offspring ($r=0.58$, $p<0.05$) **(Fig. 5E)** suggesting that higher levels of choline relate to greater regional volume. No significant relationships were seen between metabolites and cingulate cortex volume at P70 or between cingulate cortex volume and the level of glutathione in either MAR-ASD or control offspring **(Fig. 5F)**. Taurine is an organic osmolyte thought to play a role in early inhibitory signaling (*76*), while choline is a precursor to a range of

compounds including acetylcholine, myelin, and cell membrane lipids (*77*). Therefore, differences in taurine and choline could potentially contribute to the altered brain development seen in MAR-ASD offspring. As an additional method to examine this relationship, we compared the development of the cingulate cortex between P30 and P70 within MAR-ASD and control animals. As expected, control offspring displayed a strong positive correlation ($r=0.92$; $p<0.001$) in cingulate cortex volume over time **(Fig. 5G)**, indicating that this region experienced a consistent rate of growth with age. However, offspring exposed to MAR-ASD aAbs did not exhibit the same relationship, as a significant correlation within cingulate cortex volume over time was absent in MAR-ASD animals **(Fig. 5G)**, potentially speaking to dysregulated development of this region in response to treatment.

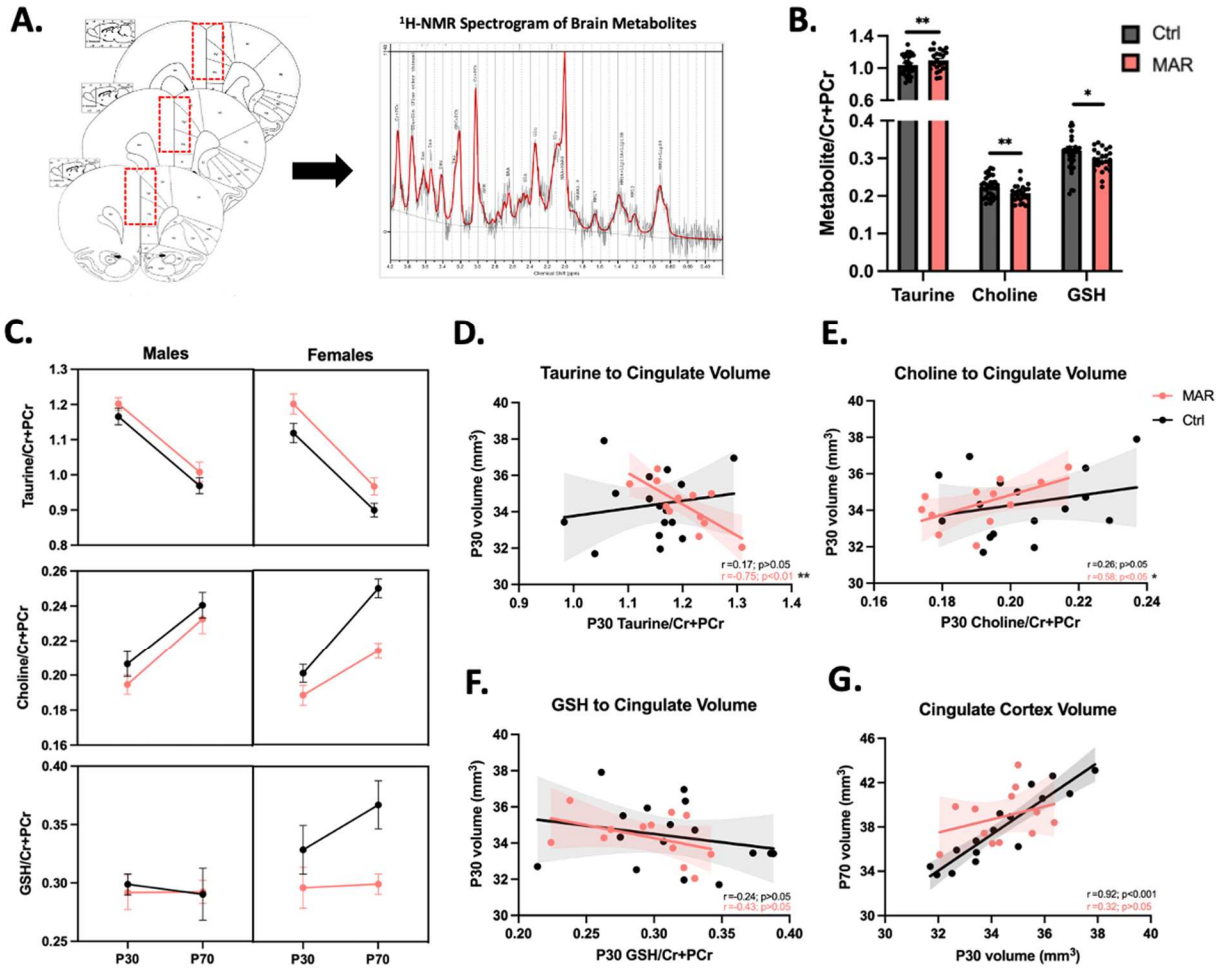

Fig. 5. MAR-ASD exposure alters neurometabolite levels in the mPFC. (A) Diagram detailing anatomical location of voxel placement with rat brain atlas as a backdrop. Also depicted is a representative ^{1}H-NMR spectrogram output that was used for model fitting and analysis. **(B)** Metabolites found to differ significantly in response to treatment including taurine, choline, and glutathione (GSH). **(C)** Metabolite differences split by sex for each metabolite. Metabolite data was collected and analyzed at the time of MR scanning, P30 & P70. Data corresponds to mean +/- SEM, * = $p<0.05$, ** = $p<0.01$. MAR-ASD; N=6/sex, Ctrl; N=8/sex. **(D-F)** Graphs depicting the relationship between metabolite levels and volume of the voxel region at P30 for taurine **(D)**, choline **(E)**, and GSH **(F). (G)** Correlation between cingulate cortex volume at P30 and P70 graphed by treatment. Pearson's r-value and related test statistic reported as a result of correlational analysis **(D-G)**. M.R.B. created animals, conducted MRS acquisition and analysis, as well as figure creation. R.J.M. assisted with MRS analysis and provided technical oversight. D.H. conducted statistical analysis of MRS data.

Discussion

Accumulating evidence supports the concept of maternal aAbs in ASD (*33, 34, 78*). Only recently however, with the creation of robust, translationally-relevant model systems (*36, 79*), are we able to properly investigate the structural and molecular underpinnings of this ASD sub-

phenotype. The first goal of this study was to ensure proper construct validity within the MAR-ASD rat model. To this end we confirmed that aAb production in MAR-ASD rat dams is robust, persistent, and does not result in overt inflammation at the time of breeding. The latter aspect is particularly important as several ASD models exist that include active inflammation during gestation as a driving factor; known as maternal immune activation (MIA) models (*61-63*). This concept is methodologically separate from what is seen in the MAR-ASD model where offspring outcomes are influenced instead by the presence of circulating aAbs in dams.

To support the concept of Ab-induced pathology in the MAR-ASD rat model, we confirmed that antigen-specific IgG was able to cross from dam to offspring in appreciable quantities. Moreover, IgG deposition was observed in the brains of MAR-ASD offspring, with specific regional and cell-type distribution. Normally IgG levels in the adult brain are extremely low, with brain IgG concentrations in adult rats observed to be ~500x lower than that seen in blood plasma (*80*). However, IgG transferred to offspring during gestation can access the brain prior to closure of the blood-brain-barrier (BBB) (*81*) and theoretically persist for some time due to the long half-life of IgG (~3wks) (*82*). Despite recent work suggesting a role for immunoglobulin signaling in glial development (*13*), few studies to date have characterized the extent of IgG deposition in the brain during perinatal development. It is important to note that we did not compare the levels of brain IgG between MAR-ASD and control offspring in this study. Additional work is underway to determine the extent of IgG deposition in the brains of exposed offspring, including region-specific distribution patterns, the range of affected cell types, and the extent to which this differs between treatment and control animals across the lifespan.

Since we were able to detect IgG in the brains of MAR-ASD exposed offspring, we sought to evaluate if the levels of aAb target proteins were altered in response to exposure. A difference in the levels of target proteins could be a proxy for aAb impact on protein viability. WB analysis of either frontal brain or cerebellar lysates suggested that the levels of LDH, STIP1, & CRMP1 proteins were not significantly altered in response to MAR-ASD aAb exposure. While protein levels were found to be similar in MAR-ASD and control offspring, it does not necessarily rule out potential impact of MAR-ASD aAbs on target protein function. Previous epitope mapping of MAR-ASD aAb binding sites reveals that antigenic targets flank key phosphorylation sites important for protein function (*83*). Therefore, future studies will include analysis of target protein phosphorylation status as well as enzymatic function where applicable. Ultimately, it will be key to understand whether MAR-ASD aAbs mediate their effects by binding to target proteins *in situ* or if off-target effects may occur, such as effects at the maternal-fetal interface where impact on placental function may play a role.

As ASD is a behaviorally defined disorder, we examined whether MAR-ASD aAb exposure altered behavioral outcomes in rat offspring. Previous passive transfer models in mice and non-human primates (NHP) revealed changes in behavioral development of offspring following MAR-ASD aAb exposure, including alterations in species-typical social behavior (*66, 84*). Furthermore, an advanced antigen-driven model initially created in mice, revealed that mouse offspring exposed to endogenously produced MAR-ASD aAbs exhibited a decrease social play behavior, an increase self-grooming behavior, and altered USVs across the lifespan (*36*). In this study we replicate those findings in rats, observing a decrease in the time and incidence of social

play behavior, an increase in the percentage of animals exhibiting self-grooming behavior, and a decreased frequency of USVs in early postnatal MAR-ASD rat offspring.

Isolation-induced USVs are often used to characterize early social communication as pups emit these 40kHz calls following maternal separation to communicate with the dam, facilitating pup retrieval. While the functional significance of pup USVs has been debated (*85*), a reduction in USVs may be indicative of early communication deficits and raises the possibility of circuit vulnerability in later social development. In support of this, our study found that MAR-ASD rat offspring displayed both a decrease in USVs at P12 and reduced social play behavior during adolescence.

Evaluation of social behavior was conducted using unconstrained social dyad testing, allowing the test animal to interact freely with a conspecific. In this assay MAR-ASD rat offspring demonstrated a reduction in the amount of time engaged in a composite measure of sociability (i.e. time spent in immediate proximity, investigating or playing with the other animal). Additionally, pronounced group differences were detected in the incidence and duration of social play behavior in MAR-ASD rats compared to controls. Play is important to normal social and cognitive development in many mammals, including rats (*86*), as well as being an intrinsically rewarding behavior. MAR-ASD rats also exhibited a higher incidence of self-grooming behavior during social dyad testing compared to controls, a finding previously observed in MAR-ASD mice (*36*).

To understand what may be driving these alterations in behavior, we conducted longitudinal sMRI analysis of offspring brain volume at P30 & P70. These ages were chosen to represent a pre-pubertal and a post-pubertal time point, respectively. The goal was to explore the potential contribution of sex hormones on the effects seen, as certain brain regions have been shown to exhibit sexually dimorphic volumetric changes following puberty in rodents (*87*). However, there were no significant treatment x time interactions on regional volumes in either sex of MAR-ASD rat offspring that passed FDR correction (FDR<5%), suggesting that either the effects of treatment did not differ by age, or we were unable to detect those differences. Effect size (partial eta squared) analysis of treatment x time interactions would support the latter argument as a few regions displayed large effect sizes at one time point opposed to another, particularly in male rats. For example in subregions of the somatosensory cortex, relative volumetric differences appeared more pronounced at P70 (fig S4A). Analysis of TBV across time in rat offspring, revealed sex-specific effects in that male MAR-ASD rats displayed a decrease in TBV while females displayed an increase in TBV. These results are consistent with our previous findings in mice, where we observed brain-wide increases in total and regional brain volumes in female mice exposed to MAR-ASD aAbs. No differences in brain volume however were observed in male MAR-ASD mice. The discrepancy between these findings may be attributable to species-specific responses to aAb exposure and brain development trajectories between mice and rats (*88-90*).

Differences in regional volumes following MAR-ASD aAb exposure also varied depending on sex and the analysis method employed. Specifically, using ABS, nearly every brain region in female rats displayed an absolute volumetric increase, reflecting the increases in TBV in these

animals and suggestive of isometric regional scaling (i.e. regions increase linearly with TBV). However, when correcting for TBV the affected regions passing FDR cutoff (<5%) were reduced to two: the PAG and the SN. This may reflect allometric scaling of these regions relative to TBV that could be indicative of abnormal neurodevelopment and/or connectivity (*91*). The PAG and SN are both located in the midbrain, with evidence for bidirectional connectivity between these regions (*92, 93*). While the SN is known for its role in movement disorders and reward signaling (*94*), and the PAG in processing of fear memories (*95*), evidence suggests that both regions are important for descending pain perception (*96, 97*). Interestingly, altered pain sensitivity is a known phenomenon in ASD (*98*). Whether this could be a result of modified descending pain pathways over effects on higher order sensory processing remains to be determined. Further, the PAG is also thought to be important for controlling a broad range of social behaviors, as part of the "social behavior neural network" (*99*). This in addition to acting as a gate for ultrasonic vocalization production (*100*), contextualizes the potential relevance of the PAG in respect to the behavioral differences observed in this study. Similar to females, male MAR-ASD rats showed a substantial reduction in the number of affected brain regions after correcting for total brain volume, again suggesting that the majority of brain regions in these animals were normally scaled to TBV. Differences in relative brain volumes were observed within regions of the cerebellum and sensory cortex in males, with a surprising increase in brain volume seen in regions of the sensory cortex, despite a decrease in TBV in male MAR-ASD rats. Interestingly, recent research has reported substantial connectivity between the cerebellum and sensorimotor/prefrontal areas in mice and rats (*101, 102*). Additionally, these cerebellar-cortical circuits have been shown to regulate social and repetitive behaviors (*102, 103*). When examining both sexes together a treatment-specific phenotype was apparent in MAR-ASD rat offspring

irrespective of sex, defined by volumetric increases in the thalamus and midbrain regions accompanied by a decrease in cerebellar volume. Functional connectivity studies will be necessary to understand whether these changes may reflect altered signaling between these regions.

Analysis of ^{1}H-MRS data collected from MAR-ASD and control offspring showed an increase in taurine alongside decreased levels of choline-containing compounds and glutathione in the mPFC of MAR-ASD aAb exposed animals. Taurine is thought to be a gliotransmitter in the brain, enriched in astrocytes, and found to influence a range of neurodevelopmental events, including: oligodendrocyte maturation, neural progenitor cell (NPC) proliferation, and synapse development in animal studies (*104-106*). Interestingly, both plasma and brain taurine levels have been implicated in neuropsychiatric and neurodegenerative disorders such as ASD (*107*), schizophrenia (*61*), and Alzheimer's Disease (*108*). It is important to note that taurine, and all other metabolites measurable using MRS, are indicative of the metabolite in its soluble form as rotational movement is needed within the molecule for proton resonance (*73*). This is particularly important when interpreting the reduction in choline seen in MAR-ASD rat offspring. Choline-containing compounds are a major component of the cell membrane. However, the choline signal measurable via MRS is predominately reflective of phosphocholine and glycerophosphocholine involved in active membrane turnover and, to a lesser extent, acetylcholine in the brain (*73, 77*). Choline-containing compounds also act as precursors for the synthesis of myelin. Since myelination has been shown to be a dynamic process across the lifespan (*109*), and white matter abnormalities are a common finding in ASD (*110, 111*). It could be the case that altered choline levels may also reflect effects on myelin turnover. Finally, glutathione (GSH) levels were found

to be reduced in MAR-ASD rat offspring compared to control animals. GSH is a potent antioxidant that maintains the redox state in cells and protects against cellular stress (*112*). Oxidative stress has long been implicated in ASD, with lower levels of GSH seen in the plasma (*113*) and brain (*114*) of individuals with ASD.

Interestingly, taurine and GSH fall within the same metabolic pathway: the cysteine:methionine metabolic pathway, both being downstream products of cysteine metabolism **(Fig. 6)**. Cysteine metabolism also results in the production of pyruvate, although pyruvate produced via this mechanism is only a minor contributor to the overall pool of pyruvate within a cell. Of interest, the interconversion of pyruvate to lactate, crucial for glycolysis, is catalyzed by the enzyme LDH. LDHA and LDHB are clinically relevant protein targets for MAR-ASD aAbs and were used as antigens to develop the MAR-ASD rodent model described herein. Moreover, existing literature suggests that taurine is capable of modifying the expression of a range of targets involved in cellular stress including LDH, CRMP-family genes, and chaperone molecules such as STUB1 (STIP1 homology and U-box containing protein 1) (*115-117*). Extrapolating upon this, it could be that aAb targeting of LDHA, LDHB, CRMP1, STIP1, or homologs thereof, may affect protein function. For example, aAbs to LDH could impact the ability to facilitate the pyruvate:lactate conversion, resulting in a metabolic imbalance and effects on brain development **(Fig. 6)**.

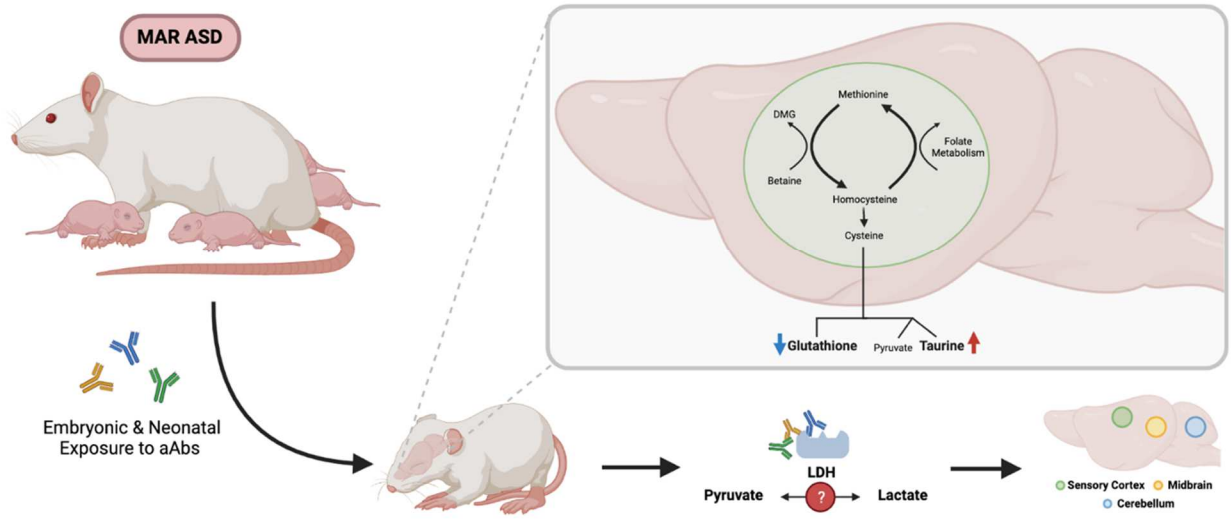

Fig. 6. Schematic depicting the effects of MAR-ASD aAb exposure on offspring. Antibodies generated by dams transfer to offspring during gestation and impact molecules involved in the cysteine metabolic pathway. This could be the result of aAb effects on target proteins or those involved in this pathway thereby affecting the homeostatic balance and leading to the noted changes in brain volume. M.R.B. conducted figure creation.

Inherent limitations exist in interpreting the data discussed in this study. Firstly, we hypothesize that MAR-ASD aAbs mediate their effects through binding to protein targets and affect protein expression or function. We did not however find evidence of altered MAR-ASD protein expression levels using WB analysis of brain tissue. Of note, this does not discount the possibility that aAbs could alter protein phosphorylation status and protein function directly, an area of active examination. Additionally, we have yet to complete a thorough characterization of brain aAb deposition by treatment. It could be that MAR-ASD pathology is actually a result of indirect mechanisms rather than direct effects on the brain, such as through alterations in placental signaling which have been linked to disrupted brain development and behavior in other studies (*118*). Finally, due to behavioral testing across the lifespan and the nature of longitudinal imaging, separate cohorts were used for sMRI/S and behavior in the current study. Therefore, we are unable to make any direct sMRI/S-behavioral associations and can only theorize on the relationship between regional volumetric differences and behavioral outcomes. Since we only

observed behavioral differences in a handful of tests, future studies can be more refined in scope allowing greater insight in brain/behavior relationships and expansion of sample sizes to detect more subtle treatment effects.

In conclusion, this study reveals that gestational exposure of rats to MAR-ASD aAbs results in longitudinal, sex-specific effects on offspring outcomes including behavior, brain structure, and neurometabolism. Strengths of this study include the translational nature of the methods used, particularly regarding sMRI and ^{1}H-MRS, for which there exists a clinical literature base with respect to ASD. Future work will be focused on understanding the molecular mechanisms underlying MAR-ASD neuropathology.

List of Supplementary Materials

Figs. S1-S5

References

1. M. J. Carson, J. M. Doose, B. Melchior, C. D. Schmid, C. C. Ploix, CNS immune privilege: hiding in plain sight. *Immunological reviews* **213**, 48-65 (2006).
2. A. Louveau, J. Herz, M. N. Alme, A. F. Salvador, M. Q. Dong, K. E. Viar, S. G. Herod, J. Knopp, J. C. Setliff, A. L. Lupi, S. Da Mesquita, E. L. Frost, A. Gaultier, T. H. Harris, R. Cao, S. Hu, J. R. Lukens, I. Smirnov, C. C. Overall, G. Oliver, J. Kipnis, CNS lymphatic drainage and neuroinflammation are regulated by meningeal lymphatic vasculature. *Nat Neurosci* **21**, 1380-1391 (2018).
3. A. Louveau, I. Smirnov, T. J. Keyes, J. D. Eccles, S. J. Rouhani, J. D. Peske, N. C. Derecki, D. Castle, J. W. Mandell, K. S. Lee, T. H. Harris, J. Kipnis, Structural and functional features of central nervous system lymphatic vessels. *Nature* **523**, 337-341 (2015).
4. K. Alves de Lima, J. Rustenhoven, S. Da Mesquita, M. Wall, A. F. Salvador, I. Smirnov, G. Martelossi Cebinelli, T. Mamuladze, W. Baker, Z. Papadopoulos, M. B. Lopes, W. S. Cao, X. S. Xie, J. Herz, J. Kipnis, Meningeal gammadelta T cells regulate anxiety-like behavior via IL-17a signaling in neurons. *Nat Immunol* **21**, 1421-1429 (2020).

5. M. Ribeiro, H. C. Brigas, M. Temido-Ferreira, P. A. Pousinha, T. Regen, C. Santa, J. E. Coelho, I. Marques-Morgado, C. A. Valente, S. Omenetti, B. Stockinger, A. Waisman, B. Manadas, L. V. Lopes, B. Silva-Santos, J. C. Ribot, Meningeal gammadelta T cell-derived IL-17 controls synaptic plasticity and short-term memory. *Sci Immunol* **4**, (2019).
6. N. C. Derecki, A. N. Cardani, C. H. Yang, K. M. Quinnies, A. Crihfield, K. R. Lynch, J. Kipnis, Regulation of learning and memory by meningeal immunity: a key role for IL-4. *J Exp Med* **207**, 1067-1080 (2010).
7. A. J. Filiano, Y. Xu, N. J. Tustison, R. L. Marsh, W. Baker, I. Smirnov, C. C. Overall, S. P. Gadani, S. D. Turner, Z. Weng, S. N. Peerzade, H. Chen, K. S. Lee, M. M. Scott, M. P. Beenhakker, V. Litvak, J. Kipnis, Unexpected role of interferon-gamma in regulating neuronal connectivity and social behaviour. *Nature* **535**, 425-429 (2016).
8. D. J. Fernandes, S. Spring, C. Corre, A. Tu, L. R. Qiu, C. Hammill, D. A. Vousden, T. L. Spencer Noakes, B. J. Nieman, D. M. E. Bowdish, J. A. Foster, M. R. Palmert, J. P. Lerch, Mouse models of immune dysfunction: their neuroanatomical differences reflect their anxiety-behavioural phenotype. *Mol Psychiatry*, (2022).
9. K. C. Rilett, M. Friedel, J. Ellegood, R. N. MacKenzie, J. P. Lerch, J. A. Foster, Loss of T cells influences sex differences in behavior and brain structure. *Brain Behav Immun* **46**, 249-260 (2015).
10. X. Gao, C. Xu, N. Asada, P. S. Frenette, The hematopoietic stem cell niche: from embryo to adult. *Development* **145**, (2018).
11. J. P. Lopez-Atalaya, K. E. Askew, A. Sierra, D. Gomez-Nicola, Development and maintenance of the brain's immune toolkit: Microglia and non-parenchymal brain macrophages. *Dev Neurobiol* **78**, 561-579 (2018).
12. K. Alves de Lima, J. Rustenhoven, S. Da Mesquita, M. Wall, A. F. Salvador, I. Smirnov, G. Martelossi Cebinelli, T. Mamuladze, W. Baker, Z. Papadopoulos, M. B. Lopes, W. S. Cao, X. S. Xie, J. Herz, J. Kipnis, Meningeal γδ T cells regulate anxiety-like behavior via IL-17a signaling in neurons. *Nature Immunology*, (2020).
13. S. Tanabe, T. Yamashita, B-1a lymphocytes promote oligodendrogenesis during brain development. *Nat Neurosci* **21**, 506-516 (2018).
14. A. Zelco, V. Borjesson, J. K. de Kanter, C. Lebrero-Fernandez, V. M. Lauschke, E. Rocha-Ferreira, G. Nilsson, S. Nair, P. Svedin, M. Bemark, H. Hagberg, C. Mallard, F. C. P. Holstege, X. Wang, Single-cell atlas reveals meningeal leukocyte heterogeneity in the developing mouse brain. *Genes Dev* **35**, 1190-1207 (2021).
15. A. P. Association, Diagnostic and Statistical Manual of Mental Disorders., (2013).
16. J. Horder, M. M. Petrinovic, M. A. Mendez, A. Bruns, T. Takumi, W. Spooren, G. J. Barker, B. Kunnecke, D. G. Murphy, Glutamate and GABA in autism spectrum disorder-a translational magnetic resonance spectroscopy study in man and rodent models. *Transl Psychiatry* **8**, 106 (2018).
17. T. C. Ford, R. Nibbs, D. P. Crewther, Glutamate/GABA+ ratio is associated with the psychosocial domain of autistic and schizotypal traits. *PLoS One* **12**, e0181961 (2017).
18. A. El-Ansary, L. Al-Ayadhi, GABAergic/glutamatergic imbalance relative to excessive neuroinflammation in autism spectrum disorders. *Journal of Neuroinflammation* **11**, (2014).
19. A. Pecorelli, F. Ferrara, N. Messano, V. Cordone, M. L. Schiavone, F. Cervellati, B. Woodby, C. Cervellati, J. Hayek, G. Valacchi, Alterations of mitochondrial

bioenergetics, dynamics, and morphology support the theory of oxidative damage involvement in autism spectrum disorder. *The FASEB Journal* **34**, 6521-6538 (2020).
20. C. Giulivi, Y.-F. Zhang, A. Omanska-Klusek, C. Ross-Inta, S. Wong, I. Hertz-Picciotto, F. Tassone, I. N. Pessah, Mitochondrial Dysfunction in Autism. *JAMA* **304**, 2389 (2010).
21. J. S. Orozco, I. Hertz-Picciotto, L. Abbeduto, C. M. Slupsky, Metabolomics analysis of children with autism, idiopathic-developmental delays, and Down syndrome. *Transl Psychiatry* **9**, 243 (2019).
22. J. Grove, S. Ripke, T. D. Als, M. Mattheisen, R. K. Walters, H. Won, J. Pallesen, E. Agerbo, O. A. Andreassen, R. Anney, S. Awashti, R. Belliveau, F. Bettella, J. D. Buxbaum, J. Bybjerg-Grauholm, M. Bækvad-Hansen, F. Cerrato, K. Chambert, J. H. Christensen, C. Churchhouse, K. Dellenvall, D. Demontis, S. De Rubeis, B. Devlin, S. Djurovic, A. L. Dumont, J. I. Goldstein, C. S. Hansen, M. E. Hauberg, M. V. Hollegaard, S. Hope, D. P. Howrigan, H. Huang, C. M. Hultman, L. Klei, J. Maller, J. Martin, A. R. Martin, J. L. Moran, M. Nyegaard, T. Nærland, D. S. Palmer, A. Palotie, C. B. Pedersen, M. G. Pedersen, T. Dpoterba, J. B. Poulsen, B. S. Pourcain, P. Qvist, K. Rehnström, A. Reichenberg, J. Reichert, E. B. Robinson, K. Roeder, P. Roussos, E. Saemundsen, S. Sandin, F. K. Satterstrom, G. Davey Smith, H. Stefansson, S. Steinberg, C. R. Stevens, P. F. Sullivan, P. Turley, G. B. Walters, X. Xu, K. Stefansson, D. H. Geschwind, M. Nordentoft, D. M. Hougaard, T. Werge, O. Mors, P. B. Mortensen, B. M. Neale, M. J. Daly, A. D. Børglum, Identification of common genetic risk variants for autism spectrum disorder. *Nature Genetics* **51**, 431-444 (2019).
23. W. E. Heavner, S. E. P. Smith, Resolving the Synaptic versus Developmental Dichotomy of Autism Risk Genes. *Trends in Neurosciences* **43**, 227-241 (2020).
24. T. Žigman, D. Petković Ramadža, G. Šimić, I. Barić, Inborn Errors of Metabolism Associated With Autism Spectrum Disorders: Approaches to Intervention. *Front Neurosci* **15**, 673600 (2021).
25. M. Arenella, G. Cadby, W. De Witte, R. M. Jones, A. J. Whitehouse, E. K. Moses, A. Fornito, M. A. Bellgrove, Z. Hawi, B. Johnson, J. Tiego, J. K. Buitelaar, L. A. Kiemeney, G. Poelmans, J. Bralten, Potential role for immune-related genes in autism spectrum disorders: Evidence from genome-wide association meta-analysis of autistic traits. *Autism*, 136236132110195 (2021).
26. S. Nazeen, N. P. Palmer, B. Berger, I. S. Kohane, Integrative analysis of genetic data sets reveals a shared innate immune component in autism spectrum disorder and its co-morbidities. *Genome Biology* **17**, (2016).
27. C. Cheroni, N. Caporale, G. Testa, Autism spectrum disorder at the crossroad between genes and environment: contributions, convergences, and interactions in ASD developmental pathophysiology. *Mol Autism* **11**, 69 (2020).
28. V. Mazina, J. Gerdts, S. Trinh, K. Ankenman, T. Ward, M. Y. Dennis, S. Girirajan, E. E. Eichler, R. Bernier, Epigenetics of Autism-related Impairment. *Journal of Developmental & Behavioral Pediatrics* **36**, 61-67 (2015).
29. S. Jain, R. J. Baer, C. E. McCulloch, E. Rogers, L. Rand, L. Jelliffe-Pawlowski, X. Piao, Association of Maternal Immune Activation during Pregnancy and Neurologic Outcomes in Offspring. *The Journal of Pediatrics* **238**, 87-93.e83 (2021).
30. L. A. Croen, Y. Qian, P. Ashwood, O. Zerbo, D. Schendel, J. Pinto□Martin, M. Daniele Fallin, S. Levy, L. A. Schieve, M. Yeargin□Allsopp, K. R. Sabourin, J. L. Ames,

Infection and Fever in Pregnancy and Autism Spectrum Disorders: Findings from the Study to Explore Early Development. *Autism Research* **12**, 1551-1561 (2019).
31. K. L. Jones, L. A. Croen, C. K. Yoshida, L. Heuer, R. Hansen, O. Zerbo, G. N. Delorenze, M. Kharrazi, R. Yolken, P. Ashwood, J. Van De Water, Autism with intellectual disability is associated with increased levels of maternal cytokines and chemokines during gestation. *Molecular Psychiatry* **22**, 273-279 (2017).
32. J. K. Grether, P. Ashwood, J. Van de Water, R. H. Yolken, M. C. Anderson, A. R. Torres, J. B. Westover, T. Sweeten, R. L. Hansen, M. Kharrazi, L. A. Croen, Prenatal and Newborn Immunoglobulin Levels from Mother-Child Pairs and Risk of Autism Spectrum Disorders. *Front Neurosci* **10**, 218 (2016).
33. A. Ramirez-Celis, M. Becker, M. Nuño, J. Schauer, N. Aghaeepour, J. Van de Water, Risk Assessment Analysis for Maternal Autoantibody Related Autism (MAR-ASD): A Subtype of Autism. *Molecular Psychiatry*, (2020).
34. D. Braunschweig, P. Krakowiak, P. Duncanson, R. Boyce, R. L. Hansen, P. Ashwood, I. Hertz-Picciotto, I. N. Pessah, J. Van de Water, Autism-specific maternal autoantibodies recognize critical proteins in developing brain. *Transl Psychiatry* **3**, e277 (2013).
35. M. R. Bruce, K. L. Jones, A. C. Vernon, J. L. Silverman, J. N. Crawley, J. Ellegood, J. P. Lerch, J. Van De Water, Sexually dimorphic neuroanatomical differences relate to ASD-relevant behavioral outcomes in a maternal autoantibody mouse model. *Molecular Psychiatry*, (2021).
36. K. L. Jones, M. C. Pride, E. Edmiston, M. Yang, J. L. Silverman, J. N. Crawley, J. Van de Water, Autism-specific maternal autoantibodies produce behavioral abnormalities in an endogenous antigen-driven mouse model of autism. *Mol Psychiatry*, (2018).
37. V. Martinez-Cerdeno, J. Camacho, E. Fox, E. Miller, J. Ariza, D. Kienzle, K. Plank, S. C. Noctor, J. Van de Water, Prenatal Exposure to Autism-Specific Maternal Autoantibodies Alters Proliferation of Cortical Neural Precursor Cells, Enlarges Brain, and Increases Neuronal Size in Adult Animals. *Cereb Cortex* **26**, 374-383 (2016).
38. C. W. Nordahl, D. Braunschweig, A. M. Iosif, A. Lee, S. Rogers, P. Ashwood, D. G. Amaral, J. Van de Water, Maternal autoantibodies are associated with abnormal brain enlargement in a subgroup of children with autism spectrum disorder. *Brain Behav Immun* **30**, 61-65 (2013).
39. B. Ellenbroek, J. Youn, Rodent models in neuroscience research: is it a rat race? *Dis Model Mech* **9**, 1079-1087 (2016).
40. M. Yang, J. L. Silverman, J. N. Crawley, Automated Three□Chambered Social Approach Task for Mice. *Current Protocols in Neuroscience* **56**, (2011).
41. E. L. Berg, N. A. Copping, J. K. Rivera, M. C. Pride, M. Careaga, M. D. Bauman, R. F. Berman, P. J. Lein, H. Harony-Nicolas, J. D. Buxbaum, J. Ellegood, J. P. Lerch, M. Wöhr, J. L. Silverman, Developmental social communication deficits in the Shank3 rat model of phelan-mcdermid syndrome and autism spectrum disorder. *Autism Research* **11**, 587-601 (2018).
42. K. M. Ku, R. K. Weir, J. L. Silverman, R. F. Berman, M. D. Bauman, Behavioral Phenotyping of Juvenile Long-Evans and Sprague-Dawley Rats: Implications for Preclinical Models of Autism Spectrum Disorders. *PLoS One* **11**, e0158150 (2016).
43. J. L. Silverman, A. Thurm, S. B. Ethridge, M. M. Soller, S. P. Petkova, T. Abel, M. D. Bauman, E. S. Brodkin, H. Harony-Nicolas, M. Wöhr, A. Halladay, Reconsidering

animal models used to study autism spectrum disorder: Current state and optimizing future. *Genes, brain, and behavior*, e12803 (2022).
44. R Core Team. (R Foundation for Statistical Computing, Vienna, Austria, 2022).
45. S. G. Self, K.-Y. Liang, Asymptotic Properties of Maximum Likelihood Estimators and Likelihood Ratio Tests under Nonstandard Conditions. *Journal of the American Statistical Association* **82**, 605-610 (1987).
46. J. Hennig, A. Nauerth, H. Friedburg, RARE imaging: A fast imaging method for clinical MR. *Magnetic Resonance in Medicine* **3**, 823-833 (1986).
47. P. A. Bottomley, Spatial Localization in NMR Spectroscopy in Vivo. *Annals of the New York Academy of Sciences* **508**, 333-348 (1987).
48. I. Tkác, Z. Starcuk, I. Y. Choi, R. Gruetter, In vivo 1H NMR spectroscopy of rat brain at 1 ms echo time. *Magn Reson Med* **41**, 649-656 (1999).
49. M. Jenkinson, C. F. Beckmann, T. E. J. Behrens, M. W. Woolrich, S. M. Smith, FSL. *NeuroImage* **62**, 782-790 (2012).
50. B. B. Avants, N. J. Tustison, G. Song, P. A. Cook, A. Klein, J. C. Gee, A reproducible evaluation of ANTs similarity metric performance in brain image registration. *NeuroImage* **54**, 2033-2044 (2011).
51. T. C Wood, QUIT: QUantitative Imaging Tools. *Journal of Open Source Software* **3**, 656 (2018).
52. N. J. Tustison, B. B. Avants, P. A. Cook, Z. Yuanjie, A. Egan, P. A. Yushkevich, J. C. Gee, N4ITK: Improved N3 Bias Correction. *IEEE Transactions on Medical Imaging* **29**, 1310-1320 (2010).
53. B. B. Avants, P. Yushkevich, J. Pluta, D. Minkoff, M. Korczykowski, J. Detre, J. C. Gee, The optimal template effect in hippocampus studies of diseased populations. *NeuroImage* **49**, 2457-2466 (2010).
54. I. Oguz, H. Zhang, A. Rumple, M. Sonka, RATS: Rapid Automatic Tissue Segmentation in rodent brain MRI. *Journal of Neuroscience Methods* **221**, 175-182 (2014).
55. P. A. Valdés-Hernández, A. Sumiyoshi, H. Nonaka, R. Haga, E. Aubert-Vásquez, T. Ogawa, Y. Iturria-Medina, J. J. Riera, R. Kawashima, An in vivo MRI Template Set for Morphometry, Tissue Segmentation, and fMRI Localization in Rats. *Front Neuroinform* **5**, 26 (2011).
56. E. A. Papp, T. B. Leergaard, E. Calabrese, G. A. Johnson, J. G. Bjaalie, Waxholm Space atlas of the Sprague Dawley rat brain. *Neuroimage* **97**, 374-386 (2014).
57. W.-L. Kuan, K. Stott, X. He, T. C. Wood, S. Yang, J. C. F. Kwok, K. Hall, Y. Zhao, O. Tietz, F. I. Aigbirhio, A. C. Vernon, R. A. Barker, Systemic α-synuclein injection triggers selective neuronal pathology as seen in patients with Parkinson's disease. *Molecular Psychiatry* **26**, 556-567 (2021).
58. W. R. Crum, S. J. Sawiak, W. Chege, J. D. Cooper, S. C. R. Williams, A. C. Vernon, Evolution of structural abnormalities in the rat brain following in utero exposure to maternal immune activation: A longitudinal in vivo MRI study. *Brain Behav Immun* **63**, 50-59 (2017).
59. M. McFarquhar, S. McKie, R. Emsley, J. Suckling, R. Elliott, S. Williams, Multivariate and repeated measures (MRM): A new toolbox for dependent and multimodal group-level neuroimaging data. *Neuroimage* **132**, 373-389 (2016).
60. M. Kinoshita, A. C. Ross, Quantitative Analysis of Immunoglobulin G Subclasses in the Rat. *Journal of Immunoassay* **14**, 149-166 (1993).

61. A. C. Vernon, P. W. So, D. J. Lythgoe, W. Chege, J. D. Cooper, S. C. Williams, S. Kapur, Longitudinal in vivo maturational changes of metabolites in the prefrontal cortex of rats exposed to polyinosinic-polycytidylic acid in utero. *Eur Neuropsychopharmacol* **25**, 2210-2220 (2015).
62. P. A. Garay, E. Y. Hsiao, P. H. Patterson, A. K. McAllister, Maternal immune activation causes age- and region-specific changes in brain cytokines in offspring throughout development. *Brain Behav Immun* **31**, 54-68 (2013).
63. S. E. P. Smith, J. Li, K. Garbett, K. Mirnics, P. H. Patterson, Maternal Immune Activation Alters Fetal Brain Development through Interleukin-6. *Journal of Neuroscience* **27**, 10695-10702 (2007).
64. K. Tokuda, Y. Kuramitsu, B. Byron, T. Kitagawa, N. Tokuda, D. Kobayashi, M. Nagayama, N. Araki, K. H. Sonoda, K. Nakamura, Up-regulation of DRP-3 long isoform during the induction of neural progenitor cells by glutamate treatment in the ex vivo rat retina. *Biochem Biophys Res Commun* **463**, 593-599 (2015).
65. T. G. Santos, I. R. Silva, B. Costa-Silva, A. P. Lepique, V. R. Martins, M. H. Lopes, Enhanced Neural Progenitor/Stem Cells Self-Renewal via the Interaction of Stress-Inducible Protein 1 with the Prion Protein. *STEM CELLS* **29**, 1126-1136 (2011).
66. M. D. Bauman, A. M. Iosif, P. Ashwood, D. Braunschweig, A. Lee, C. M. Schumann, J. Van de Water, D. G. Amaral, Maternal antibodies from mothers of children with autism alter brain growth and social behavior development in the rhesus monkey. *Transl Psychiatry* **3**, e278 (2013).
67. M. Cederlund, Microcephaly in preschool children with Autism Spectrum Disorder. *Research in Autism Spectrum Disorders* **88**, 101845 (2021).
68. S. Klein, P. Sharifi-Hannauer, J. A. Martinez-Agosto, Macrocephaly as a Clinical Indicator of Genetic Subtypes in Autism. *Autism Research* **6**, 51-56 (2013).
69. E. Fombonne, B. Rogé, J. Claverie, S. Courty, J. Frémolle, Microcephaly and macrocephaly in autism. *J Autism Dev Disord* **29**, 113-119 (1999).
70. Y. Xie, X. Zhang, F. Liu, W. Qin, J. Fu, K. Xue, C. Yu, Brain mRNA Expression Associated with Cortical Volume Alterations in Autism Spectrum Disorder. *Cell Reports* **32**, 108137 (2020).
71. A. M. D'Mello, D. Crocetti, S. H. Mostofsky, C. J. Stoodley, Cerebellar gray matter and lobular volumes correlate with core autism symptoms. *NeuroImage: Clinical* **7**, 631-639 (2015).
72. Y. Shin Yim, A. Park, J. Berrios, M. Lafourcade, L. M. Pascual, N. Soares, J. Yeon Kim, S. Kim, H. Kim, A. Waisman, D. R. Littman, I. R. Wickersham, M. T. Harnett, J. R. Huh, G. B. Choi, Reversing behavioural abnormalities in mice exposed to maternal inflammation. *Nature* **549**, 482-487 (2017).
73. M. H. Buonocore, R. J. Maddock, Magnetic resonance spectroscopy of the brain: a review of physical principles and technical methods. *Rev Neurosci* **26**, 609-632 (2015).
74. I. Kurochkin, E. Khrameeva, A. Tkachev, V. Stepanova, A. Vanyushkina, E. Stekolshchikova, Q. Li, D. Zubkov, P. Shichkova, T. Halene, L. Willmitzer, P. Giavalisco, S. Akbarian, P. Khaitovich, Metabolome signature of autism in the human prefrontal cortex. *Communications Biology* **2**, (2019).
75. E. Courchesne, P. R. Mouton, M. E. Calhoun, K. Semendeferi, C. Ahrens-Barbeau, M. J. Hallet, C. C. Barnes, K. Pierce, Neuron Number and Size in Prefrontal Cortex of Children With Autism. *JAMA* **306**, 2001 (2011).

76. T. Furukawa, J. Yamada, T. Akita, Y. Matsushima, Y. Yanagawa, A. Fukuda, Roles of taurine-mediated tonic GABAA receptor activation in the radial migration of neurons in the fetal mouse cerebral cortex. *Front Cell Neurosci* **8**, 88 (2014).
77. T. C. Ford, D. P. Crewther, A Comprehensive Review of the (1)H-MRS Metabolite Spectrum in Autism Spectrum Disorder. *Front Mol Neurosci* **9**, 14 (2016).
78. P. Dalton, R. Deacon, A. Blamire, M. Pike, I. McKinlay, J. Stein, P. Styles, A. Vincent, Maternal neuronal antibodies associated with autism and a language disorder. *Ann Neurol* **53**, 533-537 (2003).
79. C. Bagnall-Moreau, P. T. Huerta, D. Comoletti, A. La-Bella, R. Berlin, C. Zhao, B. T. Volpe, B. Diamond, L. Brimberg, In utero exposure to endogenous maternal polyclonal anti-Caspr2 antibody leads to behavioral abnormalities resembling autism spectrum disorder in male mice. *Scientific Reports* **10**, (2020).
80. H. Y. Chang, K. Morrow, E. Bonacquisti, W. Zhang, D. K. Shah, Antibody pharmacokinetics in rat brain determined using microdialysis. *MAbs* **10**, 843-853 (2018).
81. C. Kowal, A. Athanassiou, H. Chen, B. Diamond, Maternal antibodies and developing blood–brain barrier. *Immunologic Research* **63**, 18-25 (2015).
82. N. L. Dirks, B. Meibohm, Population Pharmacokinetics of Therapeutic Monoclonal Antibodies. *Clinical Pharmacokinetics* **49**, 633-659 (2010).
83. E. Edmiston, K. L. Jones, T. Vu, P. Ashwood, J. Van de Water, Identification of the antigenic epitopes of maternal autoantibodies in autism spectrum disorders. *Brain Behav Immun* **69**, 399-407 (2018).
84. D. Braunschweig, M. S. Golub, C. M. Koenig, L. Qi, I. N. Pessah, J. Van de Water, R. F. Berman, Maternal autism-associated IgG antibodies delay development and produce anxiety in a mouse gestational transfer model. *J Neuroimmunol* **252**, 56-65 (2012).
85. H. N. Shair, Acquisition and expression of a socially mediated separation response. *Behav Brain Res* **182**, 180-192 (2007).
86. L. J. Vanderschuren, V. Trezza, What the laboratory rat has taught us about social play behavior: role in behavioral development and neural mechanisms. *Curr Top Behav Neurosci* **16**, 189-212 (2014).
87. L. R. Qiu, D. J. Fernandes, K. U. Szulc-Lerch, J. Dazai, B. J. Nieman, D. H. Turnbull, J. A. Foster, M. R. Palmert, J. P. Lerch, Mouse MRI shows brain areas relatively larger in males emerge before those larger in females. *Nature Communications* **9**, (2018).
88. H. Premachandran, M. Zhao, M. Arruda-Carvalho, Sex Differences in the Development of the Rodent Corticolimbic System. *Front Neurosci* **14**, 583477 (2020).
89. L. Hammelrath, S. Škokić, A. Khmelinskii, A. Hess, N. van der Knaap, M. Staring, B. P. F. Lelieveldt, D. Wiedermann, M. Hoehn, Morphological maturation of the mouse brain: An in vivo MRI and histology investigation. *Neuroimage* **125**, 144-152 (2016).
90. L. Mengler, A. Khmelinskii, M. Diedenhofen, C. Po, M. Staring, B. P. Lelieveldt, M. Hoehn, Brain maturation of the adolescent rat cortex and striatum: changes in volume and myelination. *Neuroimage* **84**, 35-44 (2014).
91. A. E. Clipperton-Allen, O. S. Cohen, M. Aceti, A. Zucca, J. Levy, J. Ellegood, J. P. Lerch, D. T. Page, Pten haploinsufficiency disrupts scaling across brain areas during development in mice. *Transl Psychiatry* **9**, 329 (2019).
92. J. C. Lima, L. M. Oliveira, M. T. Botelho, T. S. Moreira, A. C. Takakura, The involvement of the pathway connecting the substantia nigra, the periaqueductal gray

matter and the retrotrapezoid nucleus in breathing control in a rat model of Parkinson's disease. *Exp Neurol* **302**, 46-56 (2018).
93. N. Omelchenko, S. R. Sesack, Periaqueductal gray afferents synapse onto dopamine and GABA neurons in the rat ventral tegmental area. *Journal of Neuroscience Research*, NA-NA (2009).
94. S. X. Luo, E. J. Huang, Dopaminergic Neurons and Brain Reward Pathways. *The American Journal of Pathology* **186**, 478-488 (2016).
95. L.-F. Yeh, T. Ozawa, J. P. Johansen, Functional organization of the midbrain periaqueductal gray for regulating aversive memory formation. *Molecular Brain* **14**, (2021).
96. K. S. Hemington, M. A. Coulombe, The periaqueductal gray and descending pain modulation: why should we study them and what role do they play in chronic pain? *J Neurophysiol* **114**, 2080-2083 (2015).
97. V. Coizet, E. J. Dommett, P. Redgrave, P. G. Overton, Nociceptive responses of midbrain dopaminergic neurones are modulated by the superior colliculus in the rat. *Neuroscience* **139**, 1479-1493 (2006).
98. X. Gu, T. J. Zhou, E. Anagnostou, L. Soorya, A. Kolevzon, P. R. Hof, J. Fan, Heightened brain response to pain anticipation in high-functioning adults with autism spectrum disorder. *European Journal of Neuroscience* **47**, 592-601 (2018).
99. H. E. Albers, Species, sex and individual differences in the vasotocin/vasopressin system: relationship to neurochemical signaling in the social behavior neural network. *Frontiers in neuroendocrinology* **36**, 49-71 (2015).
100. V. Michael, J. Goffinet, J. Pearson, F. Wang, K. Tschida, R. Mooney, Circuit and synaptic organization of forebrain-to-midbrain pathways that promote and suppress vocalization. *eLife* **9**, (2020).
101. T. J. Pisano, Z. M. Dhanerawala, M. Kislin, D. Bakshinskaya, E. A. Engel, E. J. Hansen, A. T. Hoag, J. Lee, N. L. De Oude, K. U. Venkataraju, J. L. Verpeut, F. E. Hoebeek, B. D. Richardson, H.-J. Boele, S. S. H. Wang, Homologous organization of cerebellar pathways to sensory, motor, and associative forebrain. *Cell Reports* **36**, 109721 (2021).
102. E. Kelly, F. Meng, H. Fujita, F. Morgado, Y. Kazemi, L. C. Rice, C. Ren, C. O. Escamilla, J. M. Gibson, S. Sajadi, R. J. Pendry, T. Tan, J. Ellegood, M. A. Basson, R. D. Blakely, S. V. Dindot, C. Golzio, M. K. Hahn, N. Katsanis, D. M. Robins, J. L. Silverman, K. K. Singh, R. Wevrick, M. J. Taylor, C. Hammill, E. Anagnostou, B. E. Pfeiffer, C. J. Stoodley, J. P. Lerch, S. du Lac, P. T. Tsai, Regulation of autism-relevant behaviors by cerebellar-prefrontal cortical circuits. *Nat Neurosci* **23**, 1102-1110 (2020).
103. I. Carta, C. H. Chen, A. L. Schott, S. Dorizan, K. Khodakhah, Cerebellar modulation of the reward circuitry and social behavior. *Science* **363**, eaav0581 (2019).
104. B. A. Beyer, M. Fang, B. Sadrian, J. R. Montenegro-Burke, W. C. Plaisted, B. P. C. Kok, E. Saez, T. Kondo, G. Siuzdak, L. L. Lairson, Metabolomics-based discovery of a metabolite that enhances oligodendrocyte maturation. *Nat Chem Biol* **14**, 22-28 (2018).
105. M. C. Shivaraj, G. Marcy, G. Low, J. R. Ryu, X. Zhao, F. J. Rosales, E. L. Goh, Taurine induces proliferation of neural stem cells and synapse development in the developing mouse brain. *PLoS One* **7**, e42935 (2012).
106. R. J. Huxtable, Taurine in the central nervous system and the mammalian actions of taurine. *Prog Neurobiol* **32**, 471-533 (1989).

107. E. Park, I. Cohen, M. Gonzalez, M. R. Castellano, M. Flory, E. C. Jenkins, W. T. Brown, G. Schuller-Levis, Is Taurine a Biomarker in Autistic Spectrum Disorder? *Adv Exp Med Biol* **975**, 3-16 (2017).
108. P. R. Louzada, A. C. P. Lima, D. L. Mendonca□Silva, F. Noël, F. G. De Mello, S. T. Ferreira, Taurine prevents the neurotoxicity of β□amyloid and glutamate receptor agonists: activation of GABA receptors and possible implications for Alzheimer's disease and other neurological disorders. *The FASEB Journal* **18**, 511-518 (2004).
109. O. Faria, D. G. Gonsalvez, M. Nicholson, J. Xiao, Activity□dependent central nervous system myelination throughout life. *Journal of Neurochemistry* **148**, 447-461 (2019).
110. Y. Zhao, L. Yang, G. Gong, Q. Cao, J. Liu, Identify aberrant white matter microstructure in ASD, ADHD and other neurodevelopmental disorders: A meta-analysis of diffusion tensor imaging studies. *Prog Neuropsychopharmacol Biol Psychiatry* **113**, 110477 (2022).
111. R. J. Jou, H. E. Reed, M. D. Kaiser, A. C. Voos, F. R. Volkmar, K. A. Pelphrey, White Matter Abnormalities in Autism and Unaffected Siblings. *The Journal of Neuropsychiatry and Clinical Neurosciences* **28**, 49-55 (2016).
112. K. Aoyama, Glutathione in the Brain. *International Journal of Molecular Sciences* **22**, 5010 (2021).
113. D. A. Geier, J. K. Kern, C. R. Garver, J. B. Adams, T. Audhya, M. R. Geier, A Prospective Study of Transsulfuration Biomarkers in Autistic Disorders. *Neurochemical Research* **34**, 386-393 (2009).
114. D. Endres, L. Tebartz Van Elst, S. A. Meyer, B. Feige, K. Nickel, A. Bubl, A. Riedel, D. Ebert, T. Lange, V. Glauche, M. Biscaldi, A. Philipsen, S. J. Maier, E. Perlov, Glutathione metabolism in the prefrontal brain of adults with high-functioning autism spectrum disorder: an MRS study. *Molecular Autism* **8**, (2017).
115. H. Liu, Y. Wang, J. Liu, W. Fu, Proteomics analysis of fetal growth restriction and taurine□treated fetal growth restriction rat brain tissue by 2D□DIGE and MALDI□TOF/TOF MS analysis. *International Journal of Molecular Medicine*, (2019).
116. B. Tan, D. J. Jiang, H. Huang, S. J. Jia, J. L. Jiang, C. P. Hu, Y. J. Li, Taurine protects against low-density lipoprotein-induced endothelial dysfunction by the DDAH/ADMA pathway. *Vascul Pharmacol* **46**, 338-345 (2007).
117. J. R. Dawson, M. Biasetti, S. Messina, J. Dominy, The cytoprotective role of taurine in exercise-induced muscle injury. *Amino Acids* **22**, 309-324 (2002).
118. C.-M. Vacher, J. J. O'Reilly, J. Salzbank, H. Lacaille, D. Bakalar, S. Sebaoui-Illoul, P. Liere, C. Clarkson-Paredes, T. Sasaki, A. Sathyanesan, Y. I. Kawasawa, A. Popratiloff, K. Hashimoto-Torii, V. Gallo, M. Schumacher, A. A. Penn, (2019).

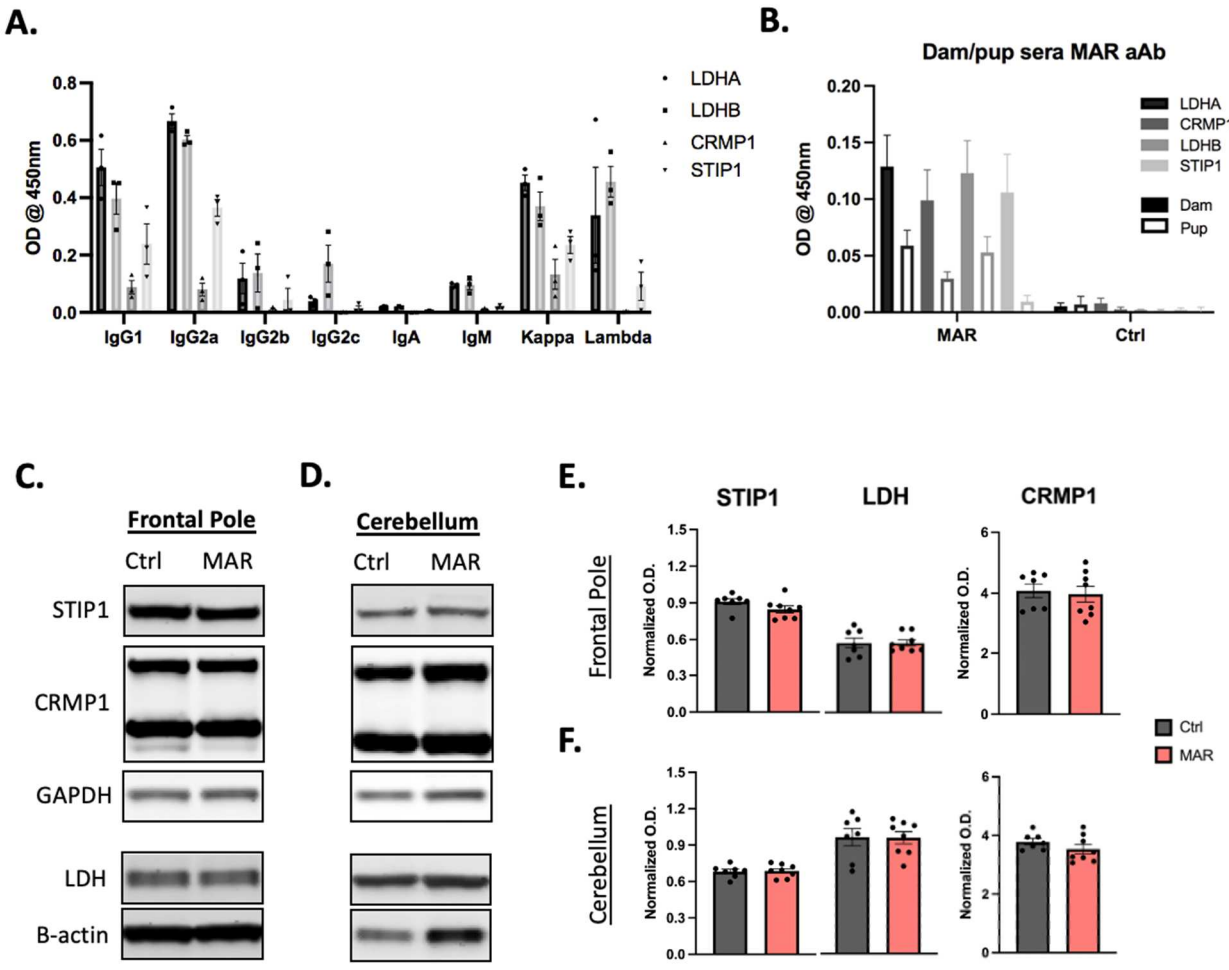

Figure S1. MAR-ASD antibody levels in offspring and effects on target proteins. (A) Distribution of antigen-specific antibody isotype and subclass in MAR-ASD offspring at P2. Data expressed as optical density (OD) values from a custom ELISA assay recorded at 450nm. **(B)** Raw OD values for dam/pup total antigen-specific IgG levels. Data split by treatment, solid-colored bars represent dam values with clear bars being offspring at P2. **(C & D)** Representative western blot reactivity for MAR-ASD protein targets with appropriate loading controls from either the Frontal Pole **(C)** or the Cerebellum **(D)**. **(E & F)** Quantification of western blot results for each brain area. MAR ASD; N=8, Ctrl; N=7, data expressed as mean +/- SEM.

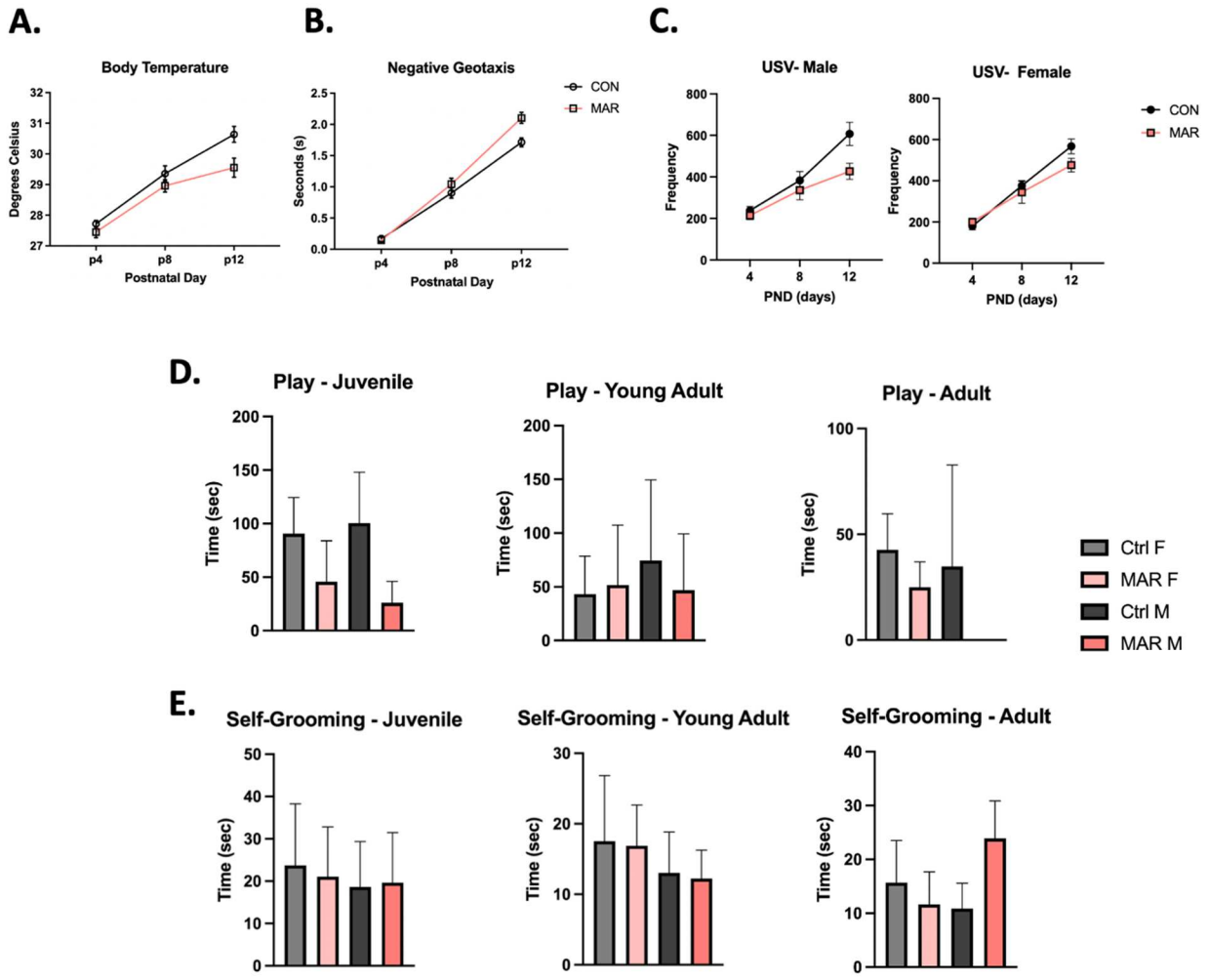

Figure S2. Behavioral outcomes by sex and timepoint. Developmental milestone data displaying treatment-specific differences in body temperature **(A)** and negative geotaxis **(B)**. **(C)** USV data split by sex and treatment. These data represented as mean +/-SEM, *=p<0.05. **(D)** Social play behavior during social dyads split by sex and treatment across each timepoint. **(E)** Self-grooming behavior split by sex and treatment across each timepoint. data represented as mean + 95% CIs. USVs/Developmental Milestones (**MAR**; N=48, **Control**; N=40), Social Dyad/Self-grooming (**MAR**; N=24; **Control**; N=20).

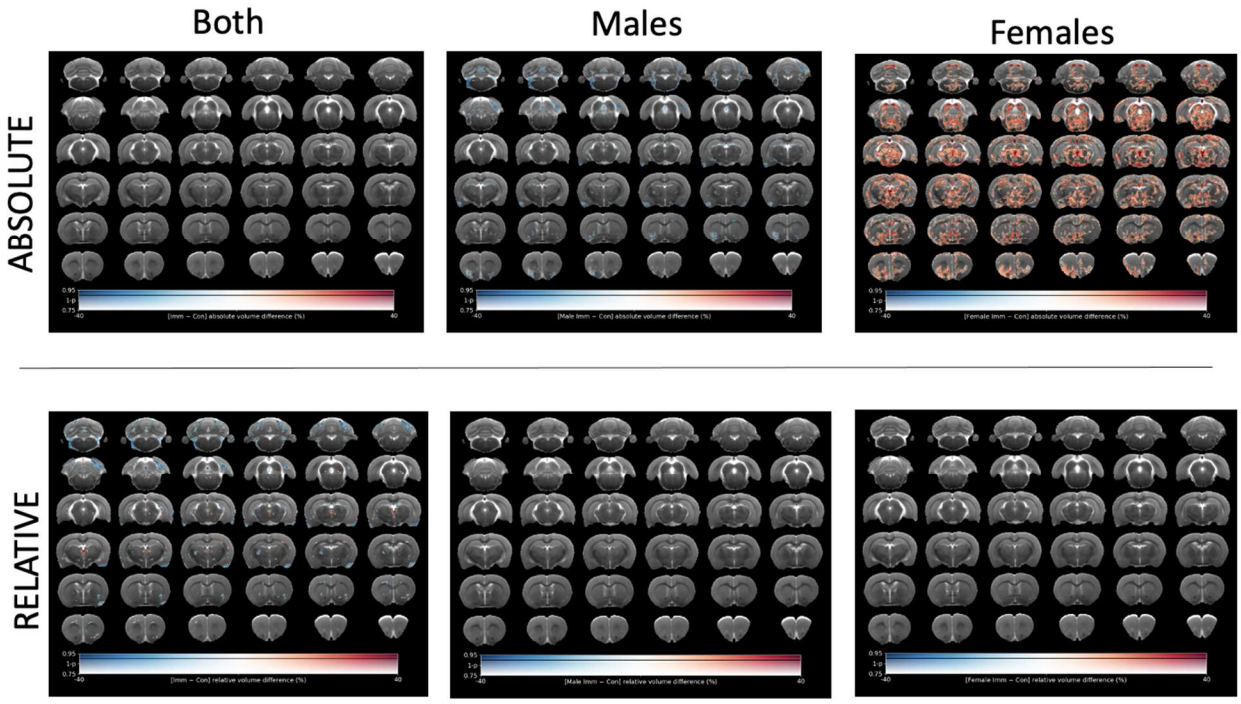

Figure S3. Voxel-wise analysis of brain volume. MRI images depicting voxel-wise data as a heatmap of the percent difference in absolute or relative volume between MAR-ASD (Imm) and control (Con) offspring. Split by sex or combined in the "both" condition. Red represents an increased volume difference while blue represents a volumetric decrease. Areas highlighted by contour represent clusters of voxels that passed 5% FDR correction. Uncorrected p-values are colored areas shown without contour.

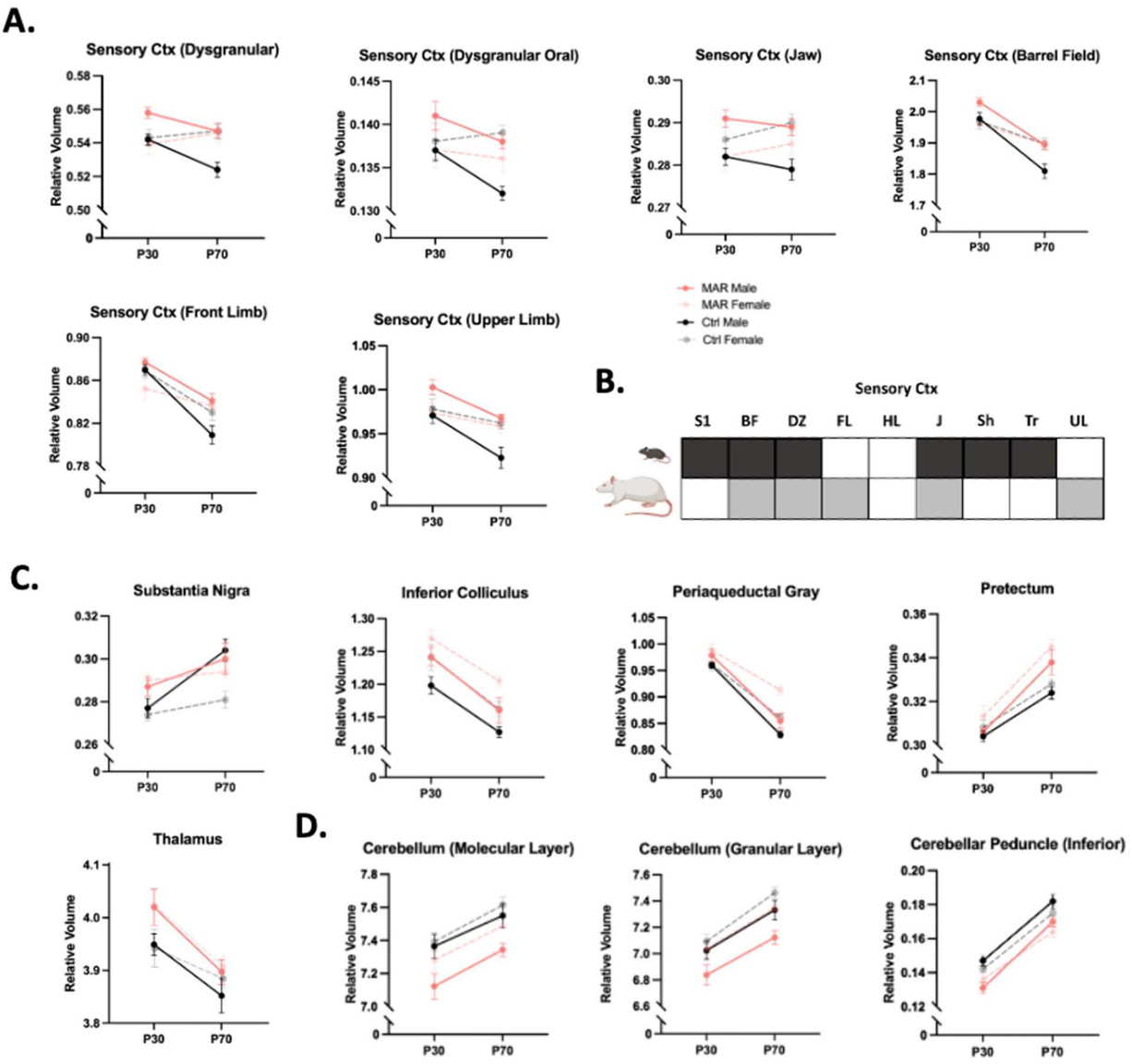

Figure S4. **Relative regional volumetric differences by time, sex, and treatment.** Regions determined to be significantly different by treatment in the sensory cortex **(A)**, midbrain **(C)**, and cerebellum **(D)**. **(B)** Comparison of regions affected by treatment within the sensory cortex between rats and mice (data taken from Bruce et al; 2021). Grey represents regions significantly different by treatment in rats and passing FDR correction ($p<0.05$, $q<0.05$). Black represents regions in MAR-ASD mice that passed significance testing but not multiple comparison testing ($p<0.05$, $q>0.05$).

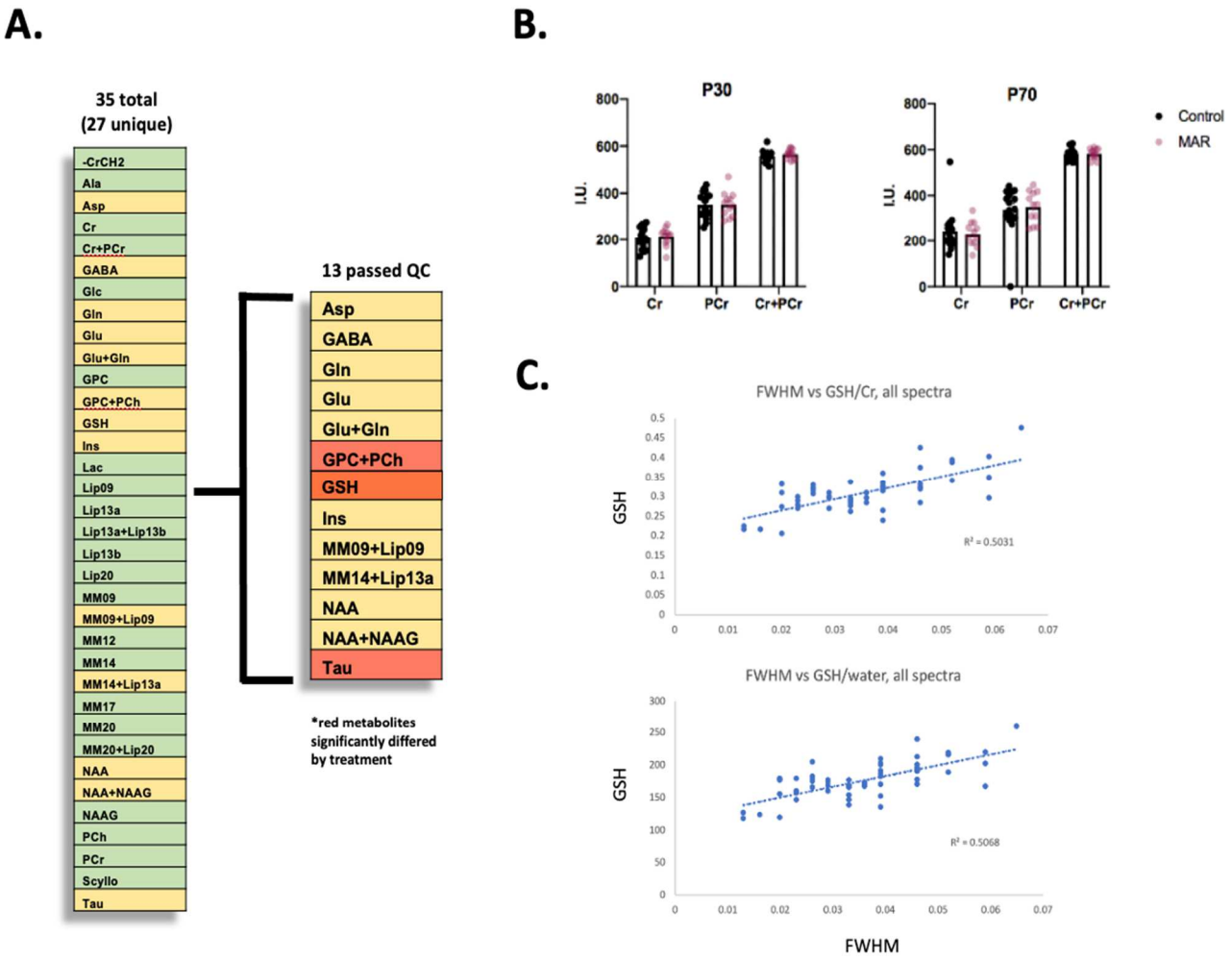

Figure S5. **Additional MRS metabolite data. (A)** Visual representation of total metabolites and quality control (QC) filtering. **(B)** Water-scaled creatine (Cr), phosphocreatine (PCr), or Cr + PCr values plotted by treatment group. Data expressed as mean +/- SEM. **(C)** Scatterplot of the correlation between glutathione (GSH) levels and full width half maximum (FWHM), shown normalized against creatine or water on separate graphs. R2 included as linear fit value.

CHAPTER 5
Conclusions and Future Directions

Conclusions and Future Directions

The subfield of neuroimmunology, which studies the intersection of the nervous and immune systems, is still in its infancy. Not long ago, the discipline was dominated by research focused on CNS autoimmune neuropathy, including multiple sclerosis (MS) and amyotrophic lateral sclerosis (ALS), where efforts were focused around reducing immune cell infiltrates and related pro-inflammatory pathology in the CNS. Now it is better understood that the interactions between the immune system and the CNS expand well past traditional CNS autoimmune diseases and are likely very important for CNS development and homeostatic functioning (*1*). Work described in Chapter 2 detailed robust cytokine signaling in the CNS during the early postnatal period, both in response to peripheral stimulation and at baseline. These data suggest that cytokine signaling may be important for normal CNS development and functioning. Additionally, it could be the case that these cytokines and signaling molecules may act locally in the brain parenchyma, as increased immunoreactivity to putative cell activation markers was seen in astrocytes in microglia. The capacity for cytokines to cross the BBB has been known for several decades (*2*), and substantial work has been conducted to understand the effects of different cytokines on the CNS (*3-5*). However, further work is needed to determine the specific mechanisms of cytokine signaling including the dominant secreting cells and range of parenchymal-resident cells that can respond to such signals. Additionally, to what extent these effects may be age-, or sex-dependent.

Cytokines are not the only immune molecules that can influence CNS signaling. Recent work has suggested that immunoglobulin, specifically immunoglobulin M (IgM), can impact oligodendrocyte-precursor cell (OPC) maturation and proliferation in the brains of neonatal mice

(*6*). Immunoglobulin has limited capacity to cross the BBB due to size, however active transport mechanisms do exist, and a range of Fc-receptors are present on CNS neurons (*7*), supporting a role for immunoglobulin signaling in the brain. This role is likely most important during development when the BBB is immature. In fact, IgG is abundant in the neonatal brain at postnatal day 2 and appears to have regional and sex-specific distribution (self-report; preliminary data). However, whether this brain IgG deposition has functional consequences has yet to be determined. Antibodies reactive to brain-enriched proteins are a common cause of neurological issues in children. One such example is the phenomenon of MAR-ASD, where mothers of children with ASD present with specific patterns of circulating aAbs to antigens important for early brain development (*8*). Chapters 3 & 4 describe experiments to understand the effects of MAR-ASD using preclinical platforms, mice, and rats respectively. Collectively these studies determined that gestational exposure to MAR-ASD aAbs results in longitudinal changes in behavior and structural brain volume, with translational significance to what is seen clinically in individuals with ASD. Additionally, alterations in levels of important neurometabolites were observed in rat offspring in the medial prefrontal cortex that could be related to the neurodevelopmental outcomes. Ultimately, mechanistic studies are needed to evaluate whether these MAR-ASD aAb are inducing pathology via direct interactions with target proteins in offspring or if there may be indirect mechanisms through modulation of placental function, for example as the antibodies must cross over this barrier to reach the fetal compartment. Current efforts are focused on cell culture experiments to address these very questions. The goal being to understand the development of this ASD endophenotype to assist in early intervention strategies or development of targeted therapeutics.

References

1. E. Nutma, H. Willison, G. Martino, S. Amor, Neuroimmunology - the past, present and future. *Clin Exp Immunol* **197**, 278-293 (2019).
2. W. A. Banks, A. J. Kastin, R. D. Broadwell, Passage of cytokines across the blood-brain barrier. *Neuroimmunomodulation* **2**, 241-248 (1995).
3. M. D. Reed, Y. S. Yim, R. D. Wimmer, H. Kim, C. Ryu, G. M. Welch, M. Andina, H. O. King, A. Waisman, M. M. Halassa, J. R. Huh, G. B. Choi, IL-17a promotes sociability in mouse models of neurodevelopmental disorders. *Nature* **577**, 249-253 (2020).
4. A. J. Filiano, Y. Xu, N. J. Tustison, R. L. Marsh, W. Baker, I. Smirnov, C. C. Overall, S. P. Gadani, S. D. Turner, Z. Weng, S. N. Peerzade, H. Chen, K. S. Lee, M. M. Scott, M. P. Beenhakker, V. Litvak, J. Kipnis, Unexpected role of interferon-gamma in regulating neuronal connectivity and social behaviour. *Nature* **535**, 425-429 (2016).
5. N. C. Derecki, A. N. Cardani, C. H. Yang, K. M. Quinnies, A. Crihfield, K. R. Lynch, J. Kipnis, Regulation of learning and memory by meningeal immunity: a key role for IL-4. *J Exp Med* **207**, 1067-1080 (2010).
6. S. Tanabe, T. Yamashita, B-1a lymphocytes promote oligodendrogenesis during brain development. *Nat Neurosci* **21**, 506-516 (2018).
7. M. Stamou, A. C. Grodzki, M. van Oostrum, B. Wollscheid, P. J. Lein, Fc gamma receptors are expressed in the developing rat brain and activate downstream signaling molecules upon cross-linking with immune complex. *J Neuroinflammation* **15**, 7 (2018).
8. D. Braunschweig, P. Krakowiak, P. Duncanson, R. Boyce, R. L. Hansen, P. Ashwood, I. Hertz-Picciotto, I. N. Pessah, J. Van de Water, Autism-specific maternal autoantibodies recognize critical proteins in developing brain. *Transl Psychiatry* **3**, e277 (2013).